Enantioselective Di-π-Methane Rearrangements and Mechanism Guided Investigations into Photochemical Reactions

By

Samuel B. Cahoon

A dissertation submitted in partial fulfillment of

the requirements for the degree of

Doctor of Philosophy

(Chemistry)

at the

UNIVERSITY OF WISCONSIN-MADISON

2022

Date of the final oral examination: 12/09/2022

The dissertation is approved by the following members of the Final Oral Committee:

Tehshik P. Yoon, Professor, Organic Chemistry

Samuel H. Gellman, Professor, Chemical Biology

Clark R. Landis, Professor, Inorganic Chemistry

Andrew J. Boydston, Yamamoto Family Professor, Materials Chemistry

Enantioselective Di-π-Methane Rearrangements and Mechanism Guided Investigations into Photochemical Reactions

Samuel Burton Cahoon

Under the supervision of Professor Tehshik P. Yoon

at the University of Wisconsin-Madison

Abstract

The development of enantioselective photochemical transformations has been the focus of an increasingly significant body of research over the past several years. Despite this increased level of attention, a catalytic highly-enantioselective photochemical rearrangement has yet to be reported for a triplet-sensitized reaction. The work in this dissertation details the development of a highly enantioselective di-π-methane reaction proceeding through triplet sensitization by an iridium sensitizer and catalytic enantiocontrol by a BINOL-phosphoric acid derived co-catalyst. Notably, these studies uncovered the dependence of di-π-methane sensitization rates on the electronic perturbation of conjugated carbonyl substituents, revealed design principles for optimal substrate structures, and investigated polarity dependent solvent effects on enantioselectivity at low temperatures. The development of this method is expected to inform strategies to broaden the applicable scope of catalytic, enantioselective, triplet-sensitized reactions.

Acknowledgements

Life before Death. Strength before Weakness. Journey before Destination.

-The Way of Kings, Brandon Sanderson

First and foremost, I feel that I owe a great debt of thanks to my principal Ph.D. advisor, Tehshik Yoon. Tehshik has been a wonderful advisor, mentor, and friend throughout my time at UW-Madison. Through all of the highs and lows that accompany the journey that is a Ph.D., Tehshik has consistently reminded me that it is, in fact, all about the journey rather than the destination. I don't believe I ever left a consultation with Tehshik in which I was not reminded that my growth as a scientist, and as a person, was about what I was becoming, rather than about what I was doing. I hope that I can say that the message finally stuck. The past six years have held extraordinary challenges for me personally, for my family, and for the world at large. Through all of this, Tehshik has patiently helped me stay grounded, focused, and oriented on the goals I cared most about achieving. His instruction was extremely influential on my development as a thinker and problem solver, and I plan to carry that forward as I continue my career.

I would also like to acknowledge the influence of Sam Gellman and Clark Landis as members of my dissertation committee and for their guidance as exemplary mentors. In addition to benefiting from their advice as referees to evaluate my development as a scientist, I appreciated the opportunity I had to observe the ways in which Sam and Clark acted as thought leaders in their scientific fields and as leaders in

our department. Through their examples, I have grown to appreciate the value of careful consideration to detail and the benefits of asking critical questions, both of yourself and others. Indeed, the goal of science is to produce an understanding that stands up to scrutiny from any angle, and to find ways to probe the unknown when it does not. Additionally, I would like to thank AJ Boydston for agreeing to serve on my final dissertation committee. AJ joined our department in the end of my second year, and I have greatly appreciated the diversity in chemical study and thought he and his group brought with them.

I cannot understate the value of the support I have received from members of the Yoon lab. The daily tasks, frequent disappointments, and intermittent emotional highs associated with research are exhausting on the best of days. Having a network of friends and colleagues who shared those experiences with me and who contributed to making the social atmosphere engaging and supportive played an important role in my success. I would especially like to thank Jesse Kidd and Steven Chapman, who both joined the lab the same year I did. I could not have thrived without their friendship. I would also like to thank Nic Reed and Chris Gravatt, with whom I shared an office for the greater portion of my time. In addition to their friendship and moral support, I owe most of what I know about laboratory technique and practical chemistry to their instruction and example.

The instrumentation staff at UW-Madison are imperative to the function of almost all aspects of research progress in the department, and my Ph.D. would not have been possible without them. Thank you to Heike Hofstetter, Charlie Fry, and Cathy Clewett for maintaining the NMR facility and facilitating our ability to acquire quality data with exceptional efficiency. Thanks to Martha Vestling and Robert Shanks for maintaining the mass spectrometry facility, Ilia Guzei for heading the X-ray crystallography lab, and Tracy Drier for running the glass-blowing facility and producing much of the glassware used in my study. Additional thanks to Jeff Nielsen, Rob McClain, and Bob McMahon for administration of the physical facilities and their daily support of the building and department that enable our research.

Finally, I owe a debt of gratitude to my family for their support. My Ph.D. was simultaneously complicated and made possible by their influence in my life. Special thanks to my wife, Autumn Cahoon, for her resilience and encouragement when I needed it most. In many ways I share all of my accomplishments with her. My family expanded by four during my Ph.D., with the births of Grace, Aiya, Blaire, and Charlotte. Managing the balance between caring for them and working on my research was challenging, and yet also incredibly rewarding. In many ways I share all of my accomplishments with them.

Table of Contents

Chapter 1 Mechanistic Understanding as a Guiding Principle for Synthetic Organic Photochemistry

1.1 Previous Publication of This Work

A version of the material presented in this chapter has been previously published:

Cahoon, S. B., Yoon, T. P., Science of Synthesis: Free Radicals: Fundamentals and Applications in Organic Synthesis, **2021**, 1, 159.

1.2 Introduction

The development of reactions utilizing light as the sole energy source to afford novel synthetic reactivity has received significant attention from synthetic and physical chemists over the past century. This interest is fueled by the unique reactivity available to the electronically excited intermediates and radical species that can be accessed through photochemical systems. While traditional photochemical methods utilized high-energy UV light to effect most reported transformations, the development of modern photocatalysts, such as common organic dyes and metal-polypyridyl complexes, allows for the use of low-energy visible light to achieve similar reactivity. This advance has fueled a renewed interest in the development of new reactions with enhanced synthetic applicability and scope. Indeed, independent publications by the Yoon, MacMillan, and Stephenson groups in 2008 and 2009 showcased the potential of visible-light-induced photocatalysis to effect synthetically powerful transformations, Figure 1.1.[1–3]

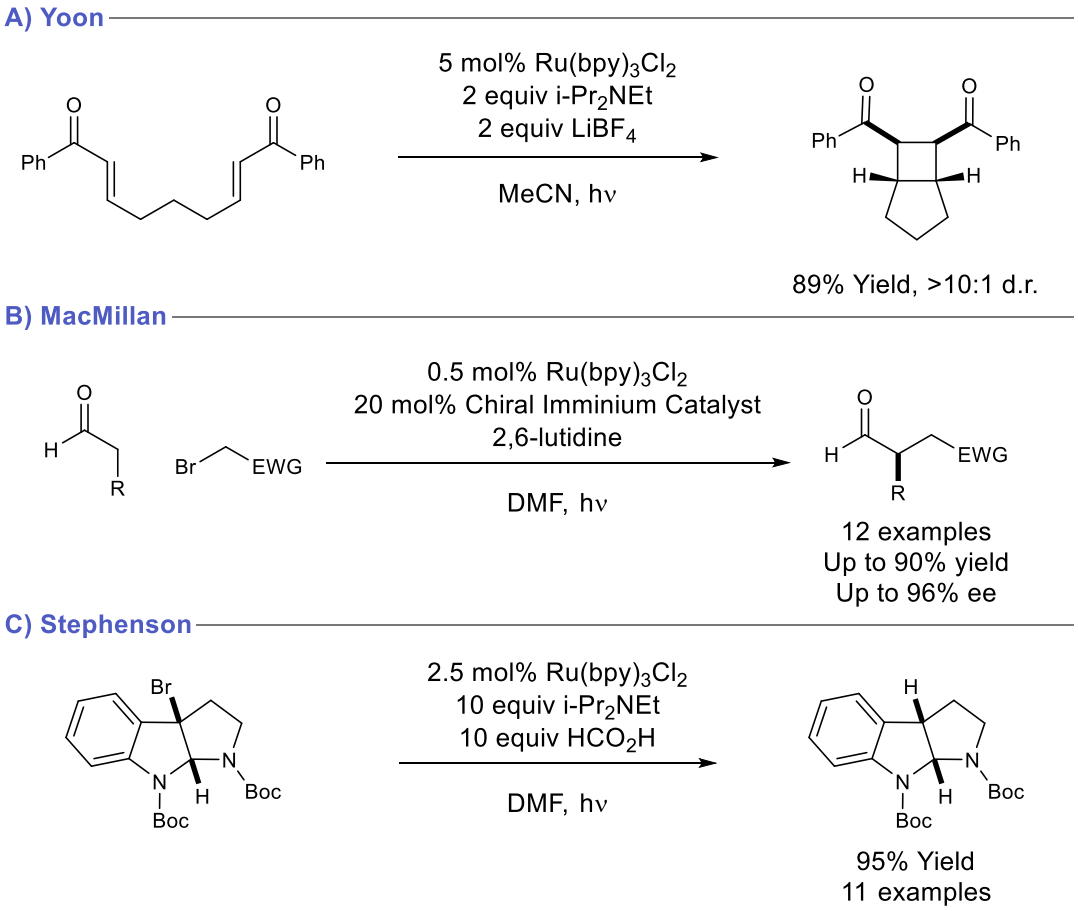

Figure 1.1 Synthetic Applications of Transition Metal Photocatalysts

Following these seminal publications, the field of synthetic organic photochemistry has undergone a veritable renaissance, with over 94,000 journal publications and nearly 9,000 reviews on the subject published since 2009.[a] The number of reported reactions in the field continues to increase each year; however, as the field approaches a more mature stage, many researchers agree that sustained development

[a] Scifinder search on 11/8/2022

of novel methods will rely on increased attention to mechanistic analysis. In support of this initiative, several excellent reviews on photocatalyst characterization and design, as well as on the importance of investigating reaction mechanisms and relevant techniques, have recently been published.[4–10] As a complement to these excellent resources, a tutorial review on mechanistic techniques and their successful applications was published during the course of the studies that will be presented in this thesis.[11]

All of the studies presented in this thesis shared the common theme of mechanism guided investigation. As such topics will be frequently visited in the following text, this chapter is included to provide a short review of the mechanisms operative in synthetic photochemistry and the analytical methods used to differentiate them and understand their elementary steps.

1.3.1 Introduction to Photochemical Mechanisms

In the simplest sense, a photochemical reaction is one in which the primary reactivity is driven by the ability of some species to absorb light and access an electronically excited intermediate. These excited-state intermediates then transfer some or all of the energy absorbed to other substrates in solution or relax back to their ground states via photon emission, vibrational or thermal relaxation, or molecular rearrangement. The value of photochemical processes lies in the ability to use light, a relatively cheap and

available resource, to generate reactive intermediates with electron configurations and orbital symmetries that would otherwise be inaccessible via thermal means.

Traditionally, such excited states were often reached via irradiation with high-energy UV light. Unfortunately, such conditions often proved to be incompatible with complicated molecular functionality and the limited scope of these processes prevented their widespread application. One solution to this drawback that has received particular attention is the use of common chromophores, such as transition metal polypyridyl complexes or organic dyes, to absorb visible light and transfer that energy to organic substrates. These photocatalysts are valued for their ease of use, generally long excited-state lifetimes, and their potential to transfer energy to organic substrates via a number of valuable reaction types. These reaction types include energy transfer (EnT), single-electron transfer (SET), atom transfer (commonly hydrogen-atom transfer or HAT), and proton-coupled electron transfer (PCET). Methods utilizing such catalysts dominate the bulk of contemporary literature reports.[7,12–18] It is notable, however, that while most small molecule organic compounds do not absorb in the visible range, development of systems taking advantage of encounter complexes, electron donor-acceptor (EDA) complexes, and acid-base pairing to shift absorption ranges to longer wavelengths and directly access excited states of small molecule organics via visible or near-visible wavelengths have become increasingly common.[19,20]

While there are relatively few modes of reactivity that are likely to be operable in a photochemical system compared to those accessible to thermal systems, the scope of organic reactions that have been developed using these mechanisms is significant. One key to the continued expansion of the synthetic applicability of photochemical methods has been the careful study and differentiation of such activation modes, and continued study will be necessary to maximize the synthetic potential of future developments. Despite the limited mechanistic possibilities, however, the fleeting nature of high-energy excited state or radical ion intermediates common to photocatalytic processes presents a unique challenge for researchers interested in elucidating the active mechanisms at play in a given system.

In the current paradigm of modern photocatalysis, visible light excitation of a catalyst yields an excited state species that subsequently interacts with an organic substrate to produce open-shell reactive intermediates via Dexter energy transfer (EnT), through a single electron transfer event (SET), or via atom transfer reactions. This initiating event is followed by a subsequent non-photochemical, product forming phase. Investigative techniques have been developed and refined to help differentiate the possible modes of activation at play and to interrogate the propagation and product forming steps of a reaction. The following sections treat these two phases and the experimental methods used to investigate them in turn.

1.3.2 Photochemical Initiation

The first step of any photochemical reaction is the excitation of some species by absorption of a photon of light. This typically leads to the formation of an electronically excited singlet-state species, or one in which electron spins are unchanged from the ground state. These transitions are referred to as "spin-allowed" due to the conservation of electron spin states. Singlet states are generally short-lived, though reactions occurring from the excited singlet have been reported.[21,22]

Typically, however, the excited singlet relaxes to a lower energy triplet state via intersystem crossing (ISC), a process that is generally fast and efficient for molecules containing heavy atoms, such as transition metal photocatalysts. The triplet is comparatively long-lived due to relaxation being a "spin-forbidden" transition, requiring the flip of electron spins, and thus is often assumed to be the reactive species in a photochemical system due to its relative persistence.

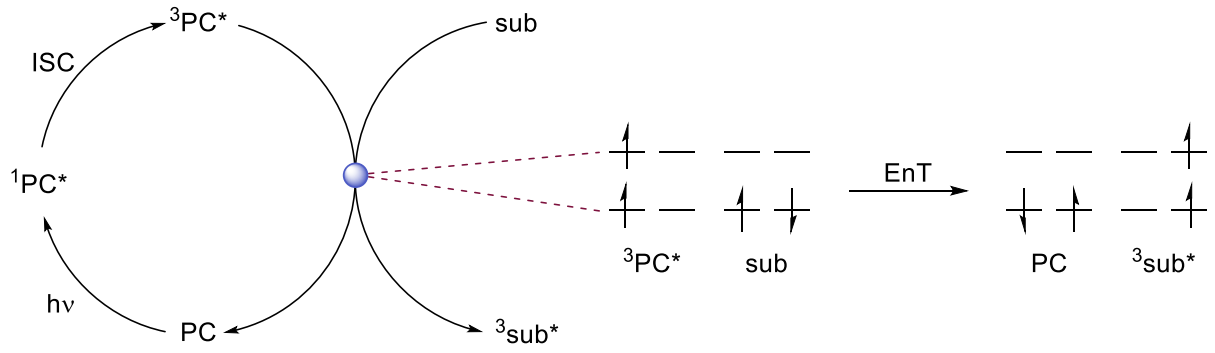

Figure 1.2 Energy Transfer Reactivity

Energy transfer takes place through a concerted two-electron swap between the singly occupied frontier orbitals of the excited triplet-state catalyst and the frontier orbitals of an organic substrate, Figure 1.2.[23] Kinetically facile transfer of electrons takes place as the catalyst returns to a ground state singlet, and the substrate is excited to a reactive triplet state. Because the actual orbital energies involved in these processes are difficult to calculate, a common mnemonic is often used to predict the ability of a catalyst to act as a triplet sensitizer in this fashion. It is generally accepted that if the triplet energy of the catalyst is greater than the triplet energy of the substrate, the reaction should be favorable. However, the degree of orbital overlap of the catalyst and substrate, and relative energies of the orbitals involved, are factors that are often difficult to predict and can cause the mnemonic to fail. In most photocatalytic systems this process occurs via a collisional interaction of sensitizer and substrate and is referred to as Dexter energy transfer.

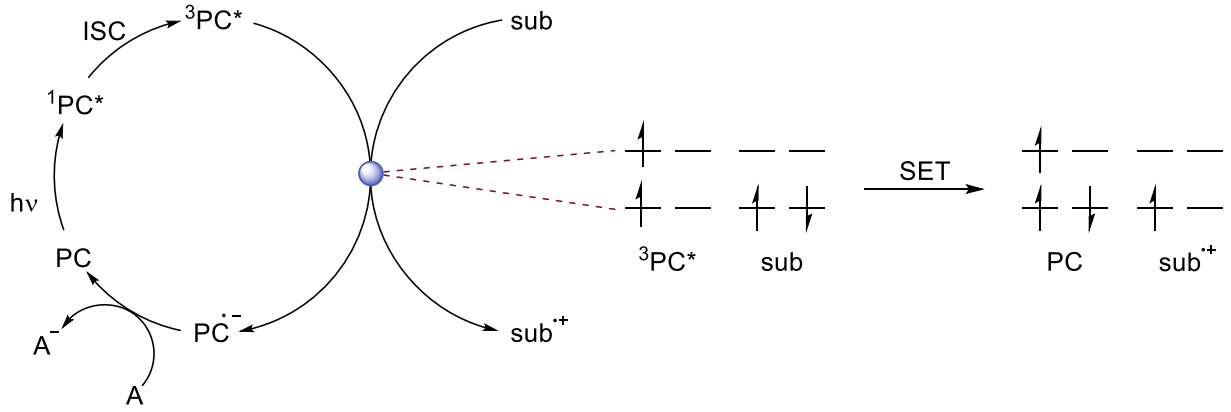

Figure 1.3 Single Electron Transfer Reactivity

The excited triplet state catalyst can also act either as a strong reductant or a strong oxidant due to the nature of the excited state presenting as both a high-energy electron donor and an electron hole, an example of which is shown in Figure 1.3. In the case shown above the excited-state photocatalyst oxidizes an organic substrate and becomes a potent ground-state one-electron reductant. In order to complete the catalytic cycle, this catalyst intermediate undergoes another electron transfer event, typically a back-electron transfer from the product of a radical chain process, to return to the original catalyst ground state. The converse reactive cycle from that pictured in Figure 1.3, with the photocatalyst first acting as a reductant then as an oxidant, is also possible, and reports of the use of both methods are common. While the nature of the photocatalytic cycle lends itself to the development of redox neutral transformations, it is, however, possible to achieve net-oxidative or net-reductive reactivity through the addition of an appropriate stoichiometric redox partner.[2,12,24–27]

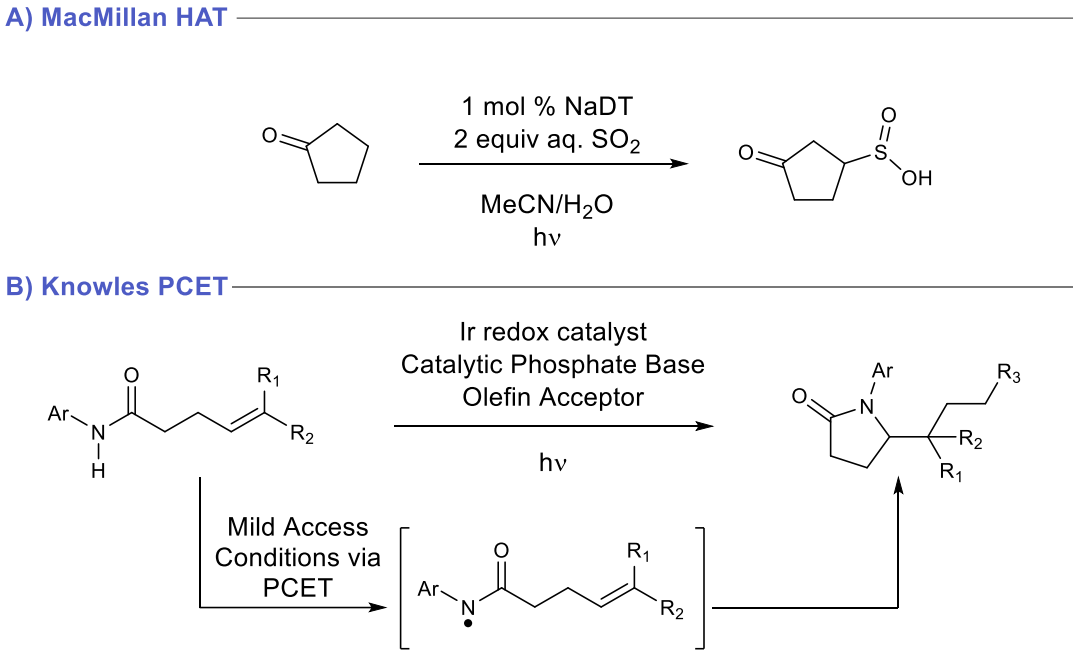

Figure 1.4 Literature examples of HAT and PCET reactivity

Atom transfer reactions, such as hydrogen atom transfer (HAT) and proton-coupled electron transfer (PCET) often rely on specialized catalysts or on ternary interactions with other species in solution. HAT reactions featured in the photochemical literature are generally of two types, (1) HAT reactions that take place after the formation of a radical intermediate produced through other processes, such as SET, or (2) primary reaction with specialized photocatalysts, such as anionic sodium decatungstate (NaDT) chromophores, that have been developed as competent HAT reagents, Figure 4.1a.[28–30] These reactions proceed through homolytic bond cleavage to yield open-shell radical intermediates, with the driving force for the transformation being provided by the relative X–H bond strengths of the two species involved in

the atom transfer step. PCET reactions, such as in Figure 1.4b, have used the combination of weak acids and mildly reducing photocatalysts or weak bases and oxidizing photocatalysts to afford radical species that would have normally been inaccessible based on their measured redox potentials.[18,24,31] These reactions typically benefit from milder activation conditions than their direct HAT counterparts.

Differentiating between these initiating reactions often begins with a thorough understanding of the properties of the excited state species in solution. The excited states of most common photocatalysts share properties that make them capable triplet sensitizers as well as potent oxidants and reductants. The exact triplet energies and excited state redox potentials of these catalysts are generally tunable via structural alteration of the catalyst body. Thus, whenever a new catalyst structure is developed it is necessary to characterize these excited state properties. This is done through a combination of UV-Vis spectroscopy, emission spectroscopy, and cyclic voltammetry.

1.3.2.1 UV-Visible Absorption Spectroscopy

UV-Visible Absorption spectroscopy (UV-Vis) is used to interrogate the wavelengths at which a given species absorbs light. This is performed by irradiating a sample across a range of wavelengths and measuring absorbance. The subsequent molar absorptivity of a compound at a given wavelength can be

calculated via Beer-Lambert law, $A = \varepsilon \times l \times c$, where A is the absorbance, ε is the molar absorptivity of the analyte, l is the path length, and c is the concentration of the analyte.

UV-Vis spectra are often used to pick an appropriate light source for a reaction. Most photocatalysts are strong chromophores and have a relatively high molar absorptivity compared to other substrates present in common synthetic reactions. However, because photocatalysts are generally present in very low concentrations, it is often desirable to irradiate the reaction solution at a wavelength that is outside the absorption window of other species in solution in order to avoid off-cycle reactivity.

The excitations measured via UV-Vis spectroscopy are singlet transitions. When reactivity from the singlet is suspected to be operable, performing UV-Vis at cryogenic temperatures can cause the broad absorptions typically seen in these experiments to coalesce into sharper bands for defined transitions. This is usually used in conjunction with fluorescence and phosphorescence spectroscopy emission data to characterize the active state of newly developed catalysts.

UV-Vis absorption spectroscopy can also be used to support the formation of photoactive encounter complexes in solution. Such an encounter complex will demonstrate an absorption profile that is greater than the sum of its individual parts. Careful selection of an appropriate light source can be used to selectively

excite the encounter complex in the presence of its separate components. This has proven to be useful for a number of reaction types, including the development of enantioselective photochemical methods.[32,33]

It is also important to note that while any solvent can be used to perform UV-Vis measurements, the nature of the solvent can have significant effects on the singlet excited states being analyzed. Due to these solvatochromic effects, the solvent used in the measurement should ideally be matched to the solvent used for the reaction of interest.

1.3.2.2 Emission spectroscopy

After excitation, the singlet excited state can undergo a number of transitions, including relaxation though vibrational or emissive pathways or conversion to a triplet excited state via ISC. Though the triplet is longer lived due to relaxation being a spin-forbidden transition, it is also capable of undergoing vibrational and emissive decay. Singlet and triplet emissive decay are respectively termed fluorescence and phosphorescence, and these emissions can be measured via spectroscopic methods. To obtain these spectra, a sample is irradiated a wavelength known to be able to excite the compound being analyzed. Emission from the sample is then measured over time at a 90° angle relative to the excitation beam. Due to relaxations in the molecular geometry of the excited state, the singlet energy obtained from fluorescence spectroscopy

often differs slightly from that obtained by absorbance spectroscopy; the difference is referred to as a Stokes shift.

There have been several methods used in the literature to estimate the triplet energy of a photocatalyst based on its phosphorescence emission spectrum. These include using the wavelength at which the leading edge of the emission is 10% of the maximal emission intensity, using the point where a line tangential to the leading edge crosses the x-axis, and using the maximal emission point. As no standard has been universally adopted in the literature, reported values for common photocatalysts have differed by as much as 200 mV, or approximately 5 kcal/mol. [10,34]

The triplet energies of small molecule organic compounds are also theoretically measurable via the same spectroscopic methods as those used for photocatalysts. However, compounds lacking a heavy atom generally exhibit inefficient ISC and have emissions that are a mix of fluorescence and phosphorescence, which can be difficult to deconvolute. Additionally, small molecule organics are often not sufficiently emissive to obtain a reliable signal. In order to overcome some of these challenges it is possible to use time resolved spectroscopic methods to distinguish between emissive modes, or to perform spectroscopy in the presence and absence of oxygen, which often competently quenches triplet states and their emissions. Computation of excited state energies through the application of Density Functional Theory (DFT)

calculations has also been used as a substitute for emission spectroscopy when approximating the triplet energy of small molecule organic substrates. However, the most common basis sets used to run these calculations can fail to accurately account for the effects of electron correlation, often leading to significant errors in the predicted values.

1.3.2.3 Electrochemistry

Cyclic voltammetry can be used to identify the ground state redox potentials of each element in a reaction system. These values are necessary for calculating the excited state redox potentials of photocatalysts, as well as to investigate the feasibility of electron transfer events in a proposed reaction mechanism, which will be discussed in the following sections. The increasing prevalence of electrochemical methods in organic synthesis has led to the publication of several educational reviews on this subject, providing both theoretical and practical coverage of cyclic voltammetry and data aquisition.[6,35–37]

1.3.2.4 Calculation of Excited-State Redox Potentials

The excited state redox potentials of a photocatalyst cannot be directly measured. The potentials can be approximated, however, from the relevant ground state redox potentials, $E^{0'}_{Ox}$ and $E^{0'}_{Red}$, and the energy of the relevant excited state of the photocatalyst, E^{0-0}, via the Rehm–Weller equations.[10]

$E^{0^*}_{Ox} = E^{0'}_{Ox} - E^{0-0}$

$E^{0^*}_{Red} = E^{0'}_{Red} + E^{0-0}$

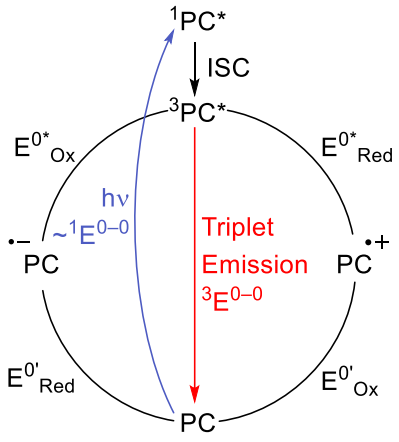

Figure 1.5 Photocatalyst Excitation State Diagram

These equations are derived from an understanding of the relative energies of the photocatalyst states depicted in Figure 1.5.[10] It is important to note that the relevant energy for E^{0-0} can be either for the singlet or the triplet state energy, depending on the persistence of the singlet state. For catalysts with relatively long-lived singlet excited states, it can be difficult to ascertain which excited state is responsible for observed redox activity. As discussed above for small organic molecules, time resolved emission spectroscopy and other molecular probes can be used to help discern the nature of active excited states.

1.3.2.5 Comparing the Thermodynamic Feasibility of Electron and Energy Transfer Steps

With substrate redox potentials and catalyst triplet energy and exited state redox potentials in hand it is occasionally possible to develop hypotheses about the operative mechanism in a photochemical system. Common intermediates of photochemical processes, such as radical ions or triplet excited state substrates, are generally not directly observable due to their high energies and reactivity. However, the thermodynamic feasibility of elementary steps can serve as informative considerations.

The feasibility of SET can be assessed from comparison of the relative redox potentials of the excited state catalyst and the reactants in solution. Occasionally, slightly unfavorable electron transfer events can be operable in a mechanism if subsequent steps provide a large enough driving force. Similarly, EnT events are considered to be favorable when the triplet energy of the catalyst is higher than that of the substrate, making the overall state change exergonic. However, the degree of orbital overlap of the catalyst and substrate, and relative energies of the orbitals involved, are factors that are often difficult to predict and can cause the mnemonic to fail. Endergonic energy transfers are also possible, but such cases require overcoming an additional kinetic barrier.[38]

While the marked infeasibility of either a SET or EnT step can serve as good evidence for operation of the other pathway, it is often the case that both reaction pathways are thermodynamically viable. In such cases, further investigation is necessary to provide adequate support for a proposed mechanism.

1.3.2.4 Alternate Chemical Initiation

The simple determination that SET is feasible in a system is often insufficient to show that it is primarily responsible for the observed reactivity. One technique that is frequently used to provide additional support for such an assertion is alternate initiation by chemical redox reagents known to effect one electron oxidations or reductions. While the overall reaction profile and yield obtained from such a reaction will likely differ significantly from the photochemical conditions, if the same product is produced in any capacity, it can be another reasonable indicator that a redox mechanism is operable in the photochemical system.

A notable application of this technique was in its use to support the proposed SET mediated reaction mechanism of some classes of Nickel photoredox cross couplings. Nocera and coworkers were able to show that they could obtain the same products reported in previous photochemical systems using a zinc metal reductant in place of a photocatalyst. Additionally, they showed that it was necessary to have only a small amount of reduced nickel present at any time to avoid shutting down the productive catalytic cycle, a point which previous investigations into the reaction mechanism had failed to fully capture. Nocera was

able to show that while photoredox catalysts excel at producing such an environment, where the concentration of redox equivalent is always low, similar conditions could be reached with careful control of a thermal system as well.[39–41]

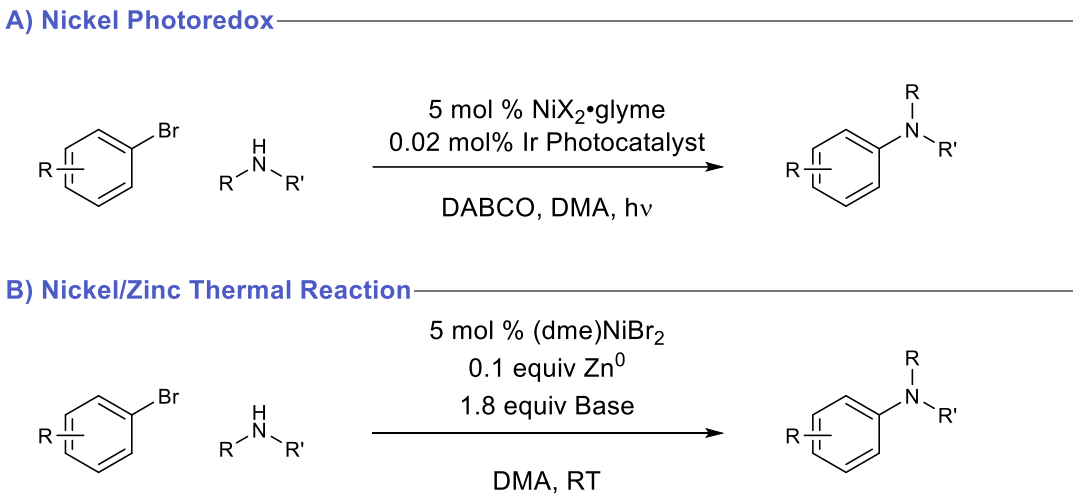

Figure 1.6 Alternate chemical initiation supports SET mechanism in Ni/Photoredox Couplings

1.3.2.5 Correlation Screens

Another experiment that can be used to differentiate between EnT and SET mechanisms is to correlate observed reactivity with either increasing excited state energy or redox potentials. The modularity and breadth of readily available photocatalysts allows for libraries to be built in which a range of triplet energies and redox potentials are represented and trends between the two are distinct. Subjection of the reaction system to such libraries, often comprised of ruthenium and iridium photocatalysts and some organic chromophores, has been used to provide support for both SET and EnT reaction mechanisms.

Because an increase in triplet energy does not necessarily correlate with an increase in excited state redox potentials, it is possible to independently compare reactivity trends across an appropriate selection of catalysts.[42] Care should be taken with this approach, as with all techniques, as differences in excited state lifetimes and the catalytic competency of the photocatalysts chosen can occasionally produce errant results that lead to false correlations. Additionally, this correlation method can be used to benchmark the approximate triplet energy of an organic substrate by using a range of catalysts to find the minimum energy a system requires to exhibit reactivity.[43] Photocatalyst triplet energies are typically much easier to measure than those of small molecule organic compounds, making this a useful approximation.

1.3.2.7 Time-Resolved Emission and Absorption Spectroscopy

Time-resolved emission spectroscopy offers a powerful method to study the kinetics of the photocatalytic initiation step. A photocatalyst can be excited using a short laser pulse, after which the intensity of emission can be monitored as a function of time. In the absence of a quencher, the intensity of emission decays with first-order kinetics, corresponding to the unimolecular relaxation of the excited state through both vibrational and emissive pathways. The addition of a quencher that reacts with the excited state, however, will increase the rate of decay. The second-order rate constant for the photoinitiation step

can be extracted from experiments that examine the change in decay rate as a function of quencher concentration, as discussed in the next section.

Time-resolved absorption spectra can be collected in a similar manner by using a probe beam to measure the absorption spectrum of the excited-state photocatalyst, typically as a difference spectrum relative to the ground-state absorption. The decay of the signals in the absorption spectrum can also be used to measure the lifetime of the excited state in the presence and absence of quenchers. However, the absorption spectra of the metal-to-ligand charge-transfer (MLCT) excited states that are characteristic of transition metal polypyridyl photocatalysts have distinct features that can be assigned to the formally oxidized metal center and the reduced ligand, respectively. The relative rate of decay of these signals provides evidence for the mechanism of photoinitiation. If the excited-state photocatalyst acts as a one-electron photooxidant, the signal corresponding to the oxidized metal center will decay at a faster rate than that of the ligand. If, on the other hand, it initiates the reaction by reducing the quencher, the reduced ligand signal will decay at a faster rate. Finally, in an energy-transfer activation step, where the oxidation state of the photocatalyst does not change, the quencher will have the same impact on the decay of both the metal and ligand signals. Thus, transient absorption spectroscopy can provide direct evidence for the

mechanism of photoinitiation. A tutorial review on the use of time-resolved spectroscopies to probe the mechanism of photocatalytic reactions has recently been published.[4]

Unfortunately, the equipment necessary to perform this kind of measurement is not commonly available in synthetic chemistry laboratories, which has led to the prevalence of other mechanistic methods in the photochemical literature.

1.3.2.8 Steady-State Stern-Volmer Quenching Studies

Stern-Volmer quenching studies can be used to interrogate the kinetics of the photocatalytic initiation step and help determine the identity of the substrate in solution that is most likely responsible for quenching the photocatalyst excited state. Unlike time resolved spectroscopies which require specialized spectrometers to perform, Stern-Volmer measurements can be performed with the same instruments used for common fluorescence and phosphorescence measurements.

These measurements are performed by obtaining emission spectra of a catalyst with varied concentrations of quencher and monitoring the decrease in observed emission intensity. This intensity ratio is related to quencher concentration by the relationship $I^0/I = 1 + k_q[Q]/k_0$, where I^0 is the emission of the unquenched catalyst, I is the emission intensity at a given quencher concentration, $[Q]$, k_q is the rate constant for bimolecular quenching, and k_0 is the decay rate of the excited state. Plotting this relationship

typically results in a linear plot with a y-intercept of 1, where the slope, k_q/k_0, is referred to as the Stern-Volmer constant. The relative rates of quenching by different species can be compared via the Stern-Volmer constant, even without the specialized equipment needed to measure the excited state decay rate, as long as the photocatalyst identity is the same for the two species being compared and no factors other than quenching are expected to influence the photocatalyst's excited state lifetime.

There are complications that can result in a non-linear Stern-Volmer plot. These include scenarios where both dynamic quenching (collisional quenching that is diffusion controlled) and static quenching (quenching by pre-associated substrates) are active. Another possible scenario that could lead to a non-linear relationship is when the quencher being introduced also absorbs at the excitation wavelength, leading to an inner filter effect. This should be avoided by picking an excitation wavelength outside of the substrate's absorption range but can also be corrected for using Beer's law.

1.3.3 Propagation of Photocatalytic Cycles and Product Formation

In addition to methods designed to probe the nature of the excitation or catalyst quenching events, methods focusing on the downstream reactivity of activated intermediates can also inform studies into the mechanisms of photochemical reactions. While EnT events typically result in excited-state intermediates that can maximally give product only once per excitation cycle, SET mechanisms often propagate via open-

shell radical intermediates. The distinct chemical reactivity of these intermediates can be investigated using quantum yield experiments and other kinetic tools, many of which are common to the study of thermally initiated radical processes.

1.3.3.1 Quantum Yield

One of the main questions to be answered when investigating a photochemical mechanism is whether the reaction proceeds through a chain propagation mechanism, as is common for radical mechanisms initiated by SET, or via single-turnover catalytic mechanisms. The optimization process for each of these mechanism types differs significantly, as does the understanding of the reactive nature of the intermediates involved.

Quantum yield measurements offer one of the most straightforward approaches to answering this question. Quantum yield is defined as the number of molecules of product produced per photon absorbed by the reaction mixture. Thus, quantum yields greater than 1 provide good evidence that a chain propagation mechanism is active. Quantum yields less than 1, however, are not sufficient evidence alone to rule out a chain propagation mechanism, due to the possible operation of non-product-forming processes that render the reaction inefficient. Examples of such inefficient processes that are often considered include back-electron transfer, vibrational or emissive relaxation of the excited state, and off cycle quenching

interactions. It is possible to account for these inefficiencies by correcting for the quenching fraction, or the ratio of the rate of quenching vs the sum of the rates of all other processes by which the excited state is depleted.[44]

1.3.3.2 Kinetic Tools

The investigation of the non-photochemical propagation phase of a photocatalytic reaction can also be probed using the classical tools of physical organic chemistry. Techniques that have been utilized include the determination of reaction kinetics, isotope effect studies, and Hammett correlations[45–48]. Additionally, radical clocks and radical trapping agents have been used to verify the presence of open-shell radical intermediates, or conversely to support proposed EnT mechanisms by lack of expected reactivity. LED-enabled NMR techniques that enable the monitoring of photochemical reactions in real time have also been developed to facilitate the data collection process for many of these strategies.[49–53]

1.3.4 Notes on other controls and classic experiments

In addition to the experiments described above, a number of control reactions specific to photochemical systems are usually necessary to support a proposed mechanism. The first of these is a control reaction run in the absence of light. It is important to maintain the temperature of the irradiated reaction for this control, as solutions can heat up to 20 °C or more under the irradiation of common light sources.[54]

Failure to adequately capture this difference in temperature could have a dramatic effect on the outcome of the control. As with any other catalytic system, control reactions where the catalytic components are omitted are also important to establishing their necessity. This is especially true when background absorption by other components in the reaction mixture could be expected.

Another experiment that has been commonly employed in the literature is that of the light/dark experiment, where reaction conversion is followed over time with alternating periods of irradiation and stirring in the absence of light. Traditionally this experiment has been employed to investigate the operation of chain propagation events or the lack thereof. As argued by Yoon and coworkers, however, this application of the experiment is misguided due to the fact that most chain processes terminate on the order of milliseconds or shorter, effectively precluding the use of NMR or other common analytical techniques to determine whether such processes operate in the absence of light.[44] This experiment can, however, be used to investigate the stability of the catalyst system. If the slope of conversion under irradiation is preserved across all periods analyzed, for example, it can be inferred that the catalyst system is robust and/or product inhibition is not a major concern.

1.4 Conclusion

Photochemistry is a powerful tool for enabling interesting and synthetically useful chemical methods. Sustained innovation in the field, however, will likely depend on increased attention to mechanistic details and rigorous understanding of investigative techniques. This chapter has presented an overview of the most common reactive modes in photocatalysis and the mechanistic techniques employed to study those methods in the photochemical literature and in the studies that will follow in this thesis.

1.5 References

(1) Ischay, M. A.; Anzovino, M. E.; Du, J.; Yoon, T. P. Efficient Visible Light Photocatalysis of [2+2] Enone Cycloadditions. *J Am Chem Soc* **2008**, *130* (39), 12886–12887. https://doi.org/10.1021/ja805387f.

(2) Narayanam, J. M. R.; Tucker, J. W.; Stephenson, C. R. J. Electron-Transfer Photoredox Catalysis: Development of a Tin-Free Reductive Dehalogenation Reaction. *J Am Chem Soc* **2009**, *131* (25), 8756–8757. https://doi.org/10.1021/ja9033582.

(3) Nicewicz, D. A.; MacMillan, D. W. C. Merging Photoredox Catalysis with Organocatalysis: The Direct Asymmetric Alkylation of Aldehydes. *Science (1979)* **2008**, *322* (5898), 77–80. https://doi.org/10.1126/science.1161976.

(4) Arias-Rotondo, D. M.; McCusker, J. K. The Photophysics of Photoredox Catalysis: A Roadmap for Catalyst Design. *Chem Soc Rev* **2016**, *45* (21), 5803–5820. https://doi.org/10.1039/c6cs00526h.

(5) Buzzetti, L.; Crisenza, G. E. M.; Melchiorre, P. Mechanistic Studies in Photocatalysis. *Angewandte Chemie - International Edition* **2019**, *58* (12), 3730–3747. https://doi.org/10.1002/anie.201809984.

(6) Roth, H. G.; Romero, N. A.; Nicewicz, D. A. Experimental and Calculated Electrochemical Potentials of Common Organic Molecules for Applications to Single-Electron Redox Chemistry. *Synlett* **2016**, *27* (5), 714–723. https://doi.org/10.1055/s-0035-1561297.

(7) Romero, N. A.; Nicewicz, D. A. Organic Photoredox Catalysis. *Chem Rev* **2016**, *116* (17), 10075–10166. https://doi.org/10.1021/acs.chemrev.6b00057.

(8) Pitre, S. P.; McTiernan, C. D.; Vine, W.; Dipucchio, R.; Grenier, M.; Scaiano, J. C. Visible-Light Actinometry and Intermittent Illumination as Convenient Tools to Study Ru(Bpy)3Cl2 Mediated Photoredox Transformations. *Sci Rep* **2015**, *5* (July), 1–10. https://doi.org/10.1038/srep16397.

(9) Pitre, S. P.; McTiernan, C. D.; Scaiano, J. C. Library of Cationic Organic Dyes for Visible-Light-Driven Photoredox Transformations. *ACS Omega* **2016**, *1* (1), 66–76. https://doi.org/10.1021/acsomega.6b00058.

(10) Singh, A.; Teegardin, K.; Kelly, M.; Prasad, K. S.; Krishnan, S.; Weaver, J. D. Facile Synthesis and Complete Characterization of Homoleptic and Heteroleptic Cyclometalated Iridium(III) Complexes for Photocatalysis. *J Organomet Chem* **2015**, *776*, 51–59. https://doi.org/10.1016/J.JORGANCHEM.2014.10.037.

(11) Cahoon, S. B.; Yoon, T. P. Photochemistry and Radical Generation: Approaches in Mechanism Elucidation. *Science of Synthesis* **2021**, *1*, 159–205. https://doi.org/10.1055/sos-SD-234-00064.

(12) Shaw, M. H.; Twilton, J.; MacMillan, D. W. C. Photoredox Catalysis in Organic Chemistry. *J Org Chem* **2016**, *81* (16), 6898–6926. https://doi.org/10.1021/acs.joc.6b01449.

(13) Twilton, J.; Le, C. (Chip); Zhang, P.; Shaw, M. H.; Evans, R. W.; MacMillan, D. W. C. The Merger of Transition Metal and Photocatalysis. *Nat Rev Chem* **2017**, *1* (7), 0052. https://doi.org/10.1038/s41570-017-0052.

(14) Prier, C. K.; Rankic, D. A.; MacMillan, D. W. C. Visible Light Photoredox Catalysis with Transition Metal Complexes: Applications in Organic Synthesis. *Chem Rev* **2013**, *113* (7), 5322–5363. https://doi.org/10.1021/cr300503r.

(15) Skubi, K. L.; Blum, T. R.; Yoon, T. P. Dual Catalysis Strategies in Photochemical Synthesis. *Chem Rev* **2016**, *116* (17), 10035–10074. https://doi.org/10.1021/acs.chemrev.6b00018.

(16) J. Genzink, M.; B. Kidd, J.; B. Swords, W.; P. Yoon, T. Chiral Photocatalyst Structures in Asymmetric Photochemical Synthesis. *Chem Rev* **2022**, *122* (2), 1654–1716. https://doi.org/10.1021/acs.chemrev.1c00467.

(17) Strieth-Kalthoff, F.; James, M. J.; Teders, M.; Pitzer, L.; Glorius, F. Energy Transfer Catalysis Mediated by Visible Light: Principles, Applications, Directions. *Chem Soc Rev* **2018**, *47* (19), 7190–7202. https://doi.org/10.1039/c8cs00054a.

(18) Gentry, E. C.; Knowles, R. R. Synthetic Applications of Proton-Coupled Electron Transfer. *Acc Chem Res* **2016**, *49* (8), 1546–1556. https://doi.org/10.1021/acs.accounts.6b00272.

(19) E. M. Crisenza, G.; Mazzarella, D.; Melchiorre, P. Synthetic Methods Driven by the Photoactivity of Electron Donor–Acceptor Complexes. *J Am Chem Soc* **2020**, *142* (12), 5461–5476. https://doi.org/10.1021/jacs.0c01416.

(20) Yuan, Y. qin; Majumder, S.; Yang, M. hua; Guo, S. rong. Recent Advances in Catalyst-Free Photochemical Reactions via Electron-Donor-Acceptor (EDA) Complex Process. *Tetrahedron Lett* **2020**, *61* (8), 151506. https://doi.org/10.1016/J.TETLET.2019.151506.

(21) Zarkadis, A. K.; Georgakilas, V.; Perdikomatis, G. P.; Trifonov, A.; Gurzadyan, G. G.; Skoulika, S.; Siskos, M. G. Triplet- vs. Singlet-State Imposed Photochemistry. The Role of Substituent Effects on the Photo-Fries and Photodissociation Reaction of Triphenylmethyl Silanes. *Photochemical & Photobiological Sciences* **2005**, *4* (6), 469–480. https://doi.org/10.1039/B502089A.

(22) Leverenz, M.; Merten, C.; Dreuw, A.; Bach, T. Lewis Acid Catalyzed Enantioselective Photochemical Rearrangements on the Singlet Potential Energy Surface. *J Am Chem Soc* **2019**, *141* (51), 20053–20057. https://doi.org/10.1021/jacs.9b12068.

(23) Turro, N. J. Energy Transfer Processes. *Pure and Applied Chemistry* **1977**, *49* (4), 405–429. https://doi.org/10.1351/pac197749040405.

(24) Tarantino, K. T.; Liu, P.; Knowles, R. R. Catalytic Ketyl-Olefin Cyclizations Enabled by Proton-Coupled Electron Transfer. *J Am Chem Soc* **2013**, *135* (27), 10022–10025. https://doi.org/10.1021/ja404342j.

(25) Romero, N. A.; Margrey, K. A.; Tay, N. E.; Nicewicz, D. A. Site-Selective Arene C-H Amination via Photoredox Catalysis. *Science (1979)* **2015**, *349* (6254), 1326 LP – 1330.

(26) Reed, N. L.; Yoon, T. P. Oxidase Reactions in Photoredox Catalysis. *Chem Soc Rev* **2021**, *50* (5), 2954–2967. https://doi.org/10.1039/D0CS00797H.

(27) Reed, N. L.; Lutovsky, G. A.; Yoon, T. P. Copper-Mediated Radical-Polar Crossover Enables Photocatalytic Oxidative Functionalization of Sterically Bulky Alkenes. *J Am Chem Soc* **2021**, *143* (16), 6065–6070. https://doi.org/10.1021/JACS.1C02747/SUPPL_FILE/JA1C02747_SI_001.PDF.

(28) Sarver, P. J.; Bissonnette, N. B.; Macmillan, D. W. C. Decatungstate-Catalyzed C(Sp3)-H Sulfinylation: Rapid Access to Diverse Organosulfur Functionality. *J Am Chem Soc* **2021**, *143* (26), 9737–9743. https://doi.org/10.1021/jacs.1c04722.

(29) Tanielian, C. Decatungstate Photocatalysis. *Coord Chem Rev* **1998**, *178–180* (PART 2), 1165–1181. https://doi.org/10.1016/S0010-8545(98)00160-X.

(30) Tzirakis, M. D.; Lykakis, I. N.; Orfanopoulos, M. Decatungstate as an Efficient Photocatalyst in Organic Chemistry. *Chem Soc Rev* **2009**, *38* (9), 2609–2621. https://doi.org/10.1039/B812100C.

(31) Choi, G. J.; Knowles, R. R. Catalytic Alkene Carboaminations Enabled by Oxidative Proton-Coupled Electron Transfer. *J Am Chem Soc* **2015**, *137* (29), 9226–9229. https://doi.org/10.1021/jacs.5b05377.

(32) Guo, H.; Herdtweck, E.; Bach, T. Enantioselective Lewis Acid Catalysis in Intramolecular [2+2] Photocycloaddition Reactions of Coumarins. *Angewandte Chemie - International Edition* **2010**, *49* (42), 7782–7785. https://doi.org/10.1002/anie.201003619.

(33) Brimioulle, R.; Bauer, A.; Bach, T. Enantioselective Lewis Acid Catalysis in Intramolecular [2 + 2] Photocycloaddition Reactions: A Mechanistic Comparison between Representative Coumarin and Enone Substrates. *J Am Chem Soc* **2015**, *137* (15), 5170–5176. https://doi.org/10.1021/jacs.5b01740.

(34) Kelly, C. B.; Patel, N. R.; Primer, D. N.; Jouffroy, M.; Tellis, J. C.; Molander, G. A. Preparation of Visible-Light-Activated Metal Complexes and Their Use in Photoredox/Nickel Dual Catalysis. *Nat Protoc* **2017**, *12*, 472.

(35) Horn, E. J.; Rosen, B. R.; Baran, P. S. Synthetic Organic Electrochemistry: An Enabling and Innately Sustainable Method. *ACS Cent Sci* **2016**, *2* (5), 302–308. https://doi.org/10.1021/acscentsci.6b00091.

(36) Yan, M.; Kawamata, Y.; Baran, P. S. Synthetic Organic Electrochemical Methods since 2000: On the Verge of a Renaissance. *Chem Rev* **2017**, *117* (21), 13230–13319. https://doi.org/10.1021/acs.chemrev.7b00397.

(37) Elgrishi, N.; Rountree, K. J.; McCarthy, B. D.; Rountree, E. S.; Eisenhart, T. T.; Dempsey, J. L. A Practical Beginner's Guide to Cyclic Voltammetry. *J Chem Educ* **2018**, *95* (2), 197–206. https://doi.org/10.1021/acs.jchemed.7b00361.

(38) Strieth-Kalthoff, F.; Henkel, C.; Teders, M.; Kahnt, A.; Knolle, W.; Gómez-Suárez, A.; Dirian, K.; Alex, W.; Bergander, K.; Daniliuc, C. G.; Abel, B.; Guldi, D. M.; Glorius, F. Discovery of Unforeseen Energy-Transfer-Based Transformations Using a Combined Screening Approach. *Chem* **2019**, *5* (8), 2183–2194. https://doi.org/10.1016/J.CHEMPR.2019.06.004.

(39) Sun, R.; Qin, Y.; Nocera, D. G. General Paradigm in Photoredox Nickel-Catalyzed Cross-Coupling Allows for Light-Free Access to Reactivity. *Angewandte Chemie - International Edition* **2020**, *59* (24), 9527–9533. https://doi.org/10.1002/anie.201916398.

(40) Sun, R.; Qin, Y.; Ruccolo, S.; Schnedermann, C.; Costentin, C.; Nocera, D. G. Elucidation of a Redox-Mediated Reaction Cycle for Nickel-Catalyzed Cross Coupling. *J Am Chem Soc* **2019**, *141* (1), 89–93. https://doi.org/10.1021/jacs.8b11262.

(41) Corcoran, E. B.; Pirnot, M. T.; Lin, S.; Dreher, S. D.; Dirocco, D. A.; Davies, I. W.; Buchwald, S. L.; Macmillan, D. W. C. Aryl Amination Using Ligand-Free Ni(II) Salts and Photoredox Catalysis. *Science (1979)* **2016**, *353* (6296), 279–283. https://doi.org/10.1126/SCIENCE.AAG0209/SUPPL_FILE/CORCORAN.SM.PDF.

(42) Welin, E. R.; Le, C.; Arias-Rotondo, D. M.; McCusker, J. K.; MacMillan, D. W. C. Photosensitized, Energy Transfer-Mediated Organometallic Catalysis through Electronically Excited Nickel(II). *Science (1979)* **2017**, *355* (6323), 380–385. https://doi.org/10.1126/science.aal2490.

(43) Daub, M. E.; Jung, H.; Lee, B. J.; Won, J.; Baik, M. H.; Yoon, T. P. Enantioselective [2+2] Cycloadditions of Cinnamate Esters: Generalizing Lewis Acid Catalysis of Triplet Energy Transfer. *J Am Chem Soc* **2019**, *141* (24), 9543–9547. https://doi.org/10.1021/jacs.9b04643.

(44) Cismesia, M. A.; Yoon, T. P. Characterizing Chain Processes in Visible Light Photoredox Catalysis. *Chem. Sci.* **2015**, *6* (10), 5426–5434. https://doi.org/10.1039/C5SC02185E.

(45) Griffin, J. D.; Zeller, M. A.; Nicewicz, D. A. Hydrodecarboxylation of Carboxylic and Malonic Acid Derivatives via Organic Photoredox Catalysis: Substrate Scope and Mechanistic Insight. *J Am Chem Soc* **2015**, *137* (35), 11340–11348. https://doi.org/10.1021/jacs.5b07770.

(46) Yayla, H. G.; Peng, F.; Mangion, I. K.; McLaughlin, M.; Campeau, L. C.; Davies, I. W.; Dirocco, D. A.; Knowles, R. R. Discovery and Mechanistic Study of a Photocatalytic Indoline Dehydrogenation for the Synthesis of Elbasvir. *Chem Sci* **2016**, *7* (3), 2066–2073. https://doi.org/10.1039/c5sc03350k.

(47) Murphy, J. J.; Bastida, D.; Paria, S.; Fagnoni, M.; Melchiorre, P. Asymmetric Catalytic Formation of Quaternary Carbons by Iminium Ion Trapping of Radicals. *Nature* **2016**, *532* (7598), 218–222. https://doi.org/10.1038/nature17438.

(48) Bahamonde, A.; Murphy, J. J.; Savarese, M.; Brémond, É.; Cavalli, A.; Melchiorre, P. Studies on the Enantioselective Iminium Ion Trapping of Radicals Triggered by an Electron-Relay Mechanism. *J Am Chem Soc* **2017**, *139* (12), 4559–4567. https://doi.org/10.1021/jacs.7b01446.

(49) Ji, Y.; DiRocco, D. A.; Kind, J.; Thiele, C. M.; Gschwind, R. M.; Reibarkh, M. LED-Illuminated NMR Spectroscopy: A Practical Tool for Mechanistic Studies of Photochemical Reactions. *ChemPhotoChem* **2019**, *3* (10), 984–992. https://doi.org/10.1002/cptc.201900109.

(50) Seegerer, A.; Nitschke, P.; Gschwind, R. M. Combined In Situ Illumination-NMR-UV/Vis Spectroscopy: A New Mechanistic Tool in Photochemistry. *Angewandte Chemie - International Edition* **2018**, *57* (25), 7493–7497. https://doi.org/10.1002/anie.201801250.

(51) Nitschke, P.; Lokesh, N.; Gschwind, R. M. Combination of Illumination and High Resolution NMR Spectroscopy: Key Features and Practical Aspects, Photochemical Applications, and New

Concepts. *Prog Nucl Magn Reson Spectrosc* **2019**, *114–115*, 86–134. https://doi.org/10.1016/j.pnmrs.2019.06.001.

(52) Skubi, K. L.; Swords, W. B.; Hofstetter, H.; Yoon, T. P. LED-NMR Monitoring of an Enantioselective Catalytic [2+2] Photocycloaddition. *ChemPhotoChem* **2020**, *4* (9), 685–690. https://doi.org/10.1002/CPTC.202000094.

(53) Swords, W. B.; Chapman, S. J.; Hofstetter, H.; Dunn, A. L.; Yoon, T. P. Variable Temperature LED-NMR: Rapid Insights into a Photocatalytic Mechanism from Reaction Progress Kinetic Analysis. *Journal of Organic Chemistry* **2022**, *87* (17), 11776–11782. https://doi.org/10.1021/ACS.JOC.2C01479/ASSET/IMAGES/LARGE/JO2C01479_0007.JPEG.

(54) Shields, B. J.; Kudisch, B.; Scholes, G. D.; Doyle, A. G. Long-Lived Charge-Transfer States of Nickel(II) Aryl Halide Complexes Facilitate Bimolecular Photoinduced Electron Transfer. *J Am Chem Soc* **2018**, *140* (8), 3035–3039. https://doi.org/10.1021/jacs.7b13281.

Chapter 2 Approaches Towards Catalysis of Di-π-methane Reactions

2.1 Abstract

The field of asymmetric photochemistry has recently seen a sharp increase in development, with the employment of substrate binding chiral sensitizers and Lewis and Bronsted co-catalysis emerging as dominant strategies for inducing enantioselectivity. To date, these strategies have proven successful in the discovery of a wide range of asymmetric photochemical cycloadditions, electrocyclizations, and radical addition reactions. However, to the best of our knowledge, only one highly enantioselective, solution phase photochemical rearrangement has been reported to date.[22] The di-π-methane rearrangement is a classic example of a triplet state photochemical rearrangement, celebrated for its generality and extensive development. This chapter details the development of Lewis- and Bronsted- acid co-catalyst systems for Iridium sensitized di-π-methane rearrangements and the subsequent development of the first highly enantioselective variant of the reaction for an all-carbon scaffold.

2.2 Background

The di-π-methane (DPM) reaction has been celebrated as one of the most general photochemical rearrangements in the literature. The rearrangement takes place upon excitation of a molecule containing two pi bonds bonded to the same sp^3 hybridized carbon to yield π-substituted cyclopropanes and related products that are often inaccessible via other means, Figure 2.1.[55–57] These reactions typically exhibit high

chemical and quantum yields and have been used as key steps for total synthesis.[58–61] The reaction also proceeds smoothly when one of the pi systems participating in the reaction are part of an aromatic ring, a carbonyl, or an imine, with the latter two cases being respectively termed the oxa- and aza- DPM variants.

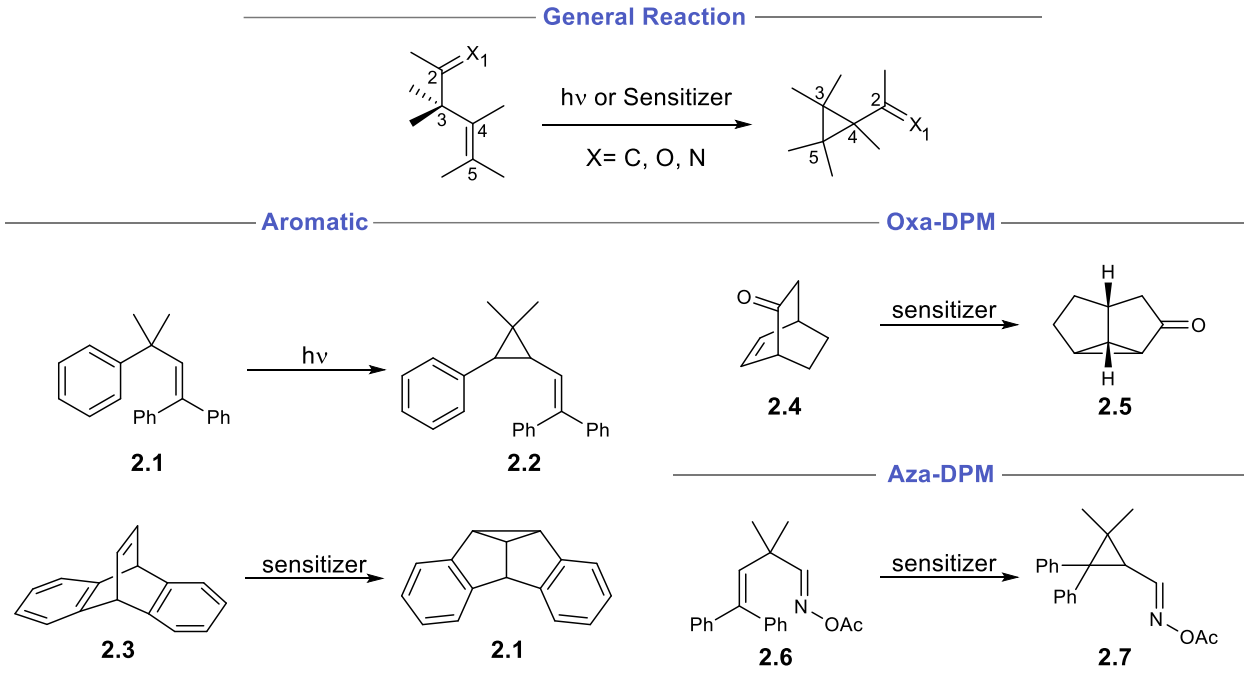

Figure 2.1 Overview of DPM Reactivity

2.2.1 A Brief Review of the di-π-methane reaction

The first example of a DPM reaction was published by Zimmerman in 1966 with the disclosure of the acetone sensitized photoisomerization of barrelene **2.8** to semibullvalene **2.9**, Figure 2.2.[62] At first termed a divinyl rearrangement, the reaction was later renamed to reflect the full extent of its reactivity.

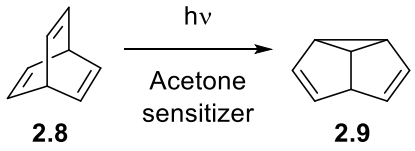

Figure 2.2

Subsequent studies expanded upon the generality of the system by investigating the reaction of a wide range of substrate structures, which also led to the development of key mechanistic insights. Researchers were quick to note a disparity between the reactivity of systems where the excited state was reached via direct irradiation and those in which a triplet sensitizer was present. This difference has been attributed to the difference in reactivity of the singlet and triplet excited states. In fact, it was reported that triplet sensitized DPM rearrangements did not occur for substrates where rotation around the double bond involved in the reaction was not constrained. Instead, the DPM rearrangement for such substrates, such as those depicted in Figure 2.3a, proceeded only under direct irradiation, presumably through the singlet excited state. It was hypothesized that the reason for this disparity was the relative propensity for the triplet excited state to dissipate energy rapidly through cis/trans isomerization of the alkene. Indeed, while triplet sensitization of cis alkene **2.13** (Figure 2.3b) led to only cis/trans isomerization of the starting material, singlet excitation exclusively yielded the cis vinyl cyclopropane product **2.14** when monitored at low conversions. Conversely, direct excitation of bullvalene type scaffolds, such as **2.8**, to the singlet state failed

to yield the desired cyclopropane products due to competing pericyclic reactivity preferentially leading to formation of cyclooctatetraene **2.17** instead, Figure 2.3c.

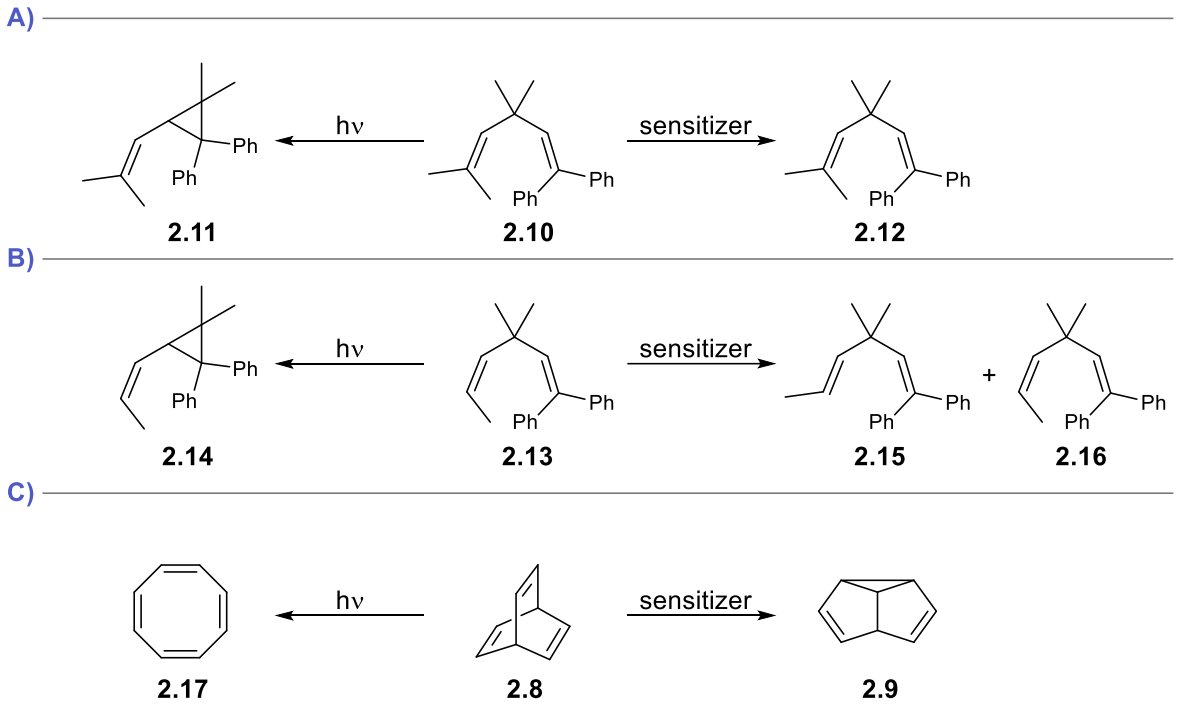

Figure 2.3 Triplet vs Singlet Reactivity in Model Systems

The mechanism of this reaction, for both singlet and triplet excited states, was proposed to follow the general pathway depicted in Figure 2.4. The intermediates drawn do not necessarily represent energy minima, but rather a logical sequence of potential structures along the energy surface. The proposed mechanism has proven useful for predicting the regioselectivity observed in most reported cases, as cyclopropane products resulting from reaction from intermediates in which the radical is most stabilized are often exclusively favored. DFT studies published by Castano and coworkers in 2004 also support the

mechanism shown in Figure 2.4b for barrelene substrates and offer further insights into the difference in single and triplet state reactivity observed for those scaffolds.[63]

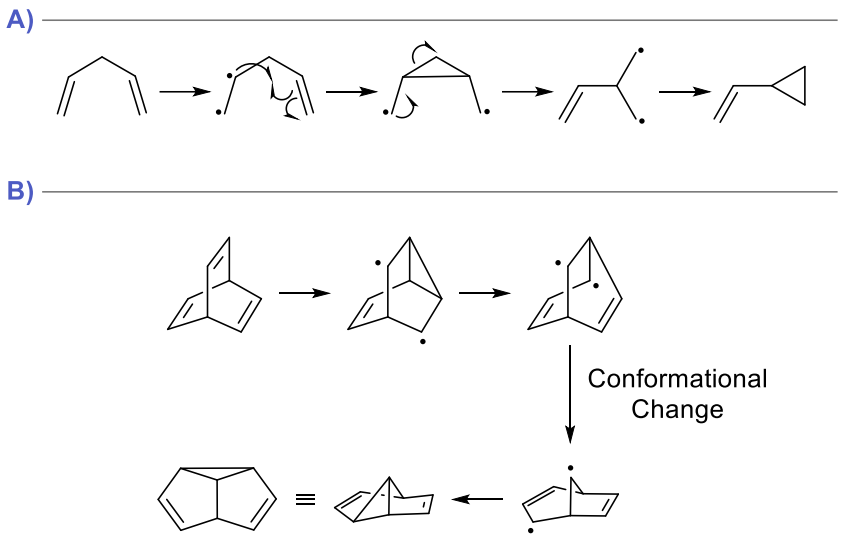

Figure 2.4 Representative Depictions of Proposed Reaction Mechanism

While initial reports showed that competing pericyclic reactions dominate the singlet reactivity for most constrained cyclic substrates, there have been reports of dibenzobarrelene substrates that proceed smoothly to the expected cyclopropane products under direct irradiation.[64–69] Typically, these reactions take place when there are no competing electrocyclization pathways available or when the substrates contain functional group substitutions on the π system. Some such reports are also for reactions performed in the solid state, which has been shown to have other effects on reaction regioselectivity as well. Possible explanations for this difference in observed reactivity include the substrates having slower competing singlet pathways or exhibiting enhanced rates of ISC to the reactive triplet.

The DPM reaction has proven to be general to a wide range of scaffolds, including those containing participating C–O and –N double bonds and even scaffolds with phosphorus substitutions at one of the sp^3 carbon bridgeheads.[70] Several excellent reviews adequately capture the breadth of these publications and detail the principles that dictate competitive rates of different variants when two possible outcomes can be envisioned from the starting materials.[55–58,61] While the bulk of these reports, whether using traditional sensitizers such as xanthone or acetophenone or direct irradiation, proceed via UV-light irradiation, a recent report by Ihmels and coworkers extends this reaction to visible light activated photochemistry by use of an iridium sensitizer.[67] This report was published during the preparation of the method presented in this chapter.

2.2.2 Enantioselective methods to date

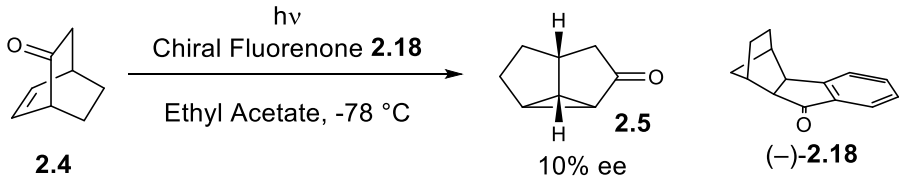

Figure 2.5

Given the history of this reaction, it is unsurprising that several efforts have been made to develop an enantioselective variant. The first efforts to develop such a reaction were published by Demuth and Schaffner in 1982, who attempted to perform a triplet sensitized oxa-DPM in an enantioselective fashion

in the preparation of building blocks for the total synthesis of cyclopentanoid natural products.[60] Unfortunately, application of chiral sensitizer **2.18**, shown in Figure 2.5, yielded only meager enantiomeric excess, as was typical of such applications at the time.[71–74] Successful synthesis of the desired enantiomeric materials was eventually furnished by chromatographic resolution of a diastereomeric mixture of the functionalized racemates.

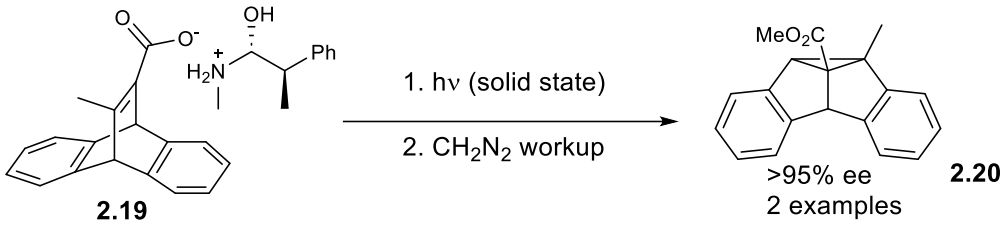

Figure 2.6

Scheffer and coworkers reported the solid-state asymmetric DPM rearrangement of two dibenzobarrelene structures using a chiral ionic handle, an example of which is shown in Figure 2.6.[75,76] Using this strategy, they were able to achieve up to 95% enantiomeric excess at 20% conversion. The ability to extend this system to other substrates was limited, however, requiring a carboxylic acid functional group and careful crystallization prior to reaction. No enantiomeric excess was observed when the reaction was run in solution.

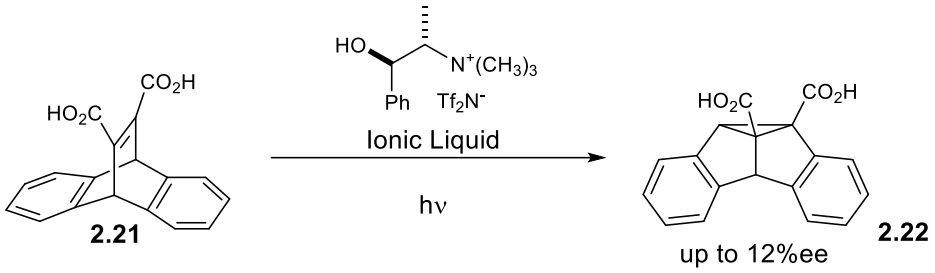

Figure 2.7

In 2005, Armstrong and coworkers reported the use of chiral ionic liquids as solvents for the enantioselective conversion of diacid functionalized dibenzobarrelene **2.21**.[77] Using this approach, they were able to obtain enantiomeric excess of up to 12%. This report represented the first use of chiral ionic liquids to enable an enantioselective unimolecular photochemical isomerization. However, this method also lacked general applicability and was not highly selective.

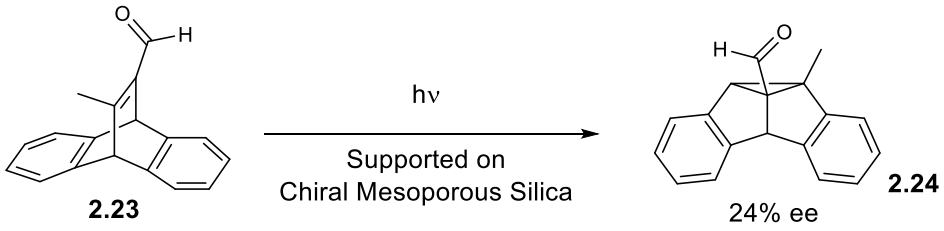

Figure 2.8

The strategy of using host-guest systems to enable enantioselective photochemical methods originated in the early 1990s, using zeolites and other macromolecular cages to provide a chiral environment.[78–82] Ihmels, Garcia, and coworkers reported an adaptation of this strategy for the DPM rearrangement of an aldehyde substituted dibenzobarrelene, **2.23**, using chiral mesoporous silica in 2005,

Figure 2.8.[65] They reported reaching an enantiomeric excess of 24% at 11% conversion using this host-guest complex. Using chiral auxiliaries in the cavity of conventional zeolites they obtained a 30% enantiomeric excess, but they also noted that uniform distribution of the substrate and chiral auxiliary in the zeolite was difficult to achieve.

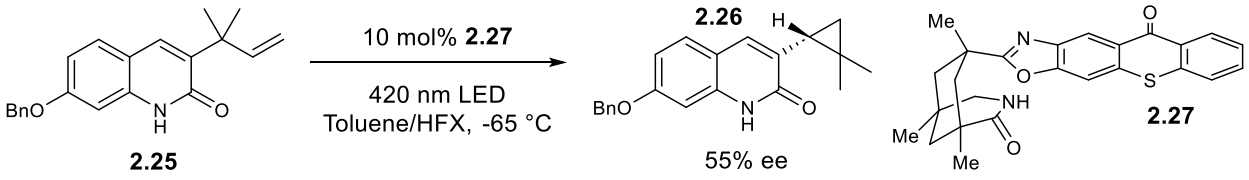

Figure 2.9

The work of Bach and coworkers in developing chiral hydrogen-bonding xanthone and thioxanthone sensitizers capable of inducing significant enantioselectivities in triplet-sensitized reactions provided a platform for major advancement towards development of an enantioselective DPM reaction. In 2019, Bach reported the use of one such catalyst, **2.27**, to enable the DPM rearrangement of 3-allyl-substituted quinolones, Figure 2.9.[83] Enantiomeric excesses of up to 55% were obtained, a significant advance over previous methods. The enantioselectivity obtained was found to arise from a triplet-state deracemization of the cyclopropane product, however, supported by the observation of racemization of the product in the presence of an achiral sensitizer and the dependance of enantiomeric excess on reaction progress, with moderate levels of *ee* reached only after an hour of reaction progress.

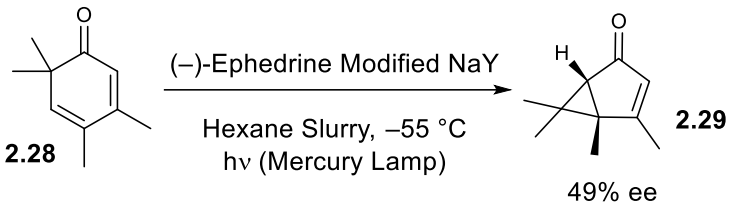

Figure 2.10

Better results have been obtained for approaches to the oxa-DPM variant of this reaction. A 2002 study by Ramamurthy and coworkers applied a zeolite supported strategy using (–)-ephedrine as the chiral inductor to achieve 49% *ee* in the oxa-DPM rearrangement of 2,4-cyclohexadienones, Figure 2.10.[84] This reaction was proposed to proceed from the excited singlet. Bach and coworkers also demonstrated a catalytic enantioselective method for the same scaffold through application of a chiral oxazaborolidine catalyst in 2019.[22] Introduction of the Lewis acid catalyst **2.31** induced a large bathochromic shift in the absorption of the bound complex, allowing for selective excitation of the acid-base pair. The method furnished a small scope of products with reasonable yields and excellent *ee*, up to 97%, Figure 2.11. Researchers confirmed that this method also proceeded from the excited singlet state, noting that it was necessary to avoid the triplet state to achieve the observed reactivity.

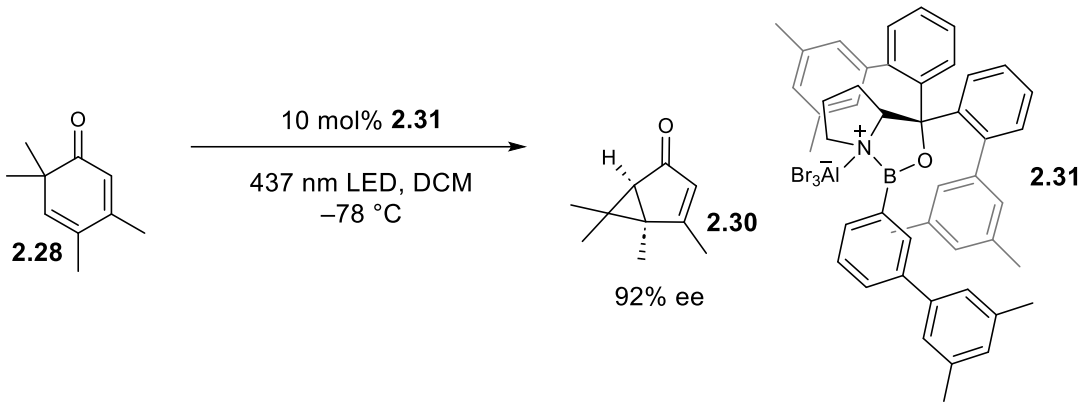

Figure 2.11

2.3 Mechanism Guided Development of Highly Enantioselective DPM

Despite the excellent advances made so far for both the all-carbon and oxa-DPM variants of the reaction, a highly enantioselective, general version of the triplet sensitized DPM rearrangement, or indeed of a triplet rearrangement of any form, has not yet been disclosed. Our lab believed that application of modern techniques in enantioselective photocatalysis could bridge the gap in this field. The remainder of this chapter discusses the development of the first highly enantioselective all-carbon DPM rearrangement in the solution phase and the strategy that informed that development.

2.3.1 Ongoing challenges in enantioselective triplet photochemistry

One of the primary challenges of asymmetric photochemistry, as in the field of asymmetric catalysis in general, is the prevention of uncatalyzed background reaction. Regardless of how enantioselective a catalyzed process is, any amount of uncatalyzed background can significantly erode the maximum

observable ee. This problem is especially prevalent in photochemical systems due to the largely collisional nature of sensitization and electron transfer processes in traditional photocatalysis and due to the propensity of some substrates to absorb light and participate in uncatalyzed excited state reactivity. As seen in early attempts at employing chiral sensitizers to induce enantioselective energy transfer, some of which were covered in the review of the DPM reaction above, the diffusion-rate controlled collisional nature of the energy transfer event often precludes the transfer of significant levels of enantioinduction.

Strategies to overcome these challenges were pioneered by the use of host-guest interactions to ensure that the substrate excited state was reached in the presence of chiral information, and early strategies relied on incorporating organic substrates into chiral pockets within macromolecular structures such as zeolites. This strategy was, however, difficult to extend to a broad range of reactions due to physical constraints with populating the zeolite pores, and requirement of an excess of chiral information.[78]

Modern enantioselective photocatalysis built upon this host-guest framework, pioneered by the publication of an enantioselective method by Krische and coworkers in 2003.[85] Krishe's method attached a benzophenone sensitizer to a chiral hydrogen-bonding receptor to induce enantioselectivity in a [2+2] cycloaddition. This report was among the first to show that weak intermolecular interactions could be used to induce reasonable levels of enantioselectivity in a sensitized process. Though this example also used a

super-stoichiometric amount of chiral information and gave relatively modest ee, it set the stage for the development of a suite of catalytic strategies based on similar intermolecular interactions.

Modern catalytic strategies use a range of intermolecular interactions to engage substrates in a chiral environment, including hydrogen bonding, Lewis acid-base interactions, and Bronsted acid-base pairing. These applications generally build on two basic strategies to avoid racemic background chemistry. One strategy focuses on producing the substrate excited state selectively within a chiral environment by tethering the substrate to a chiral sensitizer. In these cases, background is avoided by the increased propensity for energy transfer to proximally bound substrate. Both organic sensitizers and chiral-at-metal transition metal photocatalysts have been used to effect good enantiomeric selectivity in such applications.[16] Another strategy relies on changing the mechanism of reaction to avoid electronically excited substrates in the absence of chiral information. An example of this reactivity is the use of a chiral Lewis acid which, upon binding to the substrate, lowers the triplet energy of the bound complex such that sensitization becomes feasible. The free substrate, on the other hand, is incapable of being sensitized by the catalyst used and background reactivity is avoided.[86] A variation of this strategy was discussed above, in which coordination of a Lewis or Bronsted acid induces a significant bathochromic shift in the substrate's absorption, allowing for direct excitation of the bound complex by judicious choice of an appropriate light source.

Despite the significant advancement of these general strategies, some challenges remain. Due to the weak nature of the interactions involved in tethering substrates to chiral materials, diffusion away from chiral information occasionally occurs on a timescale that is competitive with the rate of reaction.[87] Alternatively, though the strategies avoid background reactivity in theory, practical applications frequently require extensive optimization to identify appropriate conditions and often still fail to completely mitigate excitation of substrate outside of the chiral environment. Finally, substrate structures are often limited to those bearing Lewis or Bronsted basic functionalities in order for them to engage with common catalyst systems. Expanding the scope of functionalities that can be applied to such methods is an important ongoing area of research.[88,89]

2.3.2 Observation of enhanced reactivity through Lewis-Acid catalysis

Our investigation into the development of an enantioselective DPM rearrangement began with the investigation of iridium sensitizer conditions for the conversion of dibenzobarrelenes to semibullvalenes. We found this substrate class to be particularly compelling due to the high levels of complexity accessed through construction of the tricyclic core and the historic prevalence of methods focused on similar structures. In the process of developing that scope, our lab observed an interesting trend in the reactivity of a series of carbonyl containing substrates, Figure 2.12. Substrates bearing aldehydes and ketones (**2.32** and

2.33) reacted readily, while **2.34**, bearing an ester functional group, reacted more sluggishly. Attempted reaction of an amide containing substrate, **2.35**, furnished almost no product, even over extended periods of irradiation.

Entry	R=	Yield
1	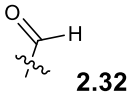 **2.32**	97%
2	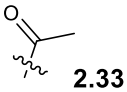 **2.33**	96%
3	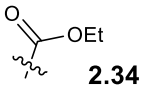 **2.34**	46%
4	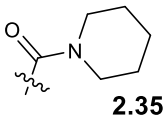 **2.35**	<1%
5	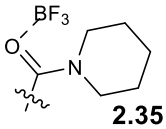 **2.35**	<13%

Figure 2.12

It was hypothesized that this observed trend in reactivity could be attributed to a difference in triplet energy for these substrates, and thus their ability to effectively quench the photocatalyst being employed.

Stern-Volmer quenching studies were carried out on a representative series and confirmed that quenching rates for the ester and amide substrates were substantially slower than for substrates with ketone or aldehyde functional groups, Figure 2.13. Inclusion of BF_3 as a Lewis acid with the amide substrate somewhat rescued the observed reactivity, Figure 2.12 entry 5, and also resulted in a marked increase in the Stern-Volmer quenching constant, Figure 2.13b. While this analysis does not rule out the possibility that the rate of downstream reactivity also plays a part in the difference in observed reactivity, it suggests that modulation of the electronic nature of the carbonyl group could effectively modulate the selectivity of the energy transfer step, a necessary prerequisite to the application of common enantioselective photocatalytic methods.

A)

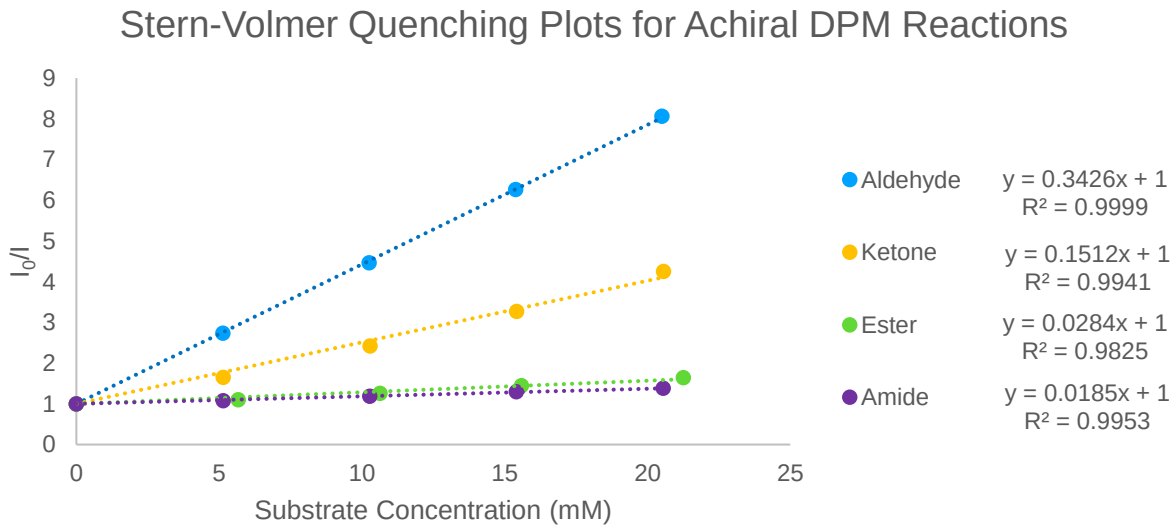

B)

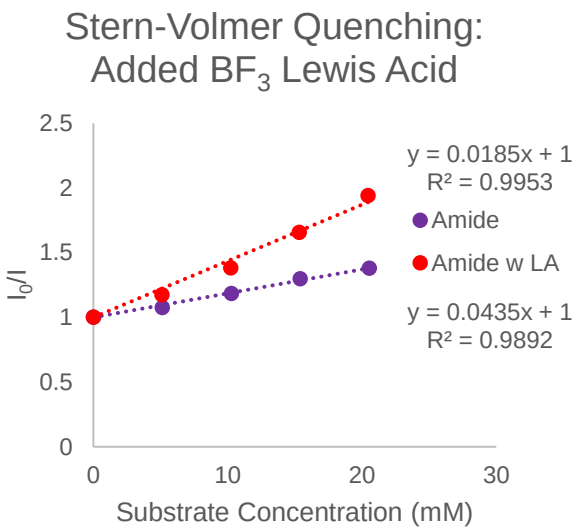

C)

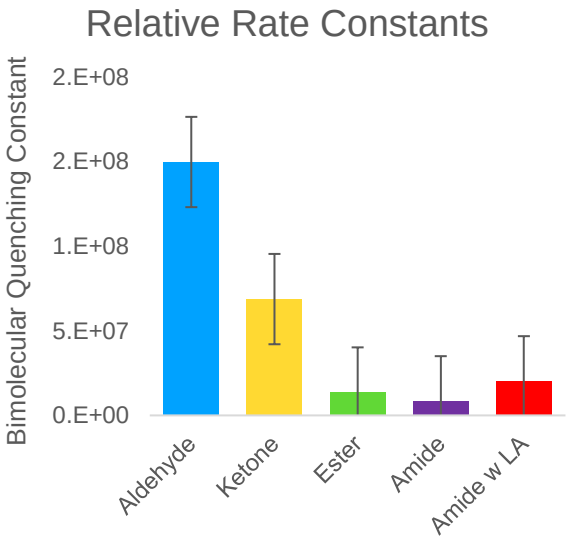

Figure 2.13

2.3.3 Substrate optimization for method development and initial screening

Unfortunately, screening of chiral Lewis acids against the amide substrate system analyzed above did not yield conditions in which high levels of enantioselectivity could be obtained. While the absolute rate of the DPM rearrangement has not been measured for these substrates, the long reaction times suggest that the process is slow and/or relatively inefficient. It is possible that diffusion away from the Lewis acid occurs on the same time scale as the reaction rate. In order to address this limitation, the substrate was redesigned to include a binding group that would more tightly bind a wide range of Lewis and Bronsted acids and that was also expected to produce a faster reaction.

Imidazole ketone handles have proven to be versatile binding groups for a number of enantioselective photocatalytic methods developed by our lab and other groups. A dibenzobarrelene substrate incorporating this handle, **2.36**, was synthesized and evaluated for suitability. Early experiments using **2.36** suggested that background reactivity of the substrate was possible under irradiation with a standard 427 nm light. Indeed, quantitative conversion to the rearranged product, **2.37**, was obtained in the absence of sensitizer within 4 hours in both toluene and DCM, Figure 2.14. This reactivity is not unprecedented. As noted in the discussion above, despite the propensity for constrained cyclic systems to undergo competitive pericyclic processes from their singlet state, other studies with similarly substituted dibenzobarrelenes have also reported clean conversion to the DPM rearrangement product under direct irradiation.

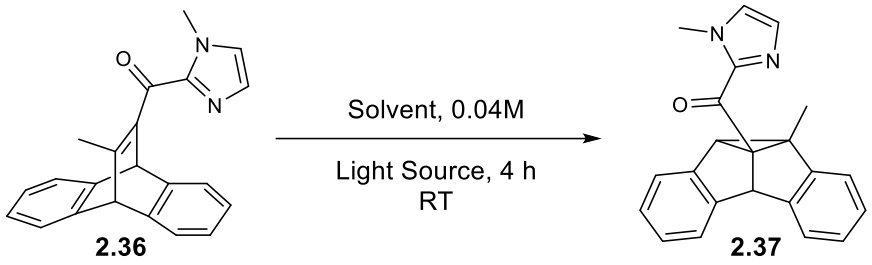

Entry	Solvent	Light Source	RSM	Yield
1	Toluene	427 nm	0%	87%
2	DCM	427 nm	0%	91%
3	Toluene	456 nm	56%	28%
4	DCM	456 nm	100%	0%

Figure 2.14

Analysis of the UV-Vis absorption spectrum of the substrate, see Supporting Information 2.6.10, led us to believe that switching to a 456 nm light would mitigate the observed background reactivity. Experimental results confirmed this assertion, with the observation of significantly attenuated reactivity in toluene and no reaction observed in DCM (Figure 2.14 entries 3 and 4).

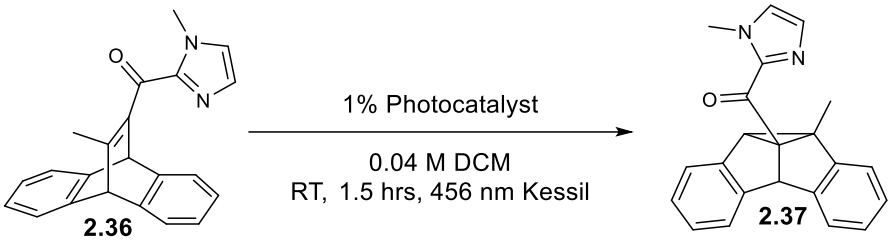

Entry	Photocatalyst	TE	RSM	Yield
1	$Ru(bpy)_3$	46 kcal/mol	89%	0%
2	$Ir(ppy)_2(dtbbpy)PF_6$ (Ir-**2.38**)	50 kcal/mol	59%	35%
3	$Ir(F\text{-}ppy)_2(dtbbpy)PF_6$	53 kcal/mol	47%	45%
4	$Ir(4\text{-}Fppy)_2(dtbbpy)PF_6$	53 kcal/mol	0%	89%
5	$Ir(dF(tBu)ppy)_2(dtbbpy)PF_6$	55 kcal/mol	0%	89%

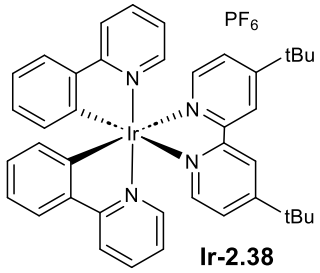

Figure 2.15

A screen of common iridium and ruthenium photocatalysts helped to benchmark the approximate triplet energy of the imidazole ketone substrate, Figure 2.15. Application of catalysts with reported triplet energies above 55 kcal/mol led to rapid conversion of starting material. Catalysts with triplet energies ranging from 50–53 kcal/mol were able to produce product but did so slowly. Use of $Ru(bpy)_3$, with a reported triplet energy of 46 kcal/mol, did not lead to product formation. This information also allowed us to select $Ir(ppy)_2(dtbbpy)PF_6$, Ir-**2.38**, as a sensitizer to screen in co-catalysis systems, as we would be able to monitor for a rate increase of the energy transfer event by monitoring reaction yield at the same timepoint.

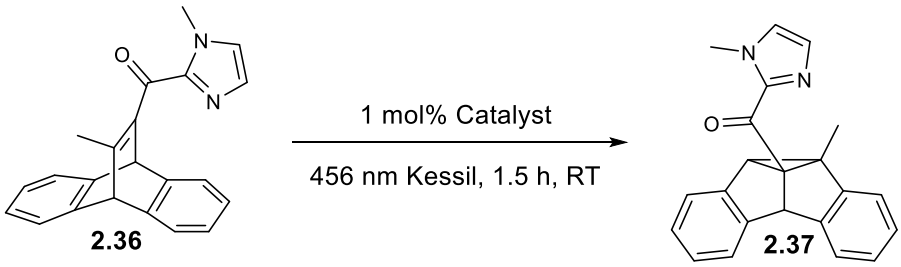

Entry	Catalyst	Deviation from Standard Conditions	RSM	Yield	ee
1	**Ir-2.38**	None	59%	35%	-
2	**Ir-2.38**	20 mol% Acetic Acid	64%	17%	-
3	**Ir-2.38**	20 mol% Benzoic Acid	52%	22%	-
4	**Ir-2.38**	20 mol% TsOH	16%	6%	-
5	**Ir-2.38**	20 mol% Sulfuric Acid	40%	6%	-
6	**Ir-2.38**	20 mol% HCl	69%	0%	-
7	**Ir-2.38**	20 mol% S-Binol Phosphoric Acid	0%	71%	10%
8	**Ir-2.38**	20 mol% $La(OTf)_3$	75%	13%	-
9	**Ir-2.38**	20 mol% $Sc(OTf)_3$	17%	0%	-
10	**Ir-2.38**	20 mol% Sc, *s*BuPyBox	37%	28%	3%
11	**Ir-2.38**	20 mol% $Al(OTf)_3$	38%	0%	-
12	**Ir-2.38**	20 mol% $Cu(OTf)_2$	84%	0%	-
13	**Ir-2.38**	20 mol% $Gd(OAc)_3$	68%	30%	-
14	**Ir-2.38**	20 mol% (S)-(–)-o-Tolyl-CBS-Oxazaborolidine	47%	36%	0%
15	**Ir-2.39**	None	0%	85%	24%
16	**Ir-2.40**	4 mol% Catalyst Loading	30%	64%	0%
17	**CPA-2.41**	20 mol% Catalyst Loading	34%	29%	47%

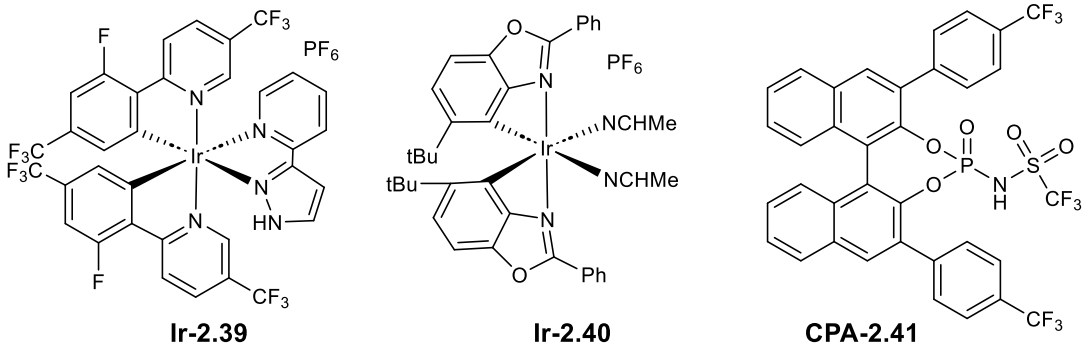

Figure 2.16

Imidazole ketone substrate **2.36** was then screened against Lewis and Bronsted acid cocatalysts and other common systems for enantioinduction in photocatalytic methods, with promising results being observed for a few systems. In particular, reactions with chiral-at-iridium catalysts with hydrogen-bonding pyridyl pyrazine ligands, Figure 2.16 entry 15, and chiral phosphoric acid derivatives, Figure 2.16 entry 17, served to induce relatively high levels of enantioselectivity. Notably, inclusion of most common Bronsted and Lewis acids resulted in poor mass balance or inhibited the reaction, suggesting that co-catalysis strategies would not be successful in this system. Indeed, the use of chiral Lewis acids, including an oxazaborolidine Lewis acid similar to that applied in Bach's oxa-DPM and a chiral scandium complex, yielded no observable ee, Figure 2.16 entries 10 and 14. Initial investigations of both the chiral-at-iridium and phosphoric acid systems led us to focus our efforts on the use of chiral phosphoric acids. A summary of efforts towards the optimization of this method using iridium catalysts can be found in the Supporting Information for this chapter.

2.3.4 Chiral phosphoric acid system: optimization and scope

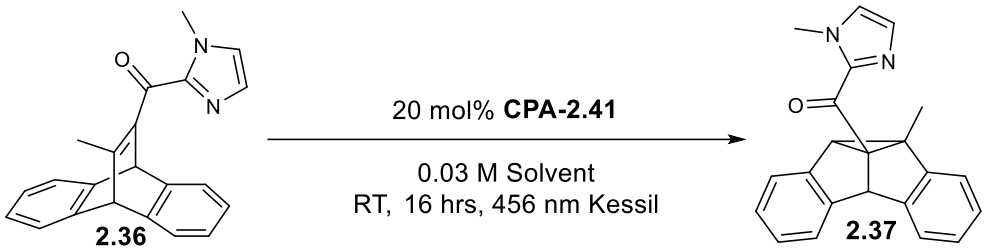

Entry	Deviation from Std. Conditions	RSM	Yield	ee
1	Toluene	24%	49%	52%
2	2:1 Tol/Pentane	14%	65%	49%
3	DCM	46%	29%	46%
4	DCE	54%	26%	42%
5	THF	61%	26%	18%
6	MeCN	65%	14%	5%
	In 2:1 Toluene/Pentane			
7	10% **CPA-2.41**	13%	53%	31%
8	20% **CPA-2.41**	14%	65%	49%
9	30% **CPA-2.41**	17%	39%	74%
10	50% **CPA-2.41**	ND	ND	80%
11	0.05 M	51%	37%	27%
12	0.03 M	14%	65%	49%
13	0.017 M	17%	47%	55%
14	0.01 M	19%	46%	62%
15	RT	19%	46%	62%
16	-30 °C	40%	48%	30%
17	-78 °C	73%	12%	30%

Figure 2.17

Initial optimization efforts using the chiral phosphoric acid as a catalyst are summarized in Figure 2.17. These studies revealed a that reaction ee was best in relatively non-polar solvents and solvent mixtures, entries 1–6. While increasing acid loading led to an increase in ee, the mass balance of the reaction suffered greatly, entries 7–10. Dilution up to 0.01 M served to increase the enantioselectivity of the reaction, but

further dilution did not yield better results, entries 11–14. Unfortunately, cooling the reaction caused the reaction to slow down and also led to diminished ee, entries 15–17.

Given that the intrinsic selectivity of the reaction was expected to be close to 80% ee, based on the results obtained with high acid loadings (Figure 2.17 entry 10), we hypothesized that some variable in our setup was preventing the attainment of maximum possible enantioselectivity. We thought that there were two sources of loss likely responsible for the diminished selectivity. The first source of selectivity loss was likely to be background reaction. Although employing a 456 nm lamp served to diminish background reactivity, conversion in toluene was still observed, Figure 2.14 entry 3. Indeed, a simple UV-Vis titration of the acid catalyst into the substrate revealed a relatively mild bathochromic shift in substrate absorbance, indicating that absorption of light by unbound substrate was likely possible, see Supporting Information. The second source of selectivity loss might be attributable to the slow rate of reaction. Bach has shown in similar systems that when the rate of dissociation between the substrate and the catalyst is competitive with the reaction rate lower enantioselectivities are observed.[87]

We reasoned that application of a dual catalysis system, wherein an iridium sensitizer was introduced as a co-catalyst, could potentially address both of these possible problems. We would expect the iridium catalyst to absorb much more strongly than free substrate within the irradiation range, potentially

mitigating background reactivity from that source. Additionally, sensitization by the iridium catalyst would directly access the excited triplet state of the substrate, bypassing the ISC step and potential rate limitations involved in that process. Qualitatively, we had observed much faster conversion rates with iridium catalysts in our previous screens than we observed with just the phosphoric acid catalyst. Additionally, a previous experiment using an iridium catalyst and simple S-Binol phosphoric acid, Figure 2.16 entry 7, had resulted in efficient co-catalysis and a moderate, but measurable, ee.

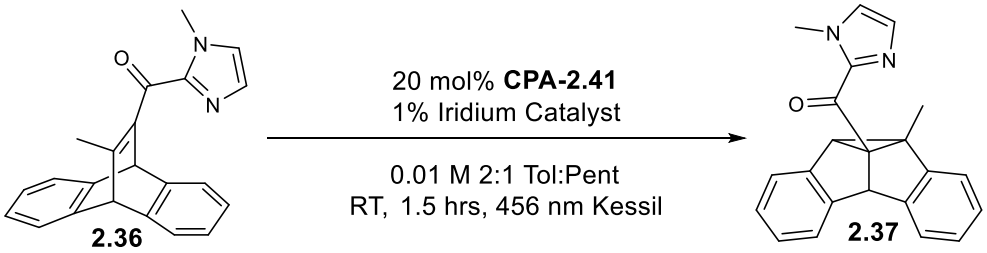

Entry	Iridium Catalyst	TE	RSM	Yield	ee
1	None (16 hrs)	-	19%	46%	62%
2	$Ir(ppy)_2(dtbbpy)PF_6$ (**Ir-2.38**)	50 kcal/mol	0%	76%	76%
3	$Ru(bpy)_3PF_6$	46 kcal/mol	77%	5%	38%
4	$Ru(bpz)_3BArF$	51 kcal/mol	83%	1%	32%
5	$Ir(3\text{-}tBuppy)_3$	unknown	0%	36%	-22%
6	$Ir(dFppy)_3$	unknown	0%	60%	26%
7	$Ir(F\text{-}ppy)_2(dtbbpy)PF_6$	53 kcal/mol	0%	72%	73%
8	$Ir(dF(CF_3)ppy)_2(dtbbpy)PF_6$	59 kcal/mol	0%	72%	55%
9	$Ir(4\text{-}Fppy)_2(dtbbpy)\ PF_6$	53 kcal/mol	0%	67%	67%
10	$Ir(dF(CF_3)ppy)_2(5,5\text{-}dCF_3bpy)PF_6$	unknown	15%	71%	37%

Figure 2.18

A screen of iridium catalysts with a range of triplet energies confirmed our hypothesis, Figure 2.18. Iridium catalysts with triplet energies around 50 kcal/mol led to an increase in observed reaction rate and

ee. Based on our previous screen in the absence of the acid catalyst, photocatalysts in this range were expected to be able to sensitize the substrate, but with a slow reaction rate. Catalysts with triplet energies much higher than this range led to generally good conversion, but poor ee, which could be attributed to indiscriminate sensitization of substrate and the substrate-acid complex. Apparent exceptions to this trend were catalysts that exhibit high excited state reduction potentials. These catalysts generally led to poor mass balance and enantioselectivity, potentially due to susceptibility of some component of the reaction mixture to degradation under highly reducing conditions.

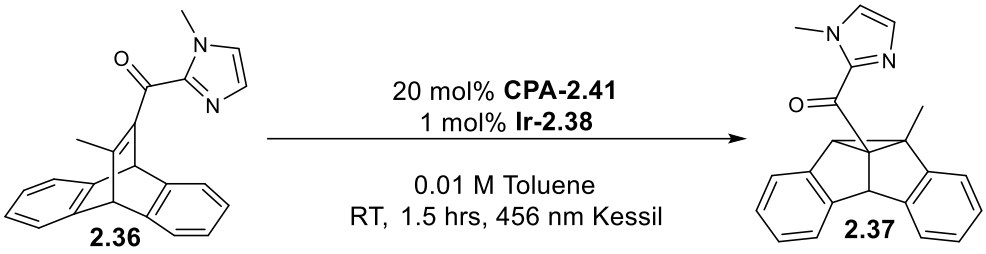

Entry	Deviation from Std. Conditions	RSM	Yield	ee
1	1% **Ir-2.38**	0%	87%	70%
2	3% **Ir-2.38**	0%	78%	72%
3	5% **Ir-2.38**	0%	75%	70%
4	100% Light Intensity	0%	87%	70%
5	50% Light Intensity	0%	84%	69%
6	25% Light Intensity	0%	75%	69%
7	0.01 M	0%	87%	70%
8	0.005 M	0%	79%	71%
9	0.0025 M	0%	76%	68%
10	DCM	0%	76%	62%
11	DCE	0%	59%	65%
12	Trifluorotoluene	0%	71%	65%
13	0 °C	0%	86%	66%

Figure 2.19

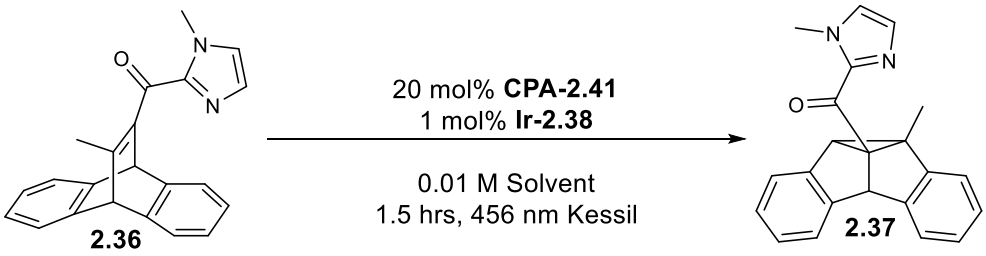

Entry	Solvent	Temp	RSM	Yield	ee
1	Toluene	RT	0%	85%	71%
2	Toluene	-78 °C	0%	86%	72%
3	0:1 Tol/DCM	RT	0%	76%	62%
4	4:1 Tol/DCM	RT	0%	58%	69%
5	0:1 Tol/DCM	-78 °C	77%	22%	79%
6	1:2 Tol/DCM	-78 °C	62%	31%	77%
7	1:4 Tol/DCM	-78 °C	58%	31%	80%
8	1:1 Tol/DCM	-78 °C	35%	50%	81%
9	2:1 Tol/DCM	-78 °C	0%	94%	85%
10	4:1 Tol/DCM	-78 °C	0%	100%	83%
11	9:1 Tol/DCM	-78 °C	0%	86%	82%
12	19:1 Tol/DCM	-78 °C	0%	90%	74%
13	4:1 Tol/THF	RT	0%	63%	72%
14	4:1 Tol/THF	-78 °C	0%	83%	72%
15	4:1 Tol/MeCN	RT	0%	60%	55%
16	4:1 Tol/MeCN	-78 °C	0%	100%	76%
17	9:1 Tol/MeCN	-78 °C	0%	81%	80%
18	19:1 Tol/MeCN	-78 °C	0%	100%	75%
19	9:1 Tol/PropCN	-78 °C	0%	81%	73%
20	2:1 Tol/DCE	-78 °C	30%	55%	83%
21	2:1 Tol/CHCl3	-78 °C	0%	85%	77%
22	1:1 Tol/EtOAc	-78 °C	ND	ND	78%
23	2:1 Tol/EtOAc	-78 °C	0%	99%	82%
24	3:1 Tol/EtOAc	-78 °C	ND	ND	73%
25	5:1 Tol/EtOAc	-78 °C	ND	ND	75%
26	2:1 TFTol/DCM	-78 °C	41%	45%	76%
27	2:1 HFX/DCM	-78 °C	16%	55%	79%
28	2:2:1 TFTol/HFX/DCM	-78 °C	22%	47%	65%

Figure 2.20

Due to the sparing solubility of the substrate in toluene and the toluene/pentane mixtures that had primarily been used in screening efforts to this point, we hypothesized that the lack of increased ee at reduced temperatures could be due to precipitation of the catalyst-substrate complex under those conditions. Gratifyingly, while inclusion of a more solubilizing co-solvent led to decreased ee at room temperature, increased ee was observed when reactions with those same solvent mixtures were cooled, Figure 2.20. This effect proved to be general for several different solvent mixtures in toluene, appearing to follow a semi-parabolic relationship between solvent polarity and maximum enantioselectivity for the mixture. Our analysis revealed that DCM was an optimal co-solvent in this application, yielding our final conditions.

A small scope study showed that our conditions were applicable to a small range of substrates in this class, Figure 2.21. Substitution of the substrate with large functional groups led to decreased reactivity and selectivity. It is possible that such substitutions inhibit formation of the substrate-acid complex and also lead to slower reaction rates of the rearrangement. Phenyl and TMS substituted starting materials, **2.49** and **2.50**, showed no conversion under reaction conditions, and cyclohexyl substituted material **2.48** reacted only at room temperature. Removing the imidazole also resulted in complete loss of reactivity under our optimal conditions, **2.51**, showcasing the need for substrate activation by the phosphoric acid catalyst. Less demanding substitutions reacted more slowly than the model substrate and with moderately attenuated

selectivity. These factors support the hypothesis that a source of selectivity loss in this system could be attributed to diffusion of the substrate on the reaction timescale.

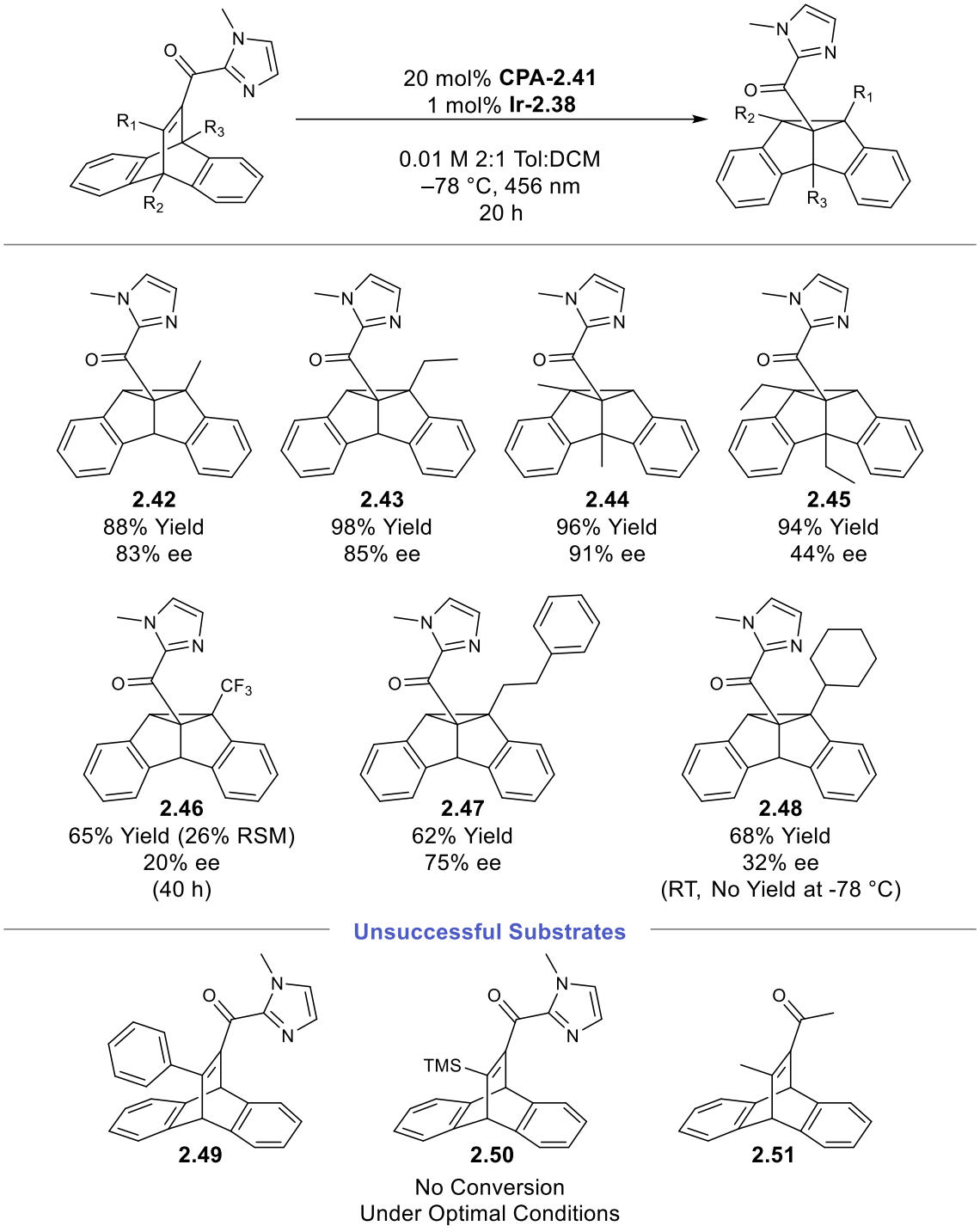
20 mol% CPA-2.41
1 mol% Ir-2.38
0.01 M 2:1 Tol:DCM
–78 °C, 456 nm
20 h
2.42
88% Yield
83% ee
2.43
98% Yield
85% ee
2.44
96% Yield
91% ee
2.45
94% Yield
44% ee
2.46
65% Yield (26% RSM)
20% ee
(40 h)
2.47
62% Yield
75% ee
2.48
68% Yield
32% ee
(RT, No Yield at -78 °C)
Unsuccessful Substrates
2.49
2.50
No Conversion
Under Optimal Conditions
2.51

Figure 2.21

2.4 Conclusion

In conclusion, we have developed the first example of a highly enantioselective triplet state photochemical rearrangement with catalytic chiral information. This study fundamentally advances available methodology for popular dibenzobarrelene DPM rearrangements and the field of catalytic enantioselective energy transfer photocatalysis. The reaction principles uncovered in this study are expected to inform development of future methods to increase the reaction generality.

2.5 Contributions

Racemic reactions and Lewis acid catalysis conditions were pioneered by Dr. Steven Chapman and continued by Tahoe Fiala. Stern-Volmer quenching studies were also conducted by Tahoe Fiala. Development of the enantioselective method and related studies were performed by the author.

2.6 Supporting Information

2.6.1 General Information

$Ir(dF(CF_3)ppy)_2(dtbbpy)PF_6$ was synthesized using the published route.[90] Other photocatalysts employed in these studies were either obtained commercially or synthesized by adaptation of the same reported procedure. 1,1,1-trifluoro-N-((4S)-4-oxido-2,6-bis(4-(trifluoromethyl)phenyl)dinaphtho[2,1-d:1',2'-f][1,3,2]dioxaphosphepin-4-yl)methanesulfonamide (CPA1) was synthesized according to the reported method.[91] Except in the case of aqueous reactions, all reaction glassware was flame- or oven-dried prior to use. All commercially available chemicals were used as purchased from Sigma Aldrich or Oakwood Chemical. Toluene, acetonitrile (MeCN), tetrahydrofuran (THF), ethyl acetate (EtOAc), and dichloromethane (CH_2Cl_2, DCM) were purified by elution through alumina and stored under Argon if used in a preparative reaction. Other solvents were distilled prior to use or obtained from Sigma Aldrich in a sure seal bottle. Solvents for chromatography were used as received from Thermo Fischer or Sigma Aldrich. Flash column chromatography was performed with Purasil 60Å silica gel.

^1H,$^{13}C\{^1H\}$, and $^{19}F\{^1H\}$ data for all previously uncharacterized compounds were obtained using Bruker Avance-400 and Avance-500 spectrometers with BBFO+ and DCH probes. ^1H spectra were internally referenced to tetramethyl silane (TMS). Multiplicities are defined using the following abbreviations: s (singlet), d(doublet), t (triplet), q (quartet), p (pentet), sept (septet), m (multiplet), and combined variations. The NMR spectrometers used in this work are supported by the NSF CHE-1048642, a generous gift from Paul J. and Margaret M. Bender, and the University of Wisconsin.

High Resolution Mass spectrometry was performed using a Thermo Q Exactive™ Plus supported by the NIH 1S10 OD020022-1.

UV-Visible spectra were recorded on a Varia Cary® 50 spectrophotometer at a resolution of 1 nm. Photoluminescence spectra were recorded on a Hitachi F-4500 fluorescence spectrophotometer with a 1 nm resolution.

IR spectra were obtained using a Bruker Alpha Platinum spectrometer (powder). Melting points were obtained using a Stanford Research Systems DigiMelt apparatus.

2.6.2 Synthesis of Starting Materials for Di-π-methane reactions

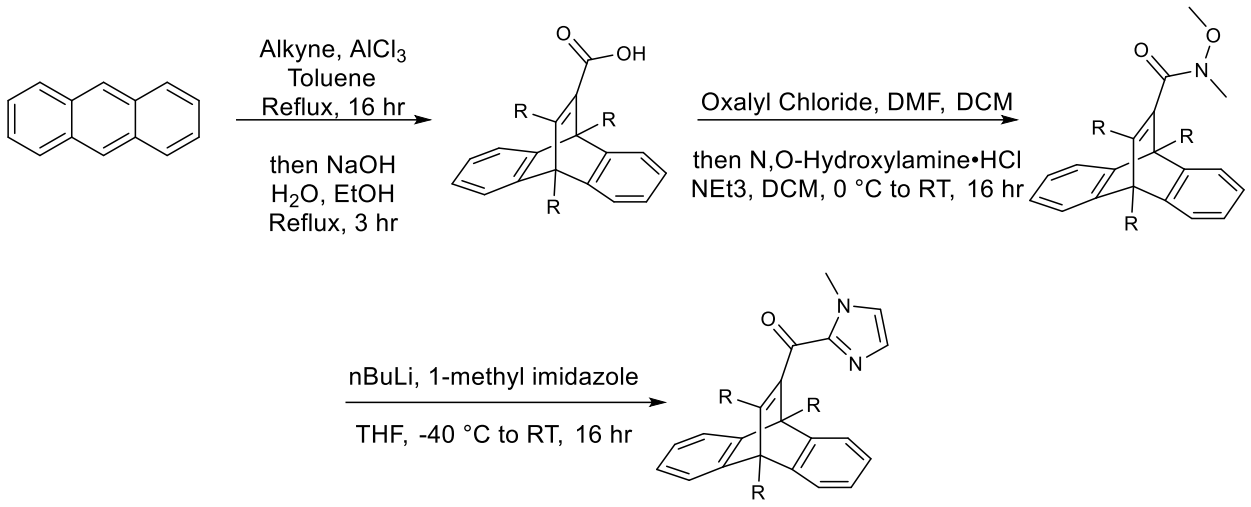

General Procedure

Substrates were prepared by Diels-Alder cycloaddition of alkynes and anthracene derivatives, followed by saponification, Weinreb amide formation, and addition of lithiated 1-methyl imidazole to form the starting material.

Anthracene (1 equiv) was suspended in toluene (0.5 M) under N_2 in a dram vial with ample headspace and septum cap with a stir bar. Alkyne (1 equiv) was added dropwise, and the solution was heated to 80 °C. Aluminum trichloride (0.95 equiv) was added as a suspension in minimal toluene and the reaction was heated further to 111 °C for 16 hours. The reaction was cooled and diluted with EtOAc. A saturated solution of Rochelle's salt was added dropwise until dark color dissipated and subsequently allowed to stir for 30 minutes. Further diluted with H2O and extracted aq. layer 3x with EtOAc. Washed combined organics with brine and concentrated. Passed through a silica plug with 3:1 Hexanes:EtOAc and concentrated. Dissolved residue in a solution of 4.5 g NaOH, 14 mL H_2O, and 32 mL EtOH, heated to reflux for 3 hrs. Cooled and acidified with 3 M HCl. Extracted aq. 3x with DCM, washed combined organic layers with brine, and dried over $MgSO_4$. Concentrated. Loaded onto silica plug, washed with excess hexanes, and eluted with 2:1 Hexanes:EtOAc.

Crude product (1 equiv), often with remaining anthracene, was dissolved in DCM (0.2 M) under N_2 in a round bottom flask with a stir bar. Oxalyl chloride (1.2 equiv) was added dropwise, followed by several drops of DMF (catalytic). Heated reaction mixture to 30 °C for 3 hours, and then concentrated under a

stream of N_2. Immediately redissolved in DCM (0.2 M) and cooled to 0 °C under N_2. Added N,O-dimethyl hydroxylamine hydrochloride (1.2 equiv) portion-wise and then NEt_3 (3 equiv) dropwise at 0 °C. Allowed to warm to RT slowly with stirring over 16 hours. Diluted in DCM and 50% AcOH. Extracted 3x DCM. Washed combined organic layers with brine. Dried over Na_2SO_4 and concentrated. Loaded onto silica plug, washed with excess hexanes, and eluted with 2:1 Hexanes:EtOAc.

1-methyl imidazole (1.2 equiv) dissolved in THF (one half volume of 0.1 M) under N_2 and cooled to -78 °C. Added n-BuLi (solution in Hexanes, 1.15 equiv) dropwise and allowed to stir for one hour. Warmed to -40 °C. Added crude Weinreb amide product in remaining THF dropwise. Allowed to slowly warm to room temperature over 16 hours with stirring. Quenched with sat aq. NH_4Cl, then added excess aq. K_2CO_3. Extracted 3x EtOAc, washed combined organic layers with brine and dried over Na_2SO_4. Purified by column chromatography in appropriate mixtures of Hexanes:EtOAc.

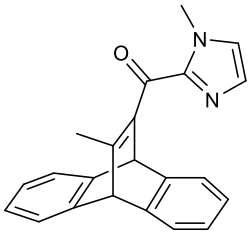

(1-methyl-1H-imidazol-2-yl)((9s,10s)-12-methyl-9,10-dihydro-9,10-ethenoanthracen-11-yl)methanone (**S2.1**):

Prepared using the general procedure from anthracene (2.50 g, 14.0 mmol) and ethyl pent-2-ynoate (1.77 g, 14.0 mmol). Purified with a 4:1 to 3:1 gradient Hexanes:EtOAc. Isolated 509 mg (1.56 mmol) as a white powder (11% Yield).

^{1}H NMR (500 MHz, $CDCl_3$) δ 7.42 (dd, J = 7.0, 1.3 Hz, 2H), 7.31 (dd, J = 7.1, 1.3 Hz, 2H), 7.17 (d, J = 1.0 Hz, 1H), 7.05 – 6.93 (m, 5H), 6.01 (s, 1H), 4.94 (s, 1H), 3.95 (s, 3H), 2.20 (s, 3H).

^{13}C NMR (126 MHz, $CDCl_3$) δ 183.67, 161.07, 145.80, 144.13, 143.88, 143.54, 129.02, 126.17, 125.16, 124.58, 123.64, 123.16, 59.62, 53.11, 35.99, 19.65.

HRMS (ESI^+) calculated for [$C_{22}H_{18}N_2O$] ([M+H]+). Requires *m/z* 327.1492; found *m/z* 327.1485.

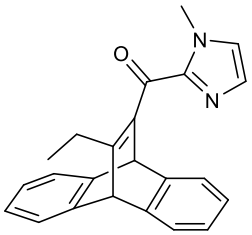

((9s,10s)-12-ethyl-9,10-dihydro-9,10-ethenoanthracen-11-yl)(1-methyl-1H-imidazol-2-yl)methanone (**S2.2**):

Prepared using the general procedure from anthracene (2.50 g, 14.0 mmol) and ethyl but-2-ynoate (1.57 g, 14.0 mmol). Purified with a 5:1 to 4:1 gradient Hexanes:EtOAc. Isolated 620 mg (1.82 mmol) as a white powder (13% Yield).

^{1}H NMR (500 MHz, $CDCl_3$) δ 7.42 (dd, J = 7.0, 1.4 Hz, 2H), 7.31 (dd, J = 7.1, 1.4 Hz, 2H), 7.17 (d, J = 0.9 Hz, 1H), 7.05 – 6.92 (m, 5H), 5.98 (s, 1H), 5.10 (s, 1H), 3.96 (s, 3H), 2.54 (q, J = 7.5 Hz, 2H), 1.13 (t, J = 7.5 Hz, 3H).

^{13}C NMR (126 MHz, $CDCl_3$) δ 183.79, 165.51, 146.10, 144.54, 143.97, 143.19, 128.99, 126.21, 125.05, 124.60, 123.69, 123.01, 57.04, 53.30, 36.00, 26.05, 11.95.

HRMS (ESI^+) calculated for [$C_{23}H_{20}N_2O$] ([M+H]+). Requires *m/z* 341.1648; found *m/z* 341.1642.

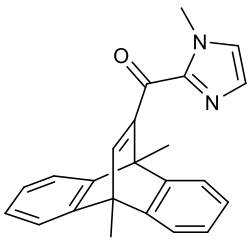

((9s,10s)-9,10-dimethyl-9,10-dihydro-9,10-ethenoanthracen-11-yl)(1-methyl-1H-imidazol-2-yl)methanone (**S2.3**):

Prepared using the general procedure from 9,10-dimethylanthracene (500 mg, 2.42 mmol) and ethyl propiolate (238 mg, 2.42 mmol). Purified with a 3:1 Hexanes:EtOAc. Isolated 335 mg (0.984 mmol) as a white powder (41% Yield).

^{1}H NMR (500 MHz, $CDCl_3$) δ 7.76 (s, 1H), 7.42 – 7.35 (m, 2H), 7.35 – 7.29 (m, 2H), 7.06 – 6.99 (m, 5H), 6.95 (d, J = 0.9 Hz, 1H), 3.89 (s, 3H), 2.46 (s, 3H), 2.23 (s, 3H).

^{13}C NMR (126 MHz, $CDCl_3$) δ 182.44, 159.71, 151.40, 148.99, 147.67, 143.37, 128.62, 126.55, 124.58, 124.41, 120.77, 120.37, 50.73, 49.60, 36.19, 15.34, 14.05.

HRMS (ESI^+) calculated for [$C_{23}H_{20}N_2O$] ([M+H]+). Requires *m/z* 341.1648; found *m/z* 341.1642.

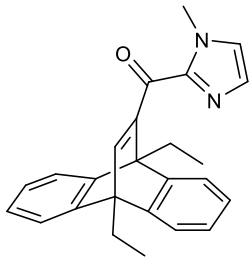

((9s,10s)-9,10-diethyl-9,10-dihydro-9,10-ethenoanthracen-11-yl)(1-methyl-1H-imidazol-2-yl)methanone (**S2.4**):

9,10-Diethylanthracene was prepared from 9,10-dibromoanthracene (2.00 g, 5.95 mmol), ethyl iodide (3.90 g, 25.0 mmol) and n-butyl lithium (16.1 mmol, 2.3 M solution in hexanes) by following a literature procedure.[92] 9,10-Diethylanthracene was obtained as a white powder in 84% yield, 1.17 g.

Prepared using the general procedure from 9,10-diethylanthracene (600 mg, 2.56 mmol) and ethyl propiolate (251 mg, 2.56 mmol). Purified with 3:1 Hexanes:EtOAc. Isolated 261 mg (0.708 mmol) as a white powder (28% Yield).

^{1}H NMR (500 MHz, $CDCl_3$) δ 7.63 (s, 1H), 7.42 – 7.33 (m, 2H), 7.25 (d, J = 9.1 Hz, 2H), 7.07 (d, J = 0.9 Hz, 1H), 6.98 (dtd, J = 8.7, 4.0, 2.2 Hz, 5H), 3.95 (s, 3H), 3.09 (s, 2H), 2.71 (q, J = 7.4 Hz, 2H), 1.45 (t, J = 7.4 Hz, 3H), 1.26 (t, J = 7.1 Hz, 3H).

^{13}C NMR (126 MHz, $CDCl_3$) δ 183.61, 154.17, 150.98, 148.33, 142.95, 129.10, 126.84, 124.26, 124.10, 121.13, 55.98, 53.60, 36.22, 20.79, 18.63, 11.27, 9.83.

HRMS (ESI^+) calculated for [$C_{25}H_{24}N_2O$] ([M+H]+). Requires *m/z* 369.1961; found *m/z* 369.1956.

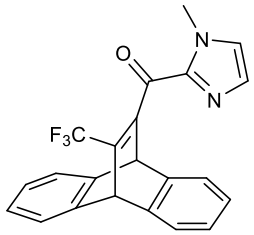

(1-methyl-1H-imidazol-2-yl)((9s,10s)-12-(trifluoromethyl)-9,10-dihydro-9,10-ethenoanthracen-11-yl)methanone (**S2.5**):

Prepared using the general procedure from anthracene (550 mg, 3.09 mmol) and ethyl 4,4,4-trifluorobut-2-ynoate (513 mg, 3.09 mmol). Purified with a 2:1 to 4:1 to 1:0 DCM:Hexanes gradient. Isolated 287 mg (0.755 mmol) as a white powder (24% Yield).

^{1}H NMR (400 MHz, $CDCl_3$) δ 7.40 (dd, J = 5.4, 3.1 Hz, 4H), 7.13 (d, J = 0.9 Hz, 1H), 7.09 – 7.01 (m, 5H), 5.51 (s, 1H), 5.36 (s, 1H), 4.01 (s, 3H).

^{19}F NMR (377 MHz, $CDCl_3$) δ -63.12.

^{13}C NMR (101 MHz, $CDCl_3$) δ 183.20, 144.09, 143.72, 142.00, 130.54, 127.50, 125.46, 125.42, 124.24, 123.51, 54.71, 50.33, 35.88.

HRMS (ESI^+) calculated for [$C_{22}H_{15}F_3N_2O$] ([M+H]+). Requires *m/z* 381.1209; found *m/z* 381.1205.

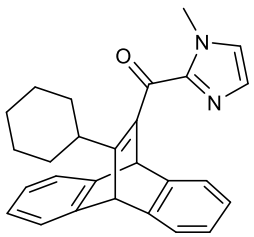

((9s,10s)-12-cyclohexyl-9,10-dihydro-9,10-ethenoanthracen-11-yl)(1-methyl-1H-imidazol-2-yl)methanone (**S2.6**):

Methyl 3-cyclohexylpropiolate was prepared by adaptation of a literature method. Ethynylcyclohexane (541 mg, 1 equiv, 5.00 mmol) was dissolved in THF and

cooled to -78 °C. Added LDA (616 mg, 2.88 mL, 2.0 molar, 1.15 Eq, 5.75 mmol) as solution in THF dropwise. Allowed to stir for 20 min. Added methyl carbonochloridate (520 mg, 423 μL, 1.1 Eq, 5.50 mmol) dropwise. Stirred at -78 C for 15 min, then warmed to 0 C over 1.5 hours. Quenched with sat aq. NH_4Cl and diluted in EtOAc. Extract aq. layers 3x with EtOAc, washed organic layers with brine, dried over $MgSO_4$, and concentrated. Purified on silica in 20:1 Hex/EtOAc to yield 720 mg (87% yield) of methyl 3-cyclohexylpropiolate as a clear oil. ^{1}H-NMR spectra matched reported values.

Prepared using the general procedure from anthracene (772 mg, 4.33 mmol) and methyl 3-cyclohexylpropiolate (720 mg, 4.33 mmol). Purified with a 5:1 to 5:2 gradient Hexanes:EtOAc. Isolated 393 mg (0.996 mmol) as a white powder (22% Yield).

^{1}H NMR (500 MHz, $CDCl_3$) δ 7.39 (dd, *J* = 6.9, 1.4 Hz, 2H), 7.29 (dd, *J* = 7.0, 1.4 Hz, 2H), 7.16 (d, *J* = 1.0 Hz, 1H), 7.03 – 6.91 (m, 5H), 5.86 (s, 1H), 5.36 (s, 1H), 3.97 (s, 3H), 2.90 (tt, *J* = 11.4, 3.9 Hz, 1H), 1.80 – 1.65 (m, 2H), 1.64 – 1.46 (m, 4H), 1.34 – 1.12 (m, 4H).

^{13}C NMR (126 MHz, $CDCl_3$) δ 184.34, 167.50, 146.47, 144.84, 144.08, 142.81, 128.96, 126.14, 124.92, 124.57, 123.69, 122.97, 53.48, 53.14, 40.48, 35.99, 31.60, 29.91, 26.14, 25.79, 22.66.

HRMS (ESI^+) calculated for [$C_{27}H_{26}N_2O$] ([M+H]+). Requires *m/z* 395.2118; found *m/z* 395.2111.

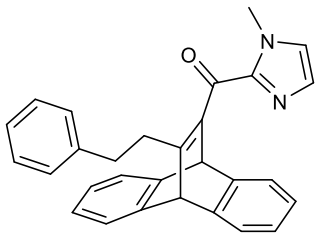

(1-methyl-1H-imidazol-2-yl)((9s,10s)-12-phenethyl-9,10-dihydro-9,10-ethenoanthracen-11-yl)methanone (**S2.7**):

Ethyl 5-phenylpent-2-ynoate was prepared by adaptation of a literature method. But-3-yn-1-ylbenzene (750 mg, 1 Eq, 5.76 mmol) was dissolved in THF and cooled to -78 °C. Added nBuLi (406 mg, 2.76 mL, 2.3 molar, 1.1 Eq, 6.34 mmol) added as solution in hexane dropwise. Allowed to stir for 1 hour. Added ethyl carbonochloridate (688 mg, 606 μL, 1.1 Eq, 6.34 mmol) dropwise. Stirred at -78 C for 2 hours, then quenched with sat aq. NH_4Cl and diluted in EtOAc. Extract aq. layers 3x with EtOAc, washed organic layers with brine, dried over $MgSO_4$, and concentrated. Purified on silica in 20:1 Hex/EtOAc to yield 883 mg (76% yield) of ethyl 5-phenylpent-2-ynoate as a clear oil. ^{1}H-NMR spectra matched expected values.

^{1}H NMR (400 MHz, $CDCl_3$) δ 7.35 – 7.18 (m, 5H), 4.21 (q, J = 7.2 Hz, 2H), 2.90 (t, J = 7.7 Hz, 2H), 2.62 (t, J = 7.6 Hz, 2H), 1.30 (t, J = 7.2 Hz, 3H).

Prepared using the general procedure from anthracene (778 mg, 4.37 mmol) and ethyl 5-phenylpent-2-ynoate (883 mg, 4.37 mmol), adding lithiated imidazole at 0 °C. Purified with a 3:1 Hexanes:EtOAc. Isolated 140 mg (0.336 mmol) as a white powder (8% Yield). Note: this material decomposes over time when stored at room temperature.

^{1}H NMR (500 MHz, $CDCl_3$) δ 7.42 (dd, J = 7.2, 1.4 Hz, 2H), 7.31 (dd, J = 7.0, 1.4 Hz, 2H), 7.19 – 7.07 (m, 4H), 7.05 – 6.94 (m, 7H), 5.96 (s, 1H), 5.12 (s, 1H), 3.86 (s, 3H), 2.82 (d, J = 2.5 Hz, 4H).

^{13}C NMR (126 MHz, $CDCl_3$) δ 183.56, 162.19, 145.96, 144.41, 144.20, 143.78, 141.34, 128.94, 128.44, 128.21, 126.23, 125.81, 125.11, 124.65, 123.71, 123.11, 57.83, 53.25, 35.97, 35.09, 33.69.

HRMS (ESI^+) calculated for [$C_{29}H_{24}N_2O$] ([M+H]+). Requires *m/z* 417.1961; found *m/z* 417.1955.

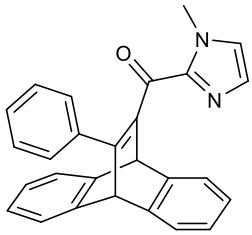

(1-methyl-1H-imidazol-2-yl)((9s,10s)-12-phenyl-9,10-dihydro-9,10-ethenoanthracen-11-yl)methanone (**S2.8**):

Prepared using the general procedure from anthracene (1.00 g, 5.61 mmol) and ethyl 3-phenylpropiolate (977 mg, 5.61 mmol). Purified with a 3:1 to 2:1 gradient Hexanes:EtOAc. Isolated 645 mg (1.66 mmol) as a yellow powder (30% Yield).

^{1}H NMR (500 MHz, $CDCl_3$) δ 7.49 – 7.44 (m, 2H), 7.38 – 7.34 (m, 2H), 7.22 – 7.15 (m, 3H), 7.13 – 7.09 (m, 2H), 7.06 – 6.97 (m, 4H), 6.84 (dd, *J* = 10.5, 1.0 Hz, 2H), 5.85 (s, 1H), 5.38 (s, 1H), 3.84 (s, 3H).

^{13}C NMR (126 MHz, $CDCl_3$) δ 184.72, 159.66, 145.46, 144.90, 144.51, 143.41, 138.34, 129.15, 127.96, 127.75, 127.42, 125.61, 125.28, 124.87, 123.88, 123.36, 59.25, 53.67, 35.45.

HRMS (ESI^+) calculated for [$C_{27}H_{20}N_2O$] ([M+H]+). Requires *m/z* 389.1648 found *m/z* 389.1643.

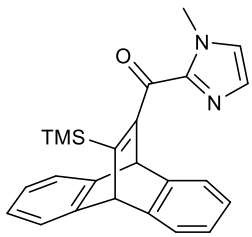

(1-methyl-1H-imidazol-2-yl)((9s,10s)-12-(trimethylsilyl)-9,10-dihydro-9,10-ethenoanthracen-11-yl)methanone (**S2.9**):

Prepared using the general procedure from anthracene (1.00 g, 5.61 mmol) and ethyl 3-(trimethylsilyl)propiolate (955 mg, 5.61 mmol). The final step was

performed on 600 mg (1.65 mmol) of weinreb amide. Purified with 0.5% to 10% gradient of MeOH in DCM. Isolated 509 mg (1.32 mmol) as a white powder (49% Adjusted Yield).

^{1}H NMR (500 MHz, $CDCl_3$) δ 7.39 (d, *J* = 6.4 Hz, 2H), 7.29 (d, *J* = 6.5 Hz, 2H), 7.17 (s, 1H), 7.03 (s, 1H), 7.01 – 6.94 (m, 4H), 5.98 (s, 1H), 5.47 (s, 1H), 3.98 (s, 3H), 0.09 (s, 9H).

^{13}C NMR (126 MHz, $CDCl_3$) δ 186.23, 162.02, 160.98, 146.35, 145.97, 144.79, 130.53, 127.71, 125.91, 125.74, 124.86, 124.13, 78.36, 78.11, 77.85, 57.26, 56.18, 37.13, 1.09, 0.01.

HRMS (ESI^+) calculated for [$C_{24}H_{24}N_2OSi$] ([M+H]+). Requires *m/z* 385.1731; found *m/z* 385.1724.

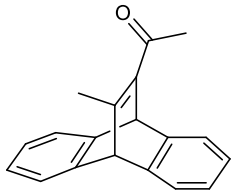

1-((9s,10s)-12-methyl-9,10-dihydro-9,10-ethenoanthracen-11-yl)ethan-1-one (**S2.10**):

Prepared using an adaptation of the general procedure from anthracene (1.00 g, 5.61 mmol) and ethyl but-2-ynoate (629 mg, 5.61 mmol). To the Weinreb amide in THF, methyl magnesium bromide (3.0 M solution in diethyl ether) was added at 0 °C and the reaction was allowed to warm to room temperature overnight. The reaction mixture was diluted with Et2O and quenched with sat. aq. NH4Cl. Extracted aq. Layers 3x with Et2O, washed combined organic layers with brine, and dried over Na2SO4. Purified with a 10:1 to 5:1 gradient Hexanes:EtOAc. Isolated 94 mg (0.36 mmol) as a white powder (6% Yield). The final step proceeded with a 40% yield based on crude mass. The diels-alder cycloaddition performed poorly in this sequence, leading to the low overall yield.

^{1}H NMR (500 MHz, $CDCl_3$) δ 7.34 (ddd, *J* = 12.8, 6.4, 1.8 Hz, 4H), 7.07 – 6.95 (m, 4H), 5.69 (s, 1H), 4.91 (s, 1H), 2.35 (s,s, 6H).

^{13}C NMR (126 MHz, $CDCl_3$) δ 196.23, 159.48, 145.10, 143.95, 143.86, 125.35, 124.79, 123.25, 123.18, 60.23, 51.18, 30.41, 20.21.

HRMS (ESI^+) calculated for [$C_{19}H_{16}N_2O$] ([M+H]+). Requires *m/z* 261.1274; found *m/z* 261.1271.

2.6.3 Synthesis of Enantioenriched Semibullvalenes

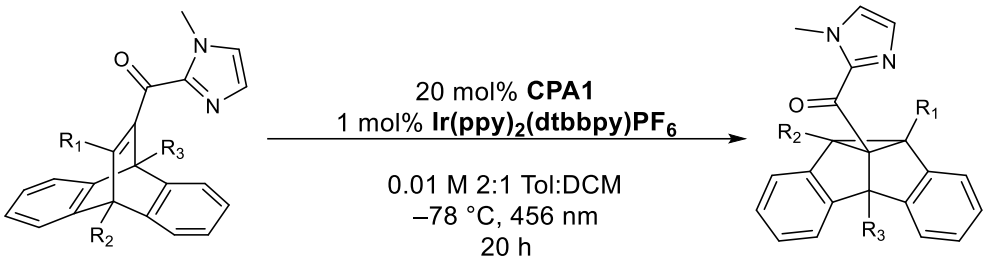

General Conditions

Dibenzobarrelene (1 equiv), $Ir(ppy)_2(dtbbpy)PF_6$ (0.01 equiv), and CPA1 (0.2 equiv) were added to a flame dried dram vial and pumped into a N_2 atmosphere glove box. The dram vial was capped with a septum cap and removed from the glovebox. DCM was added via a needle, followed by toluene by the same method, under an N_2 atmosphere provided by a Schlenk line. (0.01 M, 2:1 Toluene:DCM) The reaction mixture was stirred for 5 minutes prior to being cooled to -78 °C using a Thermo Scientific EK90 Immersion cooler. The reaction was irradiated with stirring for 20 hours using a PR160-456 LED Kessil lamp. After the irradiation period, the reaction was allowed to warm to room temperature and NEt_3 (3 mL), was added. The reaction was concentrated and purified by silica using Hexanes:EtOAc. Enantiomeric excess was determined using a Waters chiral HPLC.

Racemic standards for each substrate were obtained by reacting the respective starting materials with $Ir(dF(CF_3)ppy)_2(dtbbpy)PF_6$ under standard conditions at 0.05 mmol scale at room temperature.

Absolute stereochemistry has not yet been determined.

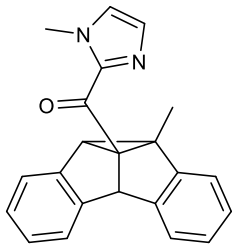

(1-methyl-1H-imidazol-2-yl)(8b-methyl-8b,8c-dihydrodibenzo[a,f]cyclopropa[cd]pentalen-4b1(4bH)-yl)methanone--(4b,8b-diethyl-8b,8c-dihydrodibenzo[a,f]cyclopropa[cd]pentalen-4b1(4bH)-yl)(1-methyl-1H-imidazol-2-yl)methanone--(4b,8b-dimethyl-8b,8c-dihydrodibenzo[a,f]cyclopropa[cd]pentalen-4b1(4bH)-yl)(1-methyl-1H-imidazol-2-yl)methanone--(8b-ethyl-8b,8c-dihydrodibenzo[a,f]cyclopropa[cd]pentalen-4b1(4bH)-yl)(1-methyl-1H-imidazol-2-yl)methanone (1/1/1/1) (**S2.11**):

Reaction run on 0.300 mmol scale, 98 mg. Purified using 3:1 Hex:EtOAc. Isolated 86 mg as a white powder (88% Yield). HPLC Conditions: Daicel CHIRALPAK AD-H column - 5µm, isocratic 20% iPrOH, 1 ml/min, 280 nm. Result 8.49 to 91.51 (83% ee).

^{1}H NMR (500 MHz, $CDCl_3$) δ 7.28 – 7.22 (m, 2H), 7.19 (dd, J = 7.0, 1.6 Hz, 1H), 7.16 – 7.06 (m, 4H), 7.03 – 6.98 (m, 2H), 6.97 (s, 1H), 5.73 (s, 1H), 4.09 (s, 1H), 3.96 (s, 3H), 1.78 (s, 3H).

^{13}C NMR (126 MHz, $CDCl_3$) δ 187.98, 150.77, 150.36, 143.62, 139.04, 137.23, 129.10, 127.31, 126.50, 126.45, 126.15, 126.12, 124.68, 123.90, 121.32, 121.00, 75.36, 57.85, 56.90, 51.47, 36.16, 15.83.

HRMS (ESI^+) calculated for [$C_{22}H_{18}N_2O$] ([M+H]+). Requires *m/z* 327.1492; found *m/z* 327.1485.

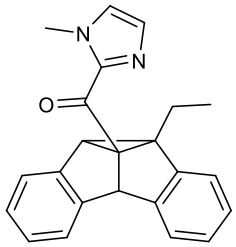

(8b-ethyl-8b,8c-dihydrodibenzo[a,f]cyclopropa[cd]pentalen-4b1(4bH)-yl)(1-methyl-1H-imidazol-2-yl)methanone (**S2.12**):

Reaction run on 0.300 mmol scale, 102 mg. Purified using 3:1 Hex:EtOAc. Isolated 100 mg as a white powder (98% Yield). HPLC Conditions: Daicel CHIRALPAK AD-H column - 5µm, isocratic 15% iPrOH, 1 ml/min, 280 nm. Result 7.67 to 92.33 (85% ee).

^{1}H NMR (500 MHz, $CDCl_3$) δ 7.29 – 7.26 (m, 1H), 7.25 – 7.22 (m, 1H), 7.19 (dd, J = 7.5, 1.4 Hz, 1H), 7.15 – 7.05 (m, 4H), 6.99 (s, 2H), 6.97 (d, J = 1.0 Hz, 1H), 5.72 (s, 1H), 4.11 (s, 1H), 3.95 (s, 3H), 2.53 (dq, J = 14.7, 7.3 Hz, 1H), 2.00 (dq, J = 14.7, 7.3 Hz, 1H), 0.84 (t, J = 7.3 Hz, 3H).

^{13}C NMR (126 MHz, $CDCl_3$) δ 188.23, 151.13, 150.81, 143.49, 137.16, 136.73, 129.10, 127.31, 126.47, 126.32, 126.11, 126.03, 124.64, 124.25, 121.57, 120.93, 74.52, 64.58, 57.02, 51.60, 36.11, 22.82, 11.86.

HRMS (ESI^+) calculated for [$C_{23}H_{20}N_2O$] ([M+H]+). Requires *m/z* 341.1648; found *m/z* 341.1642.

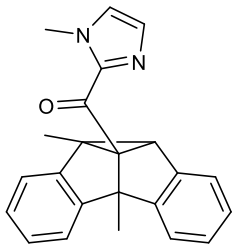

(4b,8b-dimethyl-8b,8c-dihydrodibenzo[a,f]cyclopropa[cd]pentalen-4b1(4bH)-yl)(1-methyl-1H-imidazol-2-yl)methanone (**S2.13**):

Reaction run on 0.300 mmol scale, 102 mg. Purified using 3:1 Hex:EtOAc. Isolated 98 mg as a white powder (96% Yield). HPLC Conditions: Daicel CHIRALPAK

AD-H column - 5µm, isocratic 20% iPrOH, 1 ml/min, 280 nm. Result 4.27 to 95.73 (91% ee).

^{1}H NMR (500 MHz, $CDCl_3$) δ 7.25 (q, J = 2.9 Hz, 1H), 7.16 (tt, J = 4.3, 3.4 Hz, 1H), 7.12 – 7.08 (m, 2H), 7.08 – 6.99 (m, 5H), 6.97 (d, J = 0.9 Hz, 1H), 3.95 (s, 3H), 3.91 (s, 1H), 1.76 (s, 3H), 1.64 (s, 3H).

^{13}C NMR (126 MHz, $CDCl_3$) δ 187.85, 153.44, 153.25, 144.13, 139.20, 137.35, 129.64, 126.81, 126.56, 126.46, 126.45, 126.16, 124.63, 123.64, 119.16, 118.96, 76.42, 61.75, 51.59, 47.58, 35.86, 16.90, 16.28.

HRMS (ESI$^+$) calculated for [$C_{23}H_{20}N_2O$] ([M+H]+). Requires *m/z* 341.1648; found *m/z* 341.1644.

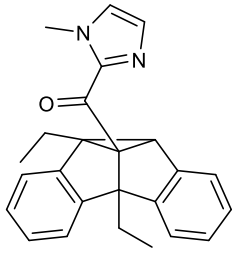

(4b,8b-diethyl-8b,8c-dihydrodibenzo[a,f]cyclopropa[cd]pentalen-4b1(4bH)-yl)(1-methyl-1H-imidazol-2-yl)methanone (**S2.14**):

Reaction run on 0.300 mmol scale, 111 mg. Purified using 3:1 Hex:EtOAc. Isolated 104 mg as a white powder (94% Yield). HPLC Conditions: Daicel CHIRALPAK OD-H column - 5µm, isocratic 1% iPrOH, 1% MTBE, 1 ml/min, 280 nm. Result 72.23 to 27.77 (44% ee).

^{1}H NMR (500 MHz, $CDCl_3$) δ 7.30 – 7.24 (m, 1H), 7.22 – 7.17 (m, 1H), 7.13 – 6.94 (m, 8H), 4.07 (s, 1H), 3.95 (s, 3H), 2.60 (dq, J = 14.9, 7.5 Hz, 1H), 2.49 (dq, J = 14.5, 7.3 Hz, 1H), 2.10 (dq, J = 15.1, 7.5 Hz, 1H), 1.89 (dq, J = 14.6, 7.3 Hz, 1H), 1.06 (t, J = 7.5 Hz, 3H), 0.69 (t, J = 7.4 Hz, 3H).

^{13}C NMR (126 MHz, $CDCl_3$) δ 188.49, 153.43, 151.23, 143.92, 137.85, 137.71, 129.20, 126.73, 126.48, 126.38, 126.27, 126.12, 124.59, 124.15, 119.67, 119.23, 75.19, 67.37, 57.40, 47.46, 35.88, 24.43, 20.95, 11.59, 9.82.

HRMS (ESI$^+$) calculated for [$C_{25}H_{24}N_2O$] ([M+H]+). Requires *m/z* 369.1961; found *m/z* 369.1955.

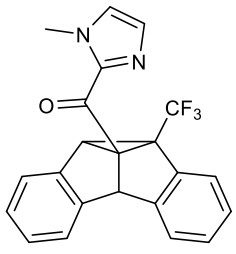

(1-methyl-1H-imidazol-2-yl)(8b-(trifluoromethyl)-8b,8c-dihydrodibenzo[a,f]cyclopropa[cd]pentalen-4b1(4bH)-yl)methanone--(1-methyl-1H-imidazol-2-yl)(8b-phenethyl-8b,8c-dihydrodibenzo[a,f]cyclopropa[cd]pentalen-4b1(4bH)-yl)methanone--(8b-cyclohexyl-8b,8c-dihydrodibenzo[a,f]cyclopropa[cd]pentalen-4b1(4bH)-yl)(1-methyl-1H-imidazol-2-yl)methanone (1/1/1) (**S2.15**):

Reaction run on 0.300 mmol scale, 114 mg. Reaction was irradiated for an extended period of time, 40 hours, using 2 456 nm Kessil lamps. Purified using 3:1 Hex:EtOAc. Isolated 74 mg as a white powder (65% Yield). 30 mg of starting material was obtained from the same column. (26% RSM) HPLC Conditions: AD-H column, isocratic 20% iPrOH. Result 39.98 to 60.02 (20% ee).

^{1}H NMR (400 MHz, $CDCl_3$) δ 7.43 (d, *J* = 7.5 Hz, 1H), 7.39 – 7.34 (m, 1H), 7.25 (d, *J* = 3.4 Hz, 1H), 7.20 (td, *J* = 7.5, 1.3 Hz, 1H), 7.17 – 7.05 (m, 5H), 7.02 (s, 1H), 5.22 (s, 1H), 4.39 (s, 1H), 3.99 (s, 3H).

^{19}F NMR (377 MHz, $CDCl_3$) δ -62.79.

^{13}C NMR (101 MHz, $CDCl_3$) δ 183.60, 134.69, 134.69, 130.20, 128.38, 127.60, 127.07, 127.00, 126.90, 125.89, 125.04, 121.62, 121.21, 59.63, 43.27, 36.01.

HRMS (ESI$^+$) calculated for [$C_{22}H_{15}F_3N_2O$] ([M+H]+). Requires *m/z* 381.1209; found *m/z* 381.1203.

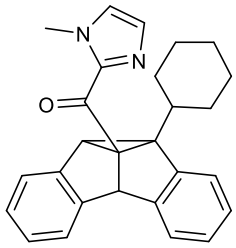

(8b-cyclohexyl-8b,8c-dihydrodibenzo[a,f]cyclopropa[cd]pentalen-4b1(4bH)-yl)(1-methyl-1H-imidazol-2-yl)methanone (**S2.16**):

Reaction run on 0.300 mmol scale, 118 mg. Purified using 3:1 Hex:EtOAc. Isolated 81 mg as a white powder (68% Yield). CHIRALPAK AD-H column - 5µm, isocratic 20% iPrOH, 1 ml/min, 280 nm. Result 33.96 to 66.04 (32% ee).

^{1}H NMR (500 MHz, $CDCl_3$) δ 7.45 (d, *J* = 7.6 Hz, 1H), 7.29 – 7.22 (m, 2H), 7.12 (d, *J* = 1.0 Hz, 1H), 7.12 – 7.06 (m, 2H), 7.06 – 7.02 (m, 1H), 7.01 – 6.95 (m, 3H), 5.54 (s, 1H), 3.95 (s, 1H), 3.94 (s, 3H), 2.17 – 2.09 (m, 1H), 2.04 – 1.95 (m, 1H), 1.91 (dd, *J* = 13.1, 4.3 Hz, 1H), 1.69 (tt, *J* = 12.4, 2.8 Hz, 2H), 1.63 – 1.53 (m, 2H), 1.36 (qt, *J* = 12.7, 3.6 Hz, 1H), 1.21 (dt, *J* = 13.3, 3.5 Hz, 1H), 1.14 – 1.02 (m, 2H).

^{13}C NMR (126 MHz, $CDCl_3$) δ 188.33, 151.50, 151.26, 143.53, 137.15, 135.81, 129.20, 127.11, 126.38, 126.12, 125.97, 125.96, 125.58, 124.61, 121.69, 120.89, 74.78, 67.17, 57.29, 50.17, 40.10, 35.98, 31.19, 29.70, 27.38, 26.56, 26.54.

HRMS (ESI$^+$) calculated for [$C_{27}H_{26}N_2O$] ([M+H]+). Requires *m/z* 395.2118; found *m/z* 395.111.

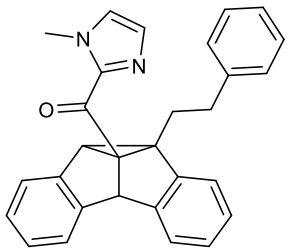

(1-methyl-1H-imidazol-2-yl)(8b-phenethyl-8b,8c-dihydrodibenzo[a,f]cyclopropa[cd]pentalen-4b1(4bH)-yl)methanone (**S2.17**): Reaction run on 0.240 mmol scale, 100 mg. Purified using 3:1 Hex:EtOAc. Isolated 62 mg as a white powder (62% Yield). HPLC Conditions: CHIRALPAK AD-H column - 5µm, isocratic 10% iPrOH, 1 ml/min, 280 nm. Result 12.64 to 87.36 (75% ee).

^{1}H NMR (500 MHz, $CDCl_3$) δ 7.33 – 7.25 (m, 2H), 7.22 (td, J = 6.4, 5.7, 1.7 Hz, 3H), 7.14 (tdd, J = 6.5, 3.8, 2.0 Hz, 5H), 7.07 – 7.03 (m, 2H), 7.03 – 6.99 (m, 2H), 6.98 (d, J = 1.0 Hz, 1H), 5.78 (s, 1H), 4.19 (s, 1H), 3.96 (s, 3H), 2.84 – 2.72 (m, 2H), 2.43 – 2.31 (m, 1H), 2.31 – 2.22 (m, 1H).

^{13}C NMR (126 MHz, $CDCl_3$) δ 187.98, 151.05, 150.79, 143.43, 141.97, 136.94, 136.83, 129.15, 128.29, 128.27, 127.45, 126.58, 126.49, 126.21, 126.18, 125.76, 124.76, 124.16, 121.71, 120.97, 74.53, 62.77, 56.93, 51.72, 36.28, 33.80, 31.91.

HRMS (ESI^+) calculated for [$C_{29}H_{24}N_2O$] ([M+H]+). Requires *m/z* 417.1961; found *m/z* 417.1956.

2.6.4 Synthesis of Starting Materials for Achiral DPM

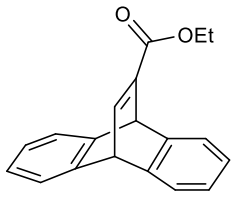

Ethyl (9s,10s)-9,10-dihydro-9,10-ethenoanthracene-11-carboxylate (**S2.18**):

A 25 mL round-bottomed flask was charged with anthracene (1.12 mmol, 1 equiv), ethyl propiolate (1.12 mmol, 1 equiv), aluminum chloride (1.12 mmol, 1 equiv), and anhydrous toluene (1.8 mL, 0.62 M with respect to substrate). The solution was stirred and heated at reflux (130 °C) for 2 h. The reaction was cooled and extracted three times into an equal volume of ethyl acetate. The organic layers were washed with brine, dried over $MgSO_4$, filtered, and concentrated *in vacuo*. Isolated pale-yellow solid (278 mg, 1.01 mmol, 90% yield). Chemical shifts were consistent with previous reports.[93]

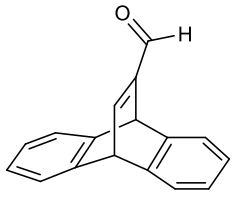

(9s,10s)-9,10-dihydro-9,10-ethenoanthracene-11-carbaldehyde (**S2.19**):

A 25 mL round-bottomed flask was charged with S2.18 (1.81 mmol, 1 equiv.) and anhydrous DCM (13 mL). The stirring solution was cooled to –78 °C, and a 1 M solution of DIBAL-H in hexane was added dropwise over 2 min. Solution stirred at –78 °C for 30 min under N_2. The reaction was warmed to room temperature and 35 mL H_2O was added. The reaction was extracted three times into an equal volume of DCM, and the organic layers were washed with a saturated aqueous solution of Rochelle's salt. The combined organic layer was dried over $MgSO_4$, filtered, and concentrated *in vacuo*. Isolated alcohol as a white solid (382 mg, 1.63 mmol, 89% yield). Chemical shifts were consistent with previous reports.[94]

A 100 mL round-bottomed flask was charged with the Dess–Martin Periodinane reagent (3.26 mmol, 2 equiv.) and sodium bicarbonate (8.15 mmol, 5 equiv.), and anhydrous DCM (15 mL). The solution was cooled to 0 °C and was added a solution of 7-hydroxymethyldibenzobi-cyclo[2.2.2]octatriene, from previous step (1.63 mmol, 1 equiv.), in anhydrous DCM (15 mL) over 5 min. The reaction was warmed to room temperature and stirred for 30 min under N_2. The reaction was quenched with a $NaHCO_3$:$Na_2S_2O_3$ solution (1:1). The reaction was extracted three times into an equal volume of DCM. The combined organic layers were washed with 1 M NaOH and with water. The organic layers were dried over $MgSO_4$, filtered,

and concentrated *in vacuo*. The crude product was purified by flash column chromatography on silica gel (9:1 Hexanes:EtOAc), affording a white solid **S2.19** (295 mg, 1.27 mmol, 78% yield).

^{1}H NMR (500 MHz, $CDCl_3$) δ 9.55 (s, 1H), 7.83 (dd, *J* = 6.1, 1.8 Hz, 1H), 7.38 – 7.37 (m, 2H), 7.35 – 7.34 (m, 2H), 7.01 – 6.99 (m, 4H), 5.74 (d, *J* = 1.6 Hz, 1H), 5.34 (d, 6.1 Hz, 1H).

^{13}C NMR (126 MHz, $CDCl_3$) δ 187.09, 158.05, 153.87, 144.53, 144.03, 125.42, 124.99, 124.00, 123.70, 51.82, 47.07.

HRMS (ESI^+) calculated for [$C_{17}H_{13}O^+$] ([M+H]+). Requires *m/z* 233.0961; found *m/z* 233.0958.

IR (ATR, powder): 3061, 2974, 2809, 2720, 1666, 1457, 1141, 747 cm^{-1}.

M.P. 109–113 °C.

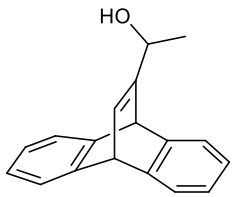

1-((9s,10s)-9,10-dihydro-9,10-ethenoanthracen-11-yl)ethan-1-ol (**S2.20**):

A 25 mL round-bottomed flask was charged with (9*s*,10*s*)-9,10-dihydro-9,10-ethenoanthracene-11-carbaldehyde S2.19 (0.43 mmol, 1 equiv.) and anhydrous THF (1.75 mL). The solution was cooled to 0 °C and a 3 M solution of methyl magnesium bromide in diethyl ether (0.17 mL) was added dropwise over 2 min. The reaction was warmed to room temperature and stirred for 30 min under N_2. The reaction was quenched with 0.5 M HCl solution (10 mL) and extracted three times into an equal volume of ethyl acetate. The organic layers were washed with brine, dried over $MgSO_4$, filtered, and concentrated *in vacuo*. Isolated a white solid **S2.20** (101 mg, 0.41 mmol, 96% yield).

^{1}H NMR (500 MHz, $CDCl_3$) δ 7.32 – 7.29 (m, 2H), 7.28 – 7.27 (m, 2H), 6.96 – 6.94 (m, 4H), 6.70 (dt, *J* = 5.97, 1.60 Hz, 1H), 5.18 (d, *J* = 1.59 Hz, 1H), 5.08 (d, *J* = 5.98 Hz, 1H), 4.54 (br, 1H), 1.30 (d, *J* = 6.42 Hz, 3H).

^{13}C NMR (126 MHz, $CDCl_3$) δ 156.14, 146.59, 146.47, 146.08, 145.96, 132.03, 124.54, 124.50, 124.49, 122.93, 122.88, 122.82, 68.43, 51.67, 50.58, 20.95.

HRMS (ESI^+) calculated for [$C_{18}H_{20}NO$] ([M+NH_4]+). Requires *m/z* 266.1539; found *m/z* 266.1536.

IR (ATR, powder): 3326, 3061, 3014, 2971, 2926, 2880, 1455, 1061, 744 cm^{-1}.

M.P. 95–98 °C.

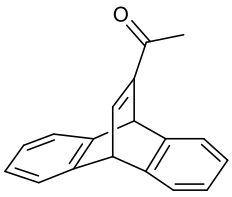

1-((9s,10s)-9,10-dihydro-9,10-ethenoanthracen-11-yl)ethan-1-one (**S2.21**):

A 50 mL round-bottomed flask was charged with the Dess–Martin Periodinane reagent (0.74 mmol, 2 equiv.), sodium bicarbonate (1.86 mmol, 5 equiv.), and anhydrous DCM (3.5 mL). The solution was cooled to 0 °C and was added a solution of 1-((9*s*,10*s*)-9,10-dihydro-9,10-ethenoanthracen-11-yl)ethan-1-ol S2.20 (0.37 mmol, 1 equiv.) in anhydrous DCM (3.5 mL) over 2 min. The reaction was warmed to room temperature and stirred for 30 min under N_2. The reaction was quenched with a $NaHCO_3$:$Na_2S_2O_3$ solution (1:1). The reaction was extracted three times into an equal volume of DCM. The combined organic layers were washed with 1 M NaOH and with water. The organic layers were dried over $MgSO_4$, filtered, and concentrated *in vacuo*. The crude product was purified by flash column chromatography on silica gel (9:1 hexanes:EtOAc), affording a white solid **S2.21** (57 mg, 0.23 mmol, 63% yield).

^{1}H NMR (500 MHz, $CDCl_3$) δ 7.80 (dd, *J* = 6.15, 1.85 Hz, 1H), 7.38 – 7.36 (m, 2H), 7.34 – 7.33 (m, 2H), 7.00 – 6.98 (m, 4H), 5.85 (d, *J* = 1.59 Hz, 1H), 5.27 (d, *J* = 6.12 Hz, 1H), 2.23 (s, 3H).

^{13}C NMR (126 MHz, $CDCl_3$) δ 193.95, 152.47, 150.04, 145.19, 144.36, 125.21, 124.81, 123.95, 123.47, 51.56, 48.36, 25.43.

HRMS (ESI$^+$) calculated for [$C_{18}H_{15}O$] ([M+H]+). Requires *m/z* 247.1117; found *m/z* 247.1115.

IR (ATR, powder): 3068, 3014, 2968, 2923, 2853, 1660, 1456, 743 cm^{-1}.

M.P. 141–145 °C.

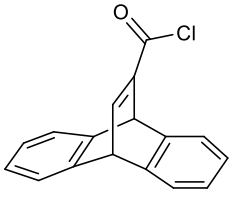

(9s,10s)-9,10-dihydro-9,10-ethenoanthracene-11-carbonyl chloride (**S2.22**):

A 25 mL round-bottomed flask was charged with a solution of sodium hydroxide (11.2 mmol, 15 equiv.) in ethanol (4 mL) and water (1.6 mL). To the solution was added 9,10-dihydro-9,10-ethenoanthracene-11-ethyl carboxylate S2.18 (0.75 mmol, 1 equiv.). The reaction was refluxed at 104 °C for 1 h open to air. The reaction was cooled to room temperature and added 0.5 M HCl solution until solution was acidic. The reaction was extracted three times into an equal volume of diethyl ether. The organic layers were dried over $MgSO_4$, filtered, and

concentrated *in vacuo*. Isolated a white solid 9,10-dihydro-9,10-ethenoanthracene-11-carboxylic acid (169 mg, 0.68 mmol, 91% yield). Chemical shifts were consistent with previous reports.[93]

9,10-dihydro-9,10-ethenoanthracene-11-carboxylic acid, from previous step (0.56 mmol, 1 equiv.), and anhydrous DCM (0.56 mL) at room temperature. To the stirring solution was added oxalyl chloride (1.4 mmol, 2.5 equiv.) and anhydrous DMF (0.01 mL). Reaction stirred for 40 min. Residual reagents and solvents removed *in vacuo*. Isolated a pale yellow solid **S2.22** (124 mg, 0.46 mmol, 82% yield).

^{1}H NMR (500 MHz, $CDCl_3$) δ 8.25 (dd, *J* = 6.38, 2.01 Hz, 1H), 7.39 – 7.35 (m, 4H), 7.05 – 7.01 (m, 4H), 5.66 (d, *J* = 1.89 Hz, 1H), 5.35 (d, *J* = 6.37 Hz, 1H).

^{13}C NMR (126 MHz, $CDCl_3$) δ 164.76, 159.55, 149.16, 144.14, 143.20, 125.60, 125.39, 123.98, 123.97, 52.16, 50.43.

IR (ATR, powder): 3070, 2991, 1731, 1456, 1137, 735 cm^{-1}.

M.P. 238–240 °C.

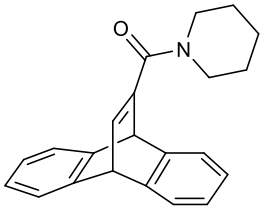

((9s,10s)-9,10-dihydro-9,10-ethenoanthracen-11-yl)(piperidin-1-yl)methanone (**S2.23**):

To a solution of piperidine (2.6 mmol, 1 equiv.) and trimethylamine (7.9 mmol, 3 equiv.) at 0 °C was added a solution of 9,10-dihydro-9,10-ethenoanthracene-11-carbonyl chloride S2.22 (2.6 mmol, 1 equiv.) in anhydrous DCM (5.2 mL). Reaction gradually warmed to room temperature and stirred overnight. Reaction was diluted with 0.5 M HCl and extracted three times into an equal volume of diethyl ether. The organic layers were washed with 2M NaOH (x2), brine (x1), dried over $MgSO_4$, filtered, and concentrated *in vacuo*. The crude product was purified by flash column chromatography on silica gel (1:1 hexanes:EtOAc), affording a white solid **S2.23** (347 mg, 1.1 mmol, 42% yield).

^{1}H NMR (500 MHz, $CDCl_3$) δ 7.34 – 7.33 (m, 2H), 7.30 – 7.28 (m, 2H), 7.04 (dd, *J* = 6.05, 1.84 Hz, 1H), 6.98 – 6.95 (m, 4H), 5.26 (d, *J* = 1.61 Hz, 1H), 5.19 (d, *J* = 6.02 Hz, 1H), 3.37 (br, 4H), 1.63 (br, 2H), 1.51 (br, 4H).

^{13}C NMR (500 MHz, $CDCl_3$) δ 167.84, 147.15, 145.34, 145.05, 139.31, 124.81, 124.74, 123.37, 123.13, 53.28, 50.97, 24.63.

HRMS (ESI^+) calculated for [$C_{22}H_{22}NO$] ([M+H]+). Requires *m/z* 316.1696; found *m/z* 316.1694.

IR (ATR, powder): 3061, 2932, 2851, 1604, 1428, 1221, 756 cm^{-1}.

M.P. 129–132 °C.

2.6.5 Photoreactions of Achiral DPM

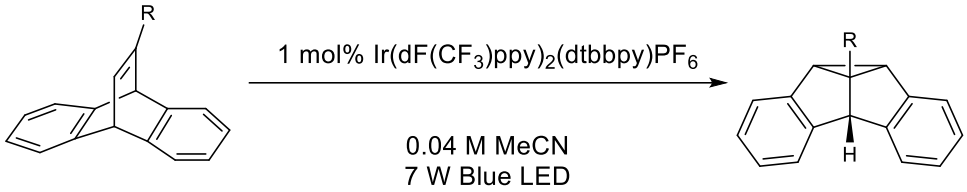

General Procedure

A 25 mL Schlenk flask was charged with a 9,10-dihydro-9,10-ethenoanthracene derivative (0.2 mmol, 1 equiv.), $Ir(dF(CF_3)ppy)_2(dtbbpy)PF_6$ ($2.1x10^{-3}$ mmol, 0.01 equiv.) and anhydrous MeCN (5.0 mL, 0.04 M). Residual oxygen was removed from solution via three freeze-pump-thaw cycles. Reaction exposed to 7 W blue lamp (10 cm distance). Crude product was purified by flash column chromatography on silica gel (9:1 hexanes:EtOAc).

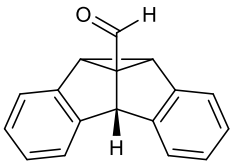

8b,8c-dihydrodibenzo[a,f]cyclopropa[cd]pentalene-4b1(4bH)-carbaldehyde (**S2.24**):

Prepared according to General Procedure using (9*s*,10*s*)-9,10-dihydro-9,10-ethenoanthracene-11-carbaldehyde **S2.19**. Irradiation time was 6 h. Following workup and purification, a white solid was isolated S2.24 (52.9 mg, 0.2 mmol, 97% yield). Chemical shifts were consistent with previous reports.[95]

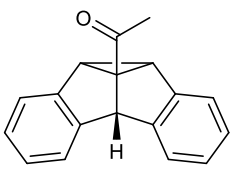

1-(8b,8c-dihydrodibenzo[a,f]cyclopropa[cd]pentalen-4b1(4bH)-yl)ethan-1-one (**S2.25**):

Prepared according to General Procedure using 1-((9*s*,10*s*)-9,10-dihydro-9,10-ethenoanthracen-11-yl)ethan-1-one **S2.21**. Irradiation time was 6 h. Following workup and purification, a white solid was isolated **S2.25** (54.9 mg, 0.22 mmol, 96% yield).

^{1}H NMR (500 MHz, $CDCl_3$) δ 7.25 – 7.24 (m, 2H), 7.17 – 7.15 (m, 2H), 7.09 – 7.03 (m, 4H), 5.05 (s, 1H), 3.86 (s, 2H), 2.17 (s, 3H).

^{13}C NMR (126 MHz, $CDCl_3$) δ 204.01, 149.98, 135.20, 127.13, 126.62, 124.62, 121.44, 72.12, 53.04, 48.00, 25.56.

HRMS (ESI^+) calculated for [$C_{18}H_{15}O$] ([M+H]+). Requires *m/z* 247.1117; found *m/z* 247.1115.

IR (ATR, powder): 3036, 2926, 1670, 1463, 1235, 763 cm^{-1}.

M.P. 192–194 °C.

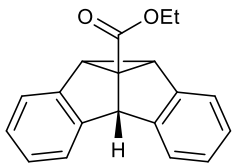

ethyl 8b,8c-dihydrodibenzo[a,f]cyclopropa[cd]pentalene-4b1(4bH)-carboxylate (**S2.26**):

Prepared according to General Procedure using 9,10-dihydro-9,10-ethenoanthracene-11-ethyl carboxylate **S2.18**. Irradiation time was 72 h. Following workup and purification, a white solid was isolated **S2.26** (50.9 mg, 0.18 mmol, 91% yield).

^{1}H NMR (500 MHz, $CDCl_3$) δ 7.24 (m, 2H), 7.16 – 7.14 (m, 2H), 7.08 – 7.03 (m, 4H), 4.96 (s, 1H), 4.19 (q, *J* = 7.13 Hz, 2H), 3.77 (s, 2H), 1.27 (t, *J* = 7.13 Hz, 3H).

^{13}C NMR (126 MHz, $CDCl_3$) δ 171.95, 150.24, 135.56, 126.95, 126.60, 124.75, 121.33, 62.20, 60.86, 53.90, 46.97, 14.33.

HRMS (ESI^+) calculated for [$C_{19}H_{17}O_2$] ([M+H]+). Requires *m/z* 277.1223; found *m/z* 277.1221.

IR (ATR, powder): 2989, 2932, 1708, 1463, 1234, 738 cm^{-1}.

M.P. 136–138 °C.

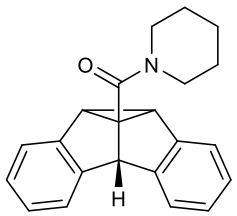

(8b,8c-dihydrodibenzo[a,f]cyclopropa[cd]pentalen-4b1(4bH)-yl)(piperidin-1-yl)methanone (**S2.27**):

Prepared according to General Procedure using ((9*s*,10*s*)-9,10-dihydro-9,10-ethenoanthracen-11-yl)(piperidin-1-yl)methanone **S2.23** and aluminum chloride (0.2 mmol, 1 equiv.). Irradiation time was 168 h. Following workup and purification by flash column chromatography (1:1 hexanes:EtOAc), a white solid was isolated **S2.27** (58.8 mg, 0.19 mmol, 93% yield).

^{1}H NMR (500 MHz, CD_3CN) δ 7.30 – 7.27 (m, 2H), 7.24 – 7.21 (m, 2H), 7.09 – 7.06 (m, 4H), 4.64 (s, 1H), 3.49 (s, 2H), 3.31 (br, 4H), 1.62 – 1.57 (m, 2H), 1.44 (br, 4H).

^{13}C NMR (126 MHz, CD_3CN) δ 168.49, 150.96, 137.20, 127.54, 127.25, 125.59, 122.10, 64.05, 57.83, 43.26, 24.83.

HRMS (ESI^+) calculated for [$C_{22}H_{22}NO$] ([M+H]+). Requires *m/z* 316.1696; found *m/z* 316.1694.

IR (ATR, powder): 3012.67, 2931.47, 2851.74, 1626.56, 1434.57, 1252.57, 1225.35, 761.36, 739.13 cm^{-1}.

M.P. 119–120 °C.

2.6.6 Survey of Phosphoric Acid Derivatives

The following data were obtained by running the standard reaction on substrate **S2.1** in 0.01 M toluene at 0.05 mmol scale at room temperature. Values listed are of the observed enantiomeric excess under those conditions. The catalysts employed were obtained by from previous projects, generous donations from the Toste group, and by independent synthesis.

A further data set contains a comparison of structures run under the previous conditions and the optimized conditions at 0.05 mmol scale, listing the observed enantiomeric excess. We found it notable that defined trends in catalytic activity were not readily identified from the data. Use of the phosphoramide vs the phosphoric acid did not result in an increase in ee for all cases, nor did catalyst proficiency seem to correlate directly with electronics or sterics.

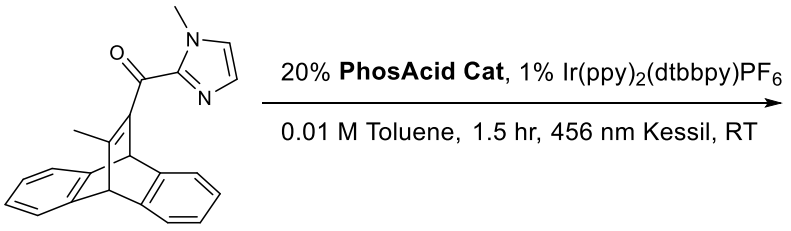

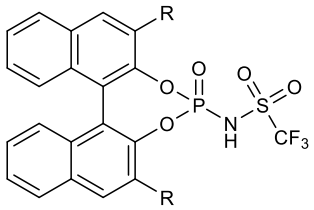

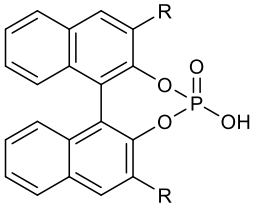

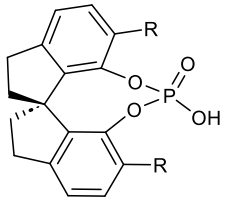

R=			
H		10%	
Me		2%	
TMS		4%	
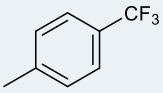	71%	38%	
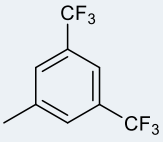	30%	50%	18%
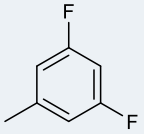			9%
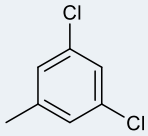			14%
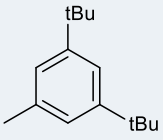	40%		0%

R=	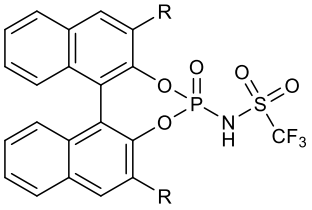	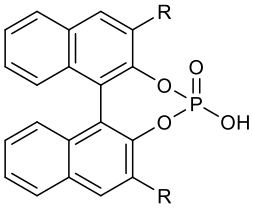	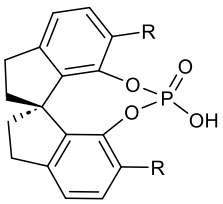
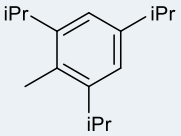		5%	
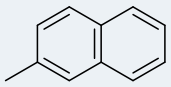		37%	
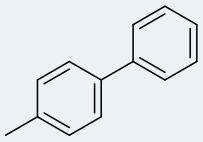			7%
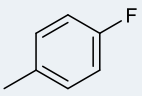		48%	
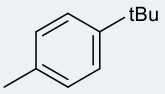		22%	
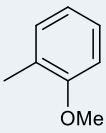		36%	
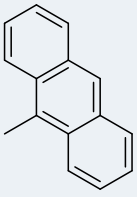		0%	
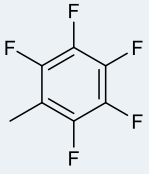		36%	

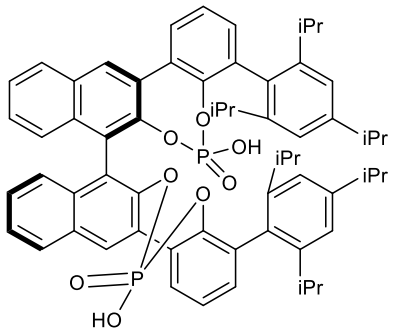

10% (R)

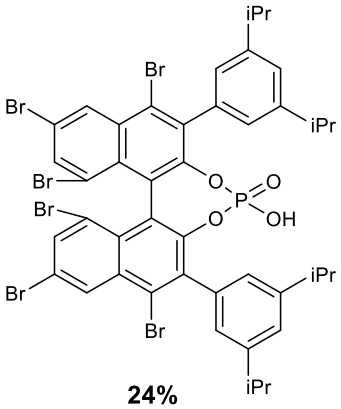

24%

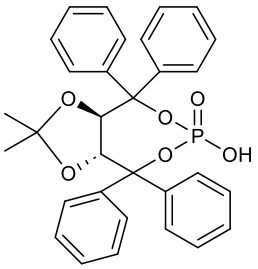

0%

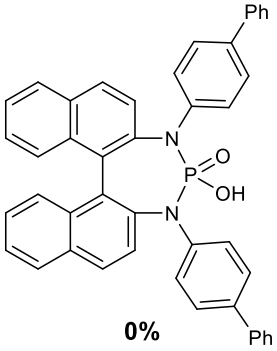

0%

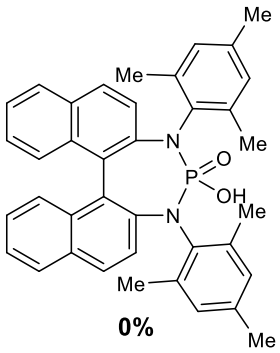

0%

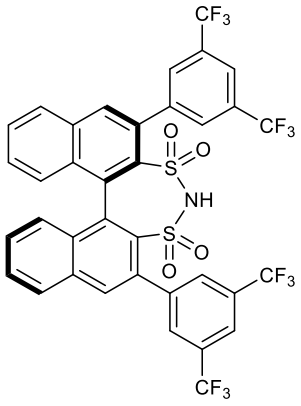

25%

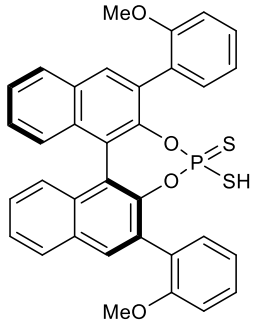

(S) **8%**

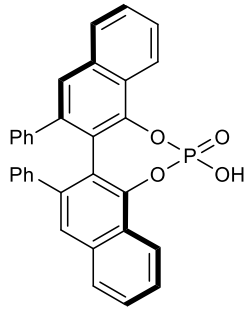

(S) **20%**

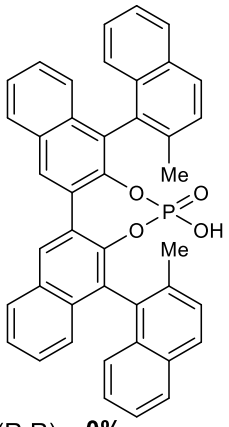

(R,R) **0%**

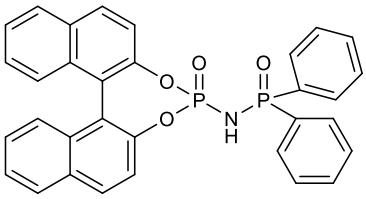

1%

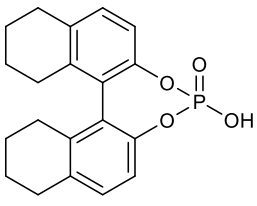

2%

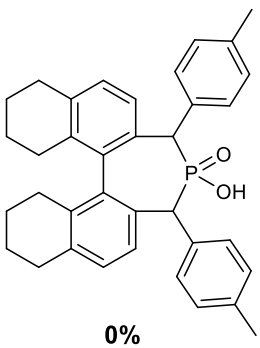

0%

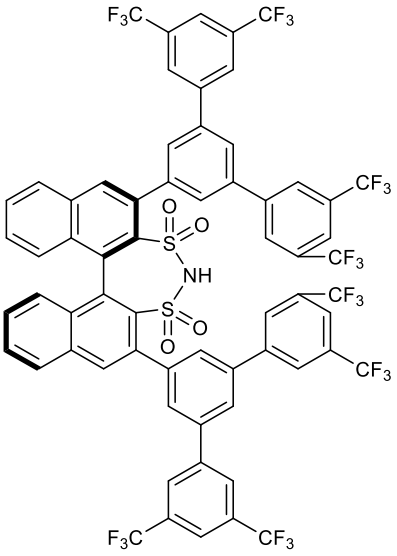

44%

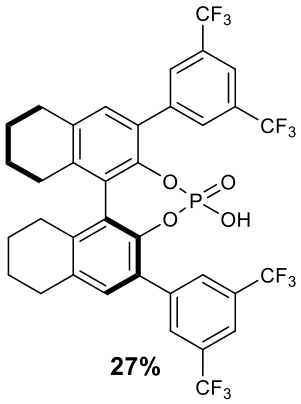

27%

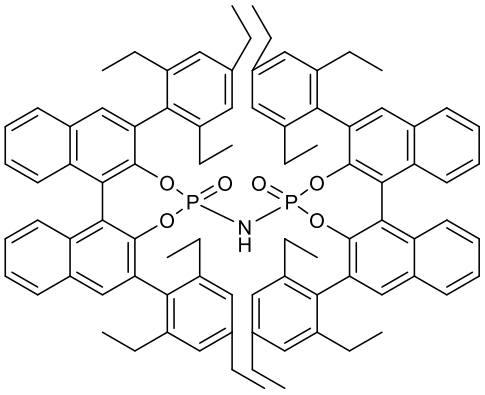

31%

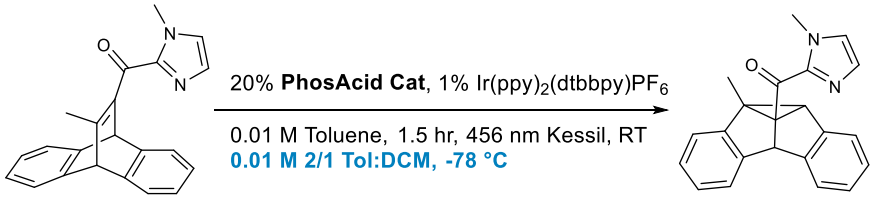

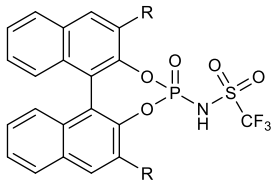

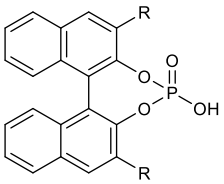

R=		
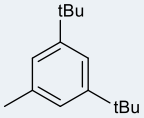	40%	**48%**
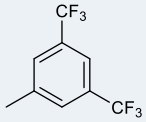	30%/**34%**	50%/**64%**
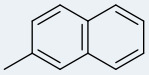	**56%**	37%
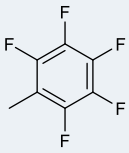		36%
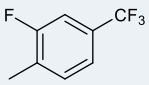	**81%**	
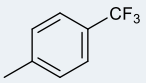	71%/**85%**	38%
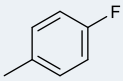	**76%**	48%
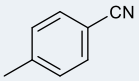	**33%**	
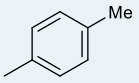	**69%**	2%
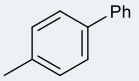	**6%**	
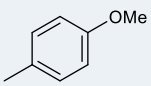	**36%**	

2.6.7 Efforts Towards Optimization of Chiral-at-Iridium Sensitized Enantioselective DPM

The following figures present a brief overview of efforts toward optimization of the triplet-sensitized, enantioselective DPM rearrangement using chiral-at-metal iridium sensitizers. Reactions were run using the general procedure under modified conditions, using only a chiral iridium sensitizer and solvents as specified. A wide range of chiral-at-iridium sensitizers were tested. Of these, Ir(2,4-$bCF_3(CF_3)bpy)_2$(pypz)BArF gave the best ee under the examined conditions. A short survey of other major variables did not serve to increase the observed ee. Cooling the reaction reduced the rate but did not affect the ee.

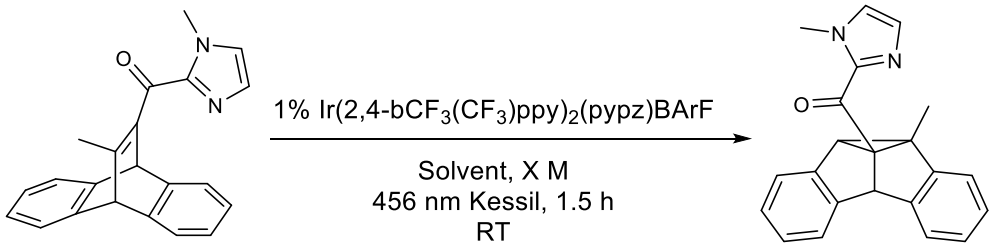

Entry	Conditions	RSM	Yield	ee
1	DCM	9%	74%	27%
2	Toluene	0%	82%	21%
3	MeCN	31%	66%	2%
4	1:1 DCM/Pentanes	5%	62%	26%
5	2:1 DCM/Pentanes	5%	62%	24%
6	5:1 DCM/Pentanes	25%	70%	25%
7	1:1 Tol/Pentanes	0%	78%	13%
8	2:1 Tol/Pentanes	0%	81%	17%
9	5:1 Tol/Pentanes	0%	77%	18%
10	0.04 M DCM	9%	74%	27%
11	0.025 M DCM	13%	58%	28%
12	0.0125 M DCM	16%	66%	28%
13	0.008 M DCM	16%	56%	27%
	In 0.04 M DCM			
14	RT	9%	74%	27%
15	0 °C	14%	63%	30%
16	-78 °C	59%	12%	27%

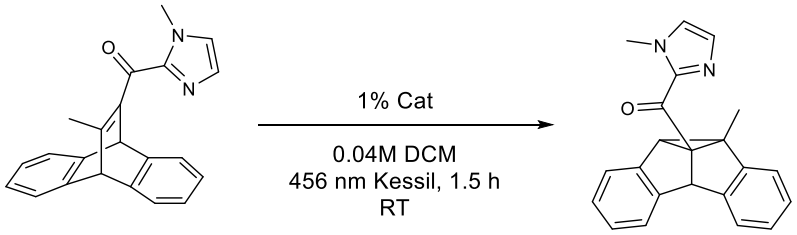

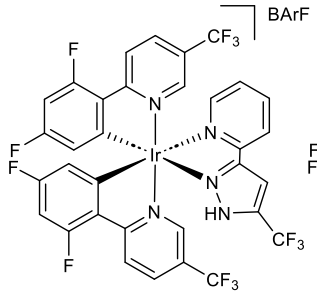

76% Yield
0% ee

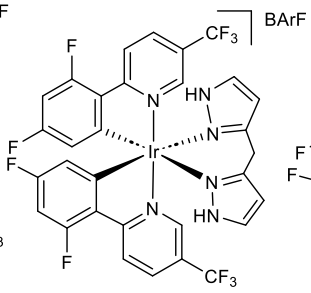

85% Yield
1% ee

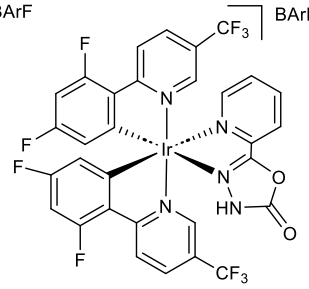

58% Yield
-2% ee

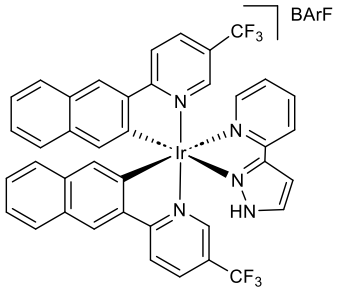

5% Yield
6% ee

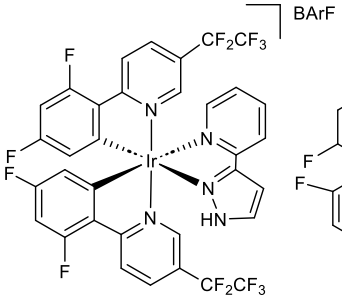

78% Yield
8% ee

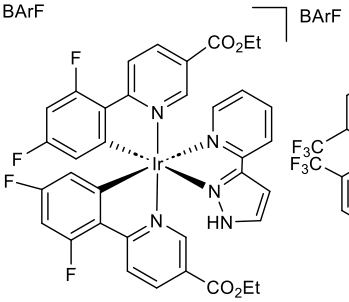

79% Yield
10% ee

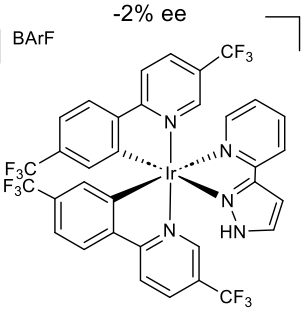

85% Yield
11% ee

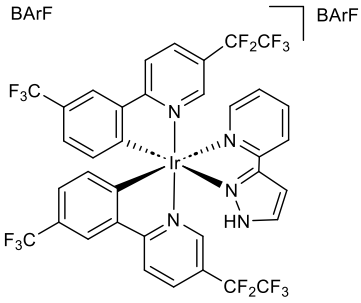

81% Yield
13% ee

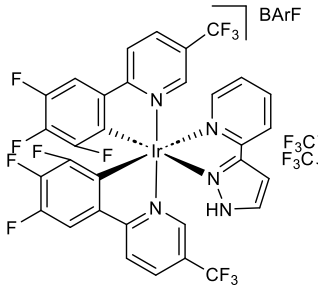

83% Yield
19% ee

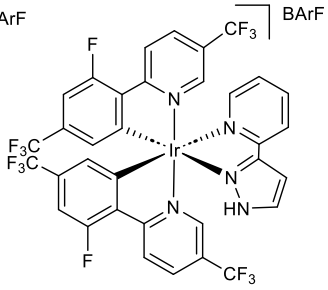

85% Yield
24% ee

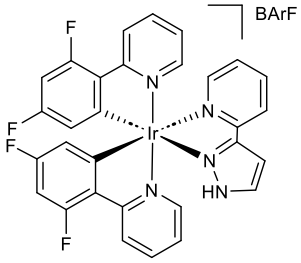

70% Yield
6% ee

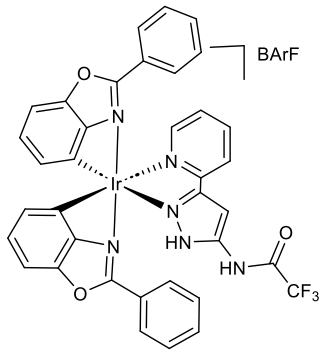

72% Yield
-6% ee

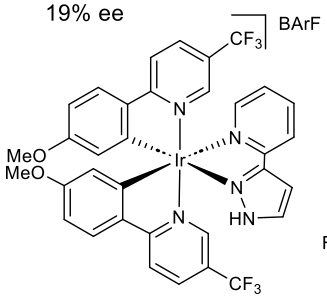

88% Yield
16% ee

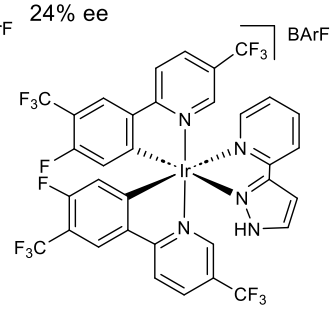

76% Yield
18% ee

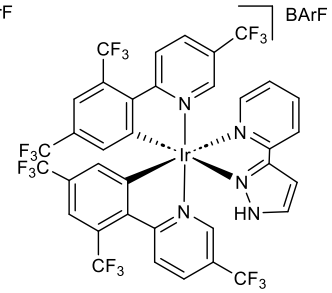

72% Yield
29% ee

2.6.8 NMR Spectra

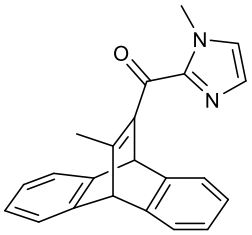

(1-methyl-1H-imidazol-2-yl)((9s,10s)-12-methyl-9,10-dihydro-9,10-ethenoanthracen-11-yl)methanone (**S2.1**):

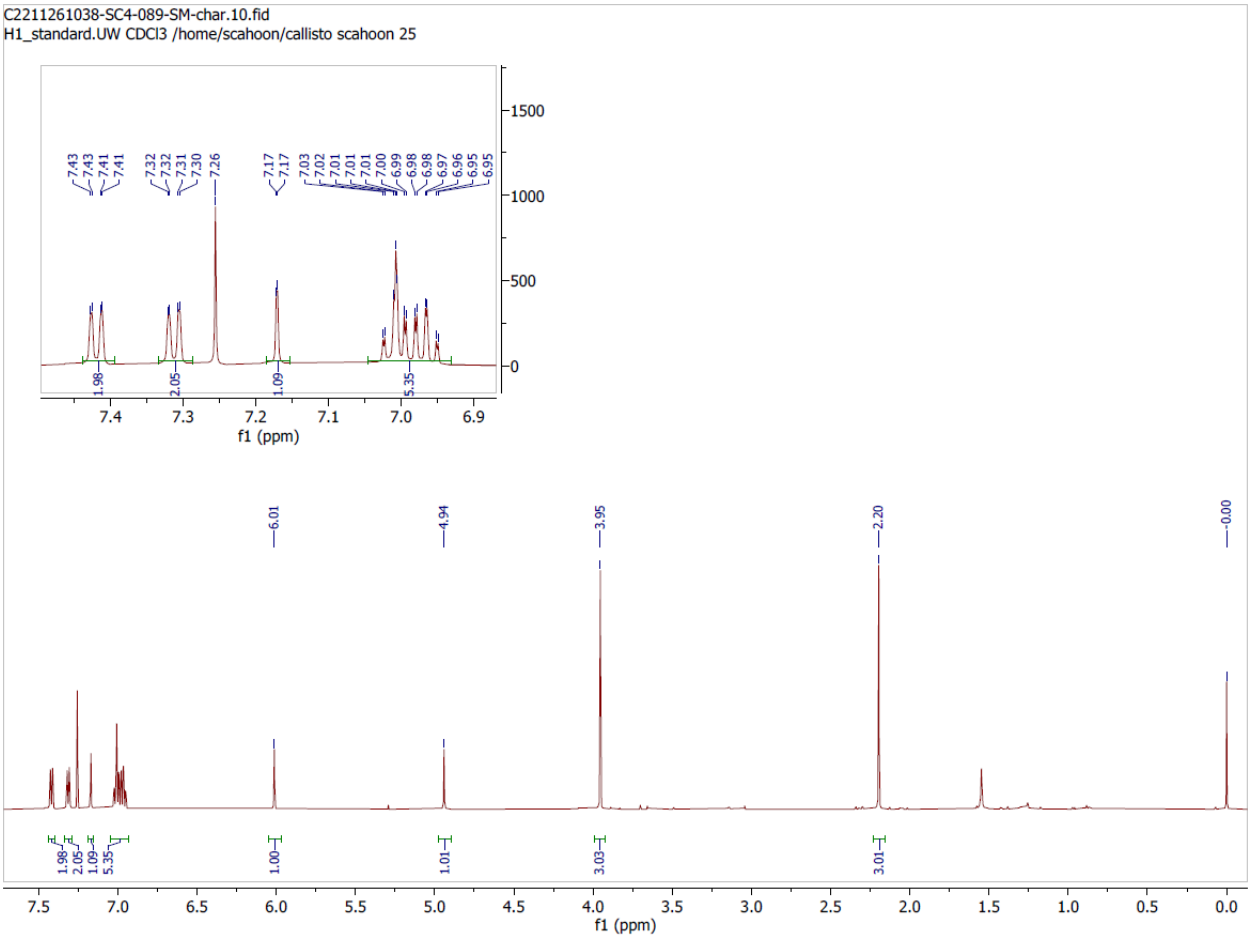

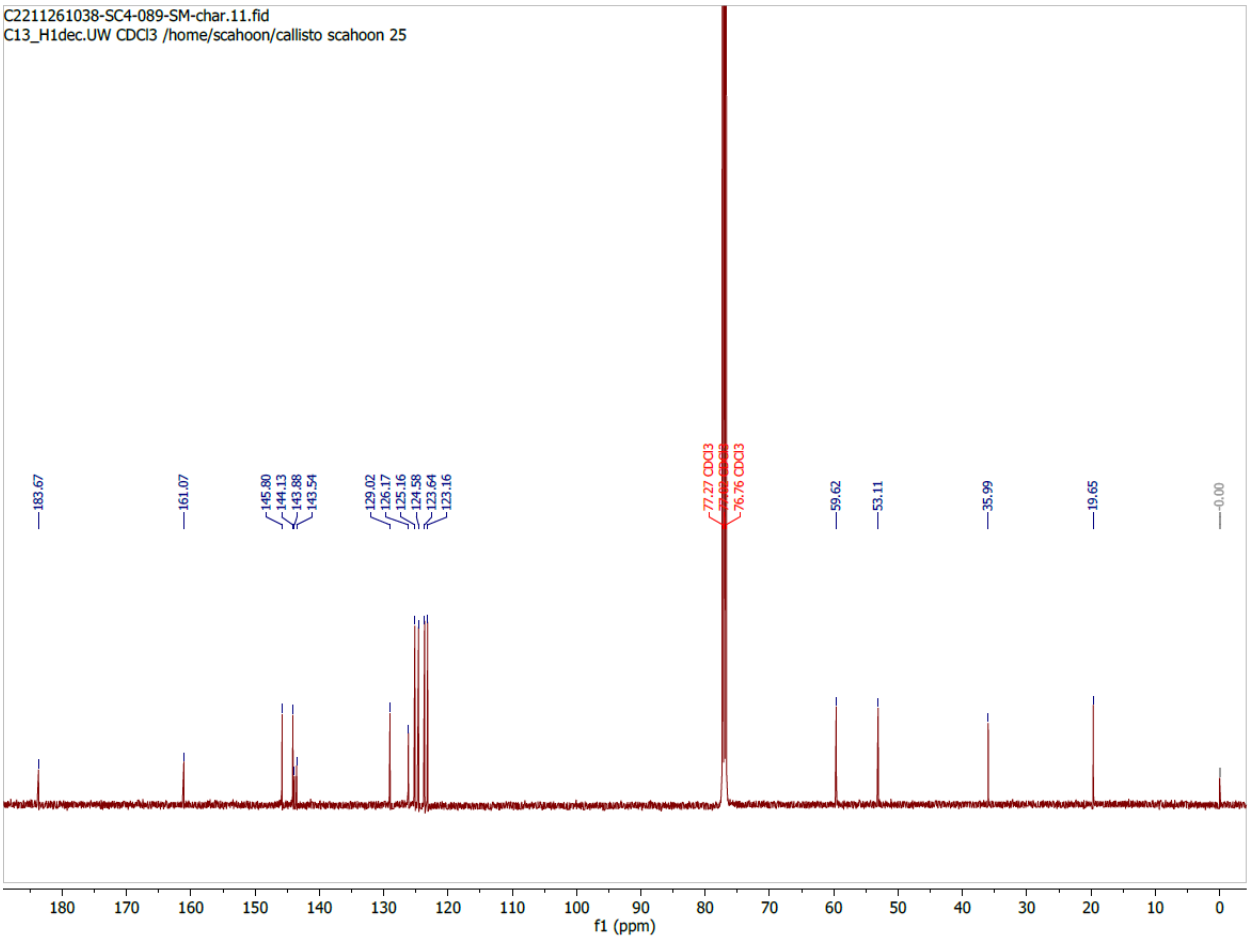
C2211261038-SC4-089-SM-char.11.fid
C13_H1dec.UW CDCl3 /home/scahoon/callisto scahoon 25
183.67
161.07
145.80
144.13
143.88
143.54
129.02
126.17
125.16
124.58
123.64
123.16
77.27 CDCl3
76.76 CDCl3
59.62
53.11
35.99
19.65
0.00
180
170
160
150
140
130
120
110
100
90
80
70
60
50
40
30
20
10
0
f1 (ppm)

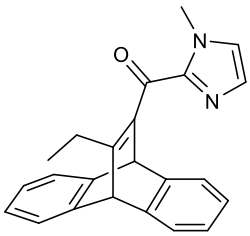

((9s,10s)-12-ethyl-9,10-dihydro-9,10-ethenoanthracen-11-yl)(1-methyl-1H-imidazol-2-yl)methanone (**S2.2**):

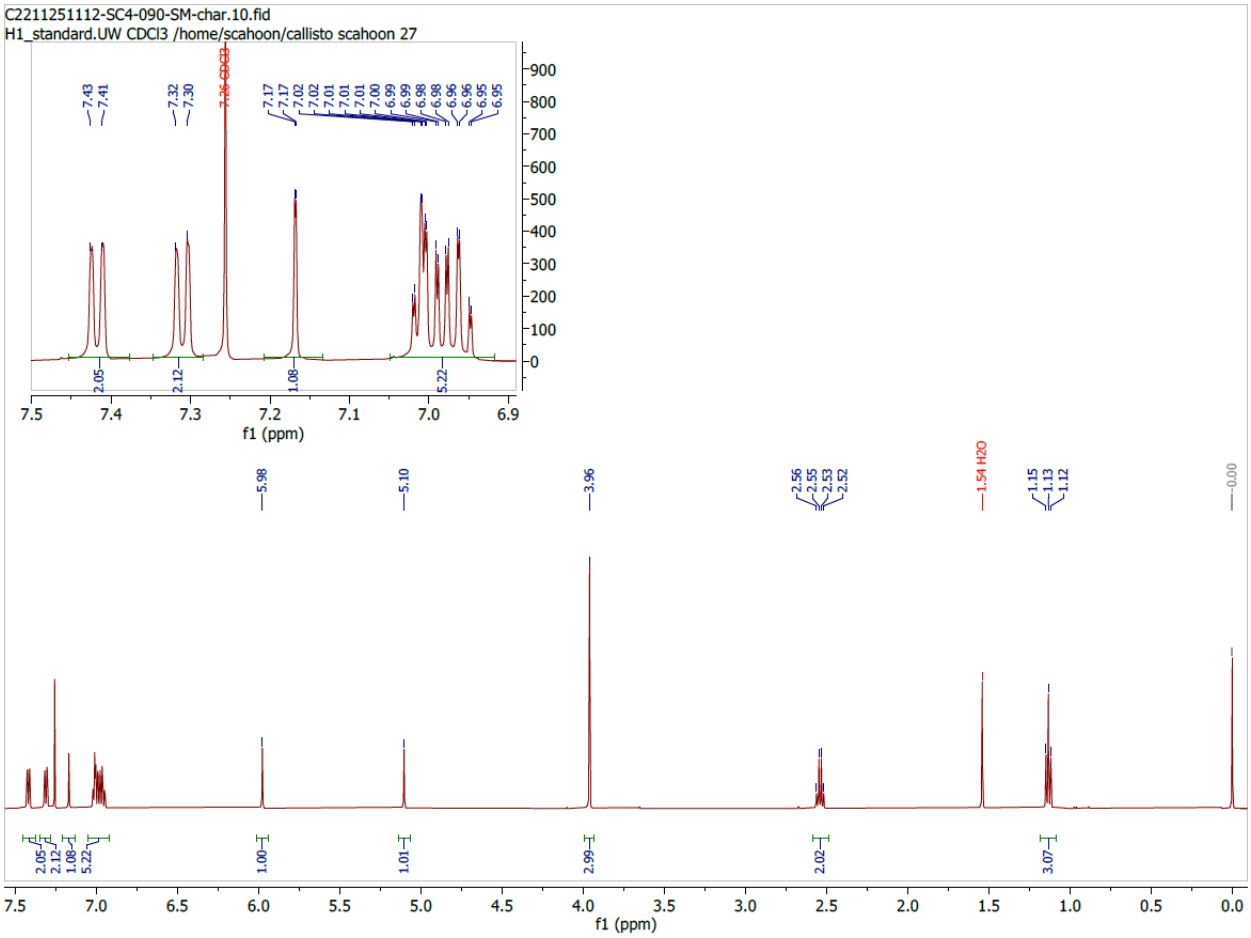

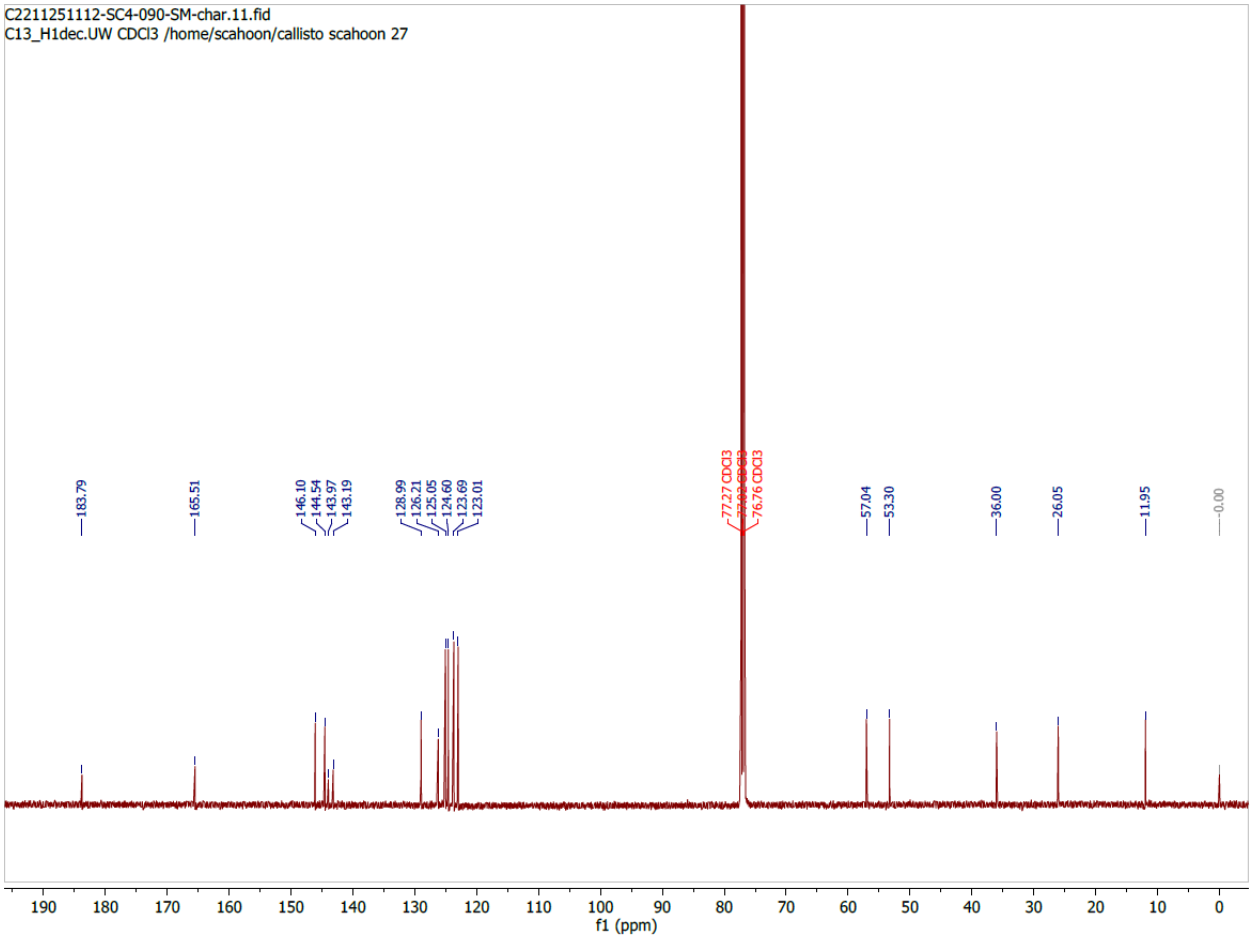
C2211251112-SC4-090-SM-char.11.fid
C13_H1dec.UW CDCl3 /home/scahoon/callisto scahoon 27
183.79
165.51
146.10
144.54
143.97
143.19
128.99
126.21
125.05
124.60
123.69
123.01
77.27 CDCl3
76.76 CDCl3
57.04
53.30
36.00
26.05
11.95
0.00
190 180 170 160 150 140 130 120 110 100 90 80 70 60 50 40 30 20 10 0
f1 (ppm)

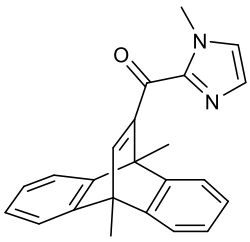

((9s,10s)-9,10-dimethyl-9,10-dihydro-9,10-ethenoanthracen-11-yl)(1-methyl-1H-imidazol-2-yl)methanone (**S2.3**):

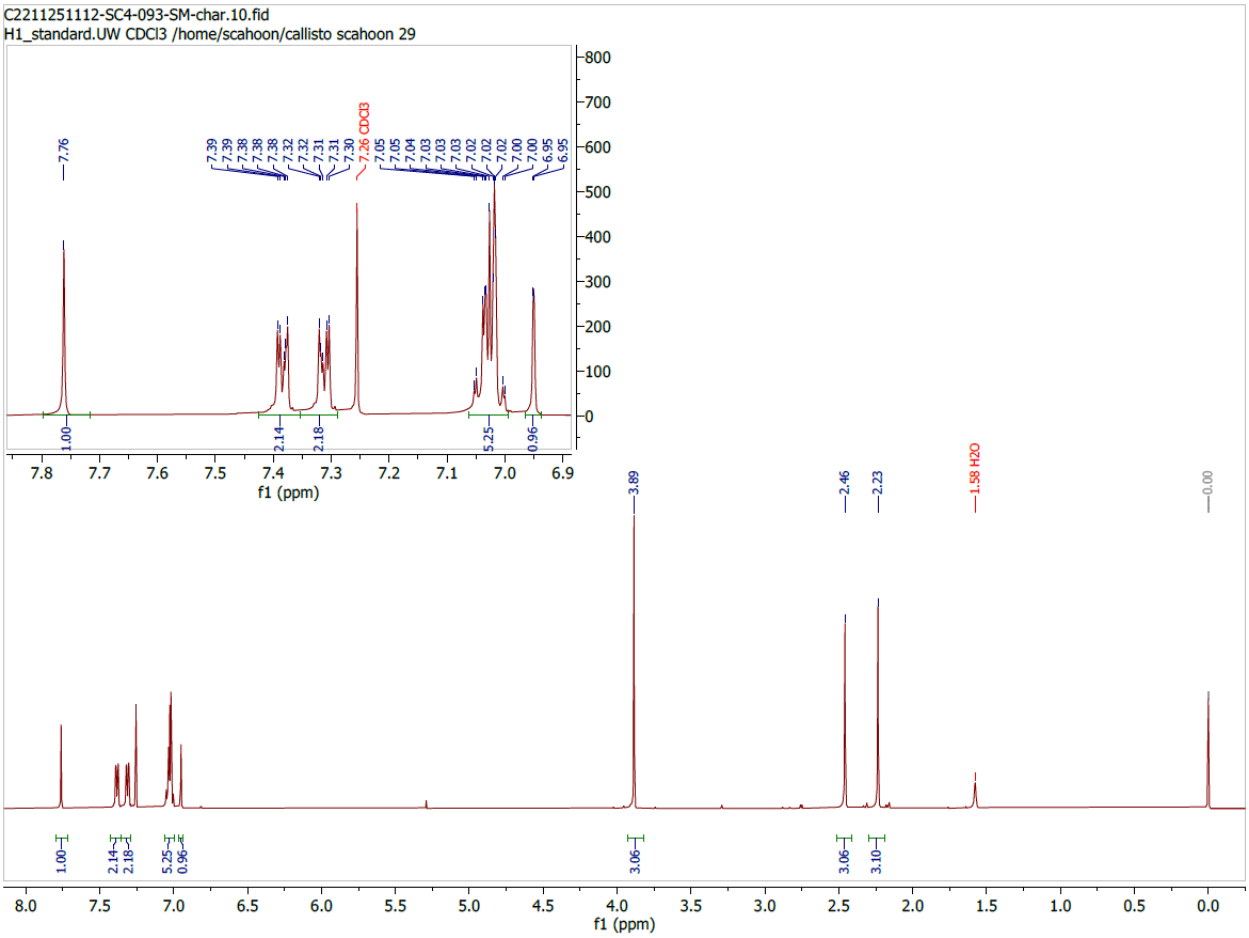

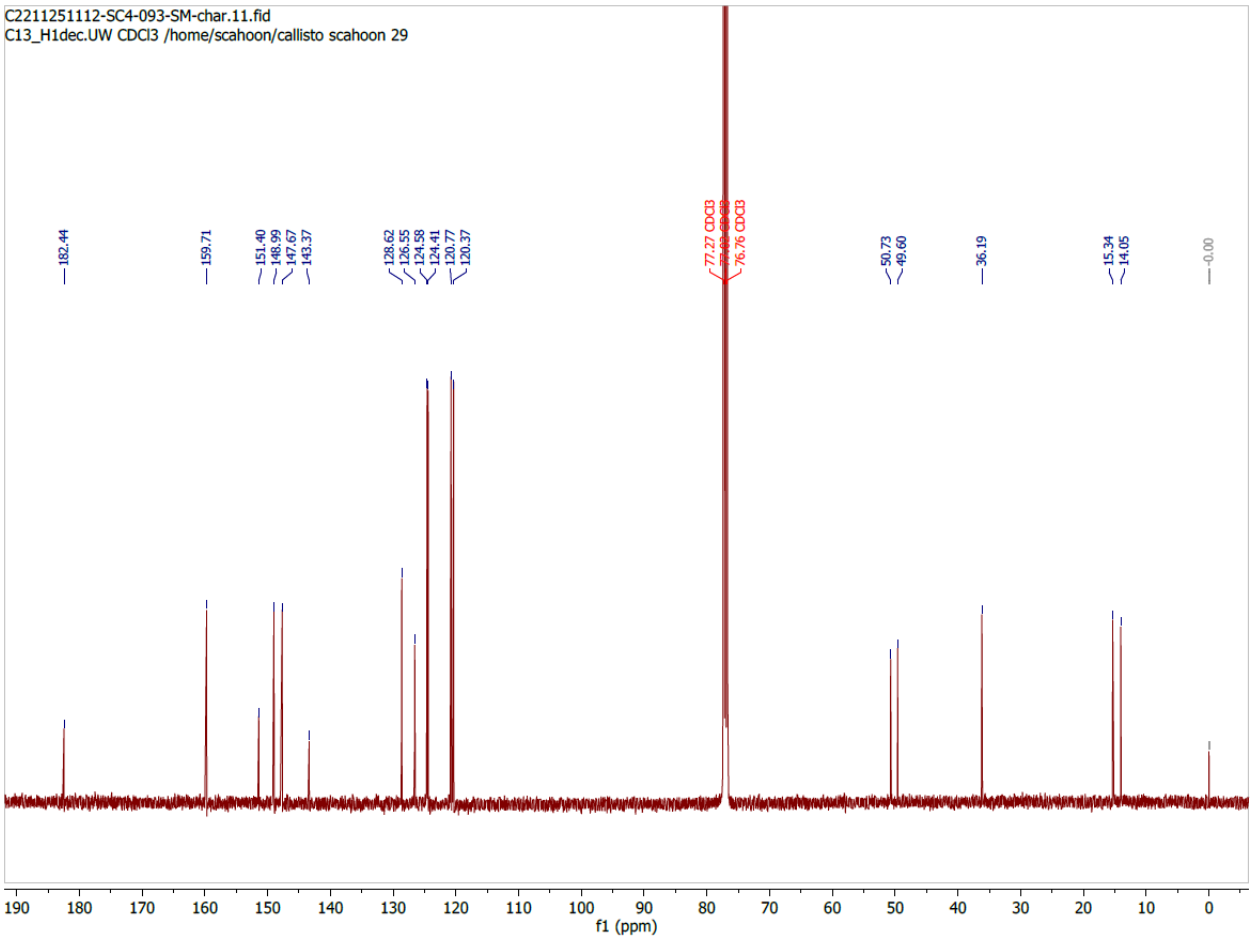
C2211251112-SC4-093-SM-char.11.fid
C13_H1dec.UW CDCl3 /home/scahoon/callisto scahoon 29
182.44
159.71
151.40
148.99
147.67
143.37
128.62
126.55
124.58
124.41
120.77
120.37
77.27 CDCl3
76.76 CDCl3
50.73
49.60
36.19
15.34
14.05
-0.00
190 180 170 160 150 140 130 120 110 100 90 80 70 60 50 40 30 20 10 0
f1 (ppm)

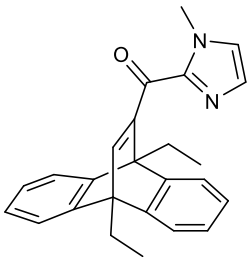

((9s,10s)-9,10-diethyl-9,10-dihydro-9,10-ethenoanthracen-11-yl)(1-methyl-1H-imidazol-2-yl)methanone (**S2.4**):

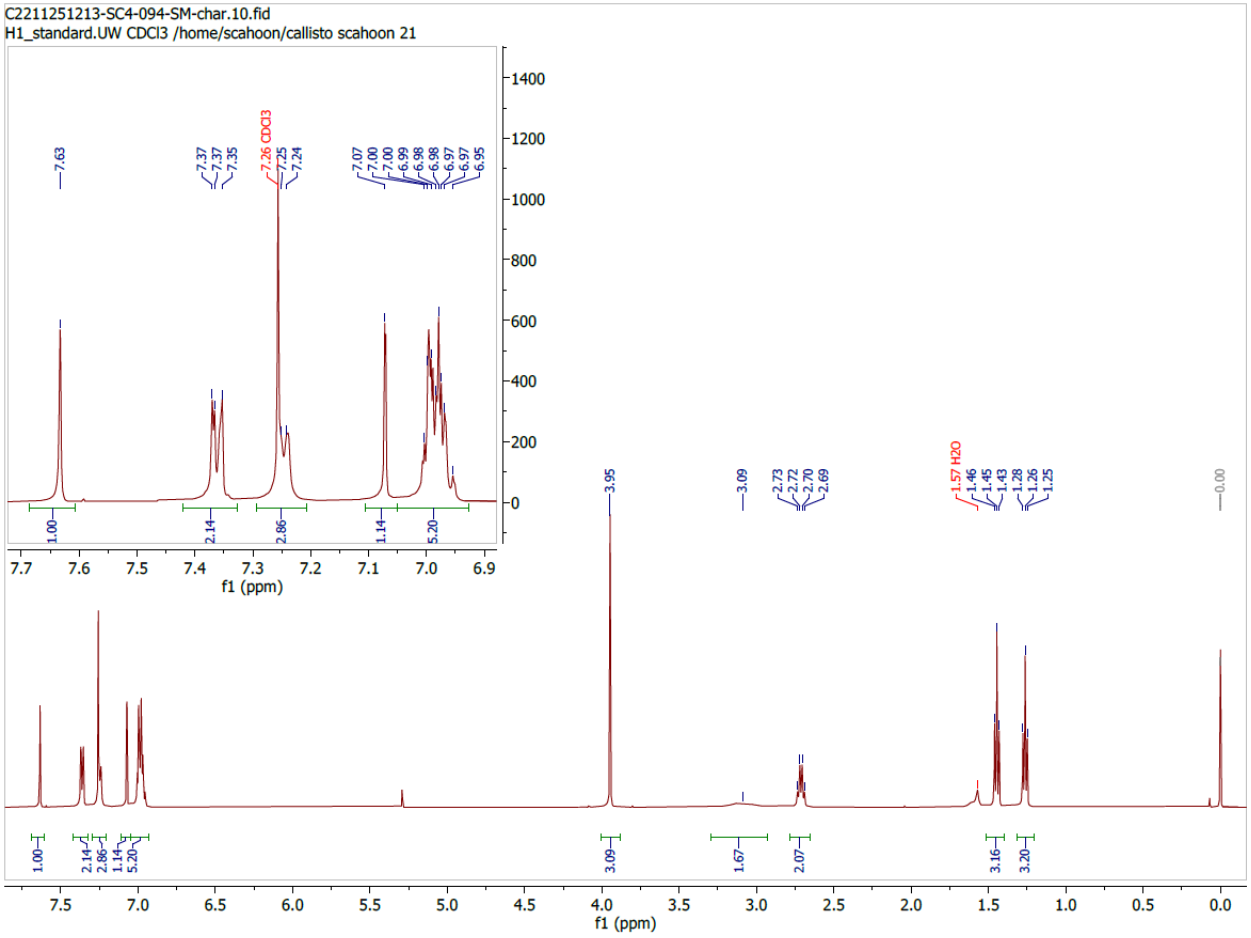

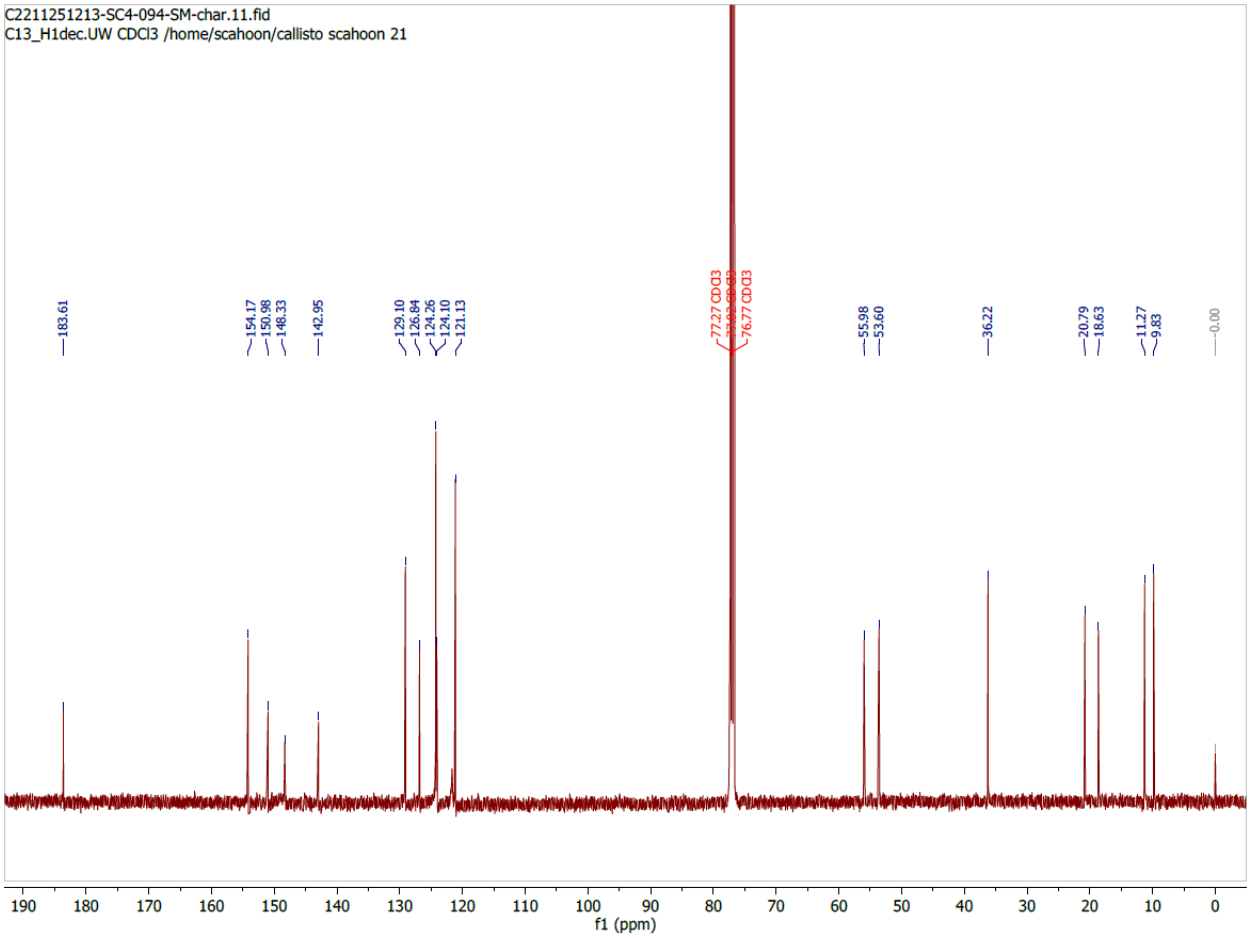
C2211251213-SC4-094-SM-char.11.fid
C13_H1dec.UW CDCl3 /home/scahoon/callisto scahoon 21
183.61
154.17
150.98
148.33
142.95
129.10
126.84
124.26
124.10
121.13
77.27 CDCl3
76.77 CDCl3
55.98
53.60
36.22
20.79
18.63
11.27
9.83
0.00
190 180 170 160 150 140 130 120 110 100 90 80 70 60 50 40 30 20 10 0
f1 (ppm)

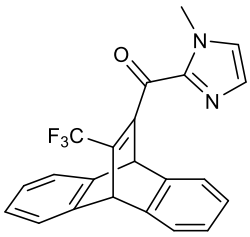

(1-methyl-1H-imidazol-2-yl)((9s,10s)-12-(trifluoromethyl)-9,10-dihydro-9,10-ethenoanthracen-11-yl)methanone (**S2.5**):

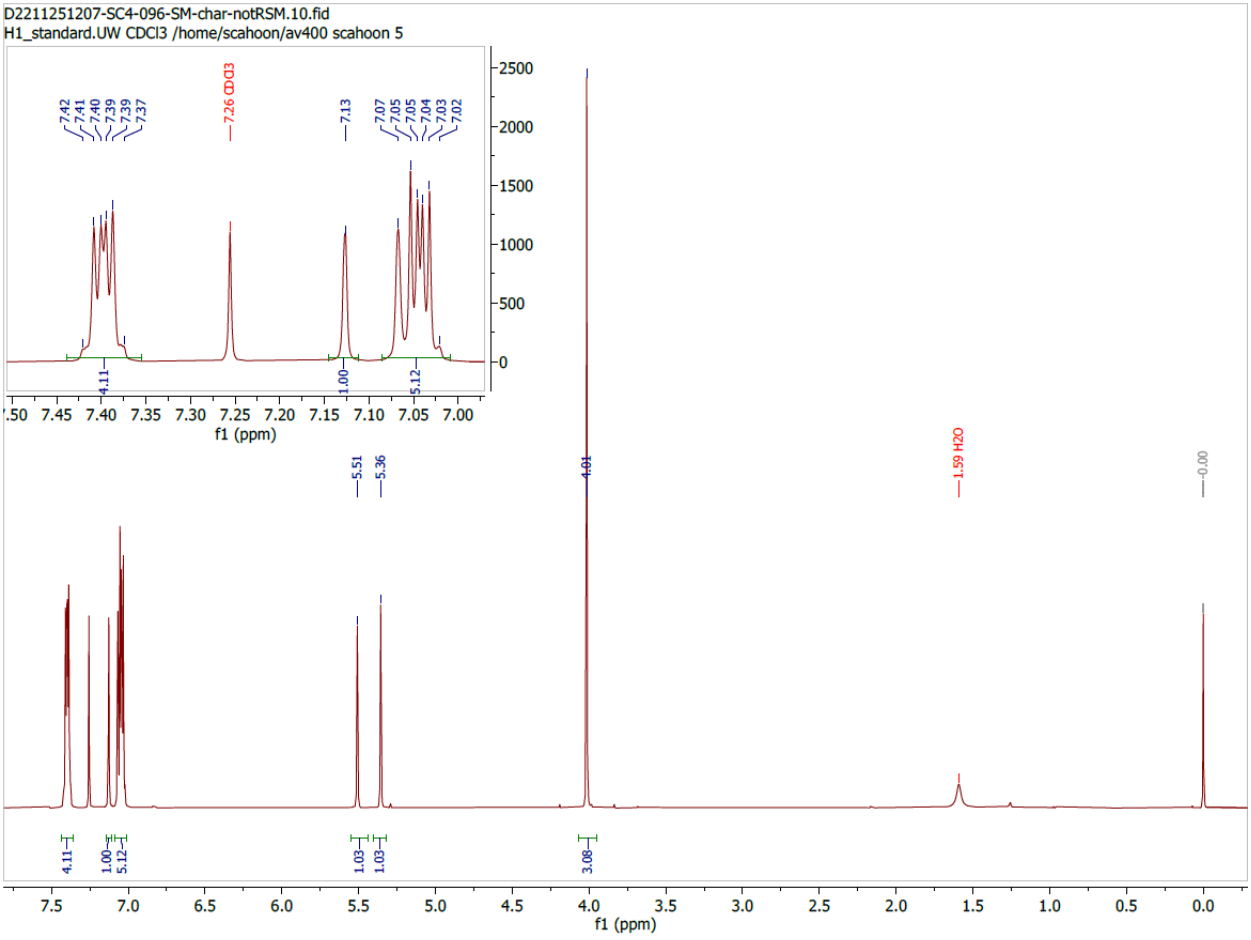

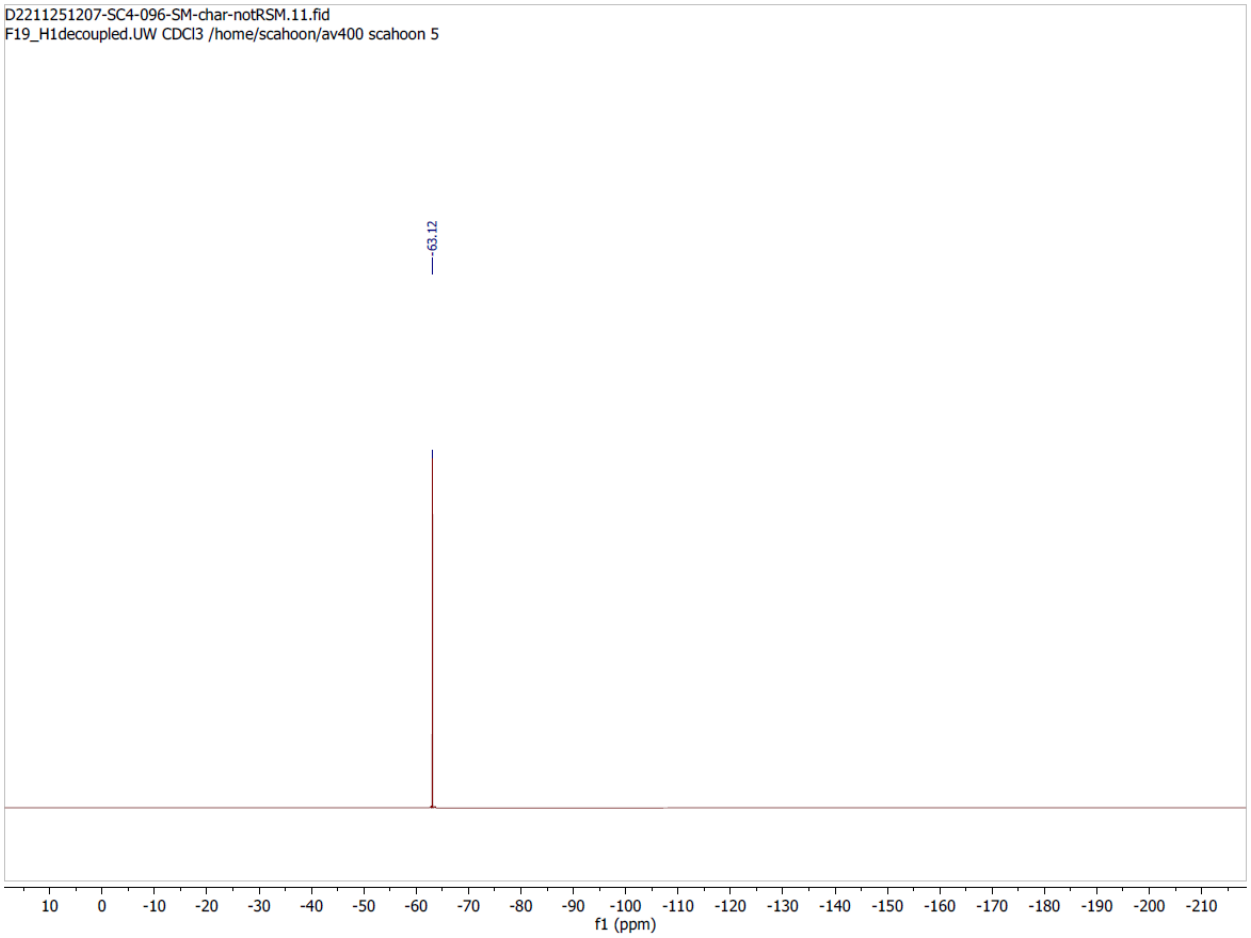
D2211251207-SC4-096-SM-char-notRSM.11.fid
F19_H1decoupled.UW CDCl3 /home/scahoon/av400 scahoon 5
-63.12
10 0 -10 -20 -30 -40 -50 -60 -70 -80 -90 -100 -110 -120 -130 -140 -150 -160 -170 -180 -190 -200 -210
f1 (ppm)

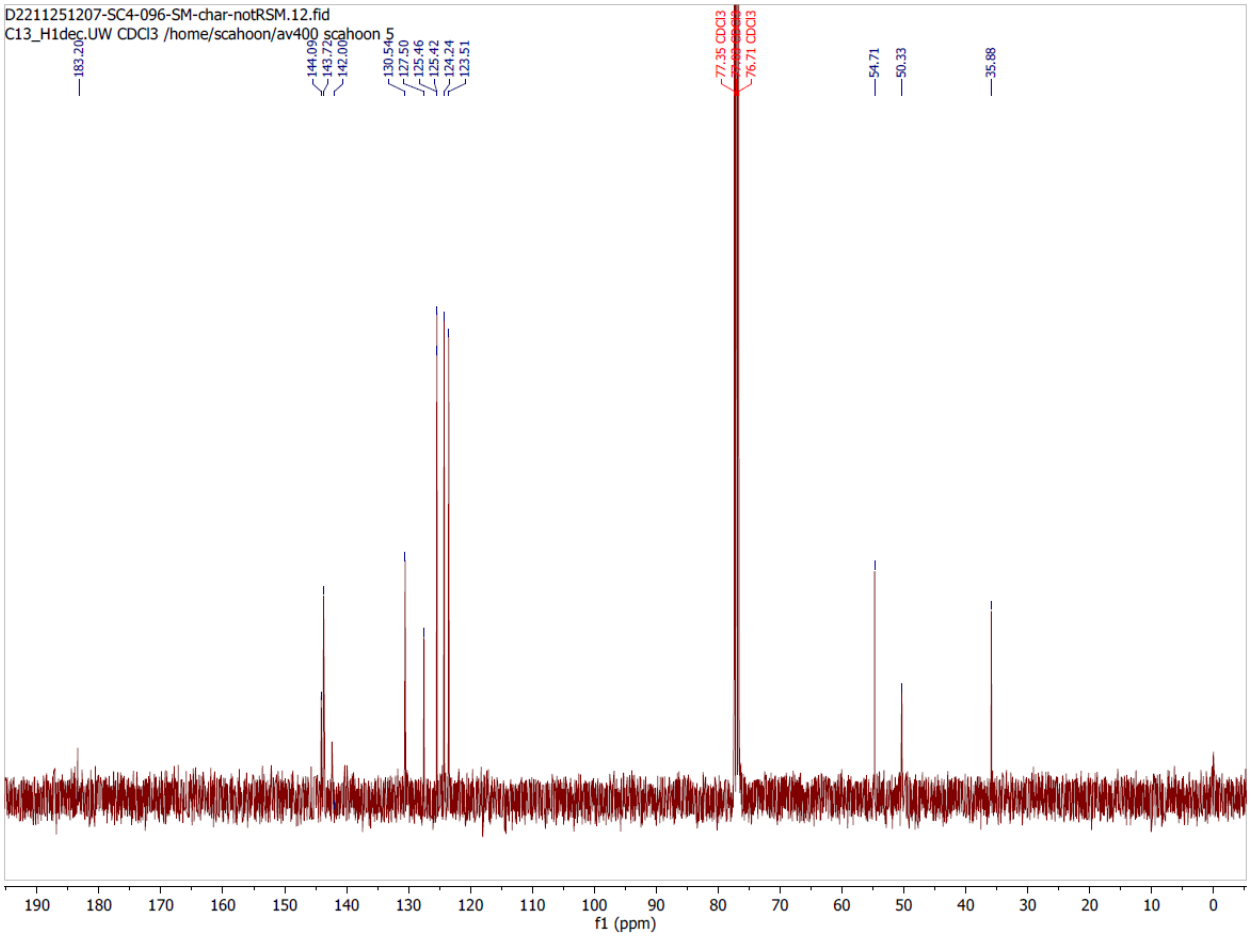
D2211251207-SC4-096-SM-char-notRSM.12.fid
C13_H1dec.UW CDCl3 /home/scahoon/av400 scahoon 5
183.26
144.09
143.72
142.00
130.54
127.50
125.46
125.42
124.24
123.51
77.35 CDCl3
76.71 CDCl3
54.71
50.33
35.88
190 180 170 160 150 140 130 120 110 100 90 80 70 60 50 40 30 20 10 0
f1 (ppm)

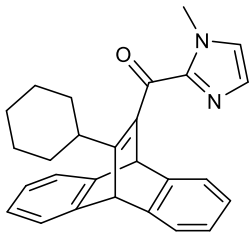

((9s,10s)-12-cyclohexyl-9,10-dihydro-9,10-ethenoanthracen-11-yl)(1-methyl-1H-imidazol-2-yl)methanone (**S2.6**):

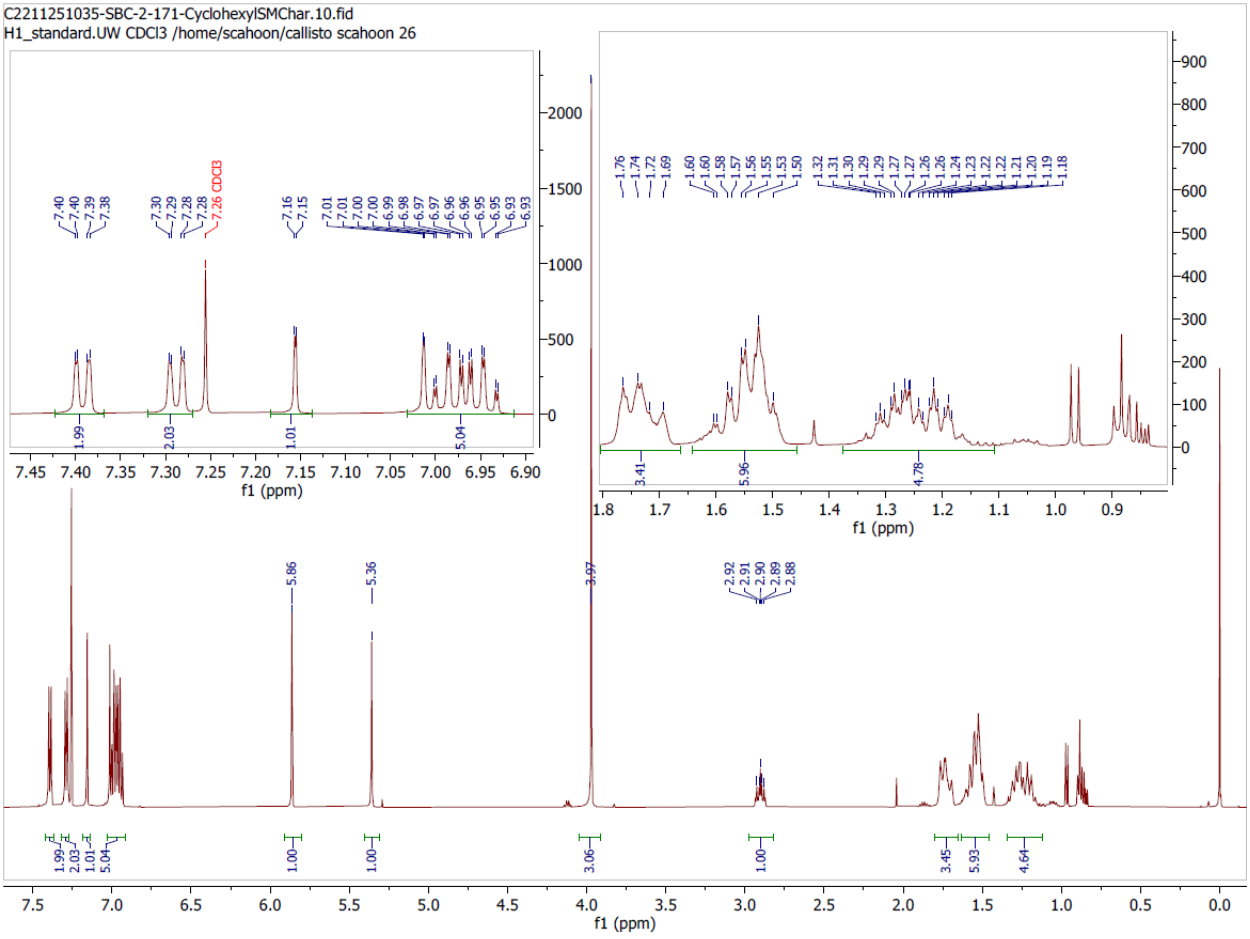

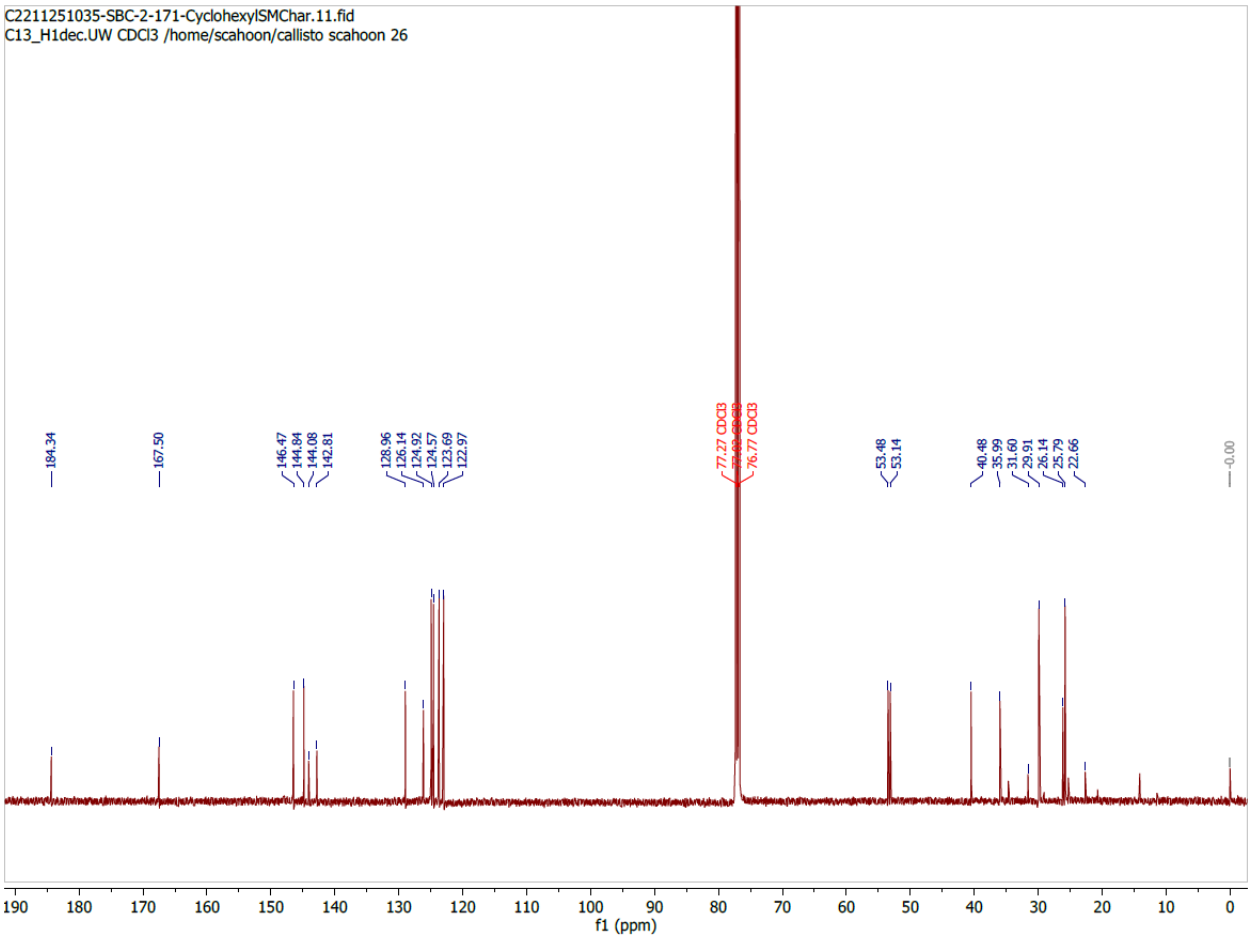
C2211251035-SBC-2-171-CyclohexylSMChar.11.fid
C13_H1dec.UW CDCl3 /home/scahoon/callisto scahoon 26
184.34
167.50
146.47
144.84
144.08
142.81
128.96
126.14
124.92
124.57
123.69
122.97
77.27 CDCl3
76.77 CDCl3
53.48
53.14
40.48
35.99
31.60
29.91
26.14
25.79
22.66
-0.00
190 180 170 160 150 140 130 120 110 100 90 80 70 60 50 40 30 20 10 0
f1 (ppm)

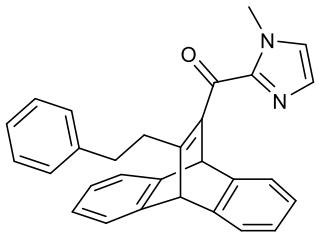

(1-methyl-1H-imidazol-2-yl)((9s,10s)-12-phenethyl-9,10-dihydro-9,10-ethenoanthracen-11-yl)methanone (**S2.7**):

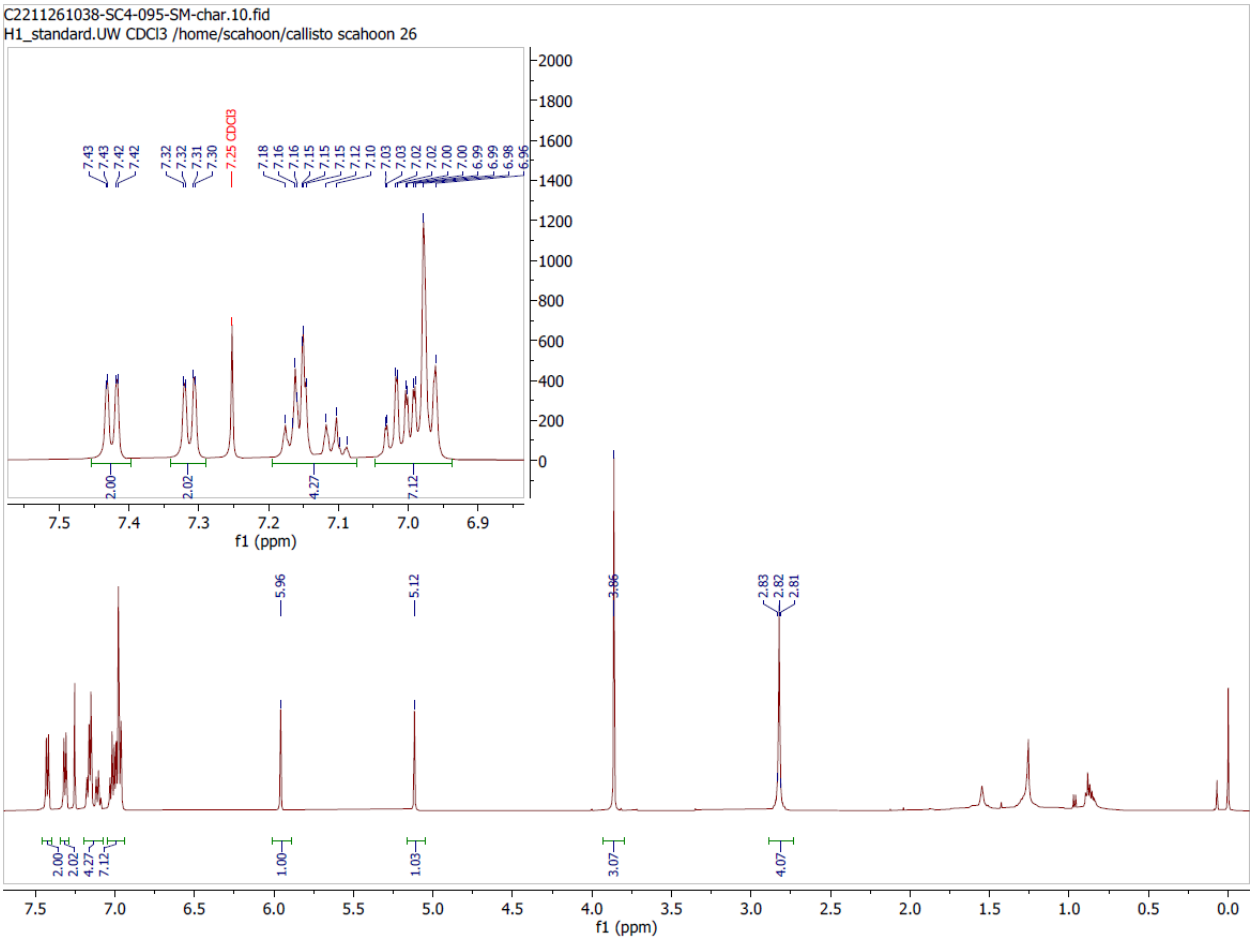

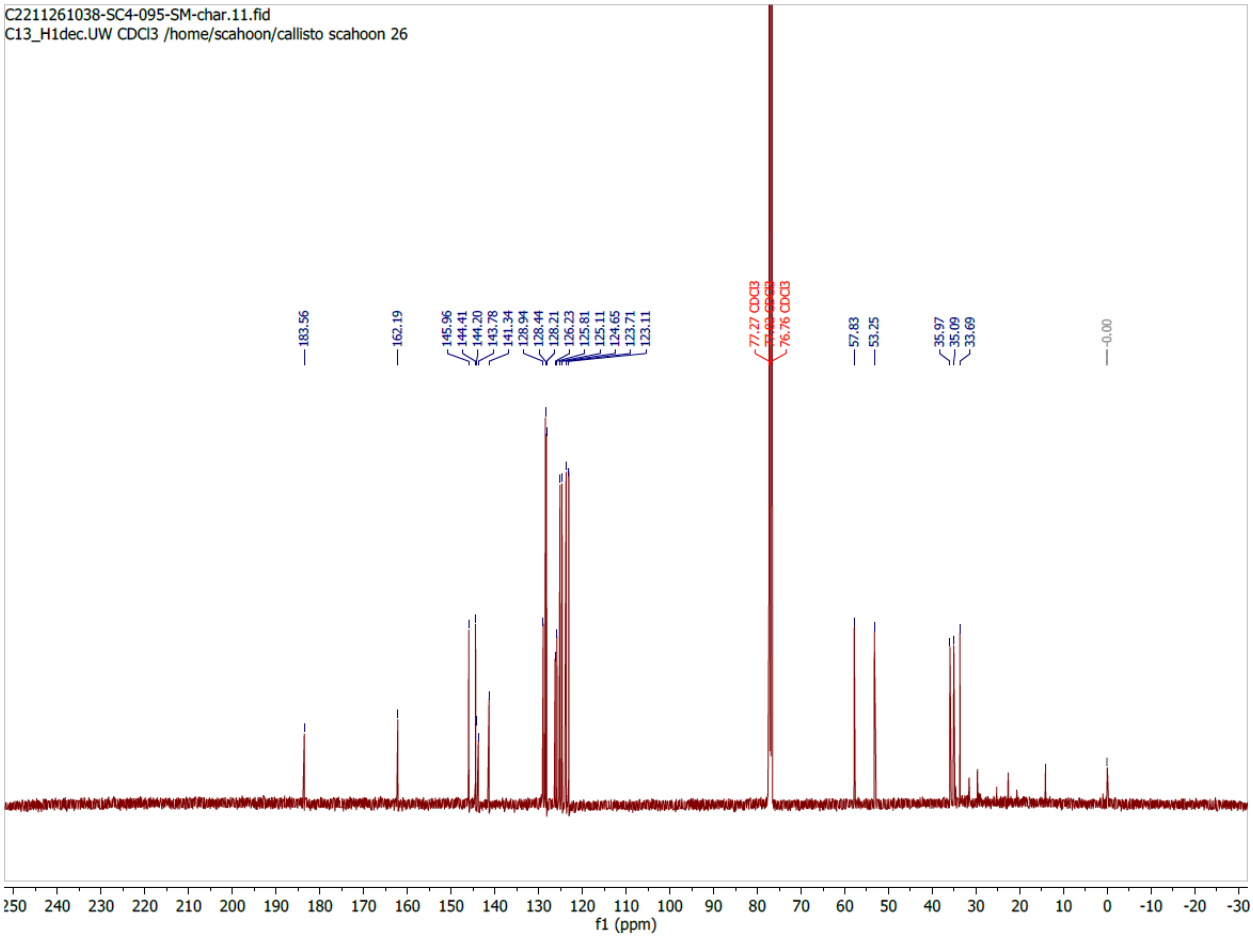
C2211261038-SC4-095-SM-char.11.fid
C13_H1dec.UW CDCl3 /home/scahoon/callisto scahoon 26
183.56
162.19
145.96
144.41
144.20
143.78
141.34
128.94
128.44
128.21
126.23
125.81
125.11
124.65
123.71
123.11
77.27 CDCl3
76.76 CDCl3
57.83
53.25
35.97
35.09
33.69
0.00
f1 (ppm)

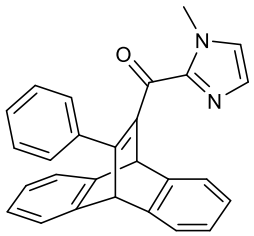

(1-methyl-1H-imidazol-2-yl)((9s,10s)-12-phenyl-9,10-dihydro-9,10-ethenoanthracen-11-yl)methanone (**S2.8**):

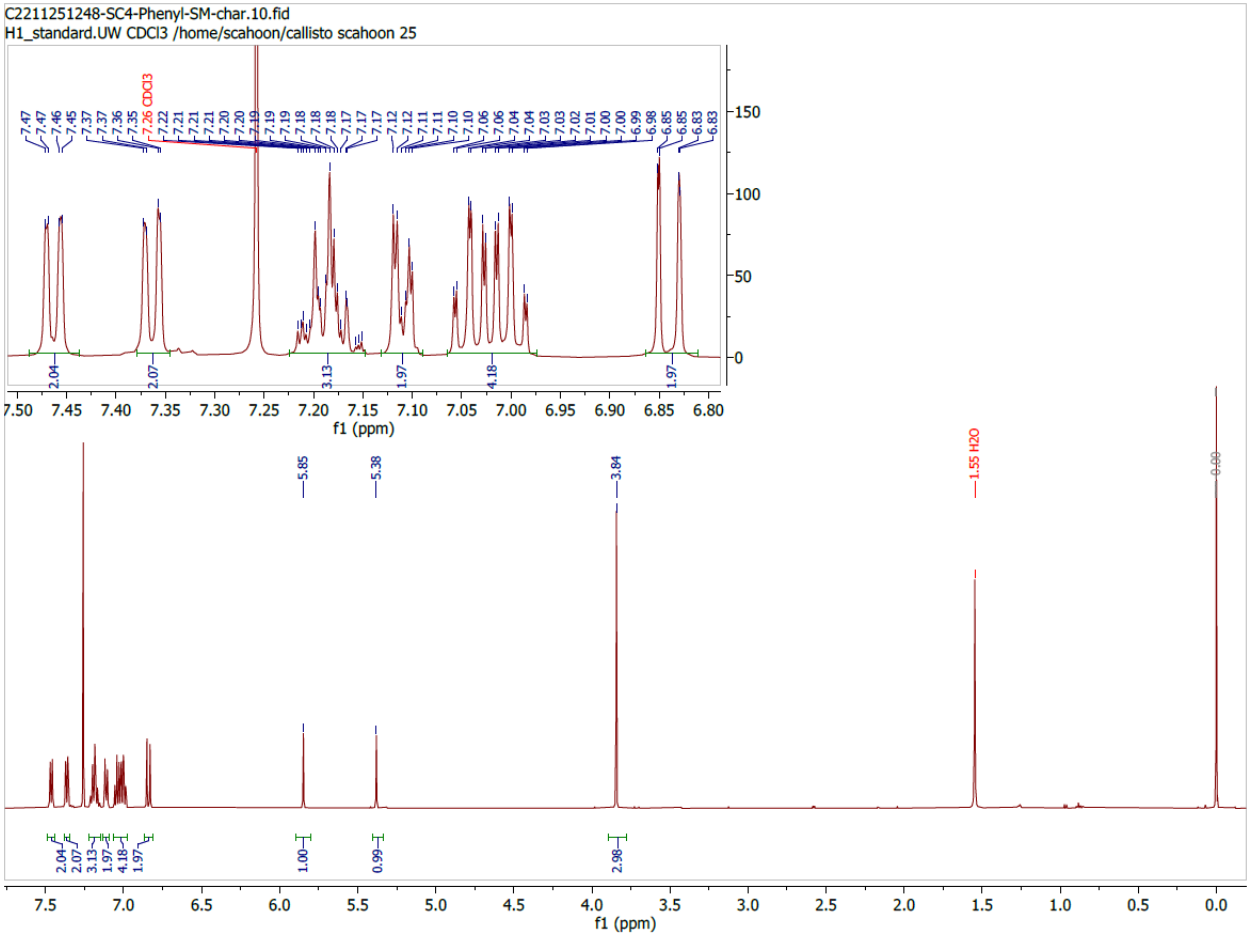

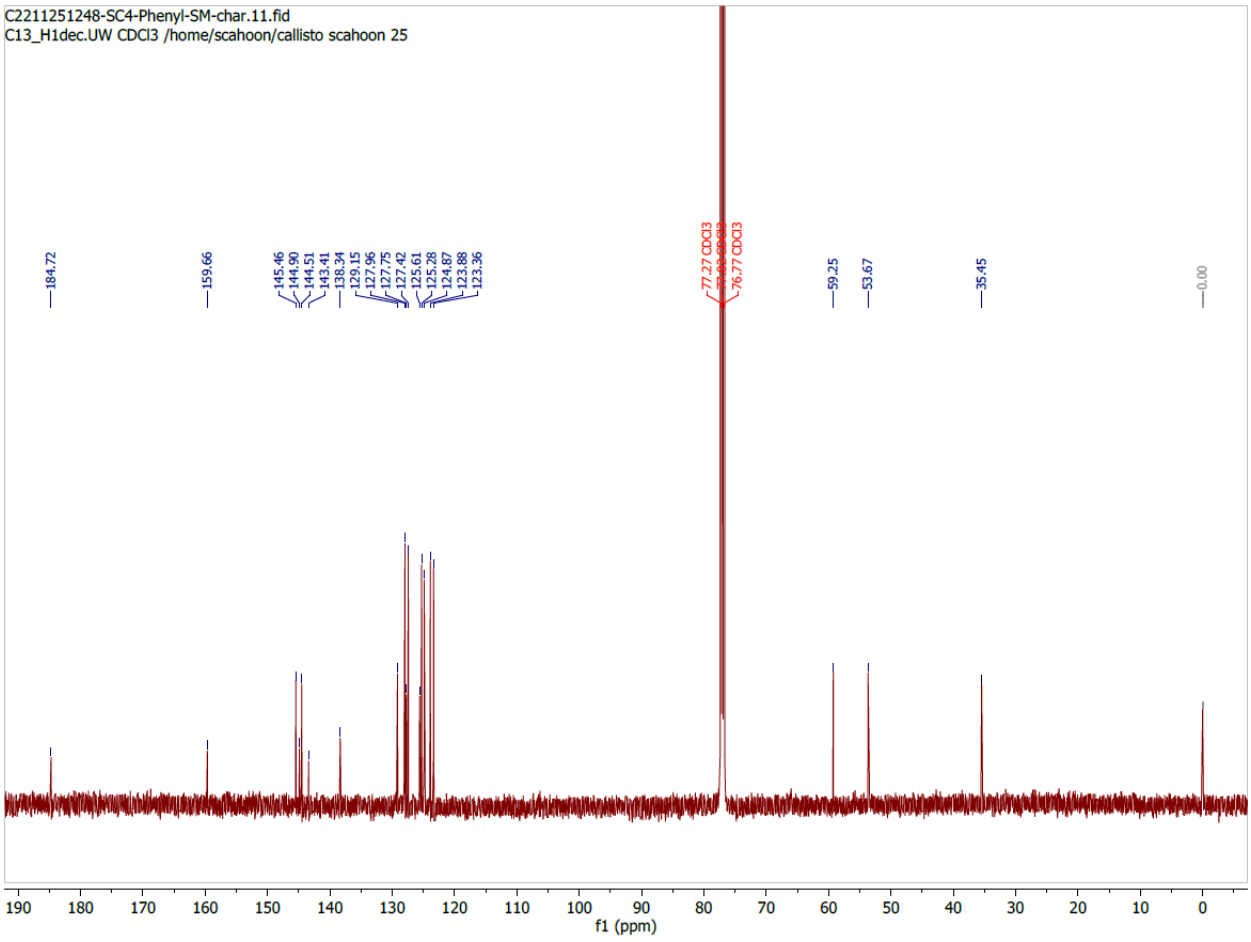
C2211251248-SC4-Phenyl-SM-char.11.fid
C13_H1dec.UW CDCl3 /home/scahoon/callisto scahoon 25
184.72
159.66
145.46
144.90
144.51
143.41
138.34
129.15
127.96
127.75
127.42
125.61
125.28
124.87
123.88
123.36
77.27 CDCl3
76.77 CDCl3
59.25
53.67
35.45
0.00
190 180 170 160 150 140 130 120 110 100 90 80 70 60 50 40 30 20 10 0
f1 (ppm)

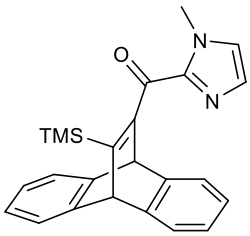

(1-methyl-1H-imidazol-2-yl)((9s,10s)-12-(trimethylsilyl)-9,10-dihydro-9,10-ethenoanthracen-11-yl)methanone (**S2.9**):

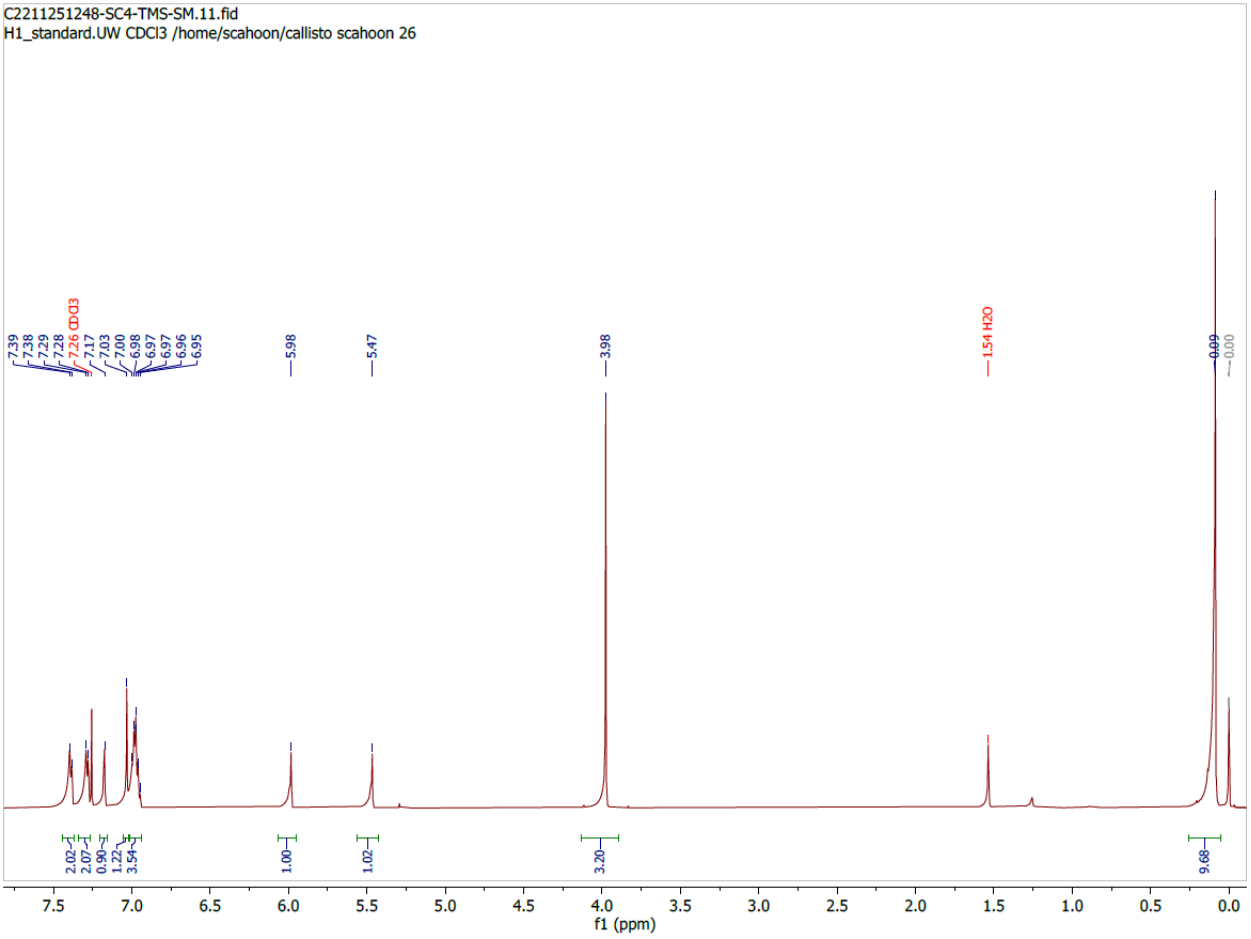

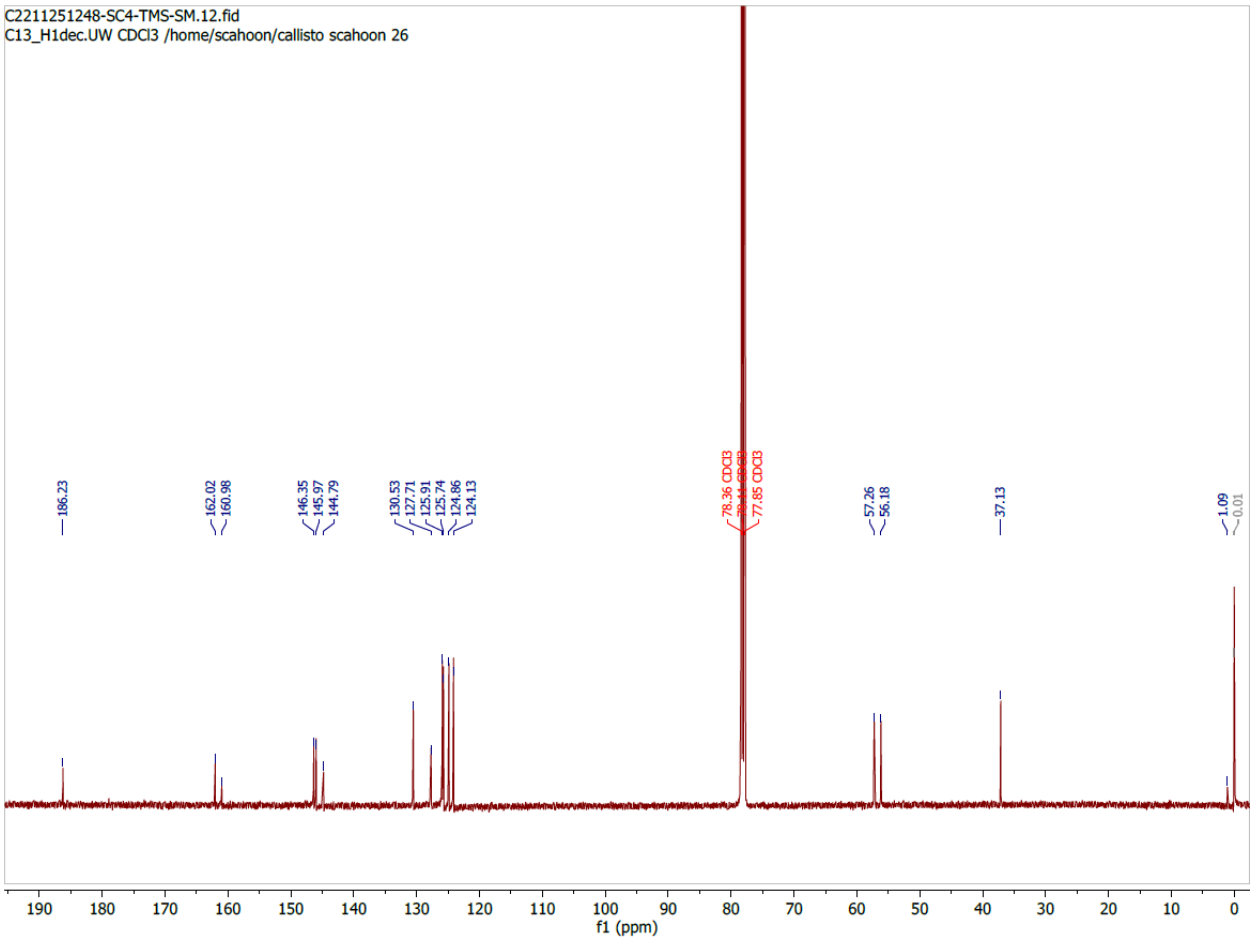
C2211251248-SC4-TMS-SM.12.fid
C13_H1dec.UW CDCl3 /home/scahoon/callisto scahoon 26
186.23
162.02
160.98
146.35
145.97
144.79
130.53
127.71
125.91
125.74
124.86
124.13
78.36 CDCl3
77.85 CDCl3
57.26
56.18
37.13
1.09
0.01
190
180
170
160
150
140
130
120
110
100
90
80
70
60
50
40
30
20
10
0
f1 (ppm)

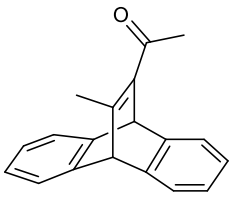

1-((9s,10s)-12-methyl-9,10-dihydro-9,10-ethenoanthracen-11-yl)ethan-1-one (**S2.10**):

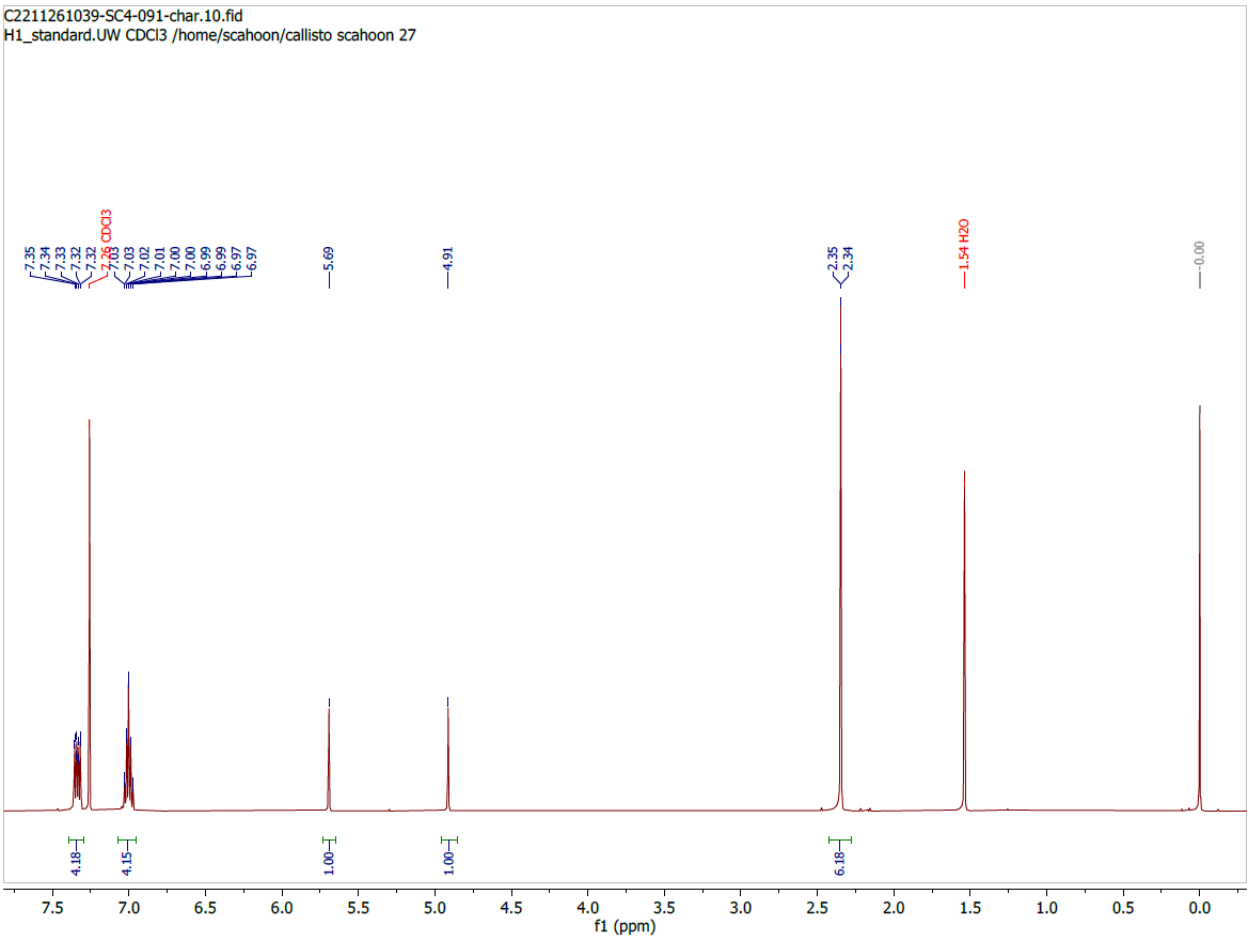

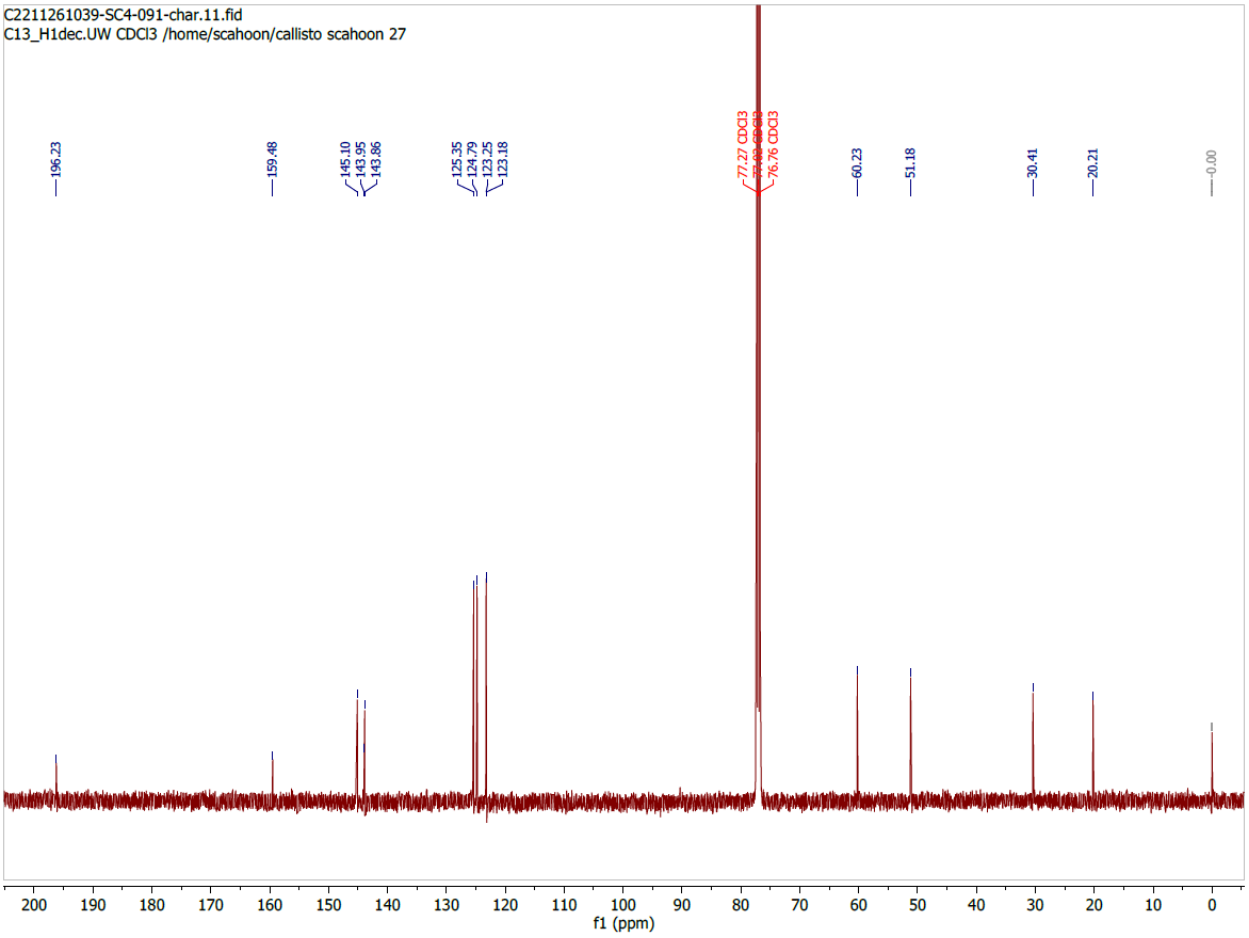
C2211261039-SC4-091-char.11.fid
C13_H1dec.UW CDCl3 /home/scahoon/callisto scahoon 27
196.23
159.48
145.10
143.95
143.86
125.35
124.79
123.25
123.18
77.27 CDCl3
76.76 CDCl3
60.23
51.18
30.41
20.21
0.00
200 190 180 170 160 150 140 130 120 110 100 90 80 70 60 50 40 30 20 10 0
f1 (ppm)

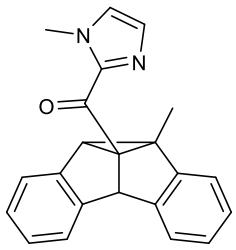

(1-methyl-1H-imidazol-2-yl)(8b-methyl-8b,8c-dihydrodibenzo[a,f]cyclopropa[cd]pentalen-4b1(4bH)-yl)methanone--(4b,8b-diethyl-8b,8c-dihydrodibenzo[a,f]cyclopropa[cd]pentalen-4b1(4bH)-yl)(1-methyl-1H-imidazol-2-yl)methanone--(4b,8b-dimethyl-8b,8c-dihydrodibenzo[a,f]cyclopropa[cd]pentalen-4b1(4bH)-yl)(1-methyl-1H-imidazol-2-yl)methanone--(8b-ethyl-8b,8c-dihydrodibenzo[a,f]cyclopropa[cd]pentalen-4b1(4bH)-yl)(1-methyl-1H-imidazol-2-yl)methanone (1/1/1/1) (**S2.11**):

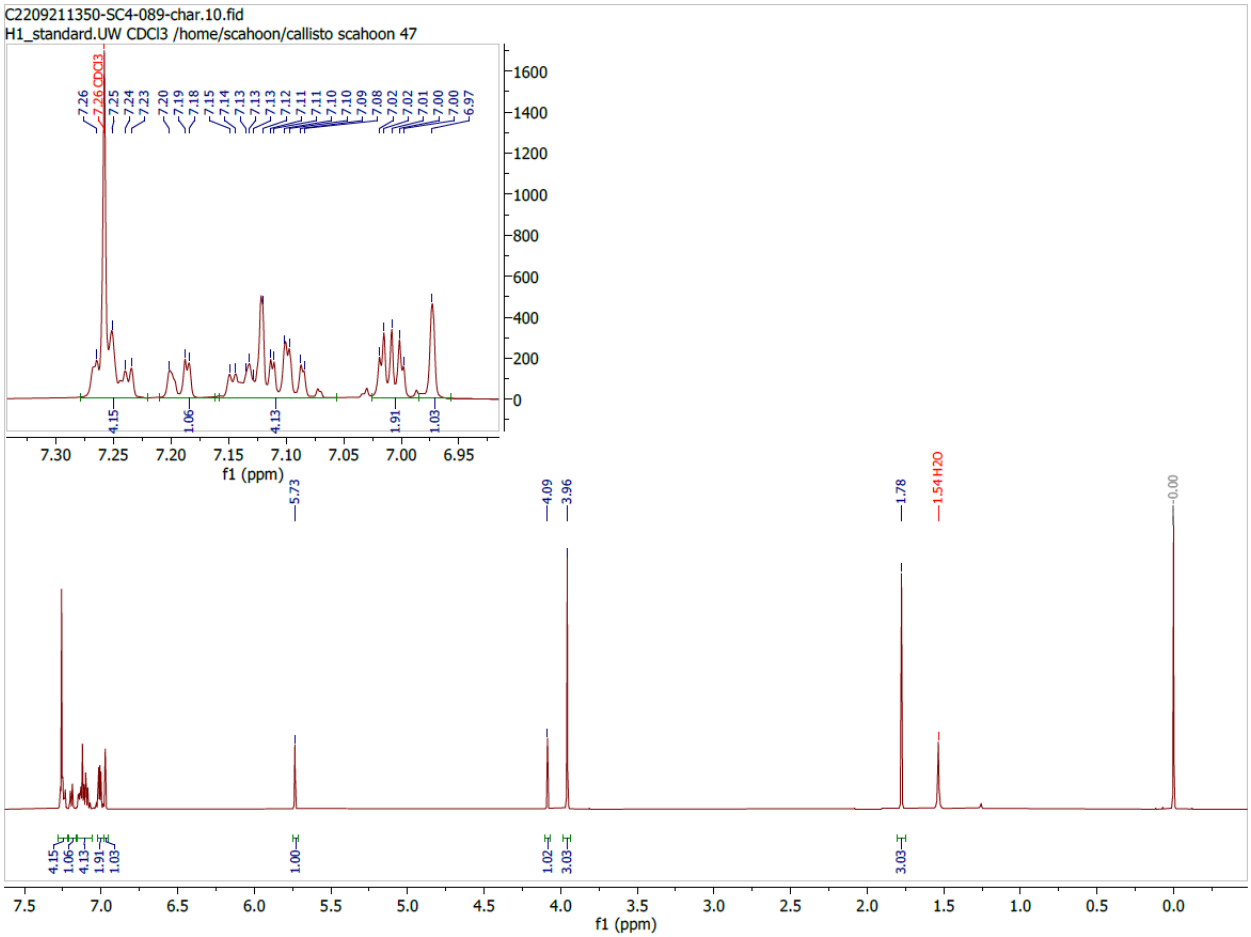

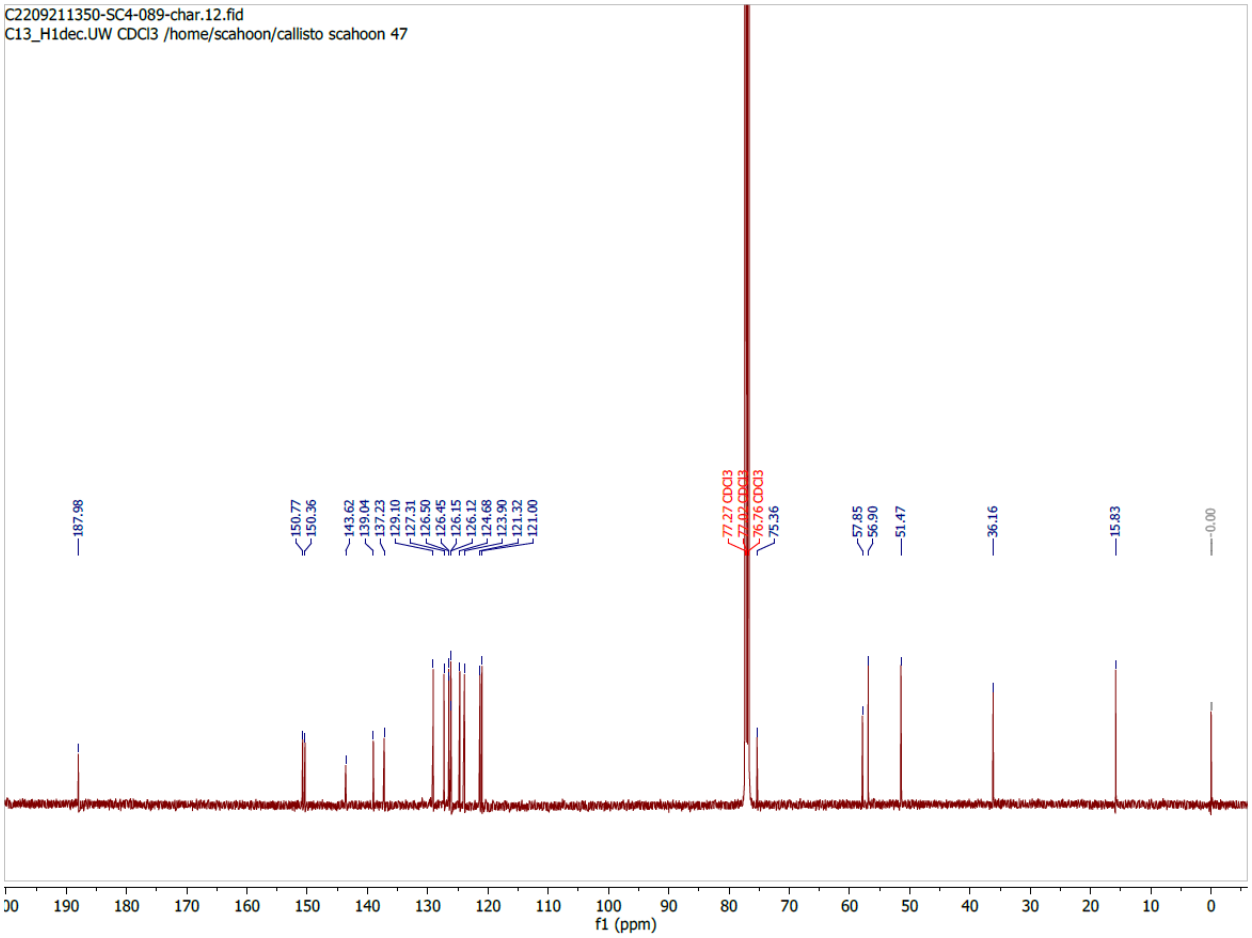
C2209211350-SC4-089-char.12.fid
C13_H1dec.UW CDCl3 /home/scahoon/callisto scahoon 47
187.98
150.77
150.36
143.62
139.04
137.23
129.10
127.31
126.50
126.45
126.15
126.12
124.68
123.90
121.32
121.00
77.27 CDCl3
77.01 CDCl3
76.76 CDCl3
75.36
57.85
56.90
51.47
36.16
15.83
0.00
f1 (ppm)

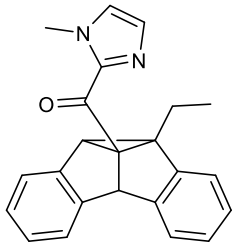

(8b-ethyl-8b,8c-dihydrodibenzo[a,f]cyclopropa[cd]pentalen-4b1(4bH)-yl)(1-methyl-1H-imidazol-2-yl)methanone (**S2.12**):

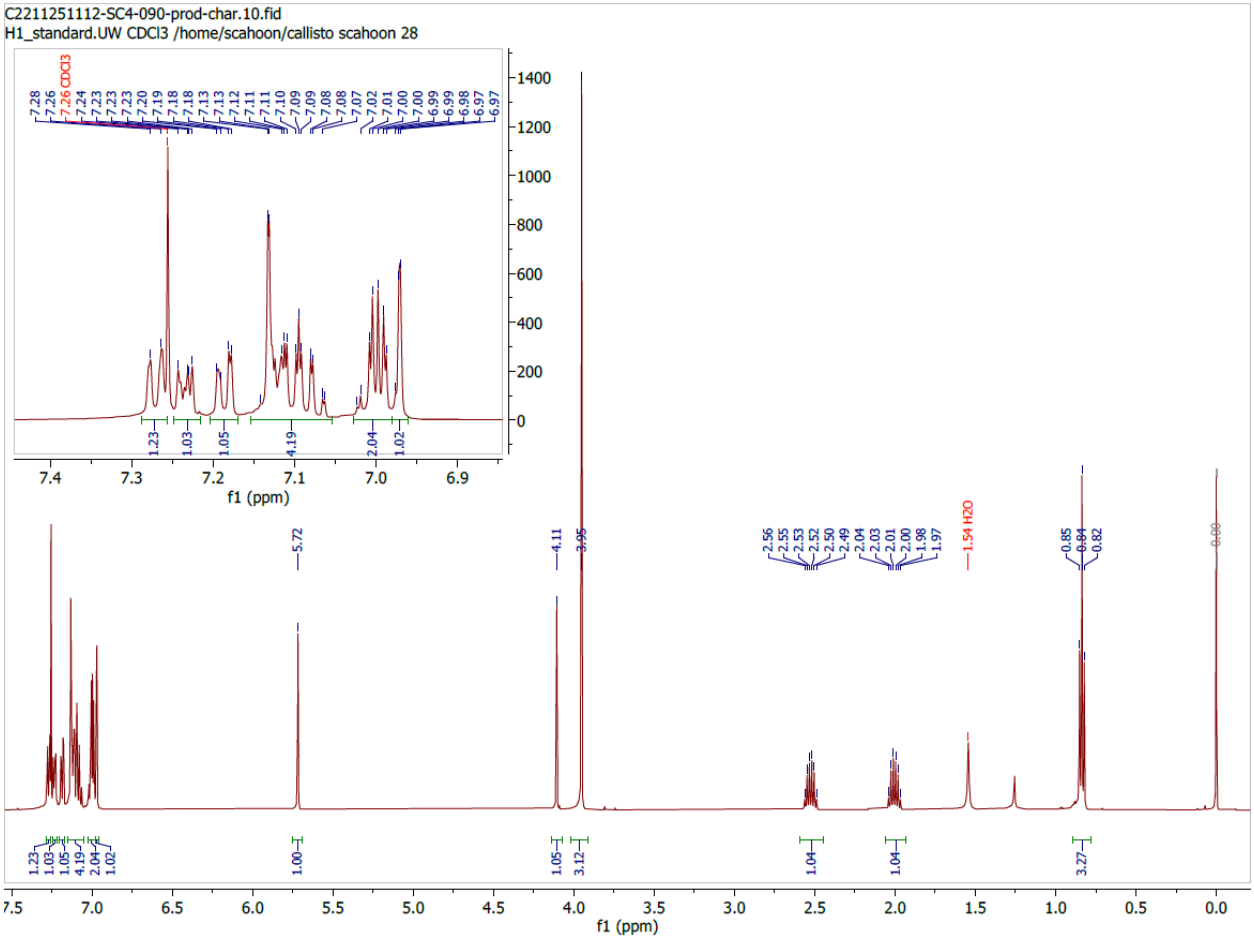

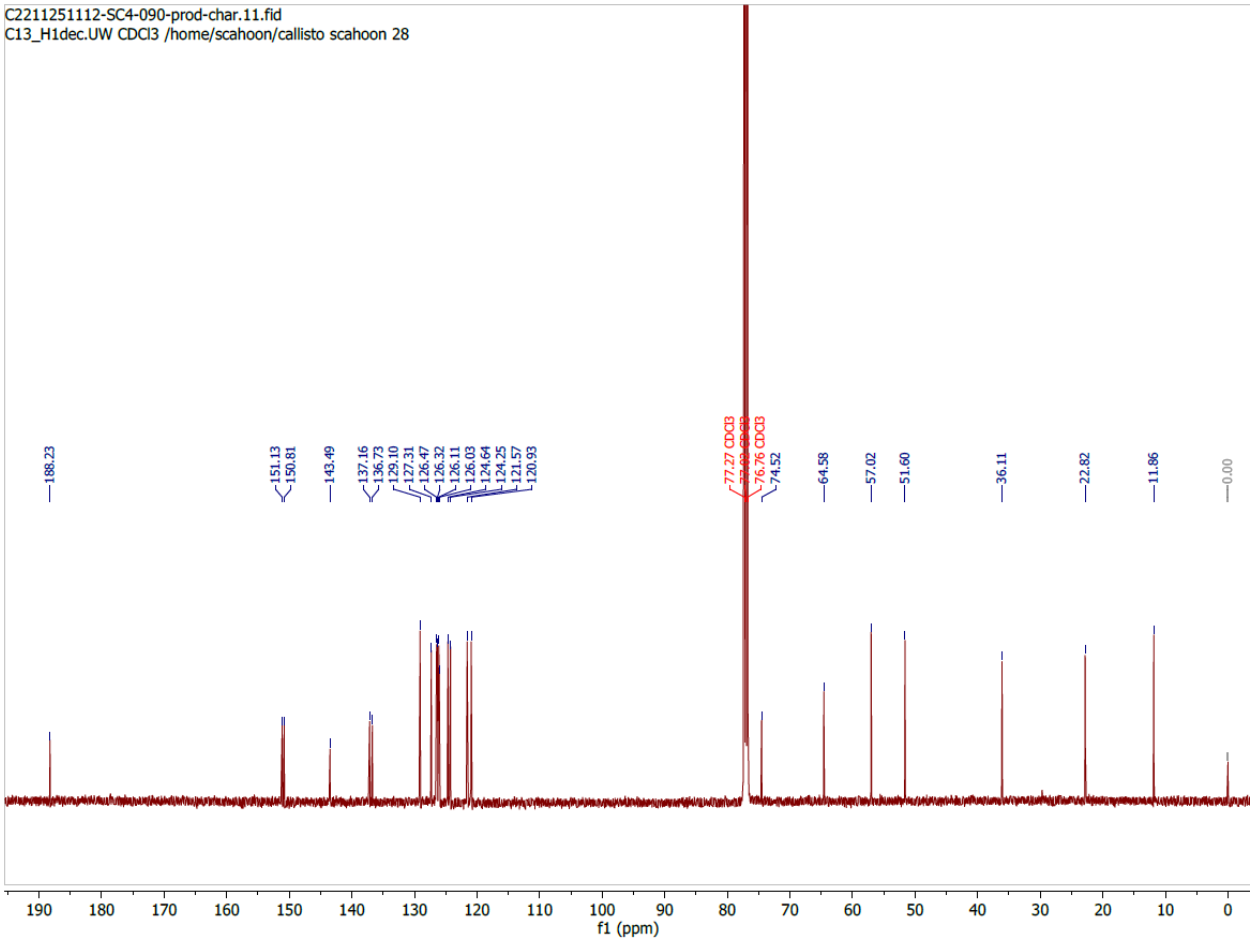
C2211251112-SC4-090-prod-char.11.fid
C13_H1dec.UW CDCl3 /home/scahoon/callisto scahoon 28
188.23
151.13
150.81
143.49
137.16
136.73
129.10
127.31
126.47
126.32
126.11
126.03
124.64
124.25
121.57
120.93
77.27 CDCl3
76.76 CDCl3
74.52
64.58
57.02
51.60
36.11
22.82
11.86
0.00
f1 (ppm)

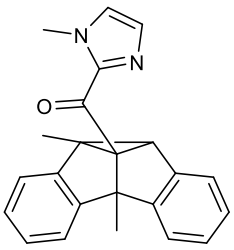

(4b,8b-dimethyl-8b,8c-dihydrodibenzo[a,f]cyclopropa[cd]pentalen-4b1(4bH)-yl)(1-methyl-1H-imidazol-2-yl)methanone (**S2.13**):

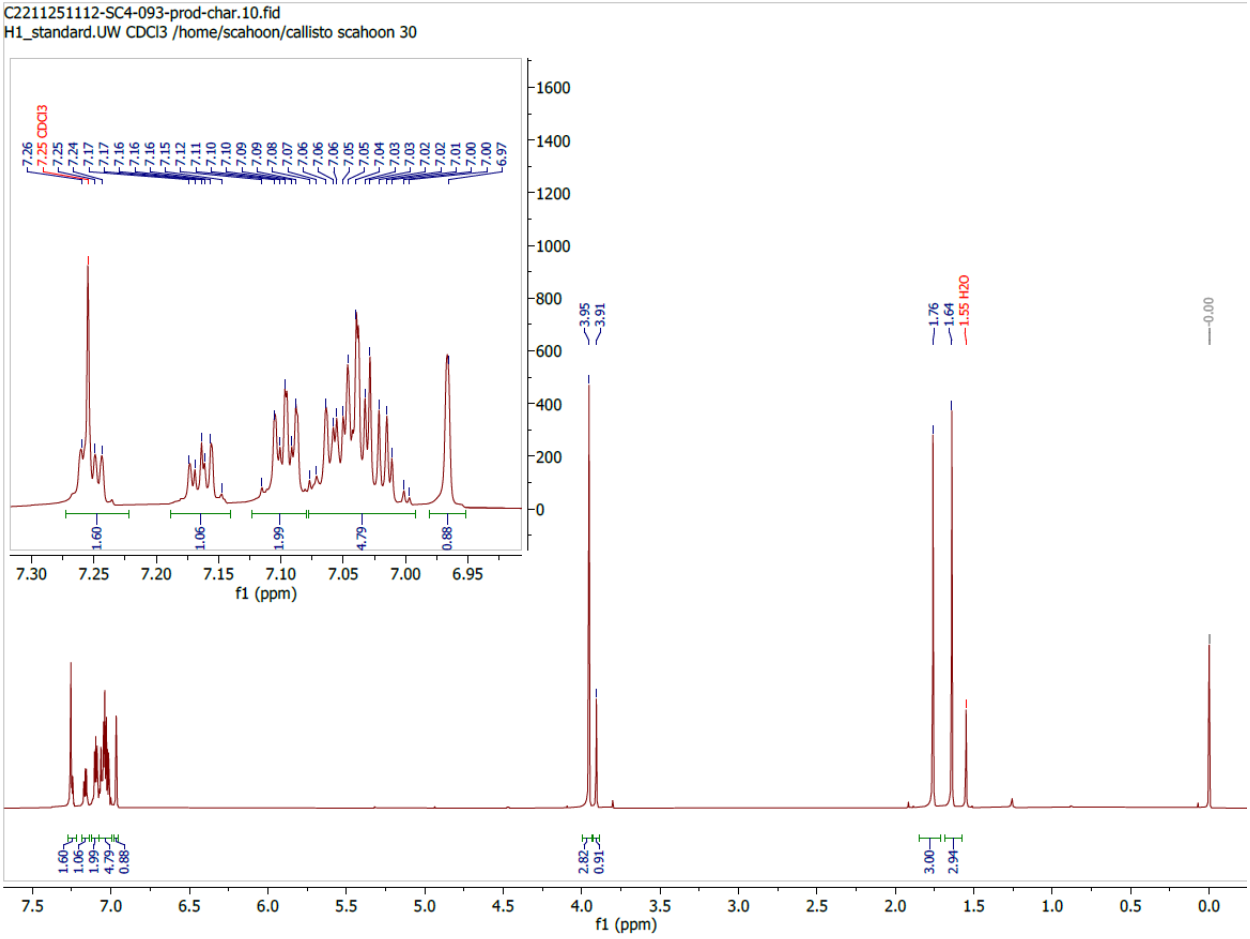

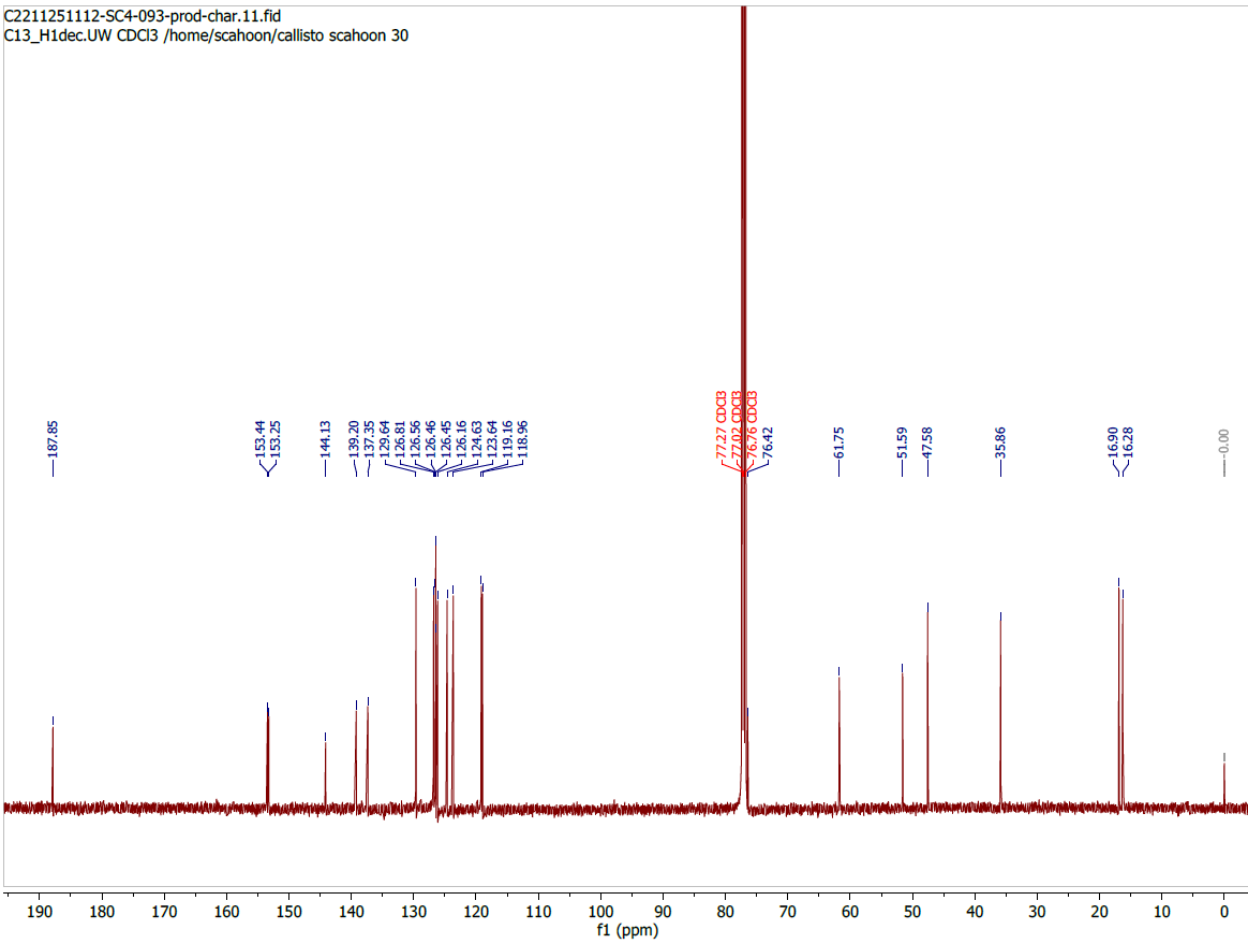
C2211251112-SC4-093-prod-char.11.fid
C13_H1dec.UW CDCl3 /home/scahoon/callisto scahoon 30
187.85
153.44
153.25
144.13
139.20
137.35
129.64
126.81
126.56
126.46
126.45
126.16
124.63
123.64
119.16
118.96
77.27 CDCl3
77.02 CDCl3
76.76 CDCl3
76.42
61.75
51.59
47.58
35.86
16.90
16.28
0.00
190 180 170 160 150 140 130 120 110 100 90 80 70 60 50 40 30 20 10 0
f1 (ppm)

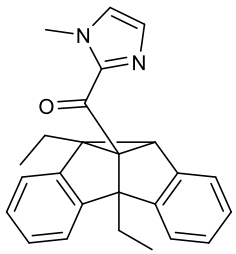

(4b,8b-diethyl-8b,8c-dihydrodibenzo[a,f]cyclopropa[cd]pentalen-4b1(4bH)-yl)(1-methyl-1H-imidazol-2-yl)methanone (**S2.14**):

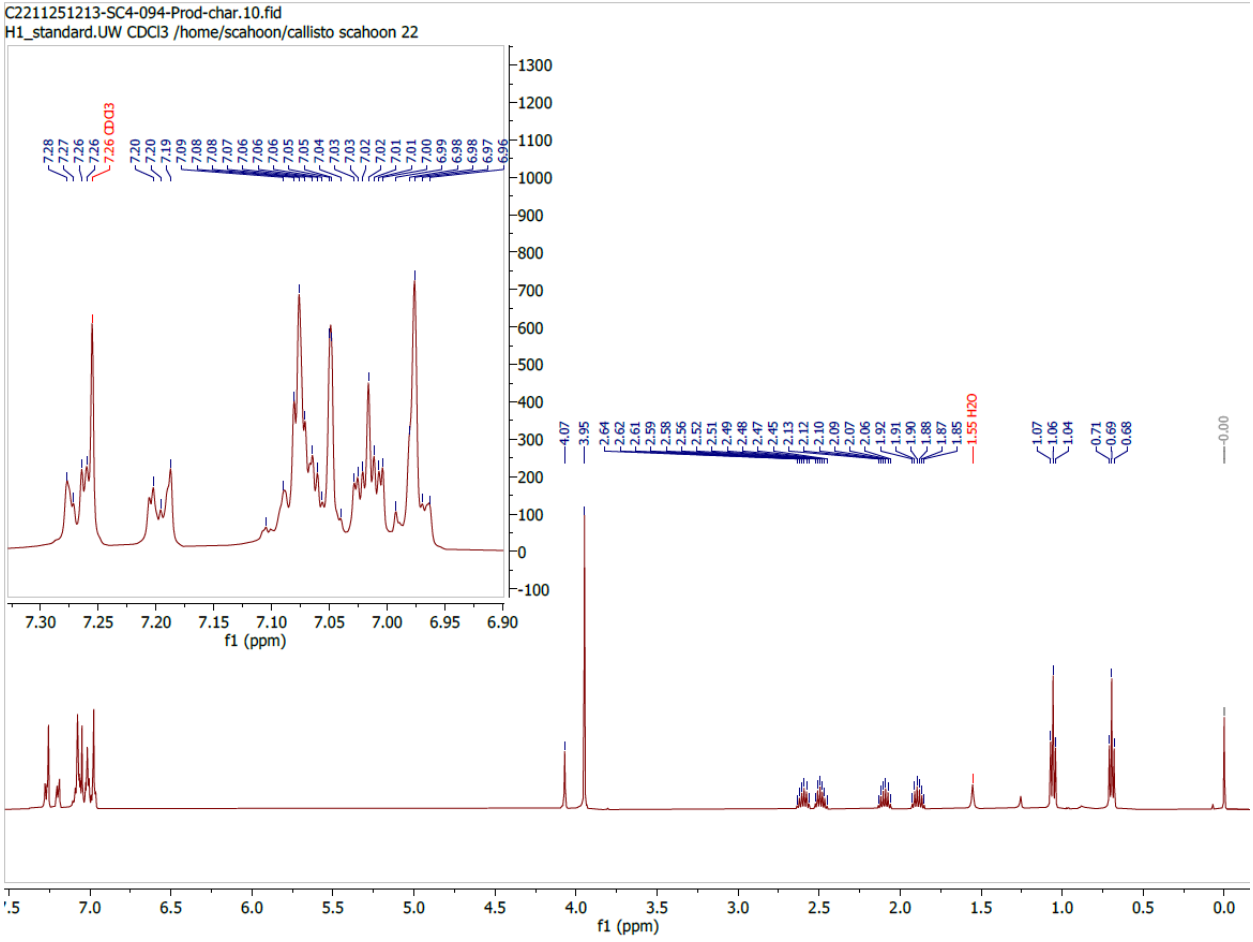

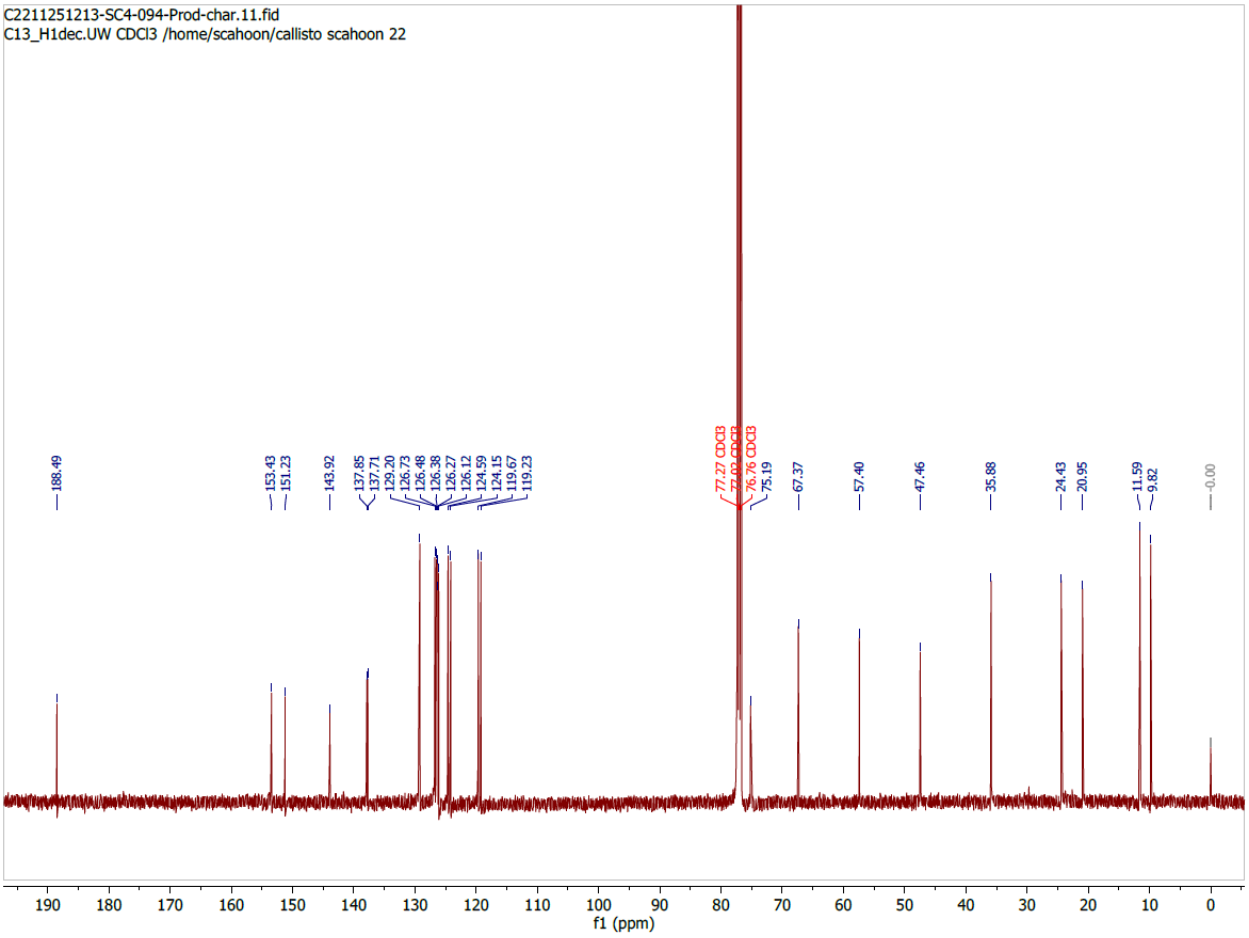
C2211251213-SC4-094-Prod-char.11.fid
C13_H1dec.UW CDCl3 /home/scahoon/callisto scahoon 22
188.49
153.43
151.23
143.92
137.85
137.71
129.20
126.73
126.48
126.38
126.27
126.12
124.59
124.15
119.67
119.23
77.27 CDCl3
77.00 CDCl3
76.76 CDCl3
75.19
67.37
57.40
47.46
35.88
24.43
20.95
11.59
9.82
-0.00
190
180
170
160
150
140
130
120
110
100
90
80
70
60
50
40
30
20
10
0
f1 (ppm)

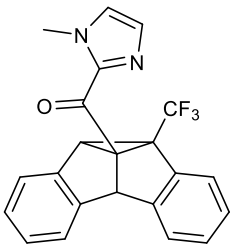

(1-methyl-1H-imidazol-2-yl)(8b-(trifluoromethyl)-8b,8c-dihydrodibenzo[a,f]cyclopropa[cd]pentalen-4b1(4bH)-yl)methanone--(1-methyl-1H-imidazol-2-yl)(8b-phenethyl-8b,8c-dihydrodibenzo[a,f]cyclopropa[cd]pentalen-4b1(4bH)-yl)methanone--(8b-cyclohexyl-8b,8c-dihydrodibenzo[a,f]cyclopropa[cd]pentalen-4b1(4bH)-yl)(1-methyl-1H-imidazol-2-yl)methanone (1/1/1) (**S2.15**):

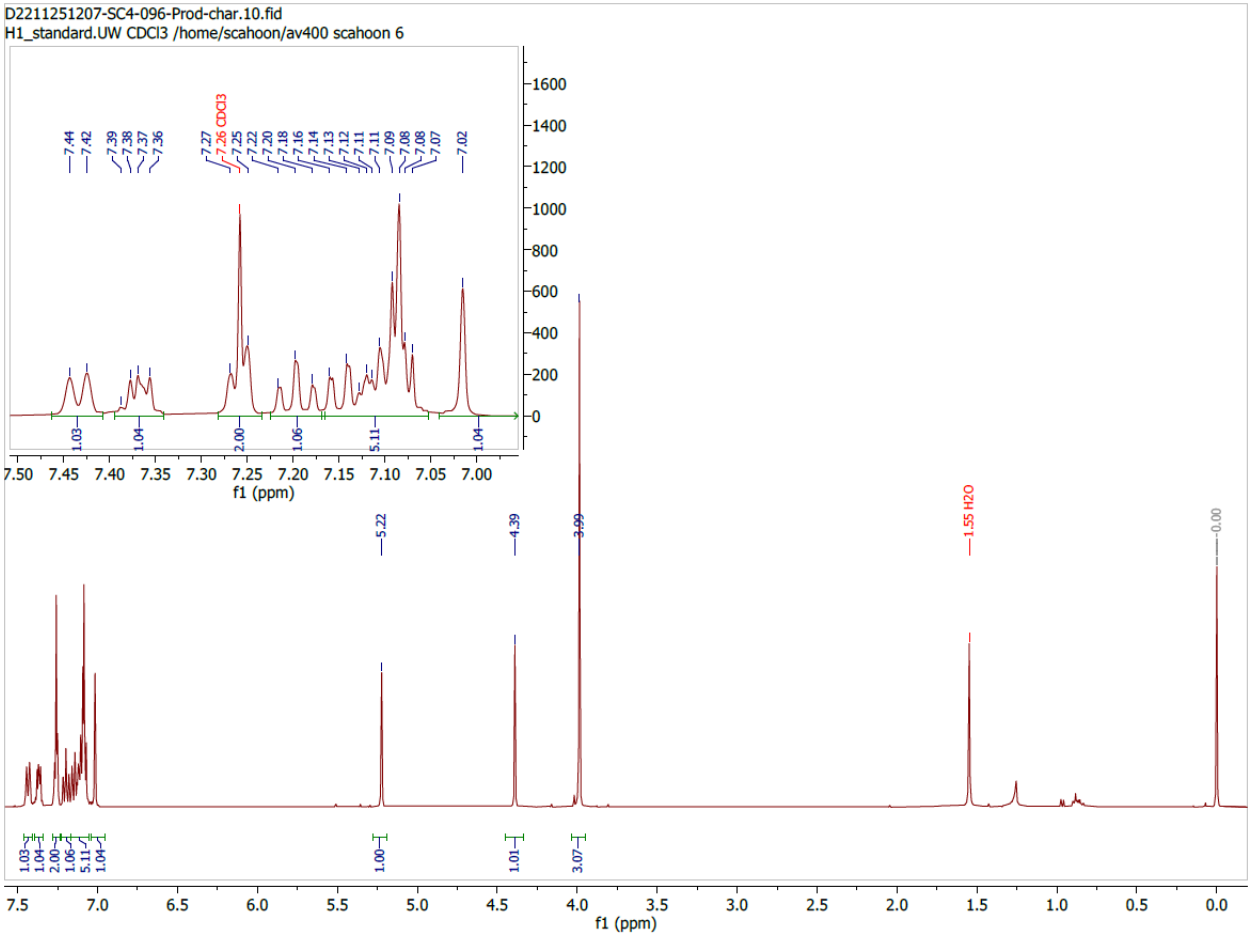

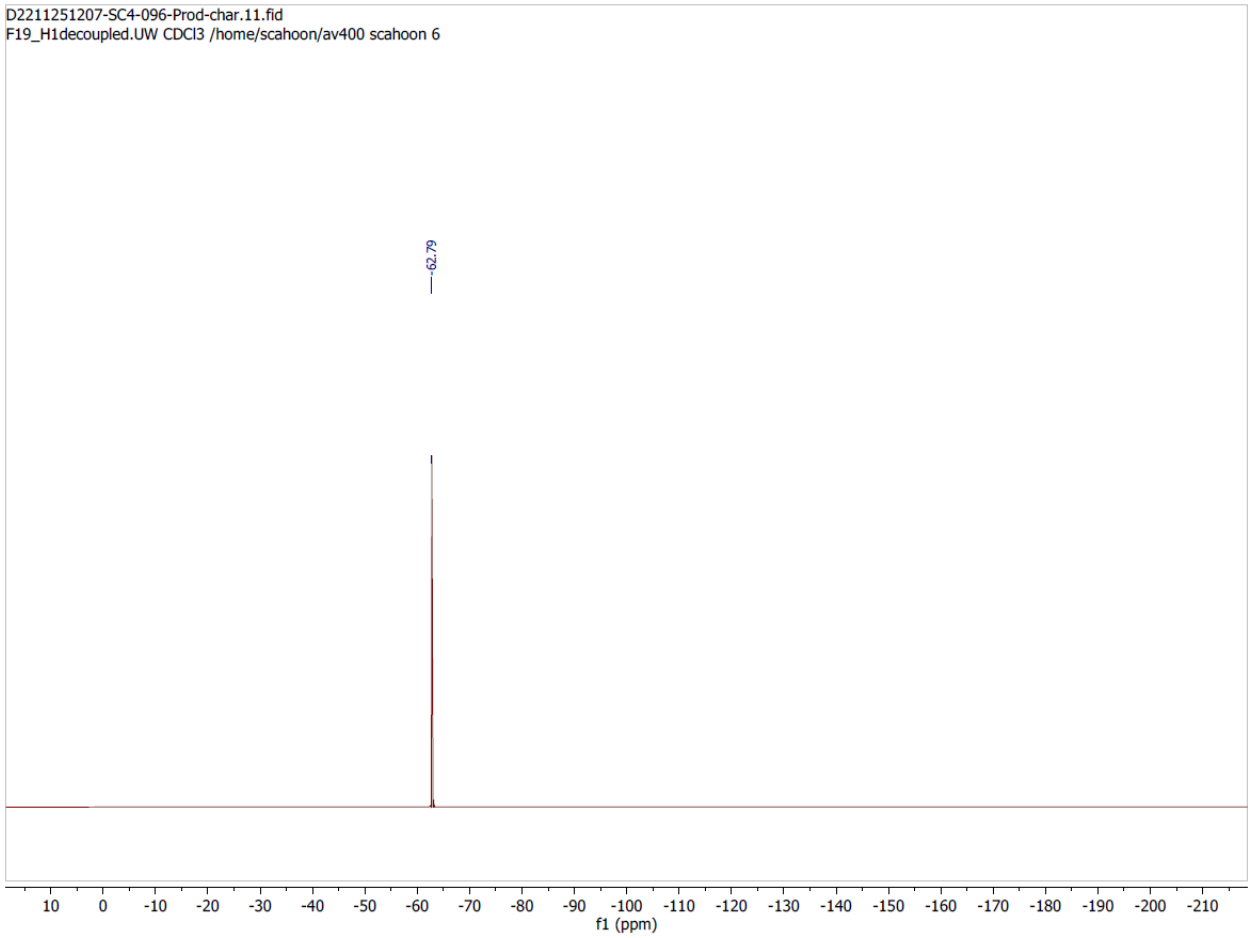
D2211251207-SC4-096-Prod-char.11.fid
F19_H1decoupled.UW CDCl3 /home/scahoon/av400 scahoon 6
-62.79
10 0 -10 -20 -30 -40 -50 -60 -70 -80 -90 -100 -110 -120 -130 -140 -150 -160 -170 -180 -190 -200 -210
f1 (ppm)

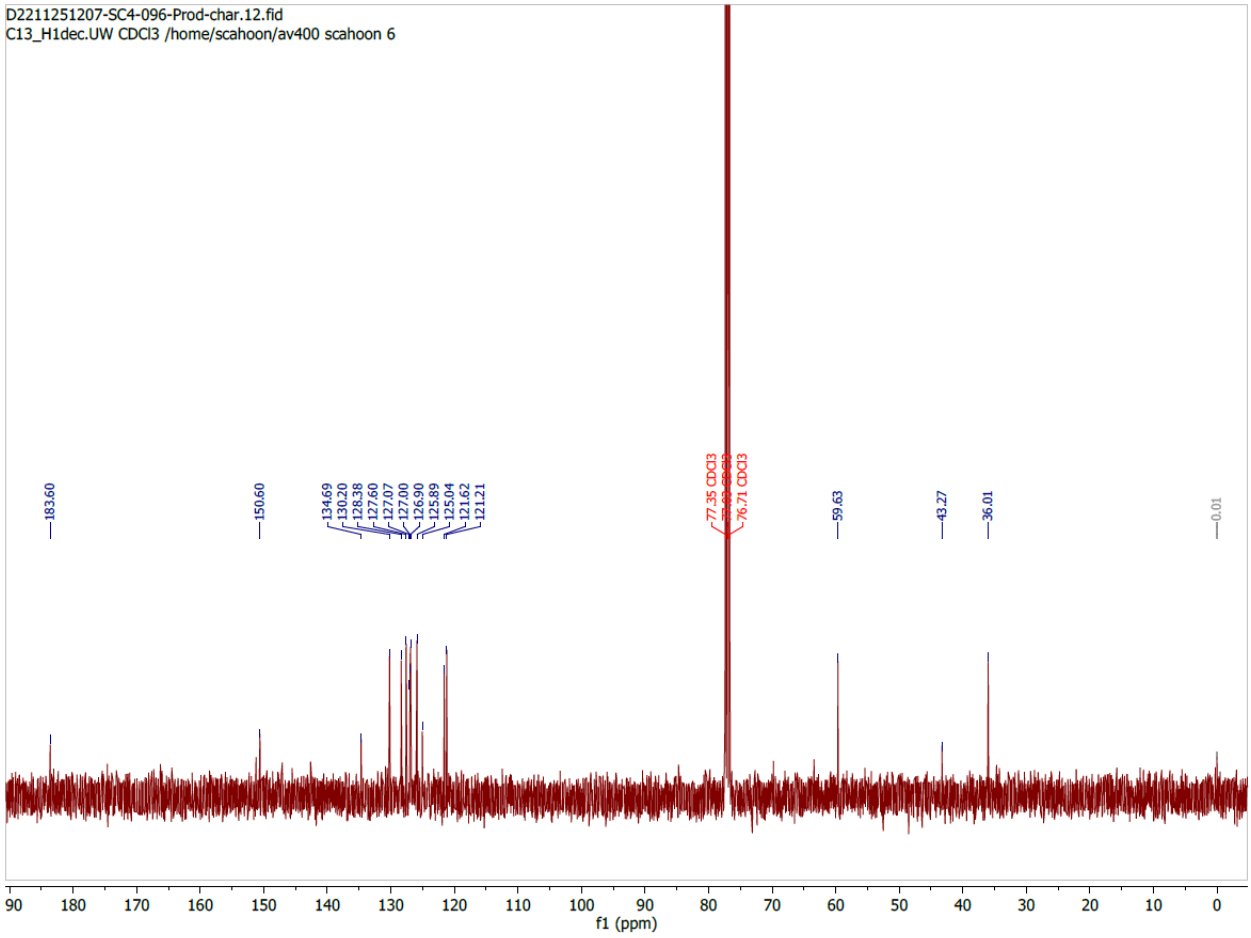
D2211251207-SC4-096-Prod-char.12.fid
C13_H1dec.UW CDCl3 /home/scahoon/av400 scahoon 6
183.60
150.60
134.69
130.20
128.38
127.60
127.07
127.00
126.90
125.89
125.04
121.62
121.21
77.35 CDCl3
76.71 CDCl3
59.63
43.27
36.01
0.01
90 180 170 160 150 140 130 120 110 100 90 80 70 60 50 40 30 20 10 0
f1 (ppm)

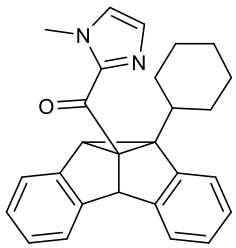

(8b-cyclohexyl-8b,8c-dihydrodibenzo[a,f]cyclopropa[cd]pentalen-4b1(4bH)-yl)(1-methyl-1H-imidazol-2-yl)methanone (**S2.16**):

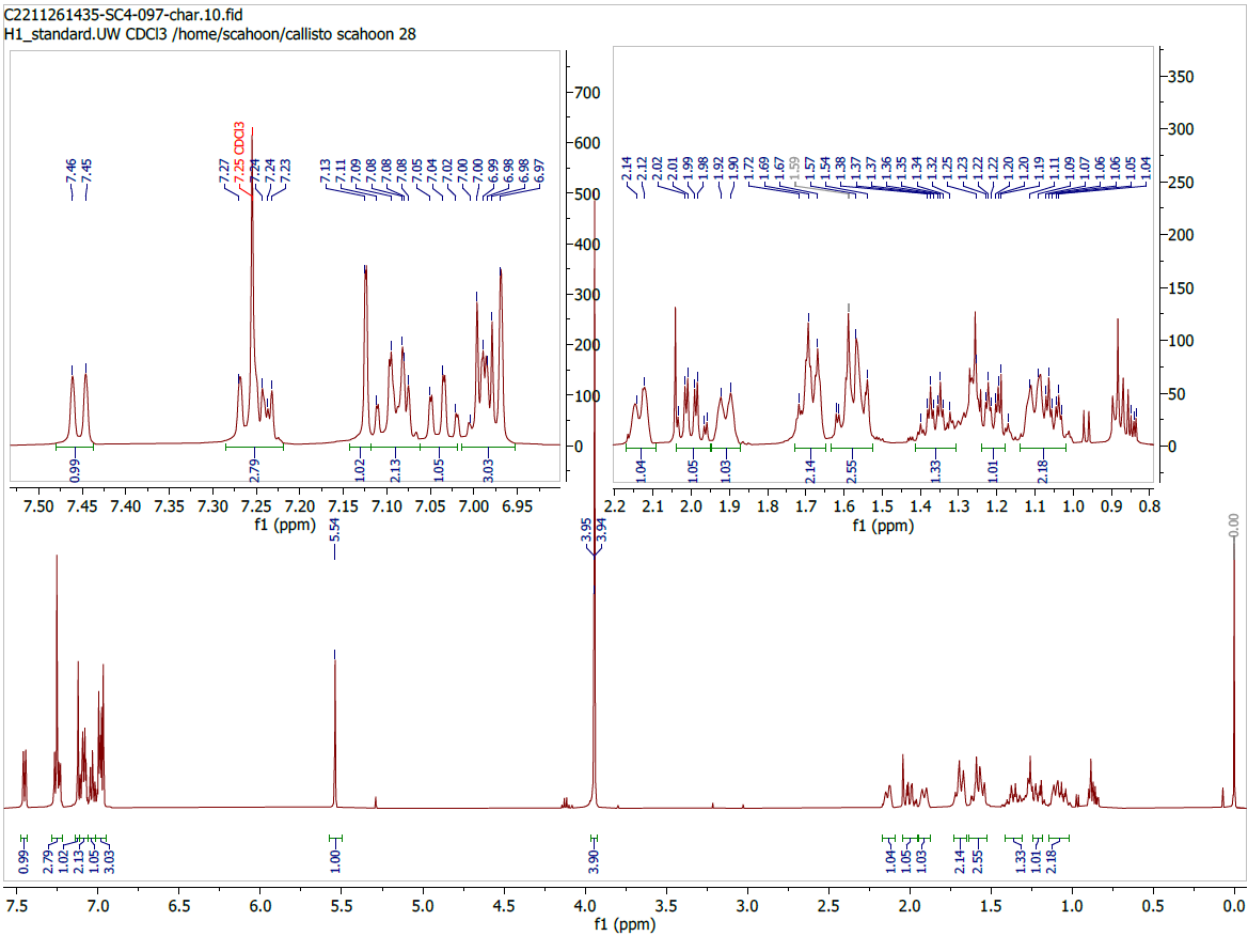

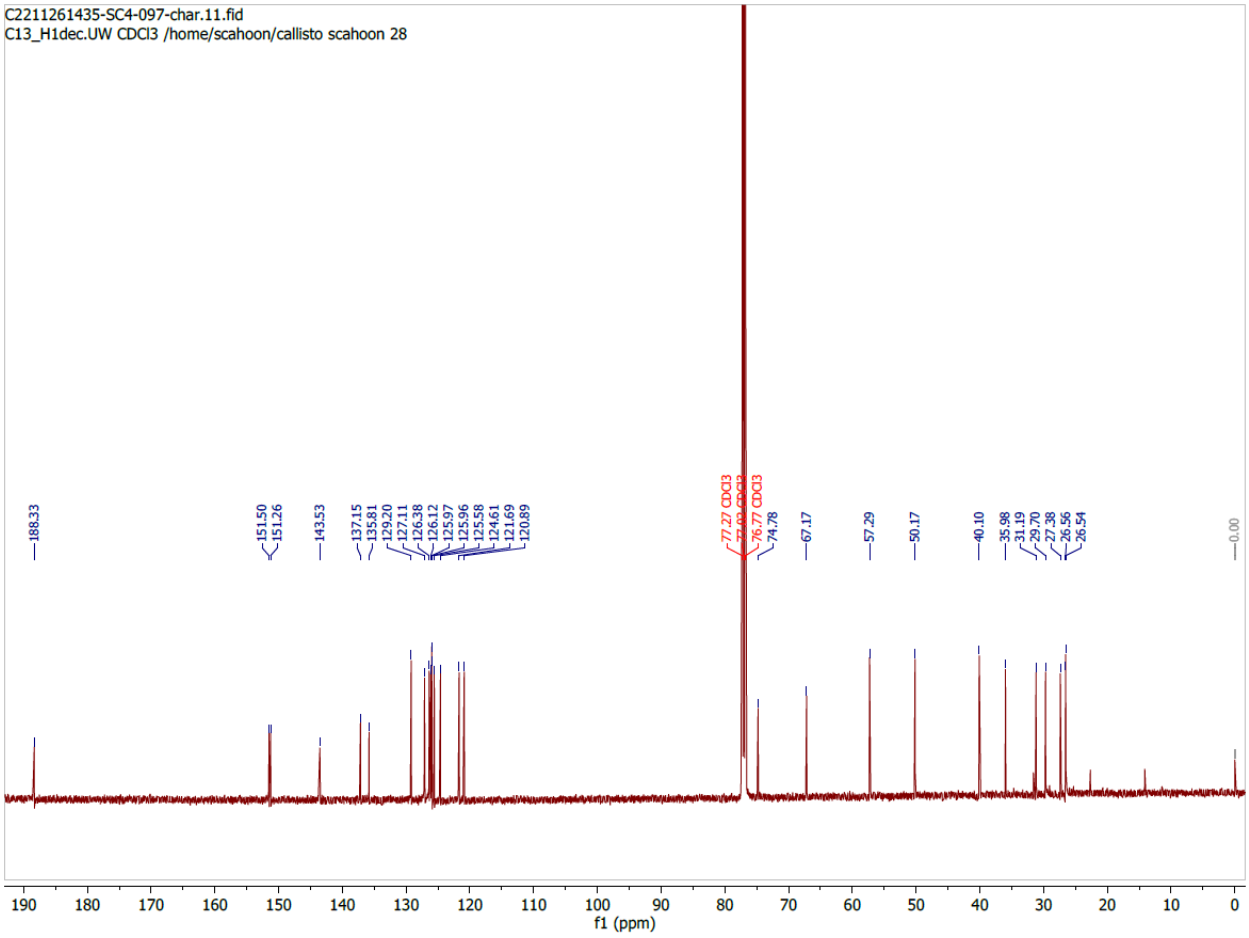
C2211261435-SC4-097-char.11.fid
C13_H1dec.UW CDCl3 /home/scahoon/callisto scahoon 28
188.33
151.50
151.26
143.53
137.15
135.81
129.20
127.11
126.38
126.12
125.97
125.96
125.58
124.61
121.69
120.89
77.27 CDCl3
77.02 CDCl3
76.77 CDCl3
74.78
67.17
57.29
50.17
40.10
35.98
31.19
29.70
27.38
26.56
26.54
0.00
190 180 170 160 150 140 130 120 110 100 90 80 70 60 50 40 30 20 10 0
f1 (ppm)

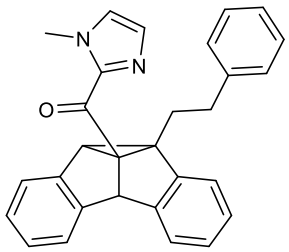

(1-methyl-1H-imidazol-2-yl)(8b-phenethyl-8b,8c-dihydrodibenzo[a,f]cyclopropa[cd]pentalen-4b1(4bH)-yl)methanone (**S2.17**):

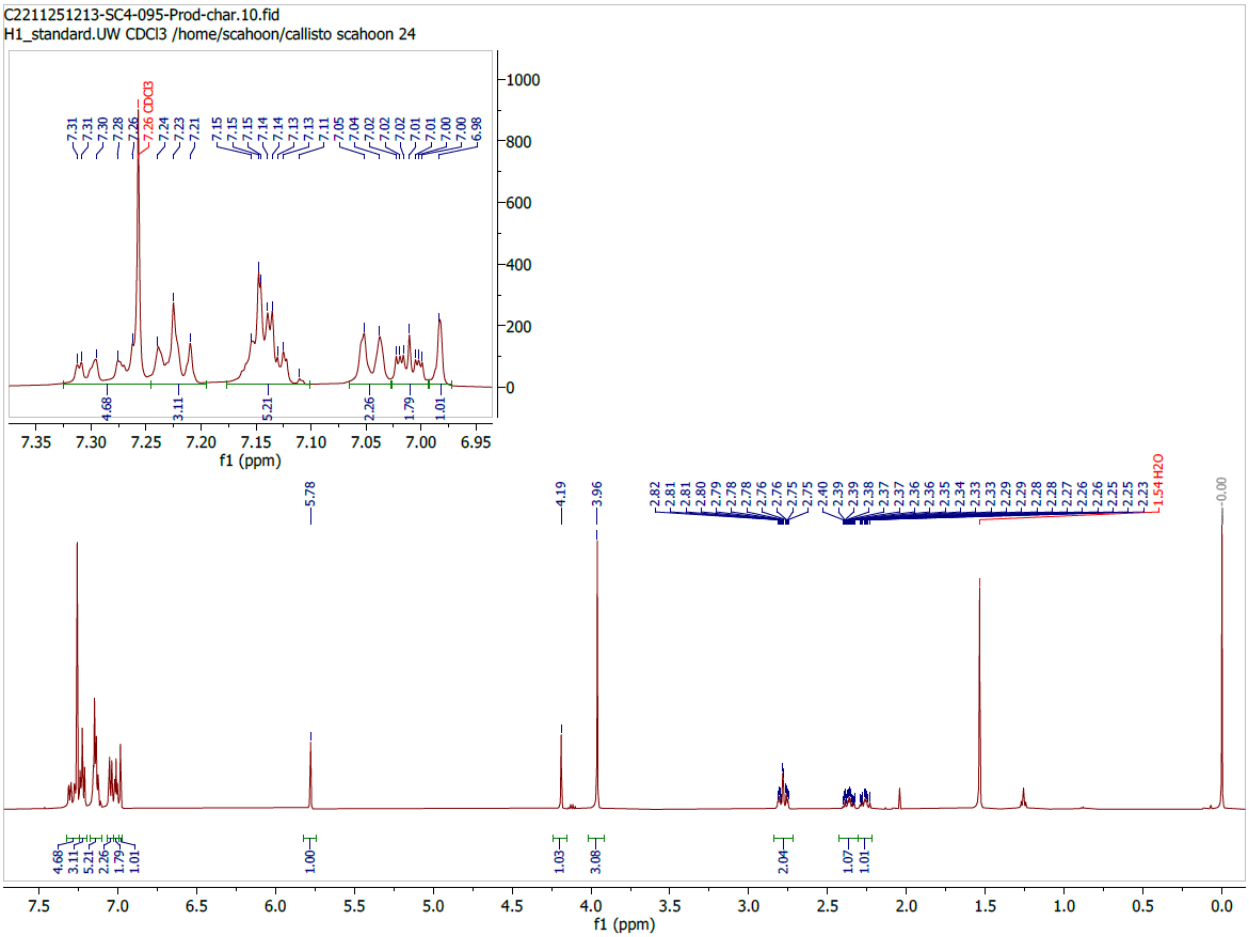

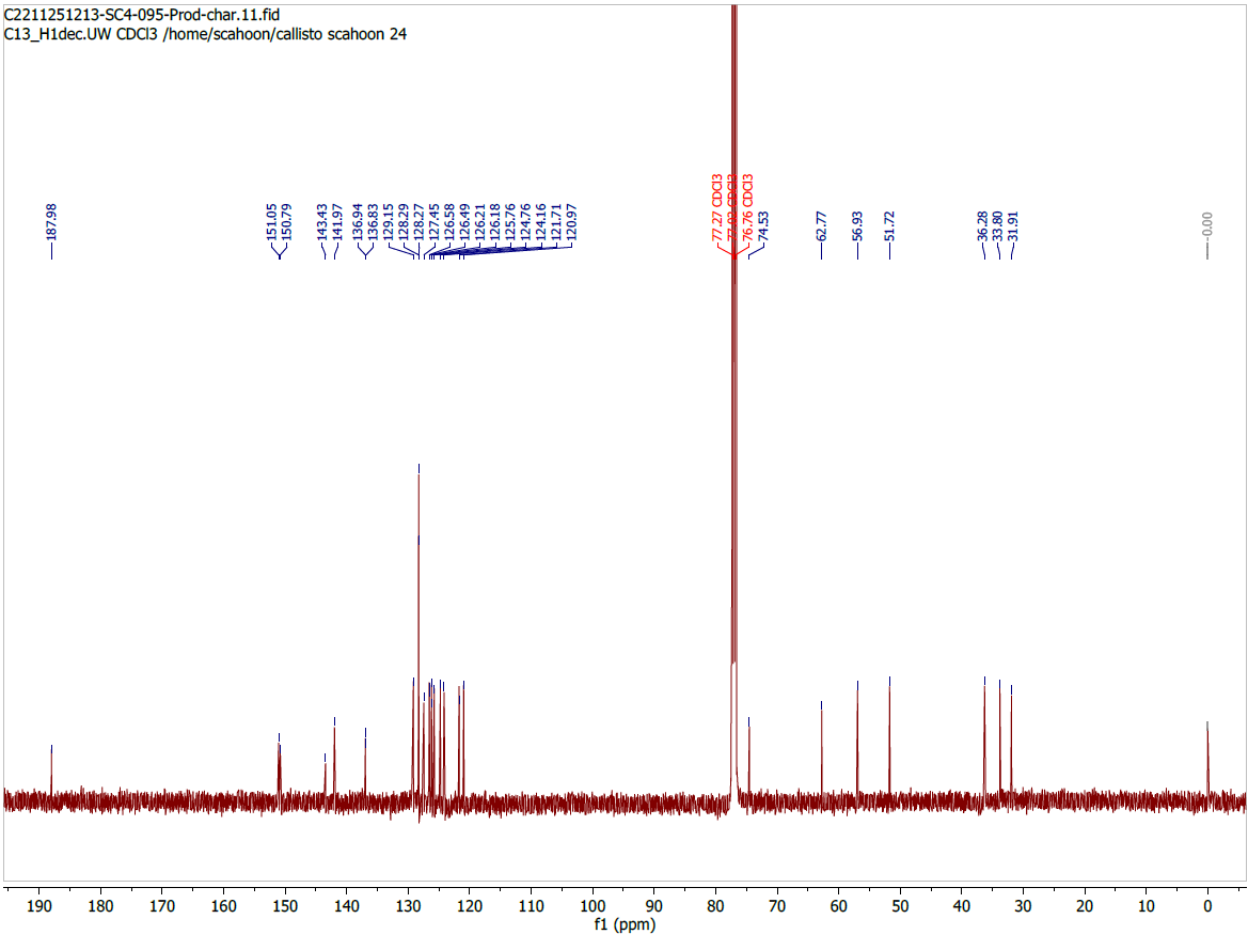
C2211251213-SC4-095-Prod-char.11.fid
C13_H1dec.UW CDCl3 /home/scahoon/callisto scahoon 24
187.98
151.05
150.79
143.43
141.97
136.94
136.83
129.15
128.29
128.27
127.45
126.58
126.49
126.21
126.18
125.76
124.76
124.16
121.71
120.97
77.27 CDCl3
76.76 CDCl3
74.53
62.77
56.93
51.72
36.28
33.80
31.91
0.00
190
180
170
160
150
140
130
120
110
100
90
80
70
60
50
40
30
20
10
0
f1 (ppm)

2.6.9 HPLC Chromatograms

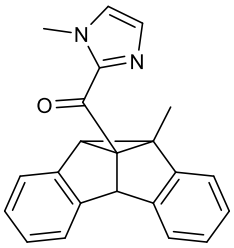

(1-methyl-1H-imidazol-2-yl)(8b-methyl-8b,8c-dihydrodibenzo[a,f]cyclopropa[cd]pentalen-4b1(4bH)-yl)methanone--(4b,8b-diethyl-8b,8c-dihydrodibenzo[a,f]cyclopropa[cd]pentalen-4b1(4bH)-yl)(1-methyl-1H-imidazol-2-yl)methanone--(4b,8b-dimethyl-8b,8c-dihydrodibenzo[a,f]cyclopropa[cd]pentalen-4b1(4bH)-yl)(1-methyl-1H-imidazol-2-yl)methanone--(8b-ethyl-8b,8c-dihydrodibenzo[a,f]cyclopropa[cd]pentalen-4b1(4bH)-yl)(1-methyl-1H-imidazol-2-yl)methanone (1/1/1/1) (**S2.11**):

HPLC Conditions: Daicel CHIRALPAK AD-H column - 5µm, isocratic 20% iPrOH, 1 ml/min, 280 nm.

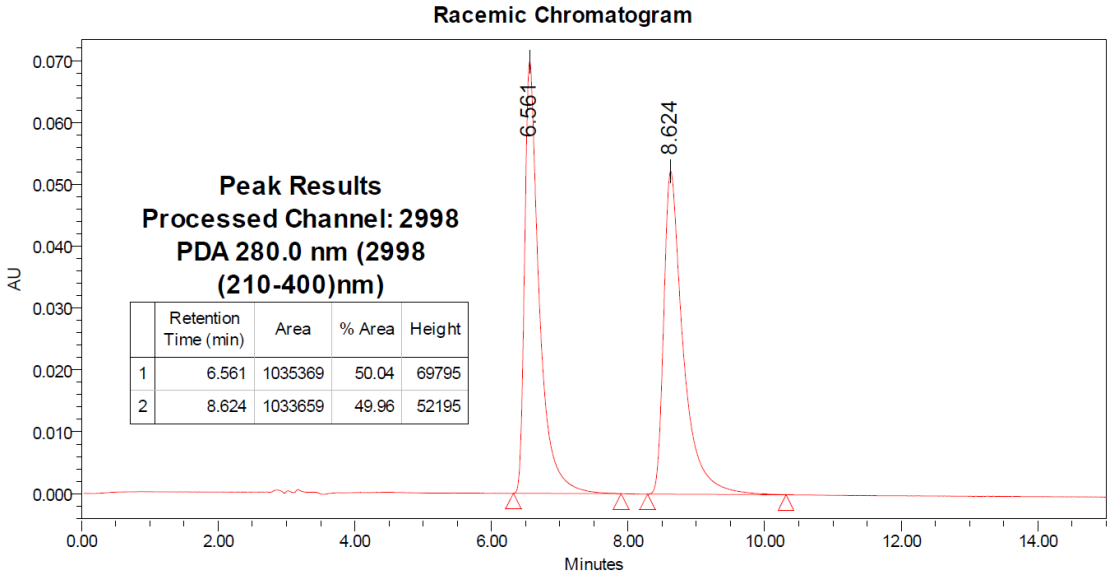

	Retention Time (min)	Area	% Area	Height
1	6.561	1035369	50.04	69795
2	8.624	1033659	49.96	52195

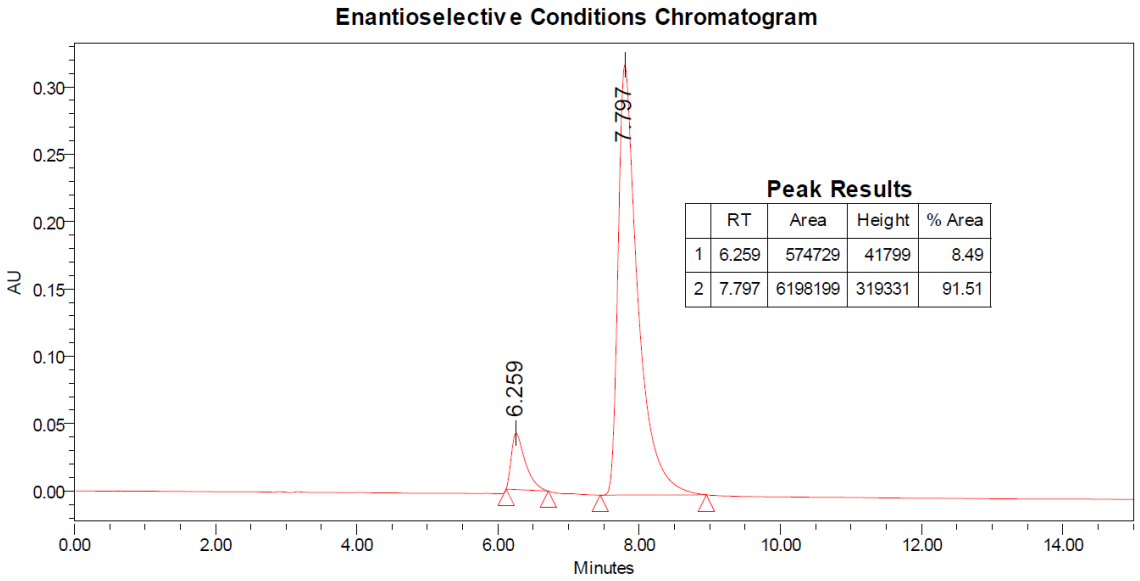
Enantioselective Conditions Chromatogram
AU
Minutes
6.259
7.797
Peak Results
RT
Area
Height
% Area
1
6.259
574729
41799
8.49
2
7.797
6198199
319331
91.51

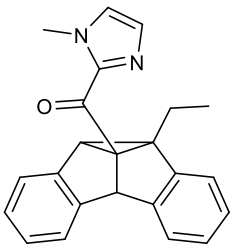

(8b-ethyl-8b,8c-dihydrodibenzo[a,f]cyclopropa[cd]pentalen-4b1(4bH)-yl)(1-methyl-1H-imidazol-2-yl)methanone (**S2.12**):

HPLC Conditions: Daicel CHIRALPAK AD-H column - 5µm, isocratic 15% iPrOH, 1 ml/min, 280 nm.

Racemic Chromatogram

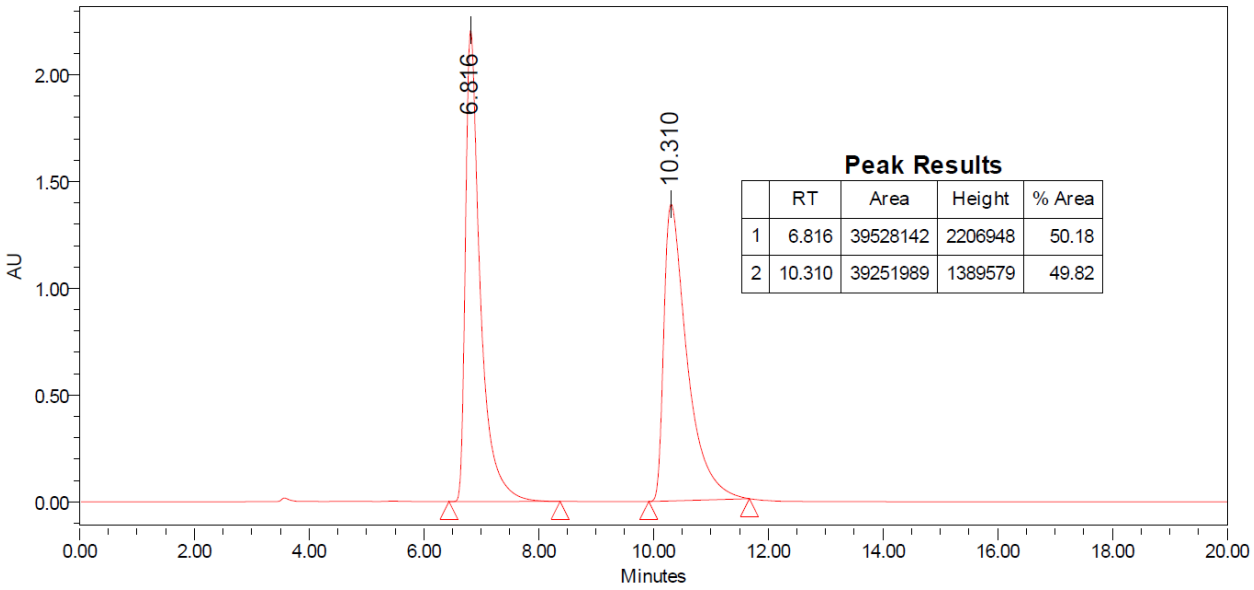

Peak Results

	RT	Area	Height	% Area
1	6.816	39528142	2206948	50.18
2	10.310	39251989	1389579	49.82

Enantioselective Conditions Chromatogram

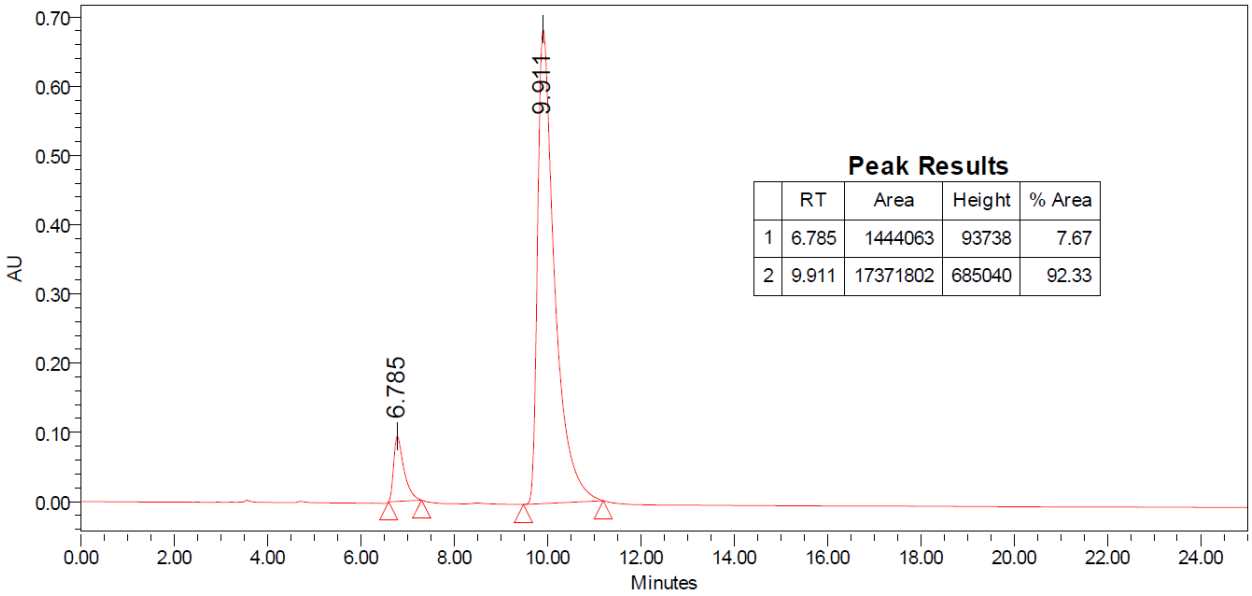

Peak Results

	RT	Area	Height	% Area
1	6.785	1444063	93738	7.67
2	9.911	17371802	685040	92.33

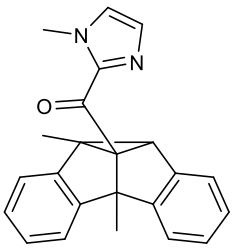

(4b,8b-dimethyl-8b,8c-dihydrodibenzo[a,f]cyclopropa[cd]pentalen-4b1(4bH)-yl)(1-methyl-1H-imidazol-2-yl)methanone (**S2.13**):

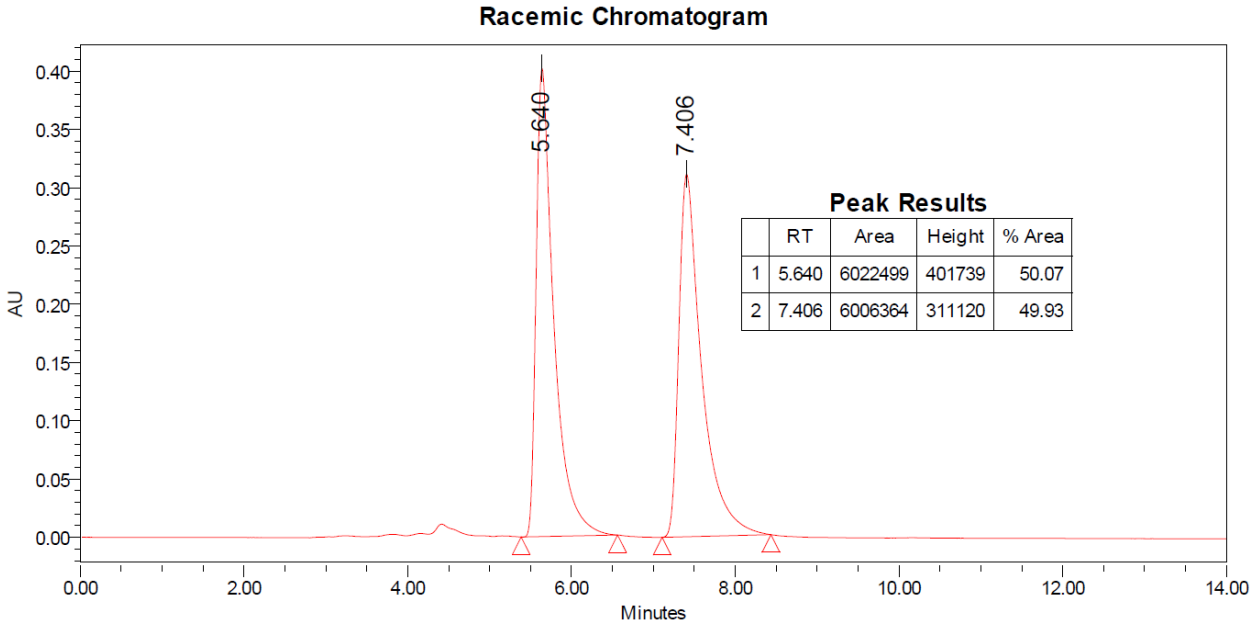

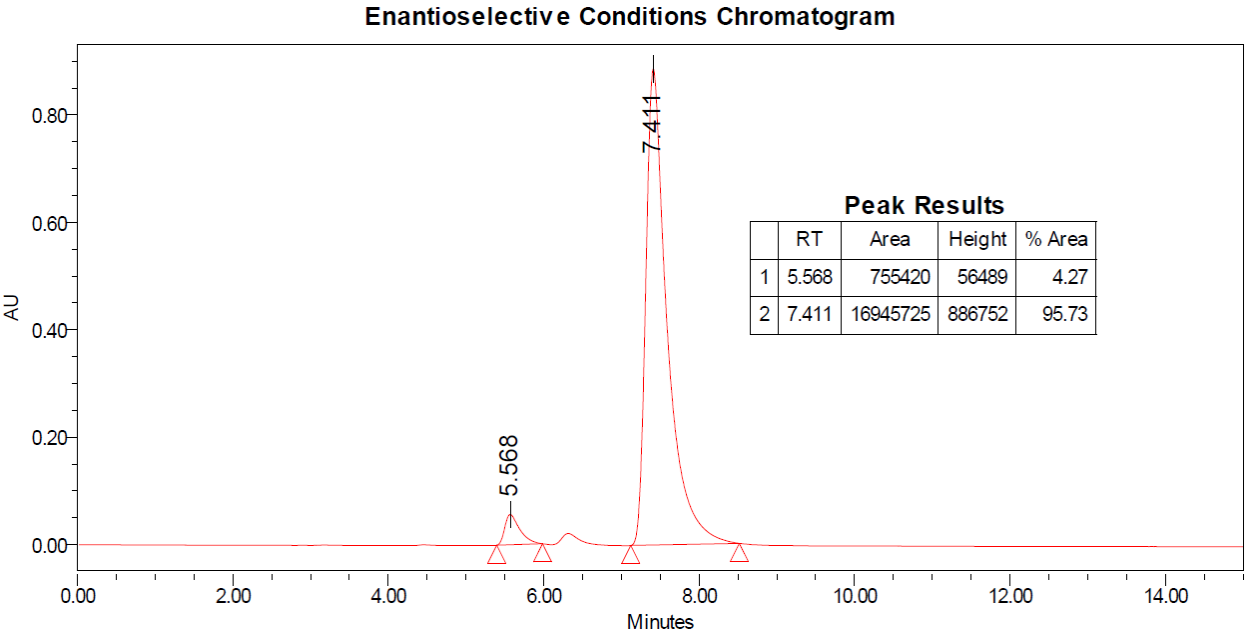

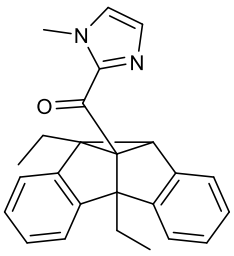

(4b,8b-diethyl-8b,8c-dihydrodibenzo[a,f]cyclopropa[cd]pentalen-4b1(4bH)-yl)(1-methyl-1H-imidazol-2-yl)methanone (**S2.14**):

HPLC Conditions: Daicel CHIRALPAK OD-H column - 5µm, isocratic 1% iPrOH, 1% MTBE, 1 ml/min, 280 nm.

Racemic Chromatogram

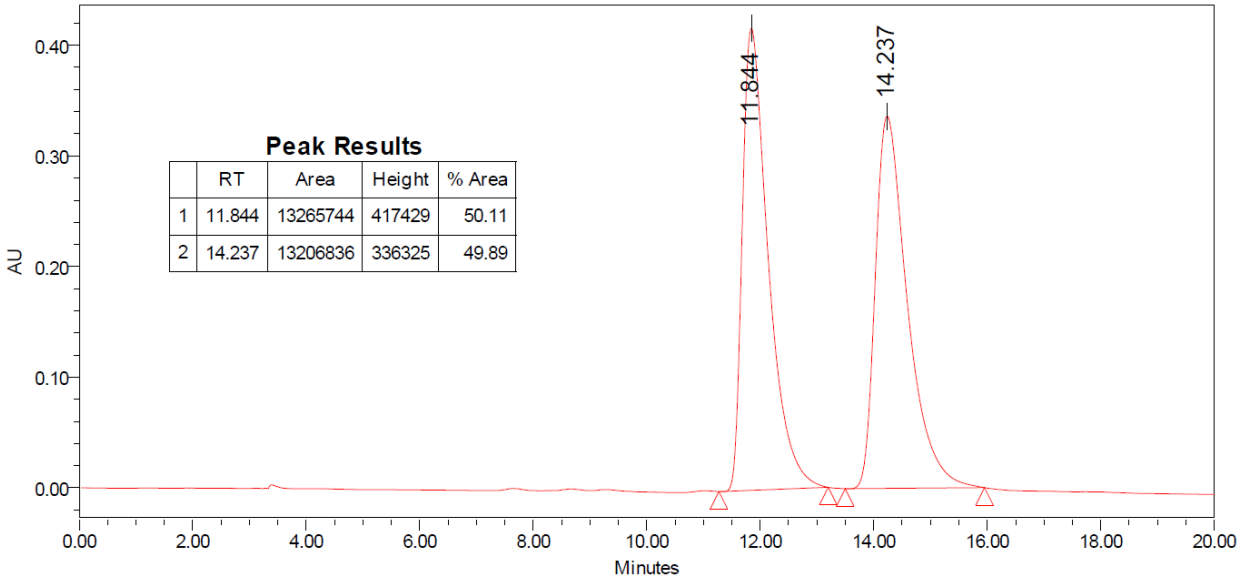

Peak Results

	RT	Area	Height	% Area
1	11.844	13265744	417429	50.11
2	14.237	13206836	336325	49.89

Enantioselective Conditions Chromatogram

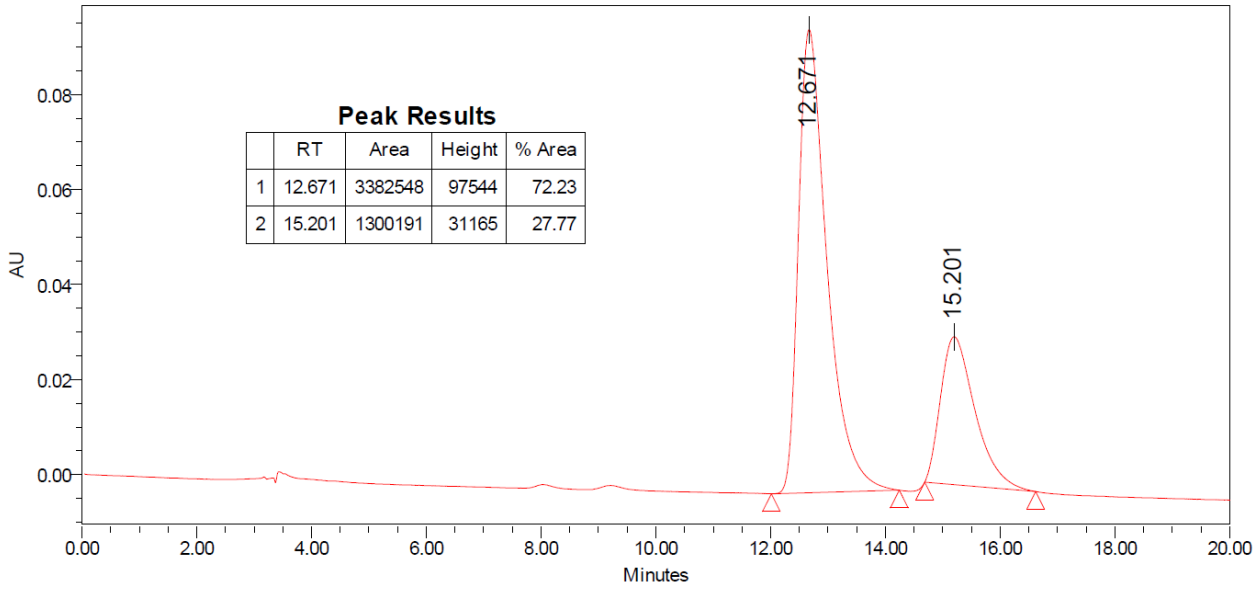

Peak Results

	RT	Area	Height	% Area
1	12.671	3382548	97544	72.23
2	15.201	1300191	31165	27.77

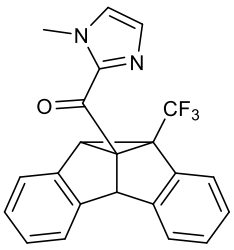

(1-methyl-1H-imidazol-2-yl)(8b-(trifluoromethyl)-8b,8c-dihydrodibenzo[a,f]cyclopropa[cd]pentalen-4b1(4bH)-yl)methanone--(1-methyl-1H-imidazol-2-yl)(8b-phenethyl-8b,8c-dihydrodibenzo[a,f]cyclopropa[cd]pentalen-4b1(4bH)-yl)methanone--(8b-cyclohexyl-8b,8c-dihydrodibenzo[a,f]cyclopropa[cd]pentalen-4b1(4bH)-yl)(1-methyl-1H-imidazol-2-yl)methanone (1/1/1) (**S2.15**):

HPLC Conditions: CHIRALPAK AD-H column - 5µm, isocratic 20% iPrOH, 1 ml/min, 280 nm

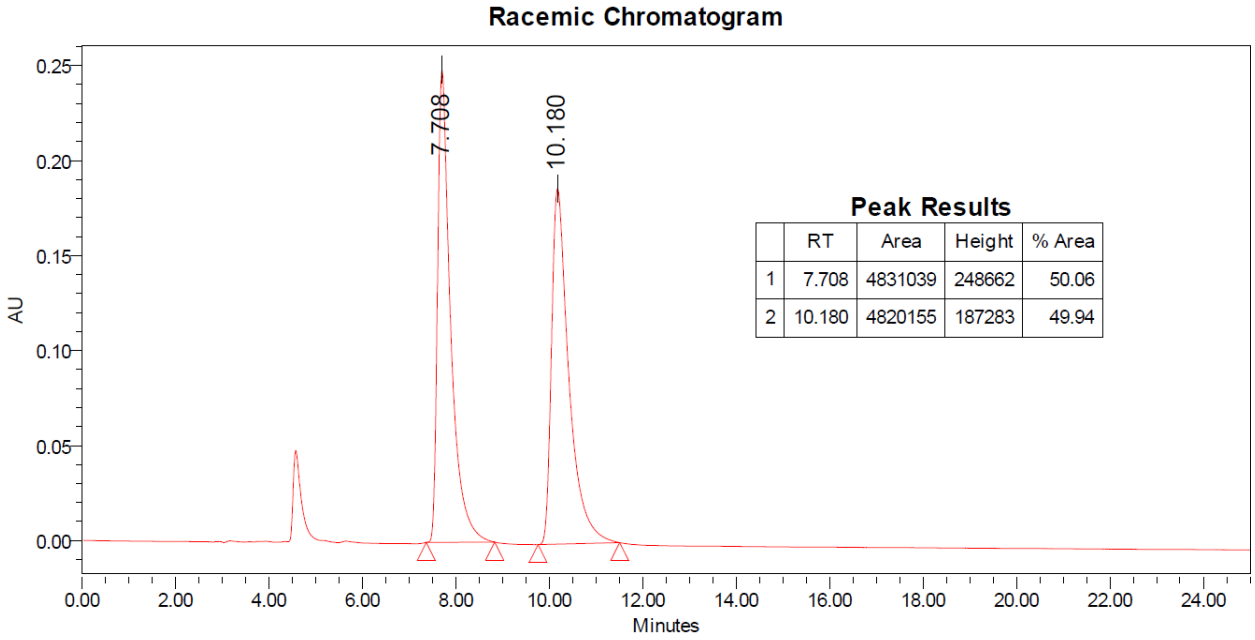

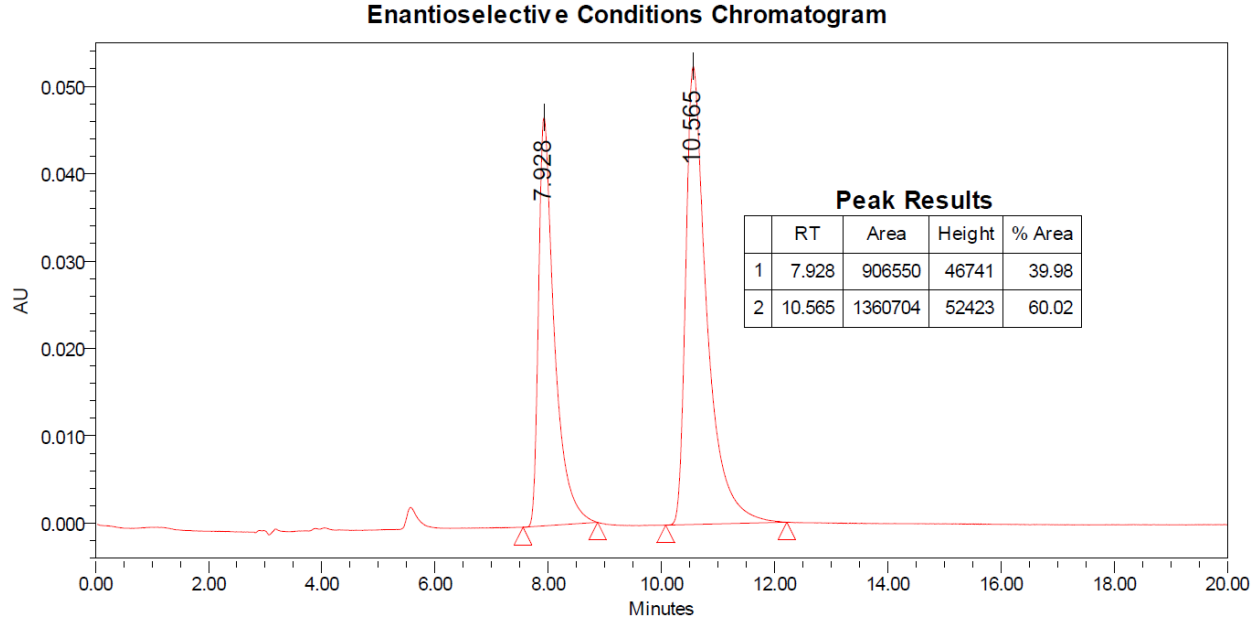

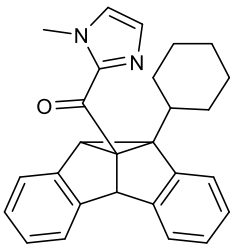

(8b-cyclohexyl-8b,8c-dihydrodibenzo[a,f]cyclopropa[cd]pentalen-4b1(4bH)-yl)(1-methyl-1H-imidazol-2-yl)methanone (**S2.16**):

HPLC Conditions: CHIRALPAK AD-H column - 5µm, isocratic 20% iPrOH, 1 ml/min, 280 nm

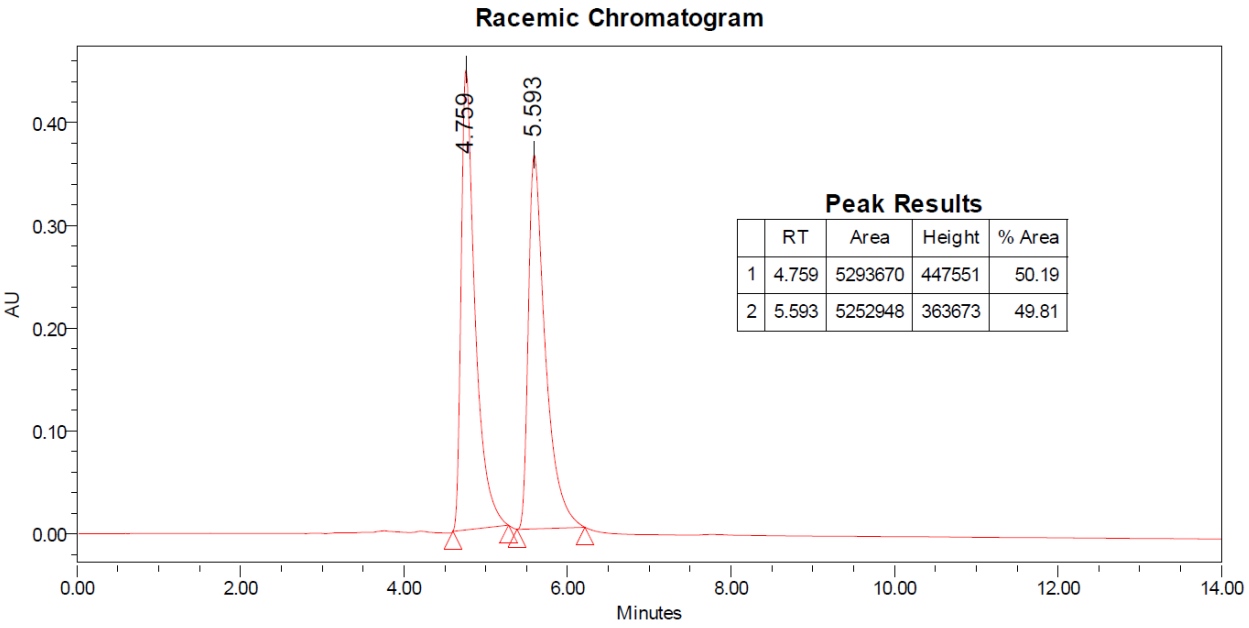

Peak Results

	RT	Area	Height	% Area
1	4.759	5293670	447551	50.19
2	5.593	5252948	363673	49.81

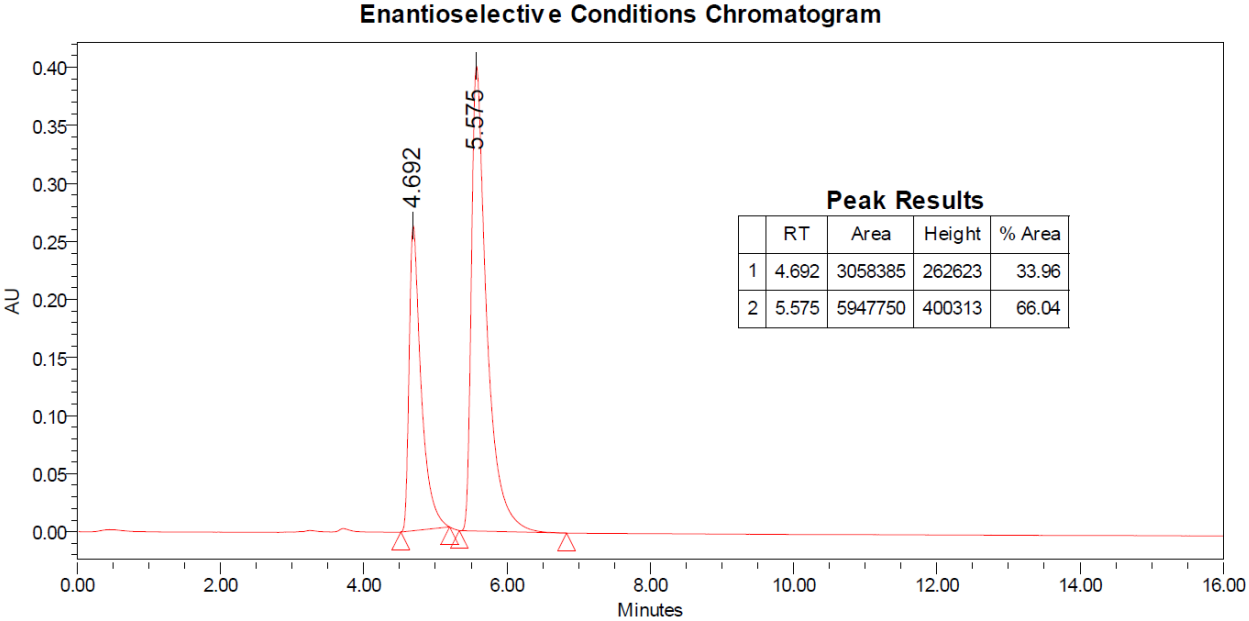

Peak Results

	RT	Area	Height	% Area
1	4.692	3058385	262623	33.96
2	5.575	5947750	400313	66.04

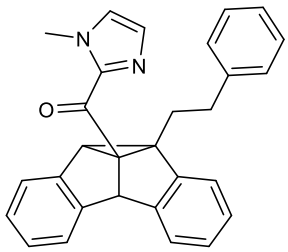

(1-methyl-1H-imidazol-2-yl)(8b-phenethyl-8b,8c-dihydrodibenzo[a,f]cyclopropa[cd]pentalen-4b1(4bH)-yl)methanone (**S2.17**): HPLC Conditions: CHIRALPAK AD-H column - 5µm, isocratic 10% iPrOH, 1 ml/min, 280 nm

Racemic Chromatogram

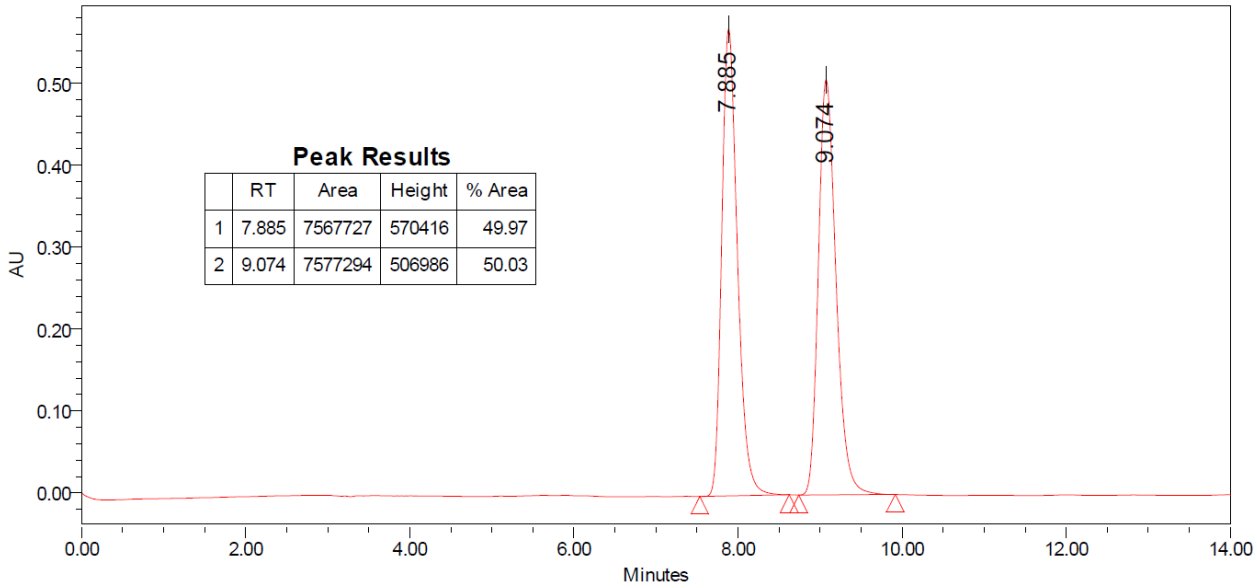

Peak Results

	RT	Area	Height	% Area
1	7.885	7567727	570416	49.97
2	9.074	7577294	506986	50.03

Enantioselective Conditions Chromatogram

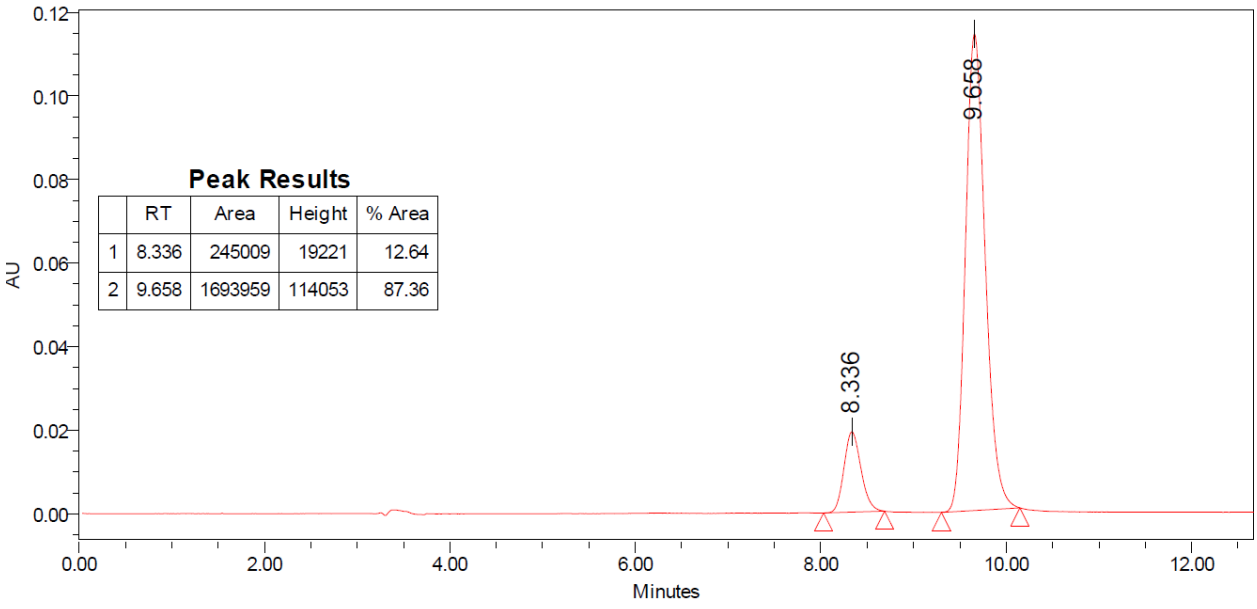

Peak Results

	RT	Area	Height	% Area
1	8.336	245009	19221	12.64
2	9.658	1693959	114053	87.36

2.6.10 Spectroscopic Data

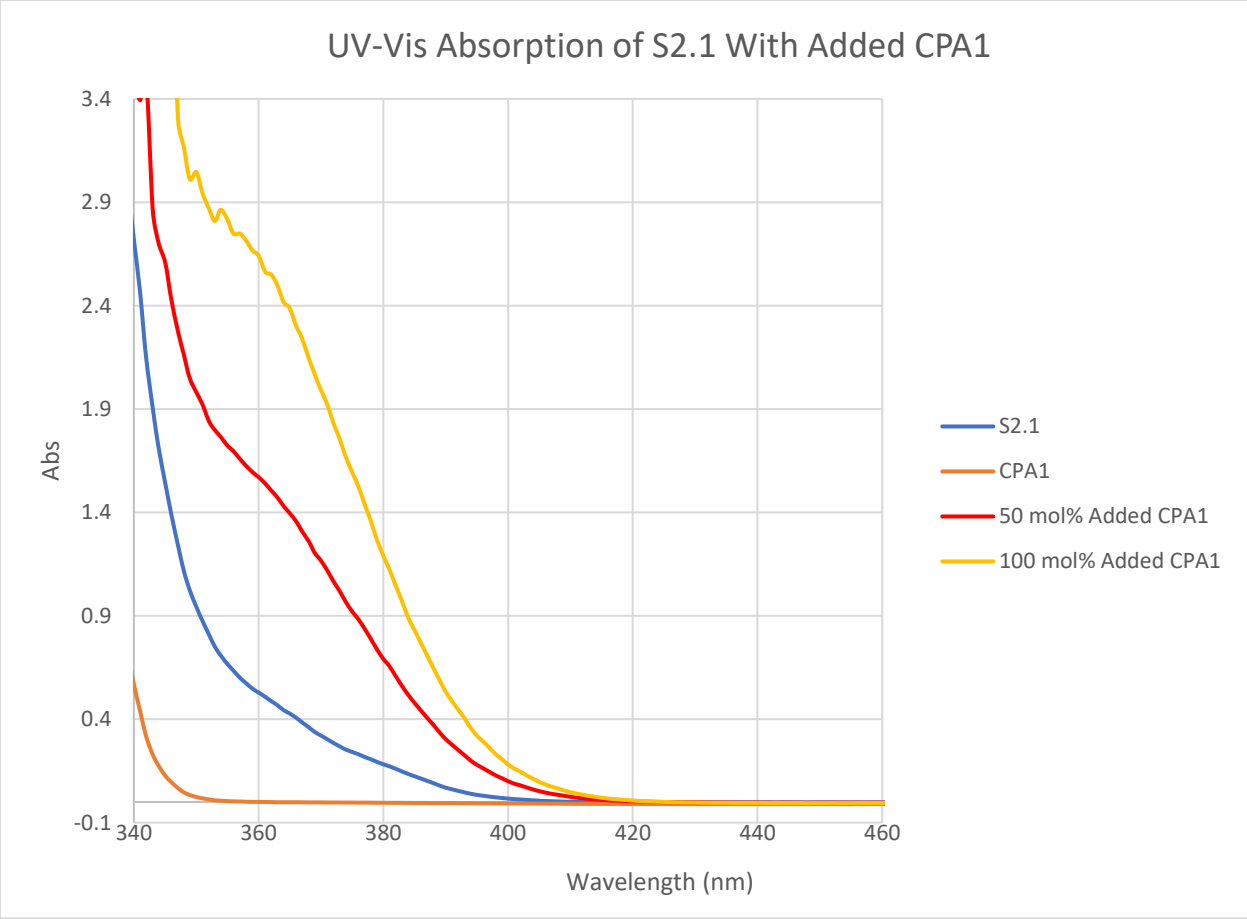

UV-Visible spectra were obtained in 2:1 toluene:pentane solutions of 1 mM with respect to **S2.1**. Samples were prepared in quartz cuvettes by appropriate mixture of three solutions, filling to 2 mL: 2 mM **S2.1**, 2 mM **CPA1**, and solvent. A blank was also prepared and used to automatically adjust for background absorption by the solvent mixture.

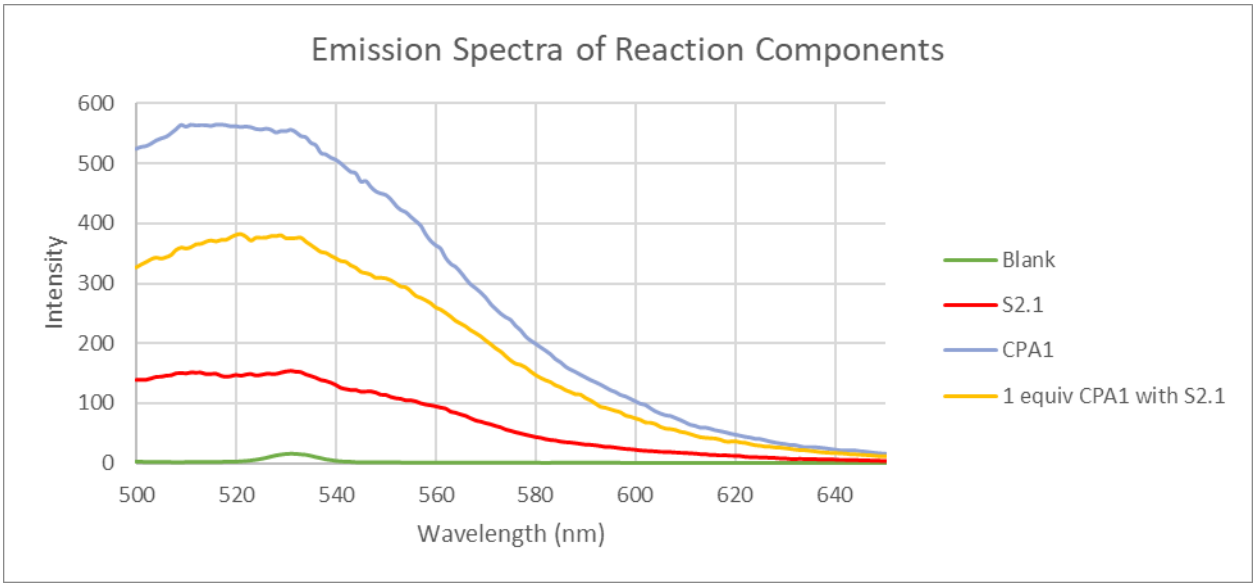

Emission data for the substrate and catalyst were obtained by preparing 2 mL samples of respective solutions at 0.01 M with respect to **S2.1**. All samples were prepared in degassed 2:1 toluene:DCM under an N_2 atmosphere in quartz cuvettes. Cuvettes were sealed with rubber septa and taped with Teflon to exclude O_2. Emission profiles were obtained using a 456 nm excitation beam and recording of the phosphorescence emission. A blank sample was also measured by the same procedure to verify that incident light from the emission source was not the source of the observed emission peaks.

Competitive absorption and emission of **S2.1**, **CPA1**, and the associated complex in the same wavelength range as would be analyzed for the iridium catalyst employed precluded the measurement of a meaningful Stern-Volmer quenching relationship for this system.

2.7 References

(55) Zimmerman, H. E.; Armesto, D. Synthetic Aspects of the Di-π-Methane Rearrangement. *Chem Rev* **1996**, *96* (8), 3065–3112. https://doi.org/10.1021/cr910109c.

(56) Hixson, S. S.; Mariano, P. S.; Zimmerman, H. E. The Di-π-Methane and Oxa-Di-π-Methane Rearrangements. *Chem Rev* **1973**, *73* (5), 531–551. https://doi.org/10.1021/cr60285a005.

(57) Houk, K. N. The Photochemistry and Spectroscopy of β,γ-Unsaturated Carbonyl Compounds. *Chem Rev* **1976**, *76* (1), 1–74. https://doi.org/https://doi.org/10.1021/cr60299a001.

(58) Ramaiah, D.; Sajimon, M. C.; Joseph, J.; George, M. v. Photoisomerisation of Dibenzobarrelenes—a Facile Route to Polycyclic Synthons. *Chem Soc Rev* **2005**, *34* (1), 48–57. https://doi.org/10.1039/b300843f.

(59) Mehta, G.; Subrahmanyam, D. A Total Synthesis of (±)-Modhephene. *J. Chem. Soc., Chem. Commun.* **1985**, 768–769. https://doi.org/10.1021/jo00918a040.

(60) Demuth, M.; Shaffner, K. Tri Cyclo[3.3.0.0 2,8]Octan-3-Ones : Photochemically Prepared Building Blocks for Enantiospecific Total Syntheses of Cyclopentanoid Natural Products. *Angewandte Chemie International Edition* **1982**, *21*, 820–836.

(61) Hoffmann, N. Photochemical Reactions as Key Steps in Organic Synthesis. *Chem. Rev.* **2008**, *108* (3), 1052–1103.

(62) Zimmerman, H. E.; Grunewald, G. L. The Chemistry of Barrelene. III. A Unique Photoisomerization to Semibullvalene. *Journal of the American Chemical Society*. 1966, pp 183–184. https://doi.org/10.1021/ja00953a045.

(63) Frutos, L. M.; Sancho, U.; Castaño, O. Triplet versus Singlet Photoreaction Mechanism in the Barrelene Di-π-Methane Rearrangement. *Org Lett* **2004**, *6* (8), 1229–1231. https://doi.org/10.1021/ol049977p.

(64) Ihmels, H.; Mohrschladt, C. J.; Grimme, J. W.; Quast, H. Regioselectivity of the Di-p-Methane Rearrangements of 1,4-Dialkoxy-9,10- Bis(Methoxycarbonyl)Dibenzobarrelenes in Solution and in the Solid State. *Synthesis (Stuttg)* **2001**, No. 8, 1175–1180.

(65) Benitez, M.; Bringmann, G.; Dreyer, M.; Garcia, H.; Ihmels, H.; Waidelich, M.; Wissel, K. Erratum: Design of a Chiral Mesoporous Silica and Its Application as a Host for Stereoselective Di-π-Methane Rearrangements (Journal of Organic Chemistry (2005) 70 (2318)). *Journal of Organic Chemistry* **2005**, *70* (13), 5350. https://doi.org/10.1021/jo056026w.

(66) Lin, S. Y.; Hsieh, H. P.; Peddinti, R. K.; Liao, C. C. Substituent Effects on Di-π-Methane and Aza-Di-π-Methane Rearrangements of Dibenzo[f,h]Quinoxalinobarrelenes. *Tetrahedron Lett* **2003**, *44* (49), 8761–8764. https://doi.org/10.1016/j.tetlet.2003.09.200.

(67) Schlosser, J.; Cibulka, R.; Groß, P.; Ihmels, H.; Mohrschladt, C. J. Visible-Light-Induced Di-π-Methane Rearrangement of Dibenzobarrelene Derivatives. *ChemPhotoChem* **2020**, *4* (2), 132–137. https://doi.org/10.1002/cptc.201900221.

(68) Garcia-Garibay, M.; Scheffer, J. R.; Trotter, J.; Wireko, F. Determination of the Absolute Steric Course of a Solid-State Photorearrangement by Anomalous Dispersion X-Ray Crystallography. *J Am Chem Soc* **1989**, *111* (13), 4985–4986. https://doi.org/10.1021/ja00195a066.

(69) Scheffer, J. R.; Trotter, J.; Garcia-garibay, M.; Wireko, F. Studies on the Di-π-Methane Photorearrangement in the Solid State. *Molecular Crystals and Liquid Crystals Incorporating Nonlinear Optics* **1988**, *156* (1), 63–84. https://doi.org/10.1080/00268948808070556.

(70) Bruce, M.; Papke, M.; Ehlers, A. W.; Weber, M.; Lentz, D.; Mézailles, N.; Slootweg, J. C.; Müller, C. Pyridyl-Functionalized 1-Phosphabarrelene: Synthesis, Coordination Chemistry and Photochemical Di-π-Methane Rearrangement. *Chemistry - A European Journal* **2019**, *25* (63), 14332–14340. https://doi.org/10.1002/chem.201903344.

(71) S. Hammond, G.; S. Cole, R. Asymmetric Induction during Energy Transfer. *J Am Chem Soc* **1965**, *87* (14), 3256–3257. https://doi.org/10.1021/ja01092a052.

(72) S. Drucker, C.; G. Toscano, V.; G. Weiss, R. General Method for the Determination of Steric Effects during Collisional Energy Transfer. Partial Photoresolution of Penta-2,3-Diene. *J Am Chem Soc* **1973**, *95* (19), 6482–6484. https://doi.org/10.1021/ja00800a071.

(73) Ouannes, C.; Beugelmans, R.; Roussi, G. Asymmetric Induction during Transfer of Triplet Energy. *J Am Chem Soc* **1973**, *95* (25), 8472–8474. https://doi.org/10.1021/ja00806a059.

(74) Inoue, Y.; Kunitomi, Y.; Takamuku, S.; Sakurai, H. Asymmetric Cis-Trans Photoisomerization of Cyclo -Octene Sensitized by Chiral Aromatic Esters. *J. Chem. Soc., Chem. Commun.* **1978**, No. 23, 1024–1025. https://doi.org/DOI https://doi.org/10.1039/C39780001024.

(75) Gudmundsdottir, A. D.; Scheffer, J. R.; Trotter, J. Ionic Chiral Handle-Induced Solid State Asymmetric Synthesis: Origin of the Asymmetric Induction Elucidated through Absolute Configuration Correlation Studies. *Tetrahedron Lett* **1994**, *35* (9), 1397–1400. https://doi.org/10.1016/S0040-4039(00)76228-9.

(76) Gamlin, J. N.; Jones, R.; Leibovitch, M.; Patrick, B.; Scheffer, J. R.; Trotter, J. The Ionic Auxiliary Concept in Solid State Organic Photochemistry. *Acc Chem Res* **1996**, *29* (4), 203–209. https://doi.org/10.1021/ar950165q.

(77) Ding, J.; Desikan, V.; Han, X.; Xiao, T. L.; Ding, R.; Jenks, W. S.; Armstrong, D. W. Use of Chiral Ionic Liquids as Solvents for the Enantioselective Photoisomerization of Dibenzobicyclo[2.2.2]Octatrienes. *Org Lett* **2005**, *7* (2), 335–337. https://doi.org/10.1021/ol047599i.

(78) Inoue, Y.; Dong, F.; Yamamoto, K.; Tong, L.-H.; Tsuneishi, H.; Hakushi, T.; Tai, A. Inclusion-Enhanced Optical Yield and E/Z Ratio in Enantiodifferentiating Photoisomerization of Cyclooctene Included and Sensitized by .Beta.-Cyclodextrin Monobenzoate. *J Am Chem Soc* **1995**, *117* (44), 11033–11034. https://doi.org/10.1021/ja00149a037.

(79) Leibovitch, M.; Olovsson, G.; Scheffer, J. R.; Trotter, J. An Investigation of the Yang Photocyclization Reaction in the Solid State: Asymmetric Induction Studies and Crystal Structure-Reactivity Relationships. *J Am Chem Soc* **1998**, *120* (49), 12755–12769. https://doi.org/10.1021/JA9823013/ASSET/IMAGES/LARGE/JA9823013F00002.JPEG.

(80) Weiss, R. G.; Ramamurthy, V.; Hammond, G. S. Photochemistry in Organized and Confining Media: A Model. *Acc Chem Res* **1993**, *26* (10), 530–536. https://doi.org/10.1021/ar00034a003.

(81) Cheung, E.; Netherton, M. R.; Scheffer, J. R.; Trotter, J. In the Footsteps of Pasteur: Asymmetric Induction in the Solid-State Photochemistry of Ammonium Carboxylate Salts. *J Am Chem Soc* **1999**, *121* (12), 2919–2920. https://doi.org/10.1021/JA9834327/ASSET/IMAGES/LARGE/JA9834327F00002.JPEG.

(82) Chong, K. C. W.; Sivaguru, J.; Shichi, T.; Yoshimi, Y.; Ramamurthy, V.; Scheffer, J. R. Use of Chirally Modified Zeolites and Crystals in Photochemical Asymmetric Synthesis. *J Am Chem Soc* **2002**, *124* (12), 2858–2859. https://doi.org/10.1021/JA016989M/SUPPL_FILE/JA016989M_S1.PDF.

(83) Tröster, A.; Bauer, A.; Jandl, C.; Bach, T. Enantioselective Visible-Light-Mediated Formation of 3-Cyclopropylquinolones by Triplet-Sensitized Deracemization. *Angewandte Chemie - International Edition* **2019**, *58* (11), 3538–3541. https://doi.org/10.1002/anie.201814193.

(84) Uppili, S.; Ramamurthy, V. Enhanced Enantio- and Diastereoselectivities via Confinement: Photorearrangement of 2,4-Cyclohexadienones Included in Zeolites. *Org Lett* **2002**, *4* (1), 87–90. https://doi.org/10.1021/ol010245w.

(85) Cauble, D. F.; Lynch, V.; Krische, M. J. Studies on the Enantioselective Catalysis of Photochemically Promoted Transformations: "Sensitizing Receptors" as Chiral Catalysts. *Journal of Organic Chemistry* **2003**, *68* (1), 15–21. https://doi.org/10.1021/jo020630e.

(86) Yoon, T. P. Photochemical Stereocontrol Using Tandem Photoredox-Chiral Lewis Acid Catalysis. *Acc Chem Res* **2016**, *49* (10), 2307–2315. https://doi.org/10.1021/acs.accounts.6b00280.

(87) Maturi, M. M.; Wenninger, M.; Alonso, R.; Bauer, A.; Pöthig, A.; Riedle, E.; Bach, T. Intramolecular [2+2] Photocycloaddition of 3- and 4-(but-3-Enyl) Oxyquinolones: Influence of the Alkene Substitution Pattern, Photophysical Studies, and Enantioselective Catalysis by a Chiral Sensitizer. *Chemistry - A European Journal* **2013**, *19* (23), 7461–7472. https://doi.org/10.1002/chem.201300203.

(88) Chapman, S. J.; Swords, W. B.; Le, C. M.; Guzei, I. A.; Toste, F. D.; Yoon, T. P. Cooperative Stereoinduction in Asymmetric Photocatalysis. *J Am Chem Soc* **2022**, *144* (9), 4206–4213. https://doi.org/10.1021/JACS.2C00063/ASSET/IMAGES/LARGE/JA2C00063_0004.JPEG.

(89) Girvin, Z. C.; Cotter, L. F.; Yoon, H.; Chapman, S. J.; Mayer, J. M.; Yoon, T. P.; Miller, S. J. Asymmetric Photochemical [2 + 2]-Cycloaddition of Acyclic Vinylpyridines through Ternary Complex Formation and an Uncontrolled Sensitization Mechanism. *J Am Chem Soc* **2022**, *2022*. https://doi.org/10.1021/JACS.2C09690/ASSET/IMAGES/LARGE/JA2C09690_0005.JPEG.

(90) Lowry, M. S.; Goldsmith, J. I.; Slinker, J. D.; Rohl, R.; Pascal, R. A.; Malliaras, G. G.; Bernhard, S. Single-Layer Electroluminescent Devices and Photoinduced Hydrogen Production from an

Ionic Iridium(III) Complex. *Chemistry of Materials* **2005**, *17* (23), 5712–5719. https://doi.org/10.1021/cm051312+.

(91) Sherbrook, E. M.; Genzink, M. J.; Park, B.; Guzei, I. A.; Baik, M. H.; Yoon, T. P. Chiral Brønsted Acid-Controlled Intermolecular Asymmetric [2 + 2] Photocycloadditions. *Nat Commun* **2021**, *12* (1), 1–7. https://doi.org/10.1038/s41467-021-25878-9.

(92) Duerr, B. F.; Chung, Y. S.; Czarnik, A. W. Syntheses of 9,10-Disubstituted Anthracenes Derived from 9,10-Dilithioanthracene. *Journal of Organic Chemistry* **1988**, *53* (9), 2120–2122. https://doi.org/10.1021/JO00244A056/SUPPL_FILE/JO00244A056_SI_001.PDF.

(93) Fruziński, A.; Karolak-Wojciechowska, J.; Alibert-Franco, S.; Santelli-Rouvier, C.; Barbe, J. Synthesis and X-Ray Structure of 11-N-Benzylamido-9,10-Dihydro-9,10-Ethenoanthracene. *Journal of Chemical Crystallography 1999 29:11* **1999**, *29* (11), 1201–1204. https://doi.org/10.1023/A:1009507701327.

(94) Cristol, S. J.; Schloemer, G. C.; James, D. R.; Paquette, L. A. Rearrangements Attending Attempts to Form the 1-Dibenzosemibullvalenylcarbinyl (1-Dibenzotricyclo[3.3.0.02,8]Octadienylcarbinyl) Cation. *Journal of Organic Chemistry* **1972**, *37* (24), 3852–3856. https://doi.org/10.1021/jo00797a019.

(95) Paquette, L. A.; Meehan, G. v. Mechanistic Features of the Base-Induced Decomposition of Dibenzosemibullvalene 1-Carboxaldehyde Tosylhydrazone. *J Am Chem Soc* **1970**, *92* (10), 3039–3044. https://doi.org/10.1021/JA00713A020/ASSET/JA00713A020.FP.PNG_V03.

Chapter 3 Development of Novel Cation Binding Photocatalysts and Applications Towards Diels-Alder Catalysis

3.1 Abstract

Novel photocatalysts capable of coordinating Lewis acidic moieties in solution were designed and their reactivity towards [2+2] cycloaddition and Diels-Alder reactions in the presence of Lewis acids was studied. Principles related to catalyst structure and stability relationships in strongly Lewis acidic conditions were established. While interesting catalytic activity in a model Diels-Alder reaction was discovered for catalysts with Lewis basic cyclometalated ligands when in the presence of mild Lewis acids, the source of this reactivity was difficult to deconvolute from background catalysis by the Lewis acid alone. Experiments probing the photophysical effects of catalyst-Lewis acid coordination on the photocatalyst excited state are also presented.

3.2 Background

Controlling the selectivity and expanding the reaction scope of photochemical reactions has been a primary focus of the Yoon group for many years. We have recognized that many of the advances in this field have stemmed from a fundamental advance in catalyst systems. Examples of such advances include the development of co-catalytic strategies that enable activation of substrates via coordination of exogenous Lewis acids and the development of novel chiral-at-metal hydrogen-bonding iridium photocatalysts capable of selective SET and EnT.[96–98] The successful development of these new systems hinged on the

development of new catalysts or the application of traditional catalysts to novel methods for substrate activation in photochemical systems.

The discovery of new catalytic systems has been a driving force for the development of novel synthetic methods for decades. Our fundamental understanding of catalyst structures, modes of activation, and design principles has led to the successful development of industrial and synthetic processes that benefit our world in profound ways. The field of catalysis has developed and found applications in so many different disciplines and systems as to preclude a comprehensive presentation of the subject. However, the general principles that guide the development of new catalytic systems generally fall into two categories: electronic and spatial activation.

The modes by which a given catalyst operates under one or both of the aforementioned categories are nearly as diverse as the systems to which they have been applied. This is a tribute to the flexibility of catalysis as well as to the creativity of the chemists who seek to utilize and understand it. Despite the vast amount of research that has already been performed in this area, development of new catalytic systems and the study of their respective mechanisms continues to be a prominent field of work for the modern chemistry research community.

Significant amounts of work have been applied to the field of design of photoactive organic and metal-based frameworks for OLED and light harvesting technologies, and the principles governing their optoelectronic properties are well understood.[99–102] Data presented in these studies is primarily centered around tuning the emission wavelengths, intensities, and efficiencies of a given system. This wealth of knowledge can be useful when designing catalysts for synthetic use as the emission wavelength of a catalyst is directly correlated to its excited state triplet energy. Many studies also report the electrochemical characterization of said chromophores, necessary for the calculation of excited state redox potentials.

There are still challenges that must be considered when designing new chromophores for photocatalysis, however. In the case of metal-based chromophores, subtle substitutions on the ligand structure can have profound effects on the photophysical properties of the active catalyst. Trends relating these substitutions to catalyst triplet energy are relatively well understood. On the other hand, tuning the excited state redox potentials of these chromophores is less straightforward. Perturbations in ligand structure that lead to an increased triplet energy do not always correlate to a decrease in the ground state reduction potential, and thus do not necessarily lead to an increased excited state oxidation potential.[10] Development of catalysts with finely tuned excited state redox potentials often requires extensive trial-and-

error based synthetic efforts that are both expensive and time-consuming. Many current studies rely on applications of known libraries of photocatalyst structures.

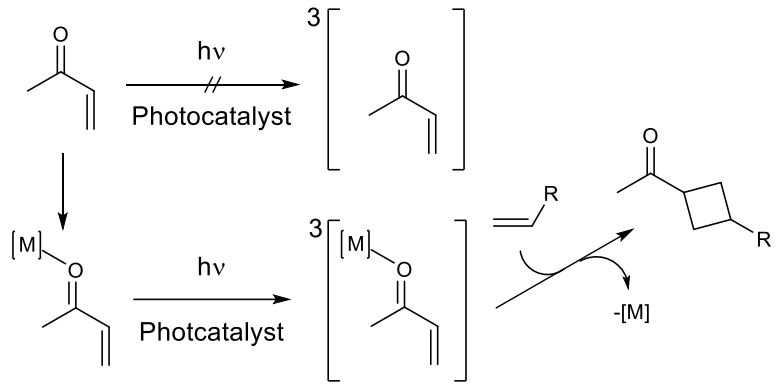

Figure 3.1

As mentioned above, the Yoon lab has previously reported methods in which substrates with Lewis basic moieties were activated towards triplet sensitization or electron transfer events through the coordination of Lewis acids.[97,103] Coordination of a Lewis acid catalyst in solution led to a shift in the electronic structure of the substrate that facilitated activation by the photocatalyst. In the case of energy transfer reactions, coordination of a Lewis acid resulted in a decrease in the triplet energy of the substrate, allowing for facile energy transfer from the photocatalyst, (Figure 3.1). This method has since been developed to include enantioselective variants. Selective activation of substrate in the presence of Lewis acid allowed us to ensure that the substrate would react in close proximity to an enantioenriched controller. This

dual catalytic strategy has become one of the premier strategies for the development of enantioselective energy transfer reaction methods.[15]

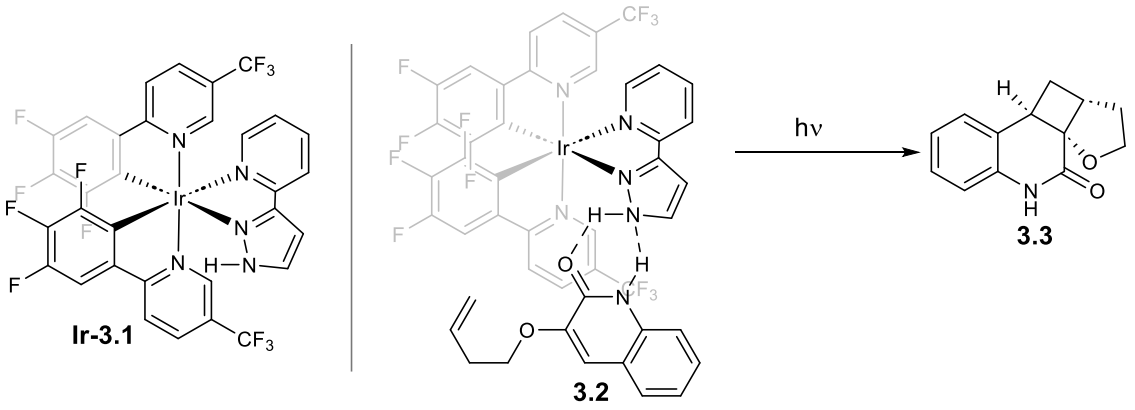

Figure 3.2

The Yoon group has also recently reported a system in which a chiral photocatalyst, **Ir-3.1**, is used as a hydrogen bond donor to activate a variety of quinolones in an enantioenriched space, (Figure 3.2).[96] The excellent enantioselectivities obtained in this system support our assertion that substrates were only activated when coordinated to the catalyst. We believe that hydrogen bonding could lead to activation of substrate through both electronic effects and spatial preorganization. Other groups have employed similar approaches; notably, Meggers and coworkers have reported the use of chiral-at-metal iridium complexes to afford a range of radical addition products with high enantioselectivities.[104,105]

At the outset of this project, we recognized a potential gap in the field's development of photocatalyst systems. Catalytic methods disclosed to date, like those discussed above, seemed to take advantage of either electronic activation by Lewis acid catalysis or spatial activation by weak intermolecular coordination, but rarely both. Additionally, the potential application of photocatalysts acting as Lewis bases was comparatively underdeveloped relative to the study of Lewis acidic systems. Furthermore, there had been to date several systems developed by Doyle, Macmillan, Molander and others that had introduced the utility of cooperative transition metal mediated reactivity with photocatalysis.[13,34,41,106–109] With the increasing popularity of such methods, we imagined that investigation of a system in which a photocatalyst was spatially tethered to other transition metal catalysts in solution could prove valuable to our understanding of the relationship between the two catalytic cycles operative in those reactions. We envisioned that an avenue to begin investigating each of these points could stem from development of a catalyst-ligand structure with distal Lewis basic binding sites capable of coordination to exogenous metals.

Our initial goal to begin this investigation was to investigate the effects of Lewis acid coordination on the electronic environment and excited state properties of the photocatalyst metal center. We reasoned that the effects of Lewis acid activation for organic substrates was relatively well understood, and that by

expanding our understanding of the effects of coordination on the photocatalyst we would be able to devise systems to study the joint effects of spatial and electronic activation.

We began by considering the data present in the few systems in which a photocatalyst had been employed in a Lewis basic interaction. In particular, one set of studies among this group, reported by Akita and coworkers, presented data that seemed relevant to our goal of understanding the general effects of metal coordination on the electronic structure of a photocatalyst.

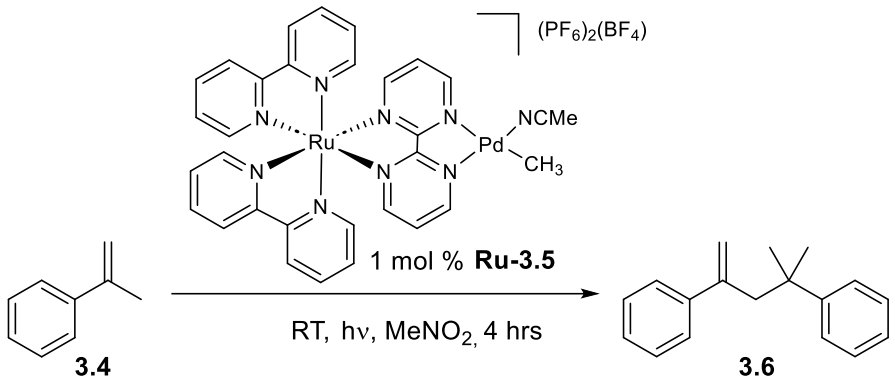

Figure 3.3

Akita developed a system in which he used a bipyrimidine (bpm) ligand to coordinate a second metal center following the synthesis of a metal-based photocatalyst, **Ru-3.5**. Akita has employed this strategy to create both ruthenium and iridium based photocatalysts bound to palladium and platinum metal centers to create heterobimetallic, light harvesting complexes.[110,111] In the case of his palladium complexes, Akita has developed catalytic methods for dimerization and polymerization of various styrene derivates, an

example of which is shown in Figure 3.3.[110,112–114] These reactions have been shown to occur primarily through activation of the palladium center through an energy transfer process proceeding through the bridging bpm ligand.[115,116] Preformation of the catalyst has been shown to be important to reactivity, as separate addition of the palladium and chromophore precursors did not result in formation of product. It is important to note that this reaction depends on the reactivity of photo-activated palladium. Inagaki and coworkers have shown that similar reactivity can be duplicated with light harvesting BINAP moieties coordinated to the reactive palladium center, rather than the iridium or ruthenium chromophores used by Akita.[117]

The characterization data presented by Akita for a derivative of **Ru-3.5** with 2,2-dimethyl substitution on the bpm ligand was of special interest to our own studies. Upon coordination to palladium, the reduction potentials of the photocatalyst underwent a sizable positive shift of approximately 500 mV. The emission profile of the catalyst was not significantly affected, however.[112] These data show that coordination of palladium through bpm resulted in a ruthenium center that would be 500 mV more oxidizing in its excited triplet state than the uncoordinated complex.

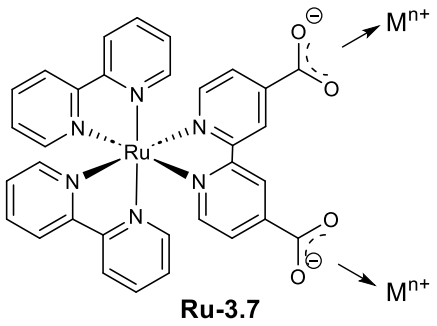

Ru-3.7

Figure 3.4

We were also informed by studies reported by Meyer and coworkers, where their lab used pendant carboxylate moieties on the bipyridine ligands of a ruthenium photocatalyst to bind a variety of cations in solution, (Figure 3.4).[118] They were able to show that adding Lewis acids to species like **Ru-3.7** had profound effects on the emission spectra of the studied catalysts. They did not report the electrochemical data necessary to allow us to characterize the potential effects of this interaction on the excited state redox potentials of the ruthenium catalyst, however.

Given these precedents, we envisioned that with certain ligands it may be possible to tune the photoredox potentials of a photocatalyst through coordination of a range of Lewis acids. Our goal was to characterize these effects and to find a reaction system in which Lewis acid coordination would effect an observable change in catalyst reactivity. We envisioned that success in this area would lead to an increased understanding of how photocatalysts respond to exogenous metal coordination and the development of reaction design principles to study cooperative catalytic systems.

3.3 Development and characterization of catalysts with bipyrimidine ligands and application to [2+2] photocycloaddition reactions

Catalyst design was first approached using bipyrimidine ligands, similar to the systems developed by Akita and coworkers. Both ruthenium, **Ru-3.8**, and iridium, **Ir-3.9**, complexes bearing these ligands were synthesized and the effects of Lewis acid coordination were investigated, Figure 3.5a.

Cyclic voltammetry experiments were performed in the presence of a variety of Lewis acids to examine coordination effects on catalyst redox potentials. Unfortunately, CV traces performed on solutions containing a mixture of the photocatalyst and Lewis acid revealed a loss of reversible redox behavior usually characteristic to these catalyst structures. Interestingly, a ruthenium bipyrazine (bpz) catalyst, with a ligand structure we expected to coordinate other Lewis acids less tightly than bpm, showed the same irreversible redox behavior in the presence of Lewis acids, see Supporting Information.

A model [2+2] reaction was used to gauge catalyst activity for **Ir-3.9**, Figure 3.3b. Significant inhibition of reaction efficiency was observed when the reaction was performed in the presence of even relatively mild Lewis acids, entries 1–5. In contrast, experiments performed with a similar iridium photocatalyst (**Ir-3.12**), bearing a non-Lewis acid coordinating dtbbpy ligand in place of bpm, revealed an enhancement of the reaction rate under analogous conditions, entries 7 and 8.

A)

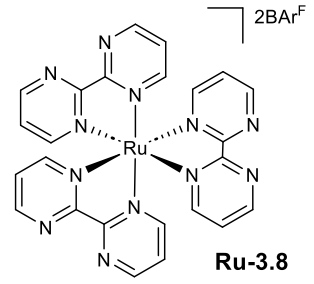

Ru-3.8

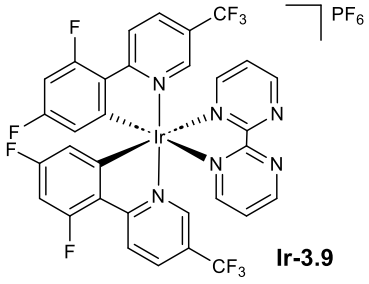

Ir-3.9

B)

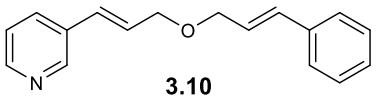

3.10

2% Cat, 50% Additive

0.05M in DCM, CFL

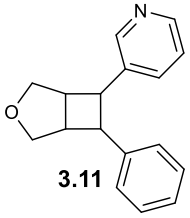

3.11

Entry	Catalyst	Additive	Time	Conversion
1	**Ir-3.9**	-	24	33%
2	**Ir-3.9**	$Sc(OTf)_3$	24	11%
3	**Ir-3.9**	$Mg(OTf)_2$	24	7%
4	**Ir-3.9**	$Zn(OTf)_2$	24	7%
5	**Ir-3.9**	$(CH_3CN)_4CuOTf$	24	11%
6	**Ir-3.12**	-	24	100%
7	**Ir-3.12**	-	1	42%
8	**Ir-3.12**	$Sc(OTf)_3$	1	58%

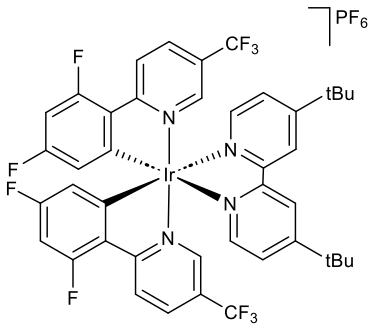

Ir-3.12

Figure 3.5

These studies led us to conclude that the photocatalysts we had synthesized were not stable to highly Lewis acidic conditions. This can be rationalized when considering the relative lability of the bpm ligand and its propensity to preferentially bind to the strongly Lewis acidic species employed in our measurements. Although Akita had previously shown that similar bpm bearing complexes were stable in the presence of metal centers with comparable Lewis acidities to iridium, such as palladium, the goal of our

study was to expand these limits. This led us to examine ligand structures that were expected to be more robust under the desired conditions.

3.4 Development and characterization of catalysts with Lewis basic cyclometalated ligands and application to Diels-Alder photocatalysis

We envisioned that inclusion of the Lewis basic binding moiety on the cyclometalated ligand of an iridium complex would allow us to overcome the complications associated with competitive ligand coordination observed in the bpm complexes. Careful choice of the ligand proved to be necessary for successful synthesis of the iridium complex, as poorly defined mixtures of homoleptic and heteroleptic complexes were obtained from heating iridium chloride with simple pyridyl pyrimidines. Examination of complexes developed for OLED applications, however, led to us to believe that the 2-(2,4-difluorophenyl)-3-methylpyrazine, DFMPPZ, ligand could be used to make a photochemically viable iridium complex. These efforts led to the successful synthesis of **Ir-3.13**.

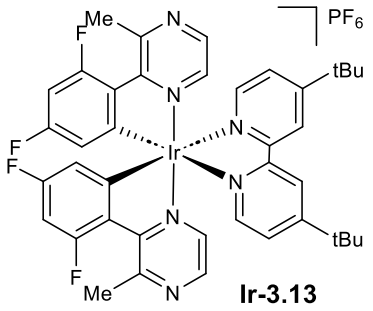

Ir-3.13

Figure 3.6

Initial characterization of the excited state properties of **Ir-3.13** led us to believe that it would be a viable catalyst for a [4+2] Diels-Alder cycloaddition recently developed by our lab.[119,120] Surprisingly, no reaction was observed when the catalyst was irradiated in the presence of trans-anethol (**3.14**) and isoprene (**3.15**), Figure 3.7 entry 1. Inclusion of a variety of Lewis acids, however, served to turn on reactivity. Some Bronsted acids also proved to be viable activators for this reaction, entry 13. The photoactivity of some of these Lewis acids, even in the absence of iridium catalyst, proved to be a complicating factor in this analysis, entries 6 and 8. The Lewis acid activation effect was also general to additives that were otherwise inert, however, with zinc salts being notable for a lack of other expected reactivity, entry 10. The use of stronger Lewis acids, such as scandium and lanthanum triflates, could not be evaluated under these reaction conditions due to the facile polymerization of trans-anethole in the presence of acid.

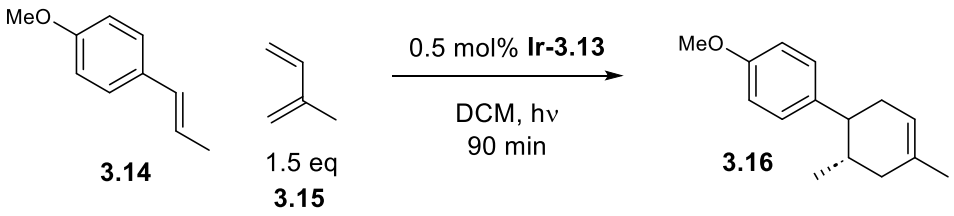

Entry	Catalyst	Additive	Light	RSM	Yield
1	**Ir-3.13**	-	Blue LED	98%	0%
2	**Ir-3.13**	$Ni(OTf)_2$	Blue LED	0%	96%
3	**Ir-3.13**	$Cu(TFA)_2 \cdot H_2O$	Blue LED	0%	90%
4	None	$Cu(TFA)_2 \cdot H_2O$	Blue LED	77%	4%
5	**Ir-3.13**	$Cu(ClO_4)_2$	Blue LED	3%	92%
6	None	$Cu(ClO_4)_2$	None	17%	40%
7	**Ir-3.13**	$Mg(ClO_4)_2$	Blue LED	4%	80%
8	None	$Mg(ClO_4)_2$	None	41%	41%
9	**Ir-3.13**	$Zn(TFA)_2 \cdot H_2O$	Blue LED	0%	84%
10	None	$Zn(TFA)_2 \cdot H_2O$	Blue LED	60%	2%
11	**Ir-3.13**	$Zn(TFA)_2 \cdot H_2O$	None	79%	0%
12	**Ir-3.13**	$Zn(OTf)_2$	Blue LED	0%	99%
13	**Ir-3.13**	TFA	Blue LED	0%	74%
14	**Ir-3.13**	$Cu(OBz)_2$	Blue LED	60%	4%
15	**Ir-3.13**	$TiCl_4$	Blue LED	0%	0%
16	**Ir-3.13**	$BF_3 \cdot Et_2O$	Blue LED	0%	0%
17	**Ir-3.13**	TBAOTf	Blue LED, 3 hr	80%	20%

Figure 3.7

Characterization of the photocatalyst excited state in the presence of zinc Lewis acids failed to produce a measurable effect, though the conditions required for these techniques could present complications to the analysis. No shift in the excited state emission was observed on addition of zinc salts, though apparent quenching of the excited state was observed. This apparent quenching might also be

attributed to the low solubility of these Lewis acids in most solvents and the presence of an inner filter effect. The UV-Vis absorption profile for the catalyst was also apparently unaffected by the presence of Lewis acids. Attempts to characterize any changes in ground state redox potentials were also inconclusive. No change was observed in the presence of zinc triflate salts, though this could again be attributed to low solubility of the salt in DCM. Zinc trifluoroacetate salts are more soluble, but are also incredibly hygroscopic, and inclusion of these salts led to observation of poorly defined redox peaks that precluded characterization. We were also cognizant of the fact that CV measurements are performed in the presence of excess electrolyte, which could inhibit or outcompete the weak binding interactions expected between the catalyst and mild Lewis acids. We did not believe that the catalyst was degrading upon addition of zinc salts, however, due to its consistent competence under reaction conditions. Additionally, a light dark experiment performed on the reaction revealed a constant conversion rate across irradiation periods, Figure 3.8. The results of these characterization experiments are included in the Supporting Information section of this chapter.

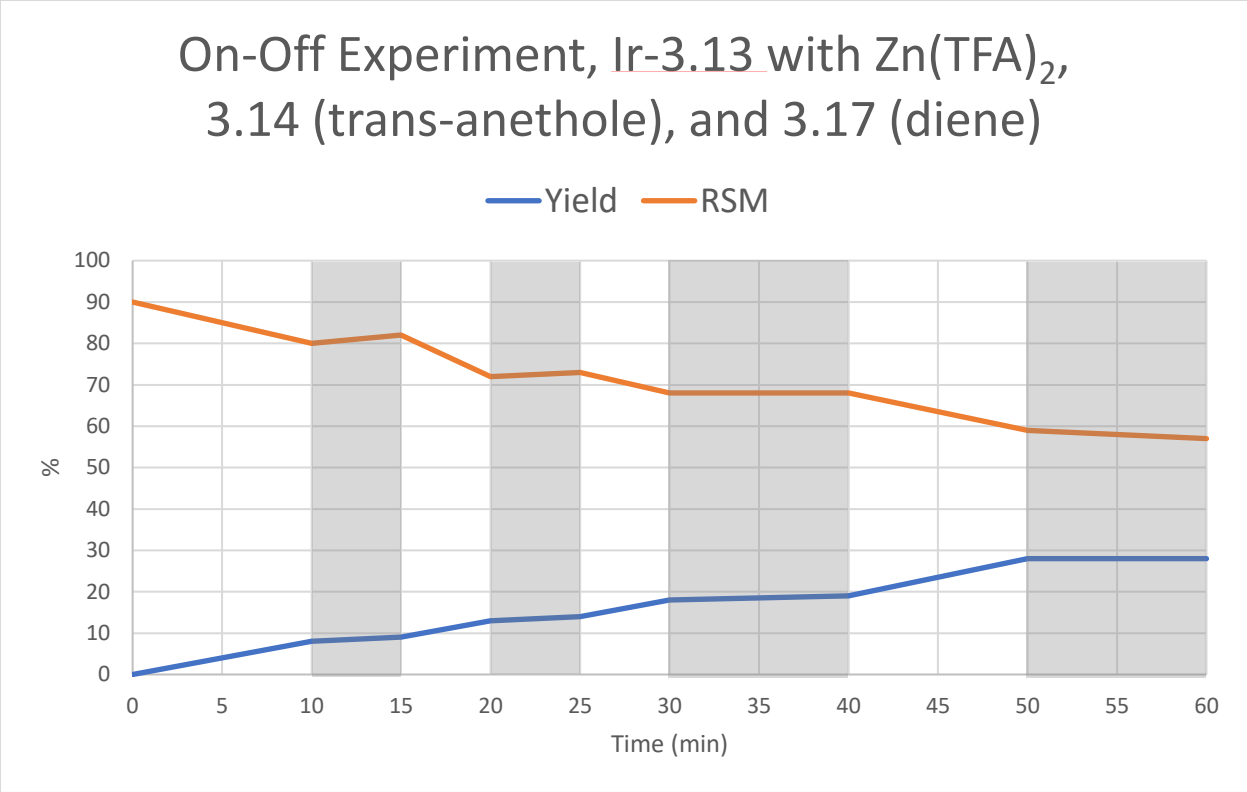

Figure 3.8

We next attempted to examine the effects of Lewis acid on the quenching event through Stern-Volmer quenching studies. Unfortunately, these studies also proved to be inconclusive, with no major difference in apparent quenching rate observed between the two samples, see Supporting Information. Preliminary catalyst lifetime measurements, performed by Dr. Wesley Swords, seemed to indicate that there was a minor decrease in catalyst lifetime in the presence of zinc salts. Accounting for this change would lead to a mildly increased quenching rate in the presence of zinc, though not enough to fully explain the

observed difference in reactivity. Unfortunately, the primary data for those lifetime measurements were lost in the failure of a data backup system.

Quantum yield analysis would most likely have been the most appropriate photochemical characterization experiment to approach next, however at this point in our analysis we returned to the careful examination of important control reactions for our observed reaction enhancement. Initial screening had been exclusively conducted using isoprene as a coupling partner. During the investigation of a possible scope for this reaction, included in the Supporting Information, it was found that this catalyst system reacted more readily with 2,4-dimethyl-1,4-butadiene (**3.17**), with some conversion observed even in the absence of Lewis acid despite the overall slower reaction rate, Figure 3.9. Attempts using the standard conditions with isoprene (**3.15)** to compare the cooperative effects of Lewis acids on the reaction of photocatalysts without a potential Lewis acid binding site had been complicated by either complete lack of reactivity for the catalysts examined or by the reaction proceeding too quickly to observe rate enhancement. Switching to **3.17**, however, allowed us to make an effective comparison of reaction rates for our catalyst (**Ir-3.13**) and a representative non-binding catalyst (**Ir-3.12**). Unfortunately, while rate enhancement for Lewis acid additives in the presence **Ir-3.12** was not as stark in all cases as for **Ir-3.13**, the activation effects were not exclusive to our new system.

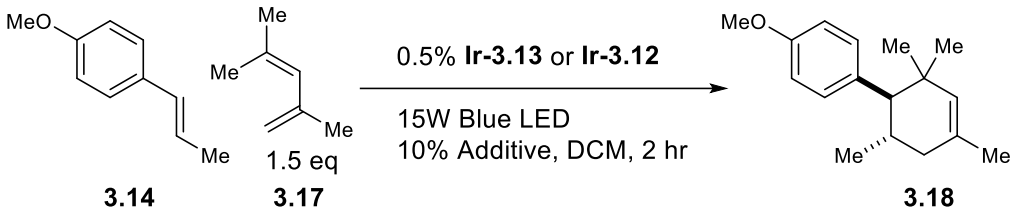

3.14 **3.17** **3.18**

		Ir-3.13		**Ir-3.12**	
Entry	Additive	Yield	RSM	Yield	RSM
1	-	33%	46%	10%	82%
2	$Mg(OTf)_2$	37%	49%	-	-
3	$Ni(OTf)_2$	69%	17%	80%	18%
4	$Cu(OTf)_2$	8%	50%	-	-
5	$Cu(TFA)_2 \cdot H_2O$	93%	0%	92%	0%
6	$Zn(TFA)_2 \cdot H_2O$	94%	0%	55%	35%
7	$Zn(OTf)_2$	38%	54%	-	-

Figure 3.9

3.5 Conclusion

Combined consideration of the physical characterization data and the newly obtained reaction controls led us to reconsider whether there was any significant effect of the Lewis basic ligand on the observed reaction phenomenon. Indeed, if there is an effect, it is likely minor and would be difficult to deconvolute from the general, well-established Lewis acid catalysis of Diels-Alder reactions. At this point, other projects in development required increased levels of attention and this investigation was paused for later reevaluation.

3.6 Supporting information

3.6.1 General Information

$Ru(bpm)_3(BArF)_2$,[121] $Ru(bpz)_3(BArF)_2$,[122] $Ir(dF(CF_3)ppy)_2(dtbbpy)PF_6$,[10] and the DFMMPPZ ligand[123] were synthesized by previously reported procedures. Dienes used in photoreactions were distilled prior to use. Trans-anethole was passed through silica and alumina plugs neat to remove inhibitor; purity was checked via NMR before use. All other commercially available chemicals were used as purchased from Sigma Aldrich or Oakwood Chemical unless otherwise specified. Acetonitrile (MeCN) and dichloromethane (CH_2Cl_2) were purified by elution through alumina and stored under argon.

A 23 W (1200 lumens) SLI Lighting Mini-Lynx compact fluorescent light bulb or a Parr 38 16 W 450 nm blue LED was used for all photochemical reactions unless otherwise stated.

Flash column chromatography was performed with Silicycle 40-63Å silica (230- 400 mesh).

Yields for all photocatalytic reactions were determined by ^1H NMR analysis of the unpurified reaction mixture. ^1H data for all previously uncharacterized compounds were obtained using Varian Inova-400 and Varian Unity-500 spectrometers and are referenced to TMS (0.0 ppm), unless otherwise stated. These facilities are funded by the NSF CHE-1048642 and a generous gift from Paul J. and Margaret M. Bender.

Electrochemical measurements were made using a Pine research WaveNow potentiostat/galvanostat.

UV-Visible spectra were recorded on a Varia Cary® 50 spectrophotometer at a resolution of 1 nm. Photoluminescence spectra were recorded on a Hitachi F-4500 fluorescence spectrophotometer with a 1 nm resolution.

3.6.2 Photocatalyst Synthesis

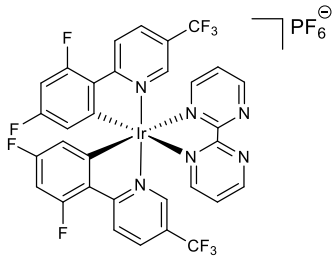

Ir(dF(CF$_3$)ppy)$_2$(bpm)PF$_6$ (**S3.1**):

The general procedure for synthesis of heteroleptic iridium complexes reported by Weaver was followed, using dF(CF$_3$)ppy as the cyclometallating ligand and bpm as the dative ligand (39%).[10]

^{1}H NMR (400 MHz, DMSO-d_6) δ 9.39 (dd, J = 4.8, 2.1 Hz, 2H), 8.51 – 8.40 (m, 4H), 8.29 (dd, J = 5.6, 2.1 Hz, 2H), 7.90 (t, J = 5.4 Hz, 2H), 7.88 (s, 2H), 7.11 (ddd, J = 11.9, 9.3, 2.4 Hz, 2H), 5.70 (dd, J = 8.4, 2.3 Hz, 2H).

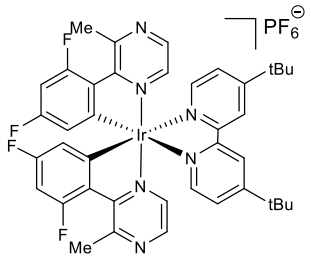

Ir(DFMPPZ)$_2$(dtbbpy)PF$_6$ (**S3.2**):

The general procedure for synthesis of heteroleptic iridium complexes reported by Weaver was followed, using DFMPPZ as the cyclometallating ligand and dtbbpy as the dative ligand.[10] The product was recrystallized from CH_2Cl_2 layered with benzene at room temperature (46%).

^{1}H NMR (400 MHz, $CDCl_3$) δ 8.48 (d, J = 1.7 Hz, 2H), 8.31 (d, J = 3.1 Hz, 2H), 7.50 – 7.43 (m, 5H), 6.62 (ddd, J = 11.6, 8.7, 2.3 Hz, 3H), 5.41 (dd, J = 8.0, 2.3 Hz, 2H), 2.84 (d, J = 11.0 Hz, 6H), 1.45 (s, 18H).

3.6.3 Intramolecular [2+2]

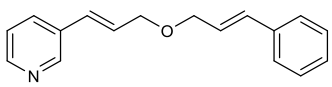

3-((E)-3-(Cinnamyloxy)prop-1-en-1-yl)pyridine (**S3.3**):

Triethyl phosphonoacetate (4 mL, 20 mmol) was dissolved in 20 mL THF and cooled to -78 °C. n-BuLi (10.2 mL, 22 mmol) was added dropwise and the mixture was stirred for 5 min. 3-Pyridinecarboxaldehyde (1.88 mL, 20 mmol) was added and the mixture was stirred for a further 5 min before warming to room temperature. The reaction mixture was stirred at room temperature for 2 h. The reaction mixture was diluted in Et_2O and then quenched with the slow addition of water. The organic layer was isolated and washed three times with water and then concentrated. The remaining oil was acidified with 10 mL 10% HCl, and then washed three times with CH_2Cl_2. The mixture was returned to a pH of 7

using sat. aq. $NaHCO_3$, and then the mixture was extracted three times with CH_2Cl_2. The combined organic layers were dried over Na_2SO_4 and concentrated by rotary evaporation to yield (1.39 g, 39%). Spectral data matched previously reported values. This product (1.30 g, 7.33 mmol) was dissolved in 20 mL of Et_2O and cooled to -30 °C. DIBAL (14.7 mL, 14.7 mmol) was added dropwise and the reaction mixture was then warmed to room temperature and stirred for 20 hrs. The reaction was diluted in Et_2O, quenched with 1mL 10% NaOH solution, and stirred for 20 min. The mixture was then filtered through a pad of celite, and concentrated. Celite filtrates were collected, washed with 10% HCl, then neutralized with $NaHCO_3$. The resulting mixture was extracted four times with CH_2Cl_2 and concentrated. The resulting combined oils were used without further purification (646 mg, 65%). A portion of this product (203 mg, 1.5 mmol) was dissolved in 1.5 mL of THF and was added dropwise to a suspension of NaH (72 mg, 1.8 mmol) in 1.5 mL of THF. The reaction mixture was cooled to 0 °C and cinnamyl bromide (326 mg, 1.65 mmol) and tetrabutyl ammonium bromide (24 mg, 0.075 mmol) in 2 mL of THF were added dropwise. The reaction mixture was warmed to room temperature and stirred for 18 h. The reaction mixture was diluted in Et_2O and quenched with sat. aq. NH_4Cl followed by water. The aqueous layer was extracted two times with Et2O, and the combined organic layers were then washed once with brine and concentrated. The resulting oil was purified by flash column chromatography using 80:20 EtOAc:Hexanes to yield 3-((E)-3-(cinnamyloxy)prop-1-en-1-yl)pyridine as a yellow oil (223 mg, 59%).

^{1}H NMR (500 MHz, $CDCl_3$) δ 8.62 (d, *J* = 2.3 Hz, 1H), 8.47 (dd, *J* = 4.8, 1.6 Hz, 1H), 7.71 (dt, *J* = 7.9, 2.0 Hz, 1H), 7.40 (d, *J* = 7.0 Hz, 2H), 7.32 (t, *J* = 7.5 Hz, 2H), 7.28 – 7.21 (m, 2H), 6.68 – 6.65 (m, 1H), 6.63 (dd, *J* = 3.2, 1.6 Hz, 1H), 6.40 (dt, *J* = 16.0, 5.7 Hz, 1H), 6.33 (dt, *J* = 15.9, 6.1 Hz, 1H), 4.23 (d, *J* = 1.5 Hz, 2H), 4.22 (d, *J* = 1.5 Hz, 2H).

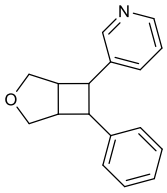

3-(7-Phenyl-3-oxabicyclo[3.2.0]heptan-6-yl)pyridine (**S3.4**):

General procedure. Photocatalyst (0.02 equiv.) and Lewis acid (0.5 equiv.), if applicable, were weighed to an oven dried Schlenk tube with a stir bar. The reaction vessel was evacuated and refilled with N_2 three times. A substrate stock solution, 0.05 M in CH_2Cl_2, (0.8 mL, 0.04 mmol) was added under a stream of N_2. The reaction mixture was degassed in a dark hood by standard freeze pump thaw with four cycles. The reaction mixture was then irradiated with a 23W CFL

at 10 cm for 24 h. The reaction flask was opened to air and the product mixture was diluted in CH_2Cl_2 and transferred to a dram vial, then concentrated. A stock solution of CH_2Br_2 in $CDCl_3$ was used to prepare NMR samples with internal standard.

^{1}H NMR (500 MHz, $CDCl_3$) δ 8.25 (d, *J* = 2.3 Hz, 1H), 8.23 (dd, *J* = 4.8, 1.6 Hz, 1H), 7.68 (dd, *J* = 4.1, 2.2 Hz, 1H), 7.18 (dt, *J* = 7.9, 2.1 Hz, 1H), 7.10 (dd, *J* = 8.1, 6.9 Hz, 2H), 7.03 – 6.99 (m, 1H), 6.97 (dd, *J* = 4.8, 0.8 Hz, 1H), 6.95 (dd, *J* = 4.9, 0.8 Hz, 1H), 6.95 – 6.91 (m, 2H), 4.12 (d, *J* = 9.5 Hz, 2H), 3.83 – 3.75 (m, 3H), 3.72 (ddd, *J* = 9.5, 5.4, 1.9 Hz, 3H), 3.33 (ddt, *J* = 40.9, 8.3, 5.2 Hz, 3H).

3.6.4 Intermolecular [2+4]

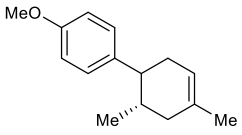

4'-methoxy-2,4-dimethyl-1,2,3,6-tetrahydro-1,1'-biphenyl (**S3.5**):

$Ir(DFMPPZ)_2(dtbbpy)PF_6$ (1.5 mg), Lewis acid (0.12 equiv.), and trans-anethole (33 mg) were weighed to a dry dram vial with a stir bar. In a dark hood was added 2 mL of CH_2Cl_2, followed by isoprene (200 μL). The reaction vessel was capped and irradiated at a distance of 10 cm. Following irradiation, phenanthrene was added as an internal standard and the resulting mixture was filtered through a silica plug with EtOAc and concentrated. NMR experiments were performed using $CDCl_3$ as the solvent. Product peaks were in agreement with previously reported values.[119]

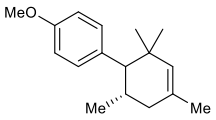

4'-methoxy-2,4-dimethyl-1,2,3,6-tetrahydro-1,1'-biphenyl (**S3.5**):

$Ir(DFMPPZ)_2(dtbbpy)PF_6$ (1.5 mg), Lewis acid (0.12 equiv.), and trans-anethole (33 mg) were weighed to a dry dram vial with a stir bar. In a dark hood was added 2 mL of CH_2Cl_2, followed by 2,4-dimethyl-1,4-butadiene (1.5 equiv). The reaction vessel was capped and irradiated at a distance of 10 cm. Following irradiation, phenanthrene was added as an internal standard and the resulting mixture was filtered through a silica plug with EtOAc and concentrated. NMR experiments were performed using $CDCl_3$ as the solvent. Product peaks were in agreement with previously reported values.[119]

3.6.5 Cyclic Voltammetry

General procedure

Samples for electrochemical analysis were prepared to be 0.1 M in electrolyte (tetrabutyl ammonium hexafluorophosphate) and 0.001 M in analyte. Solutions were prepared in MeCN unless otherwise noted in the chart annotations. CV measurements were performed using a glassy carbon working electrode, $Ag/AgNO_3$ reference electrode, and platinum wire counter electrode. Samples were prepared and sparged for at least two minutes prior to measurement to ensure exclusion of O_2. Measurements were performed at 50–100 mV/s and then ferrocene was added as an internal reference and the measurement was repeated. The glassy carbon electrode was washed and polished between sets. CV plots were corrected to SCE using ferrocene as an internal standard.

Set 1: $Ru(bpm)_3(BArF)_2$ with Lewis Acids

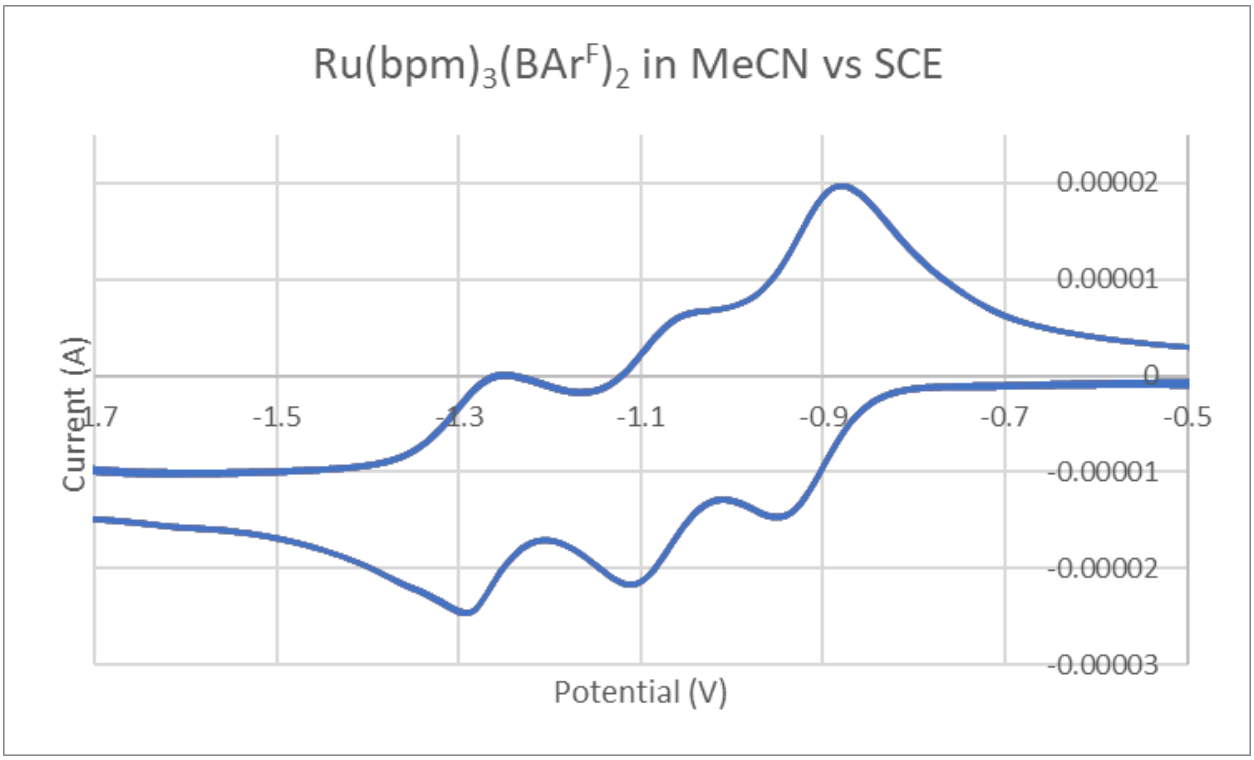

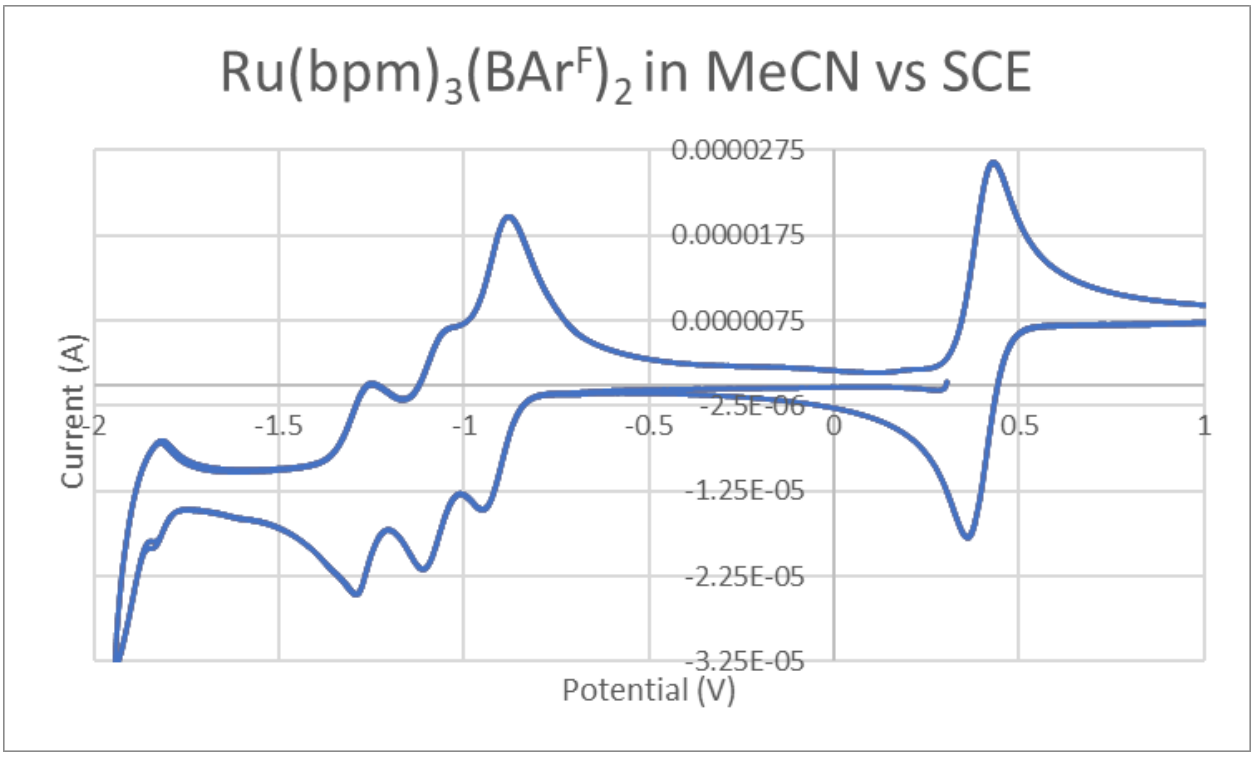

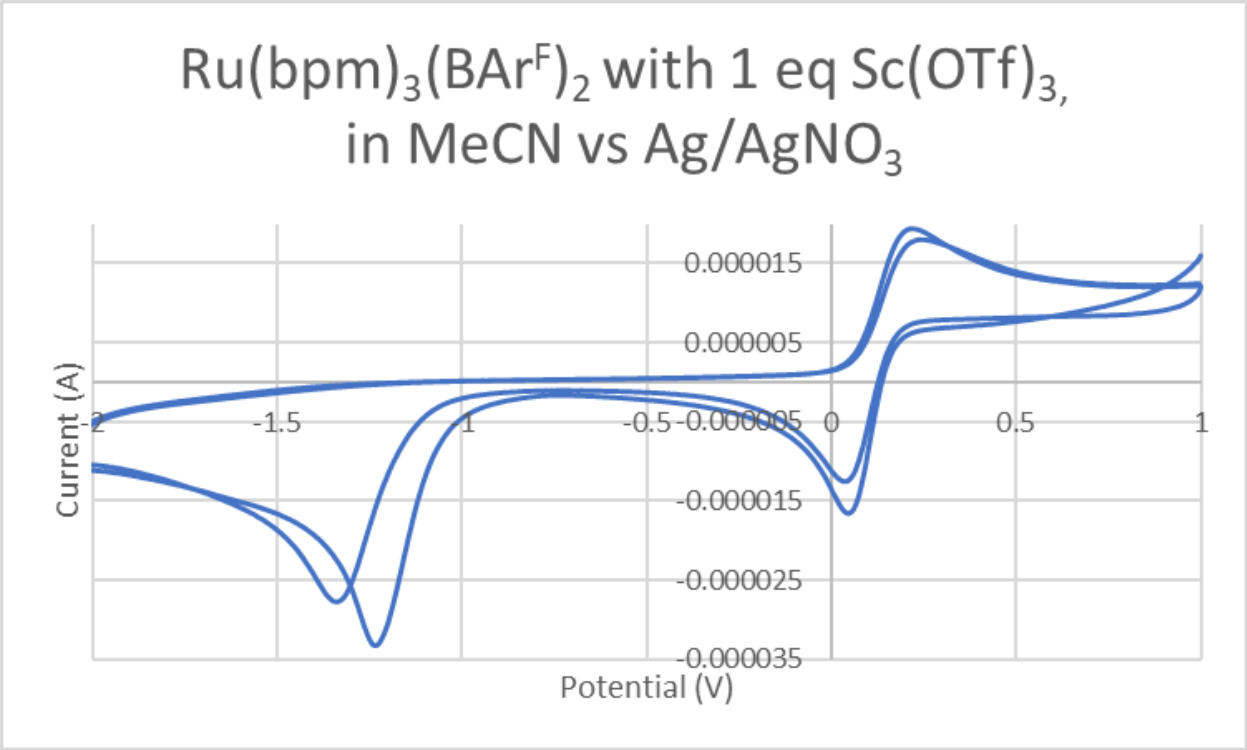
Ru(bpm)3(BArF)2 with 1 eq Sc(OTf)3,
in MeCN vs Ag/AgNO3
0.000015
0.000005
-0.000005
-0.000015
-0.000025
-0.000035
-2
-1.5
-1
-0.5
0
0.5
1
Current (A)
Potential (V)

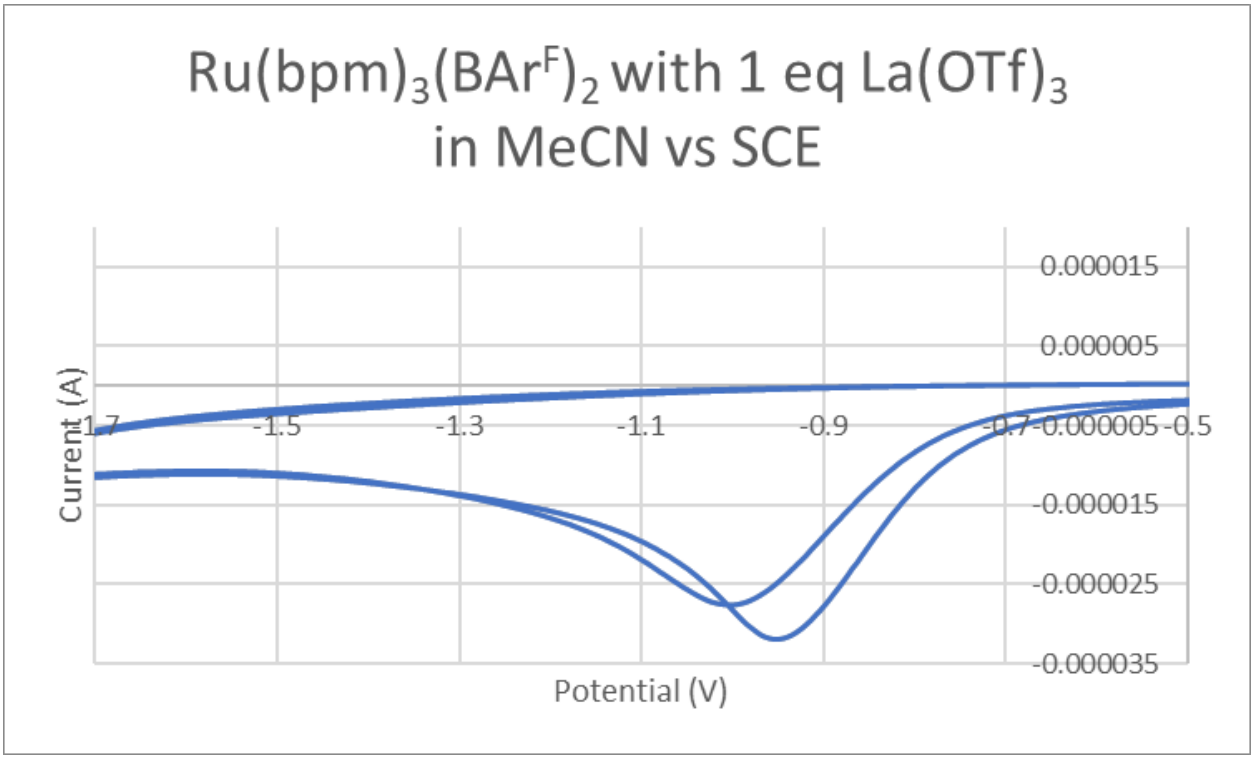
Ru(bpm)3(BArF)2 with 1 eq La(OTf)3
in MeCN vs SCE
0.000015
0.000005
-0.000005
-0.000015
-0.000025
-0.000035
-1.7
-1.5
-1.3
-1.1
-0.9
-0.7
-0.5
Current (A)
Potential (V)

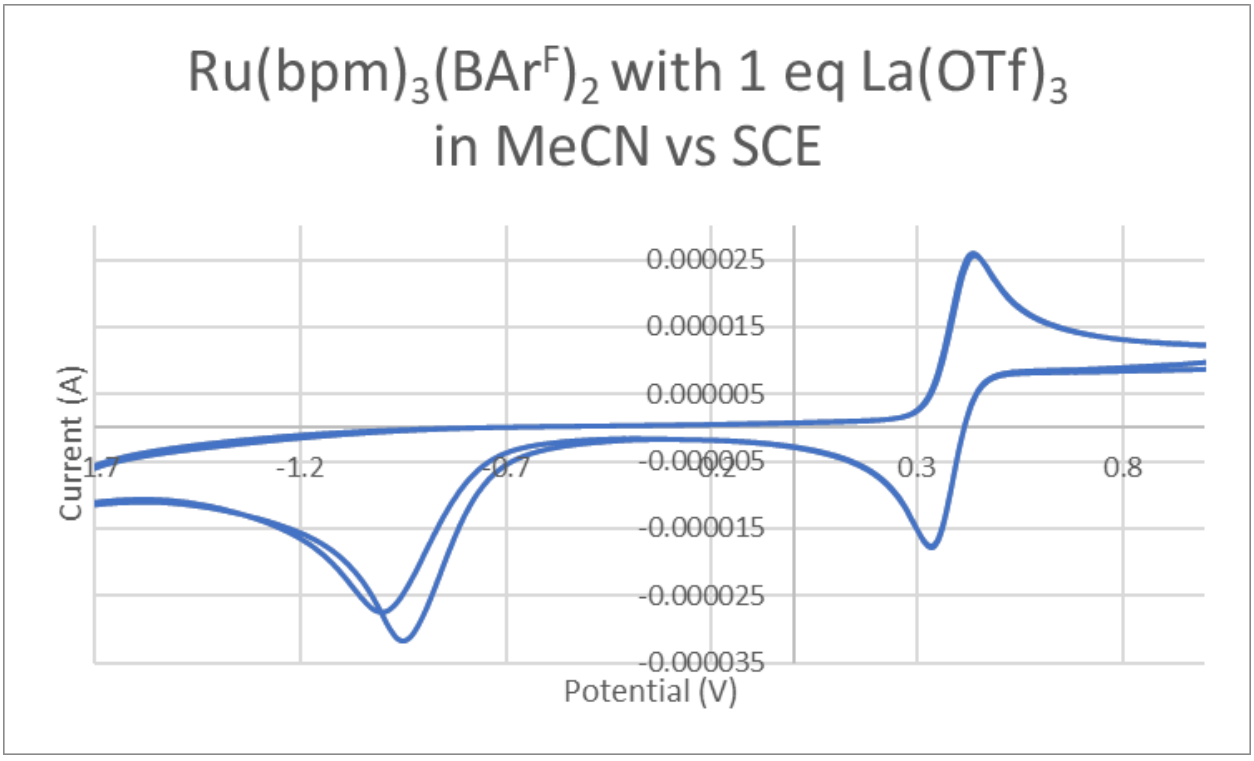
Ru(bpm)3(BArF)2 with 1 eq La(OTf)3
in MeCN vs SCE
Current (A)
0.000025
0.000015
0.000005
-0.000005
-0.000015
-0.000025
-0.000035
-1.7
-1.2
-0.7
-0.2
0.3
0.8
Potential (V)

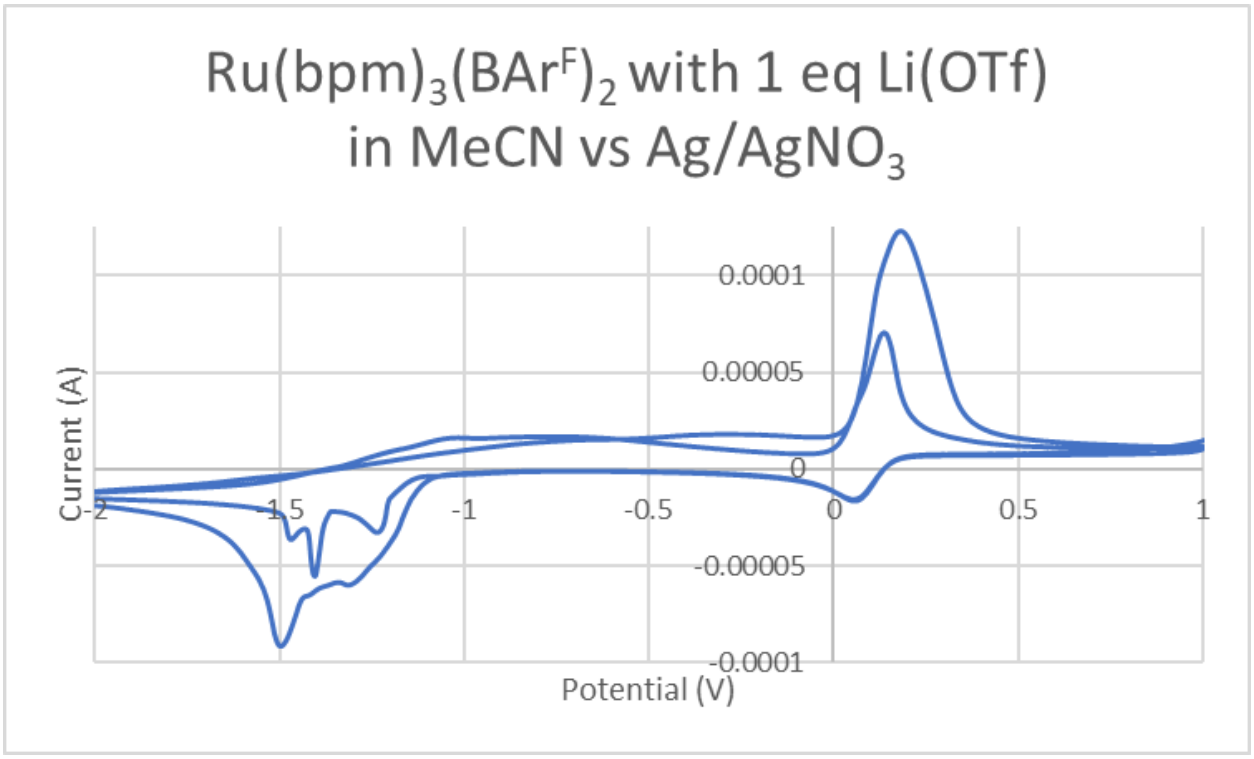
Ru(bpm)3(BArF)2 with 1 eq Li(OTf)
in MeCN vs Ag/AgNO3
Current (A)
0.0001
0.00005
0
-0.00005
-0.0001
-2
-1.5
-1
-0.5
0
0.5
1
Potential (V)

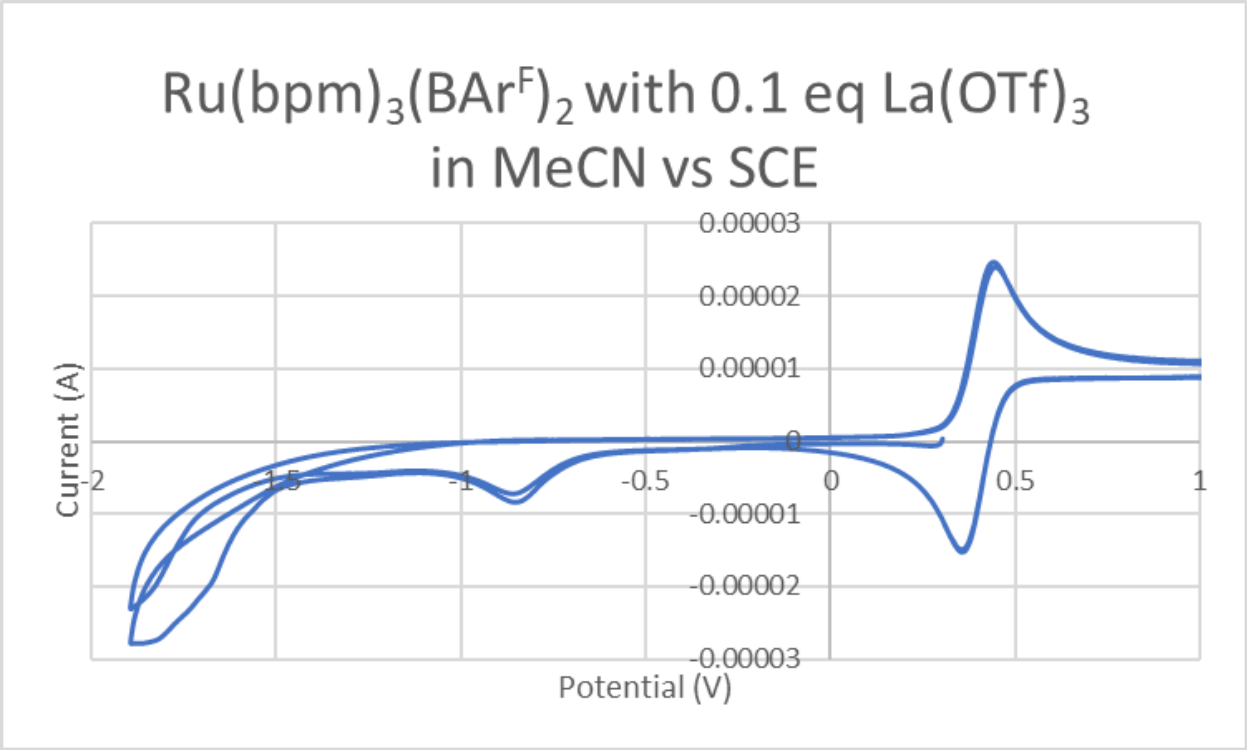
Ru(bpm)3(BArF)2 with 0.1 eq La(OTf)3
in MeCN vs SCE
Current (A)
Potential (V)
0.00003
0.00002
0.00001
0
-0.00001
-0.00002
-0.00003
-2
-1.5
-1
-0.5
0
0.5
1

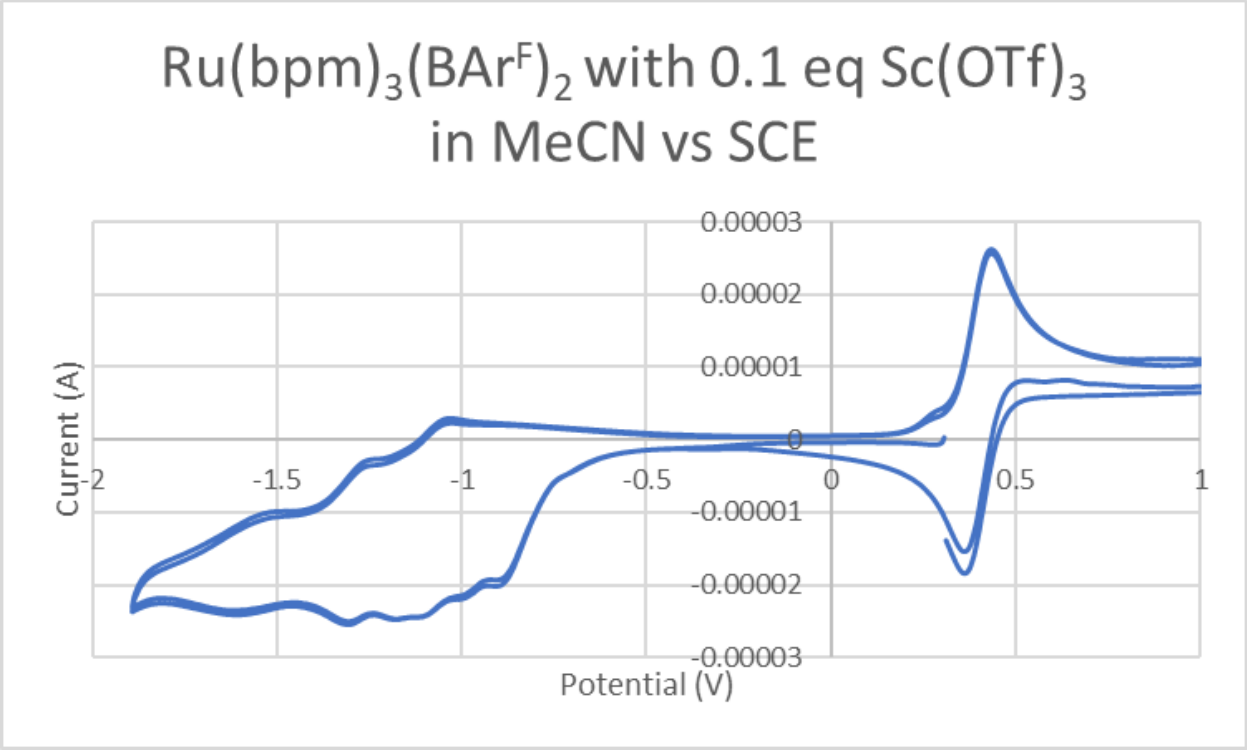
Ru(bpm)3(BArF)2 with 0.1 eq Sc(OTf)3
in MeCN vs SCE
Current (A)
Potential (V)
0.00003
0.00002
0.00001
0
-0.00001
-0.00002
-0.00003
-2
-1.5
-1
-0.5
0
0.5
1

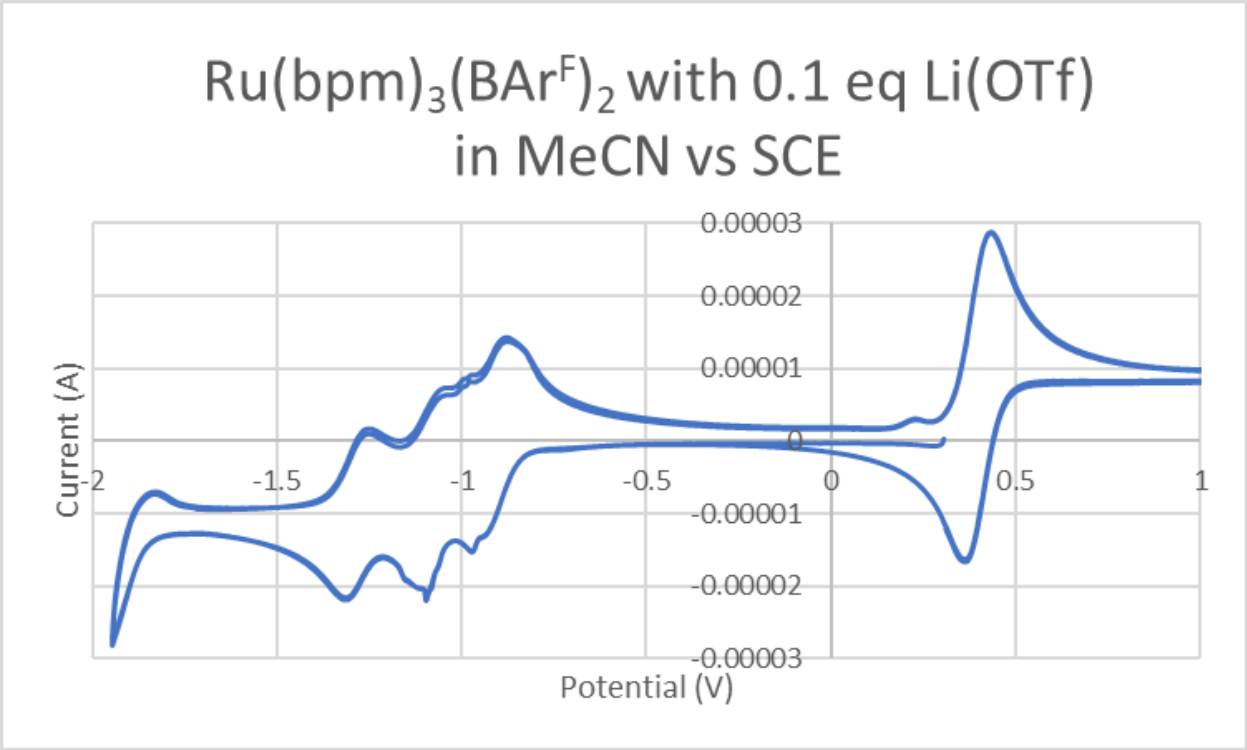
Ru(bpm)3(BArF)2 with 0.1 eq Li(OTf)
in MeCN vs SCE
Current (A)
Potential (V)
0.00003
0.00002
0.00001
0
-0.00001
-0.00002
-0.00003
-2
-1.5
-1
-0.5
0
0.5
1

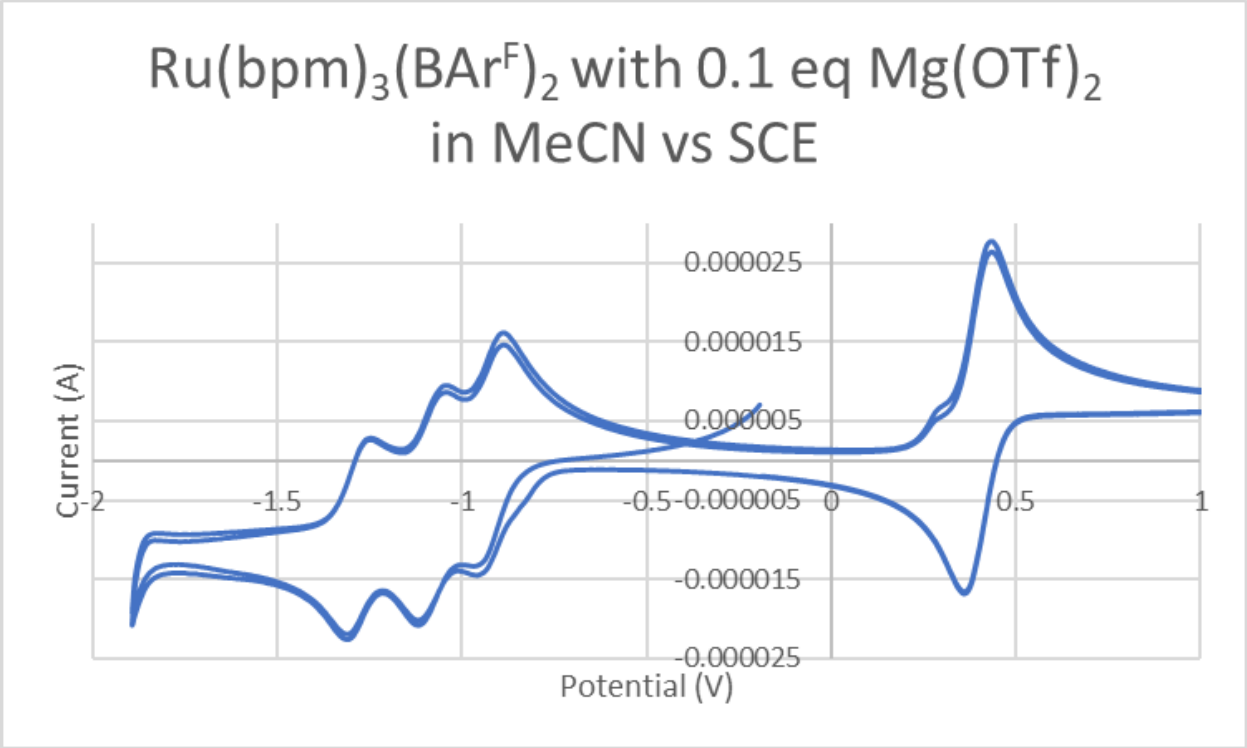
Ru(bpm)3(BArF)2 with 0.1 eq Mg(OTf)2
in MeCN vs SCE
Current (A)
Potential (V)
0.000025
0.000015
0.000005
-0.000005
-0.000015
-0.000025
-2
-1.5
-1
-0.5
0
0.5
1

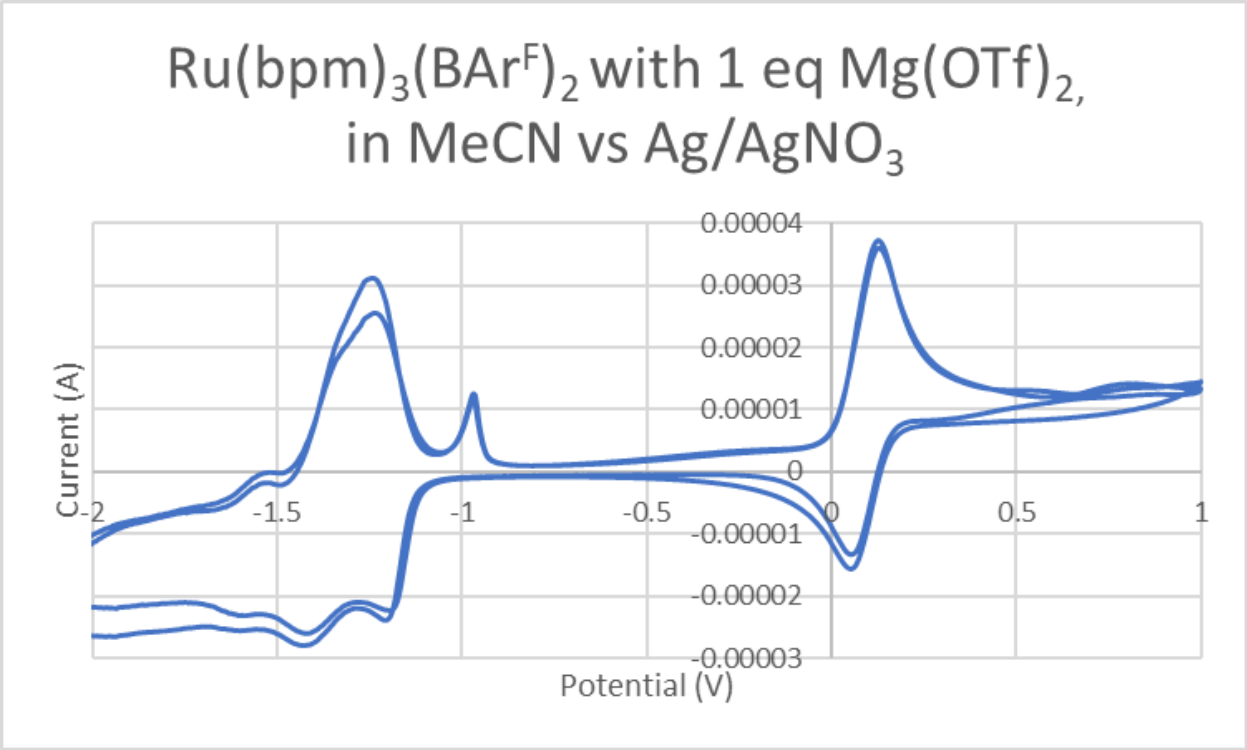
Ru(bpm)3(BArF)2 with 1 eq Mg(OTf)2,
in MeCN vs Ag/AgNO3
Current (A)
Potential (V)
0.00004
0.00003
0.00002
0.00001
0
-0.00001
-0.00002
-0.00003
-2
-1.5
-1
-0.5
0
0.5
1

Set 2: $Ru(bpz)_3(BArF)_2$ with Lewis Acids

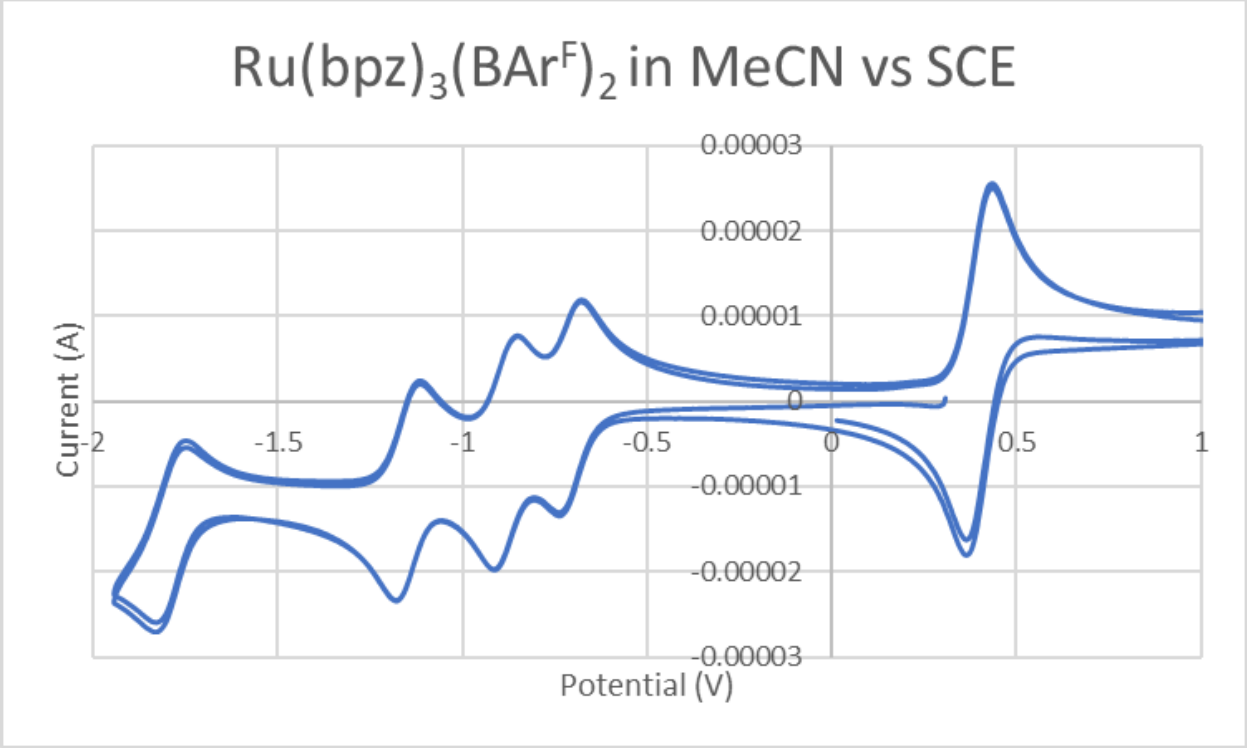

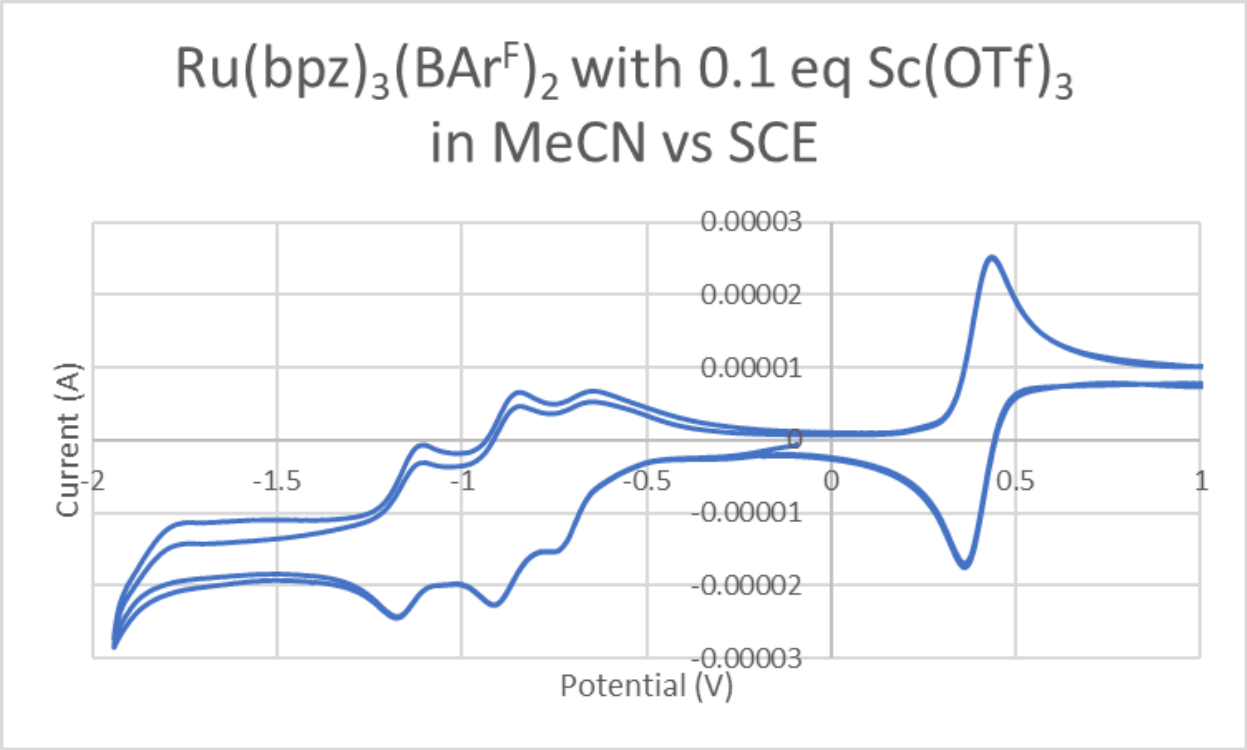
Ru(bpz)3(BArF)2 with 0.1 eq Sc(OTf)3
in MeCN vs SCE
Current (A)
Potential (V)
0.00003
0.00002
0.00001
0
-0.00001
-0.00002
-0.00003
-2
-1.5
-1
-0.5
0
0.5
1

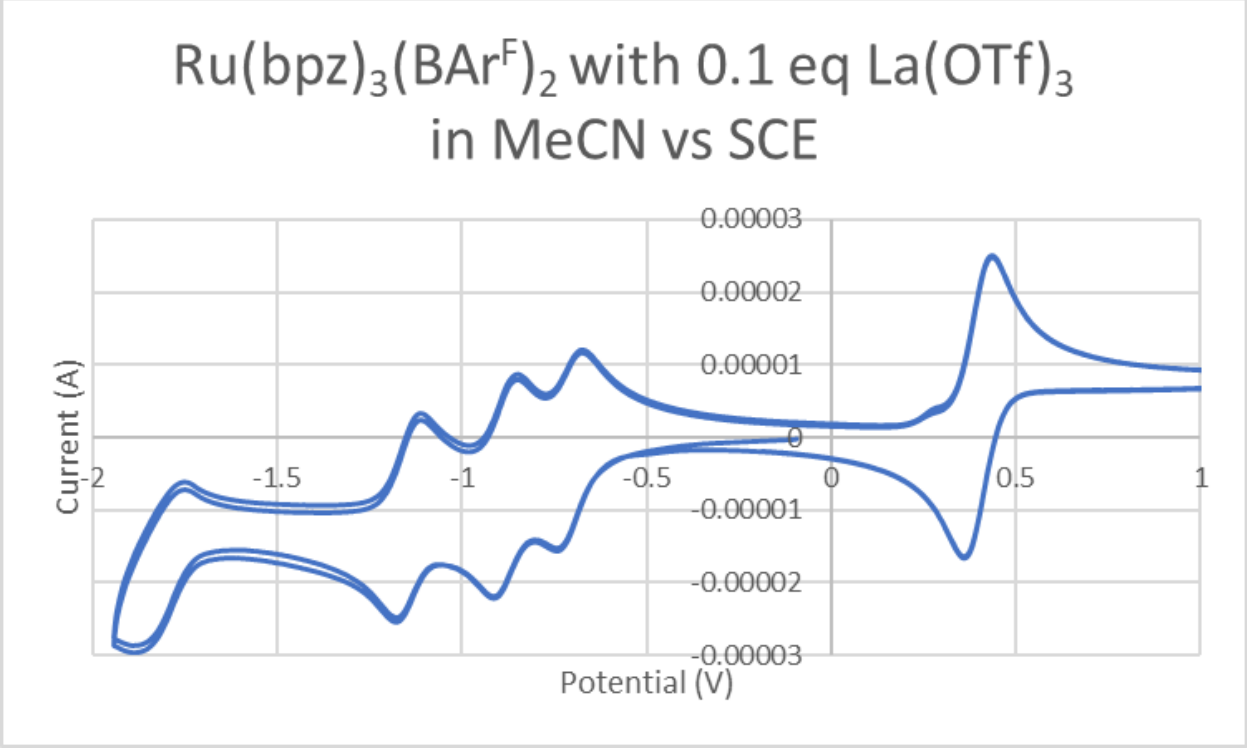
Ru(bpz)3(BArF)2 with 0.1 eq La(OTf)3
in MeCN vs SCE
Current (A)
Potential (V)
0.00003
0.00002
0.00001
0
-0.00001
-0.00002
-0.00003
-2
-1.5
-1
-0.5
0
0.5
1

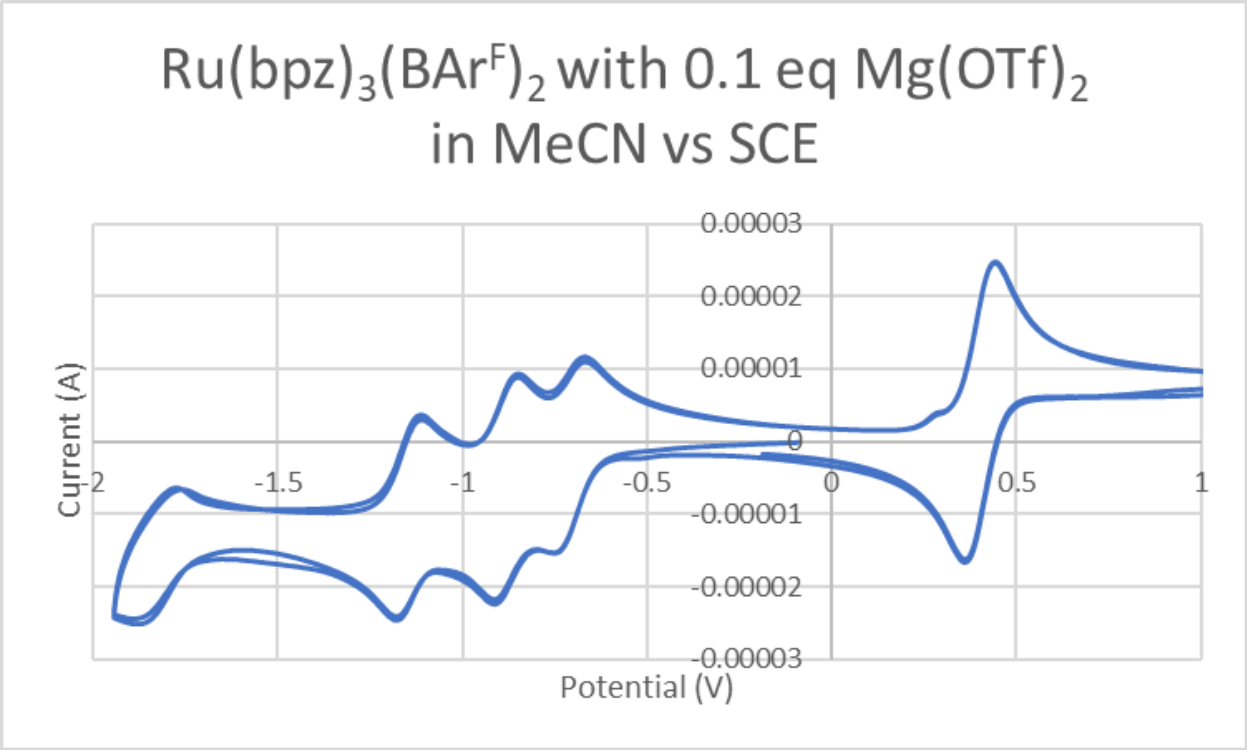
Ru(bpz)3(BArF)2 with 0.1 eq Mg(OTf)2
in MeCN vs SCE
Current (A)
Potential (V)
0.00003
0.00002
0.00001
0
-0.00001
-0.00002
-0.00003
-2
-1.5
-1
-0.5
0
0.5
1

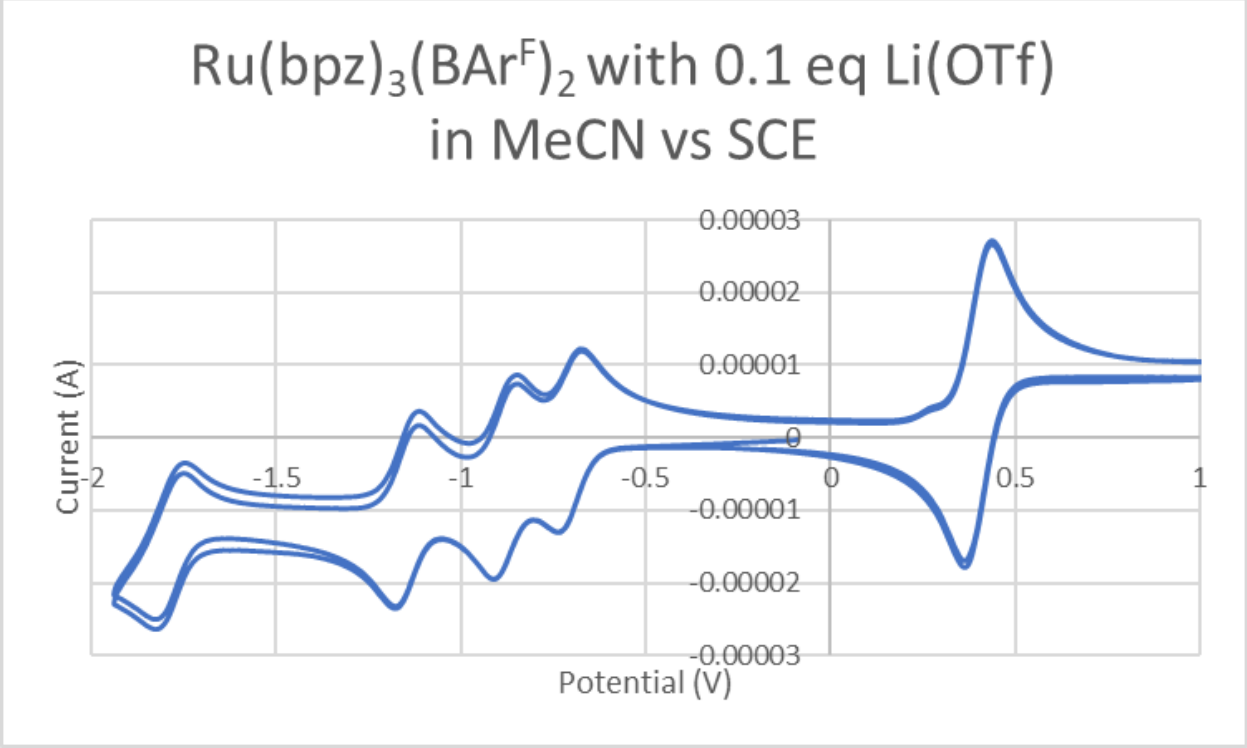
Ru(bpz)3(BArF)2 with 0.1 eq Li(OTf)
in MeCN vs SCE
Current (A)
Potential (V)
0.00003
0.00002
0.00001
0
-0.00001
-0.00002
-0.00003
-2
-1.5
-1
-0.5
0
0.5
1

Set 3: $Ir(dF(CF_3)ppy)_2(bpm)PF_6$ with Lewis Acids

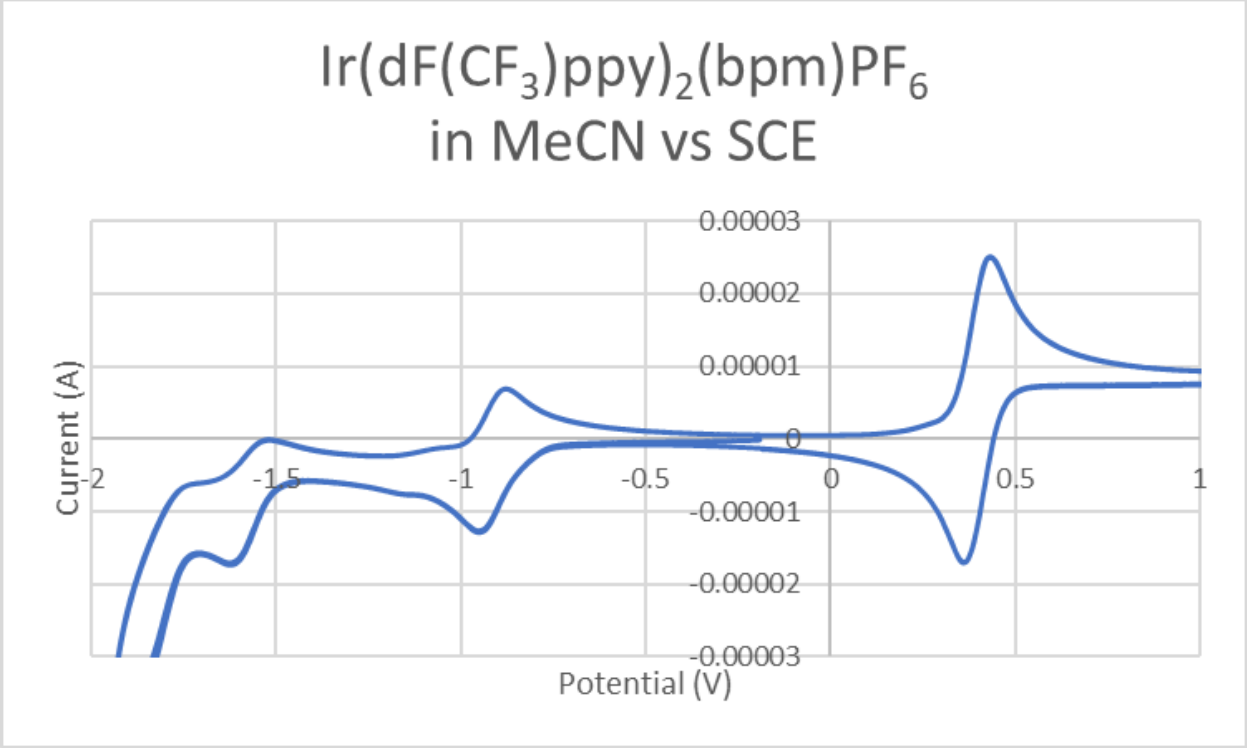

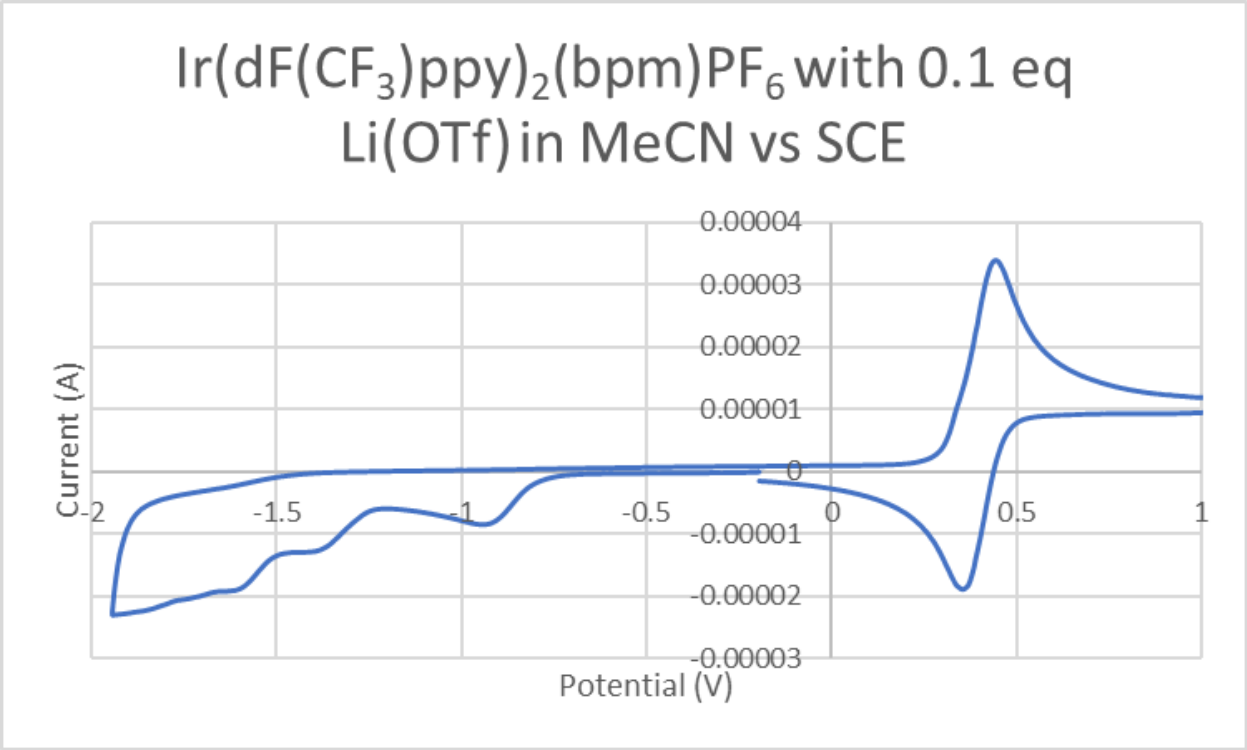
Ir(dF(CF3)ppy)2(bpm)PF6 with 0.1 eq Li(OTf) in MeCN vs SCE
Current (A)
Potential (V)
0.00004
0.00003
0.00002
0.00001
0
-0.00001
-0.00002
-0.00003
-2
-1.5
-1
-0.5
0
0.5
1

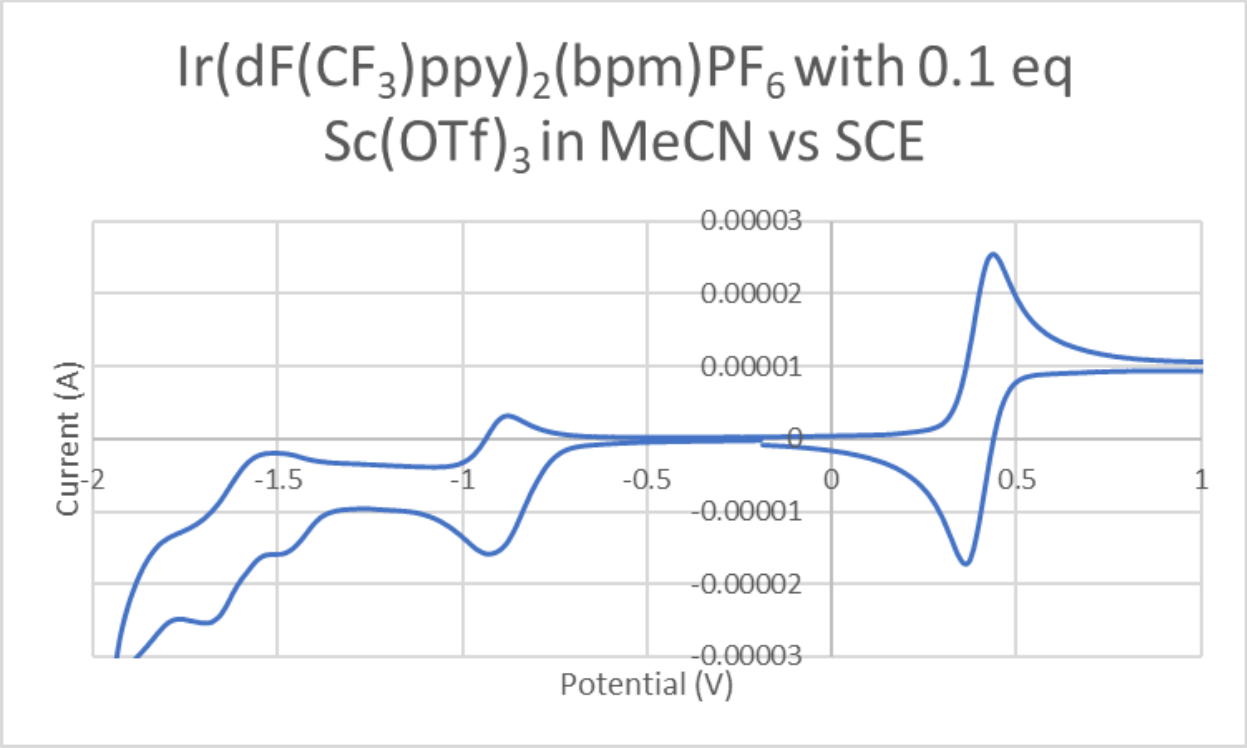
Ir(dF(CF3)ppy)2(bpm)PF6 with 0.1 eq Sc(OTf)3 in MeCN vs SCE
Current (A)
Potential (V)
0.00003
0.00002
0.00001
0
-0.00001
-0.00002
-0.00003
-2
-1.5
-1
-0.5
0
0.5
1

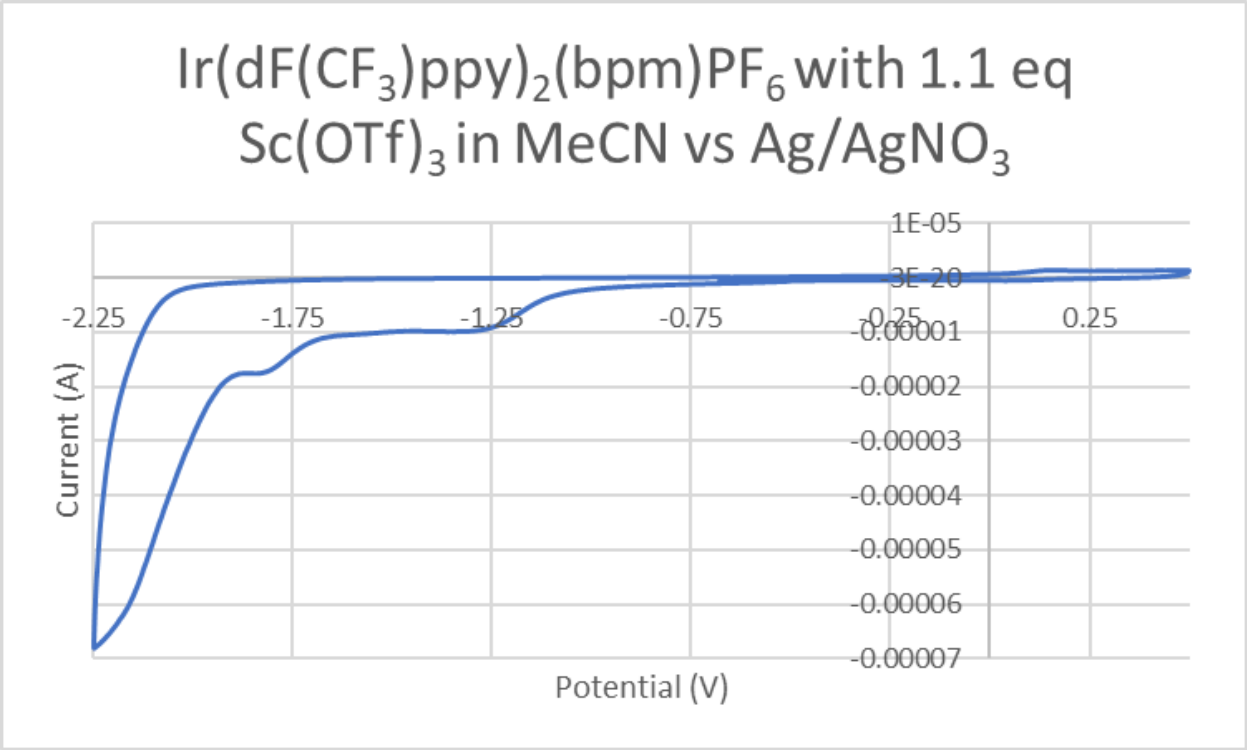
Ir(dF(CF3)ppy)2(bpm)PF6 with 1.1 eq Sc(OTf)3 in MeCN vs Ag/AgNO3
1E-05
3E-20
-0.00001
-0.00002
-0.00003
-0.00004
-0.00005
-0.00006
-0.00007
-2.25
-1.75
-1.25
-0.75
-0.25
0.25
Current (A)
Potential (V)

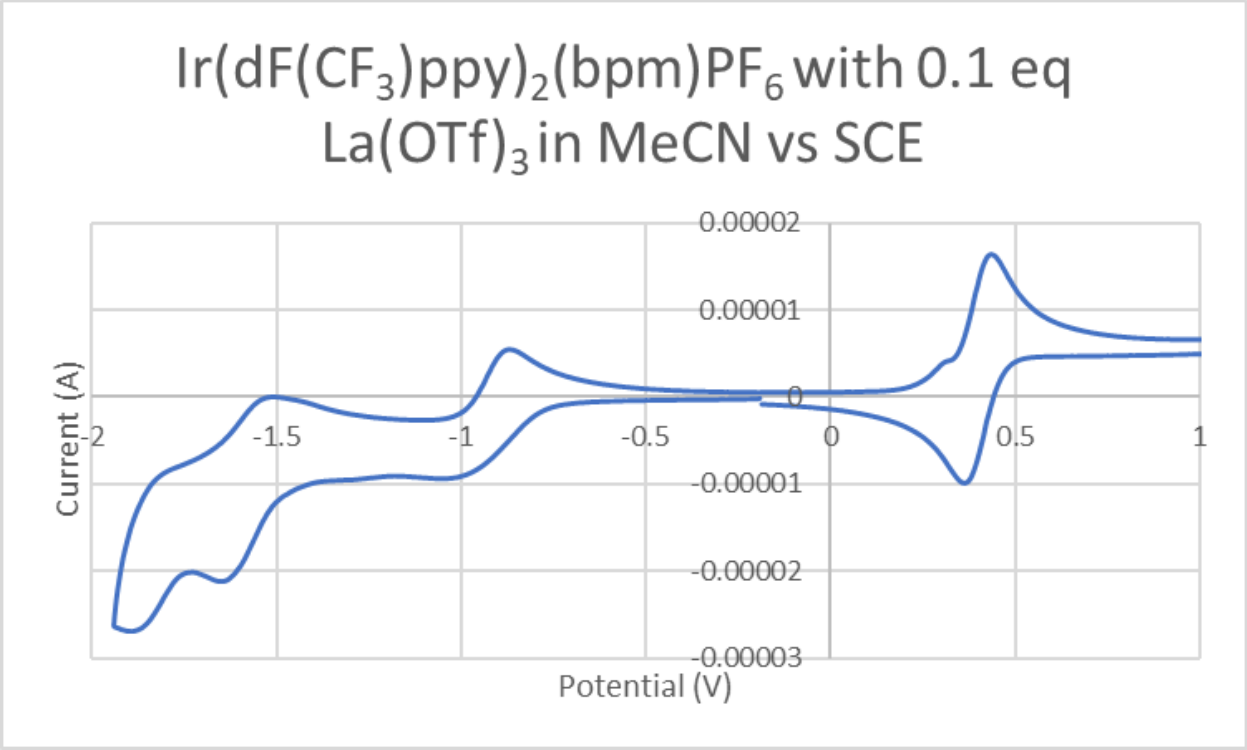
Ir(dF(CF3)ppy)2(bpm)PF6 with 0.1 eq La(OTf)3 in MeCN vs SCE
0.00002
0.00001
0
-0.00001
-0.00002
-0.00003
-2
-1.5
-1
-0.5
0
0.5
1
Current (A)
Potential (V)

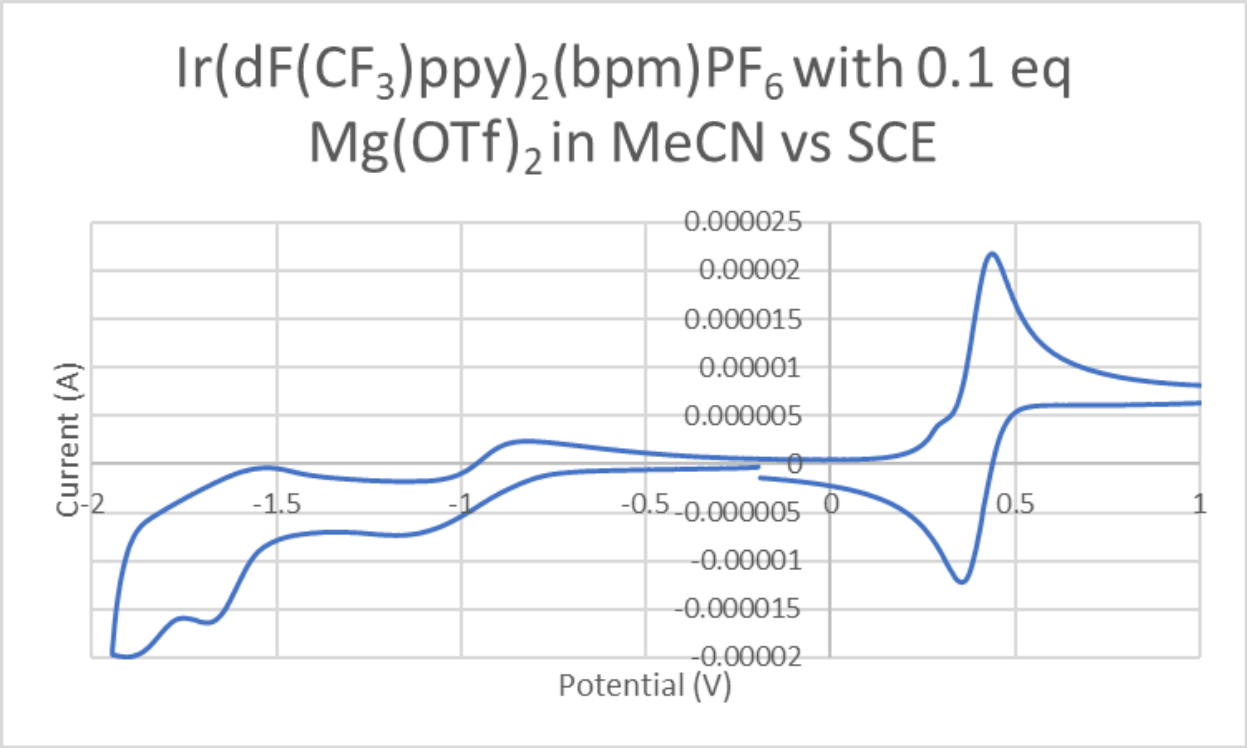
Ir(dF(CF3)ppy)2(bpm)PF6 with 0.1 eq Mg(OTf)2 in MeCN vs SCE
Current (A)
Potential (V)
0.000025
0.00002
0.000015
0.00001
0.000005
0
-0.000005
-0.00001
-0.000015
-0.00002
-2
-1.5
-1
-0.5
0
0.5
1

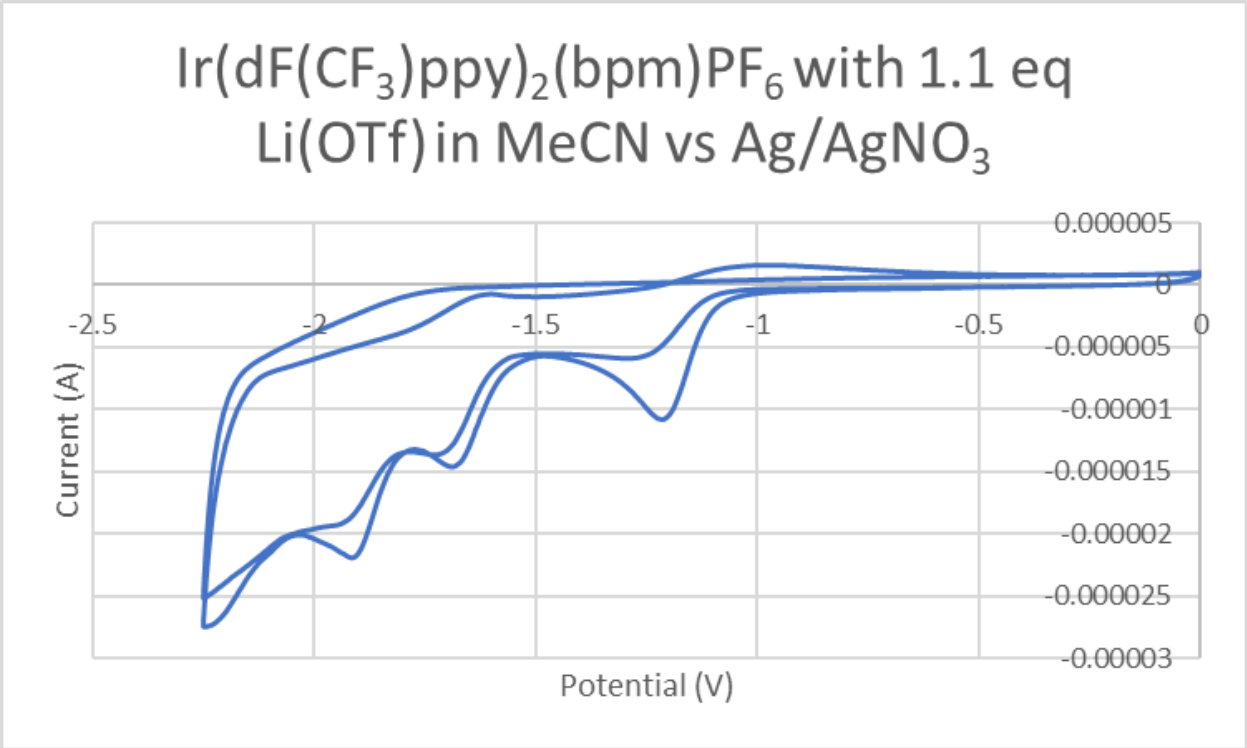
Ir(dF(CF3)ppy)2(bpm)PF6 with 1.1 eq Li(OTf) in MeCN vs Ag/AgNO3
Current (A)
Potential (V)
0.000005
0
-0.000005
-0.00001
-0.000015
-0.00002
-0.000025
-0.00003
-2.5
-2
-1.5
-1
-0.5
0

Set 4: $Ir(DFMPPZ)_2(dtbbpy)PF_6$ with Zinc Salts

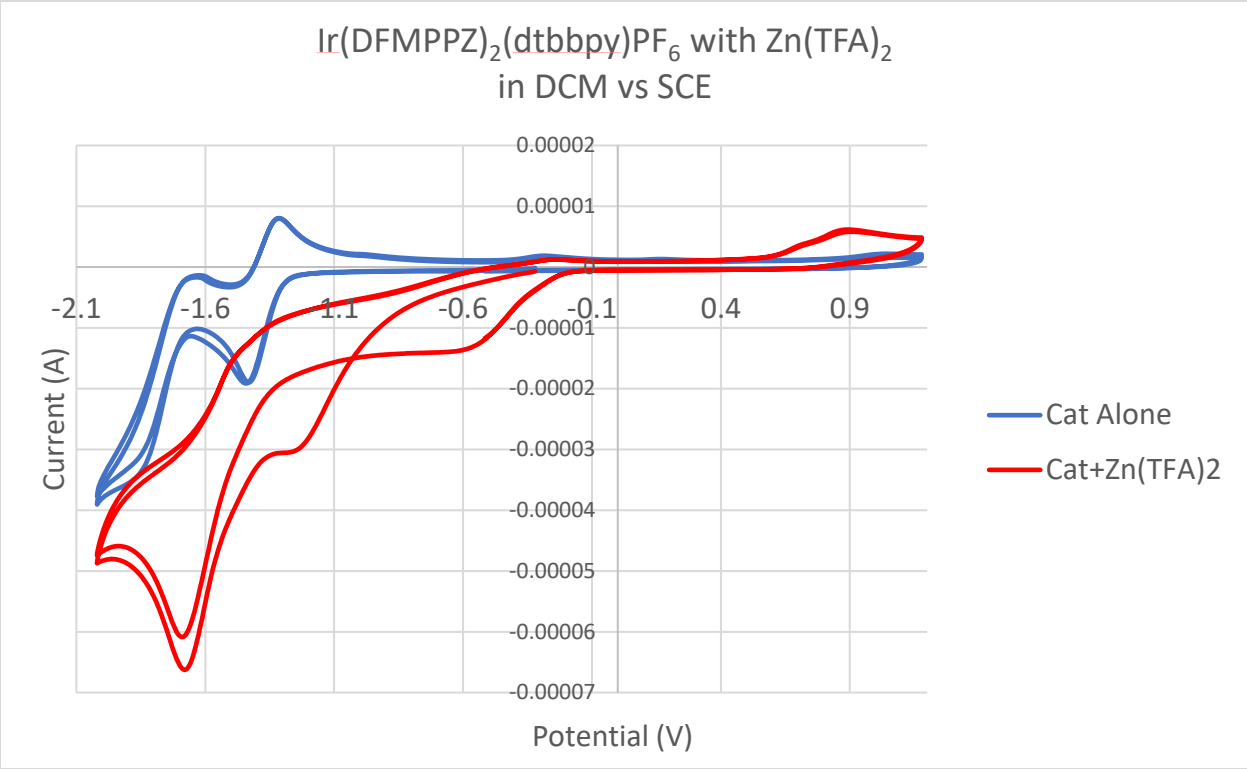

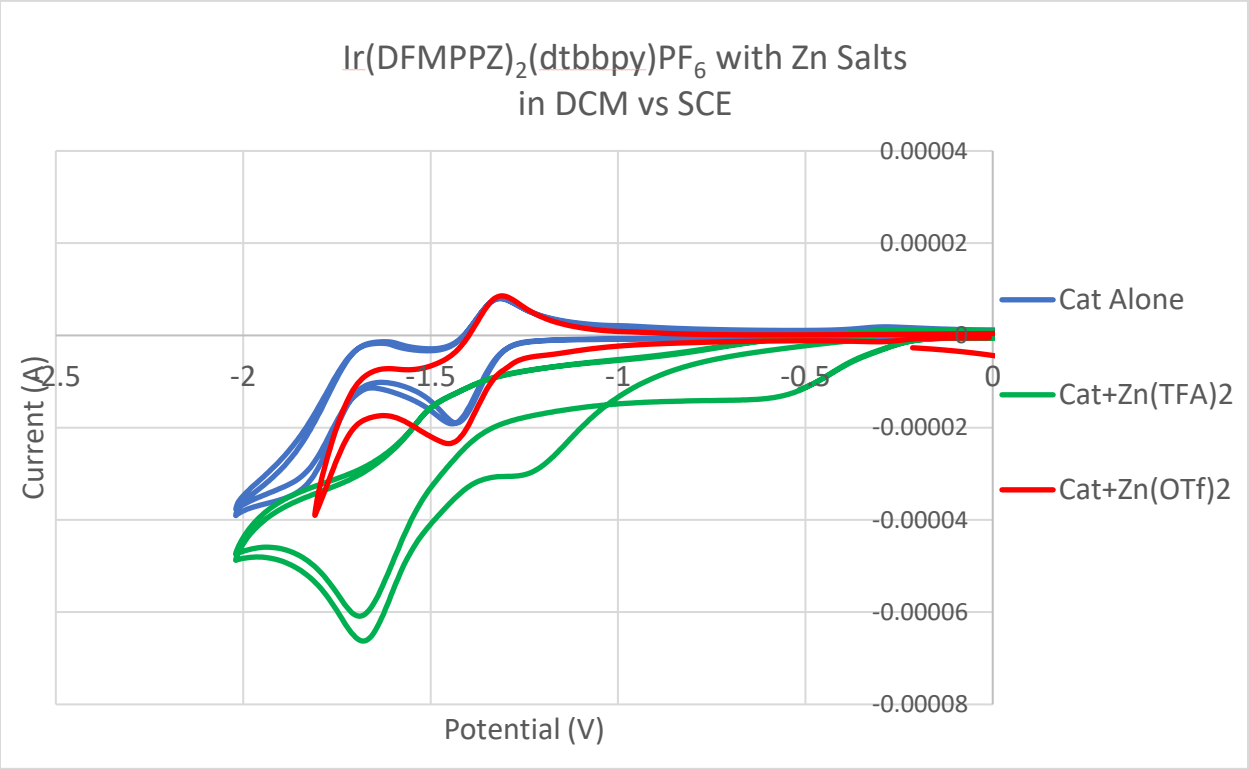
Ir(DFMPPZ)2(dtbbpy)PF6 with Zn Salts
in DCM vs SCE
0.00004
0.00002
0
-0.00002
-0.00004
-0.00006
-0.00008
-2.5
-2
-1.5
-1
-0.5
0
Current (A)
Potential (V)
Cat Alone
Cat+Zn(TFA)2
Cat+Zn(OTf)2

Set 5: Trans-Anethole with Zinc Salts

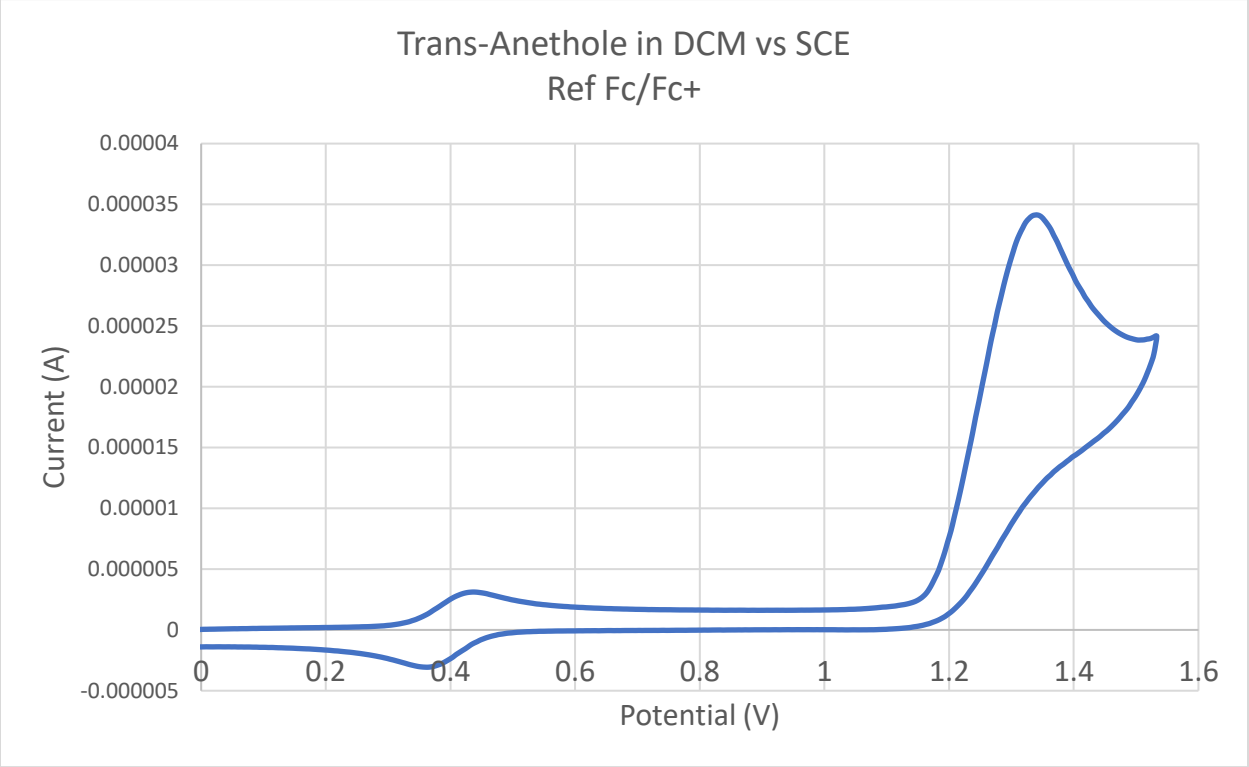

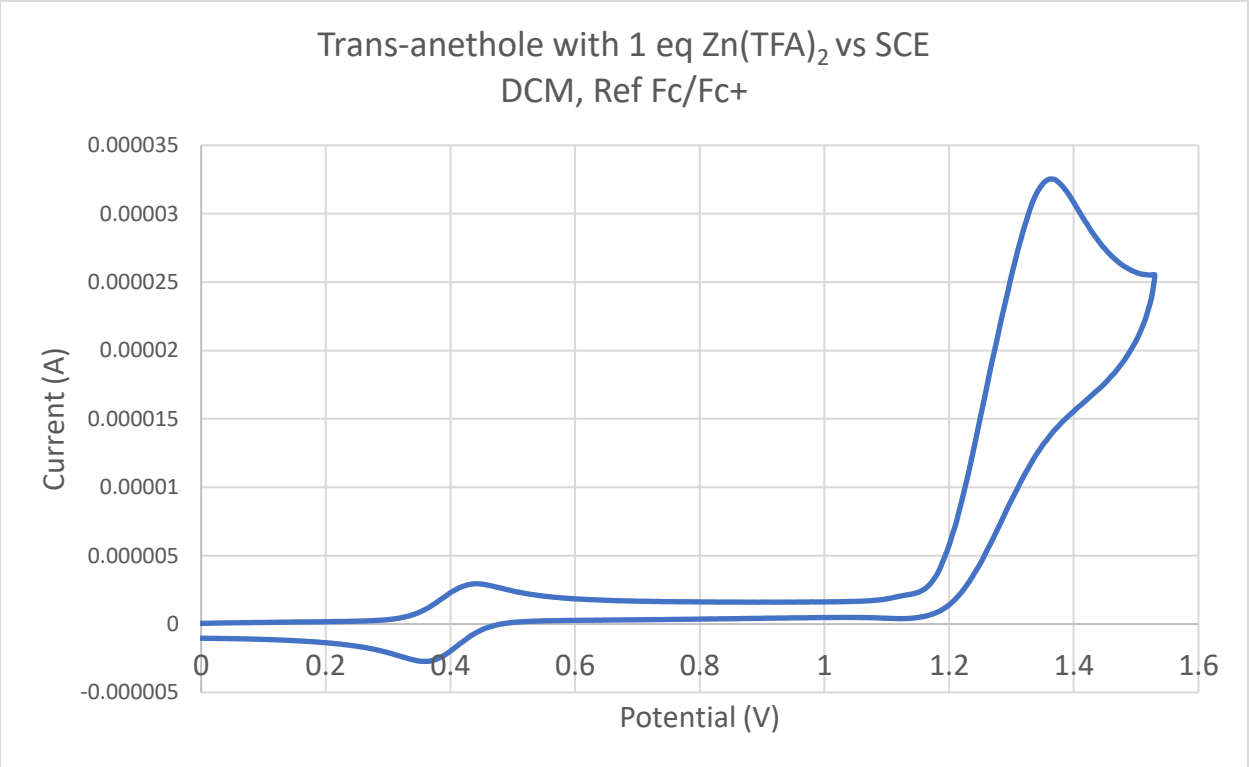

3.6.6 Other Spectroscopic Data

UV-Visible spectra and emission spectra were obtained by preparation of solutions in DCM unless otherwise specified. Solutions were prepared to be $1x10^{-4}$ to $1x10^{-6}$ M with respect to photocatalyst. Samples for emission spectroscopy were capped with a septum and sparged with N_2 for 5 minutes after sample preparation in order to ensure exclusion of O_2.

Stern–Volmer quenching relationships were obtained by preparing solutions to be $1x10^{-4}$ to $1x10^{-6}$ M with respect to photocatalyst, including substrate at specified concentrations, and having a total volume of 3 mL. Samples were sparged with N_2 for a uniform and strictly timed 3 minutes to uniformly exclude O_2. After sparging, samples were placed in a dark chamber, transported to the fluorimeter, and emission spectra were obtained.

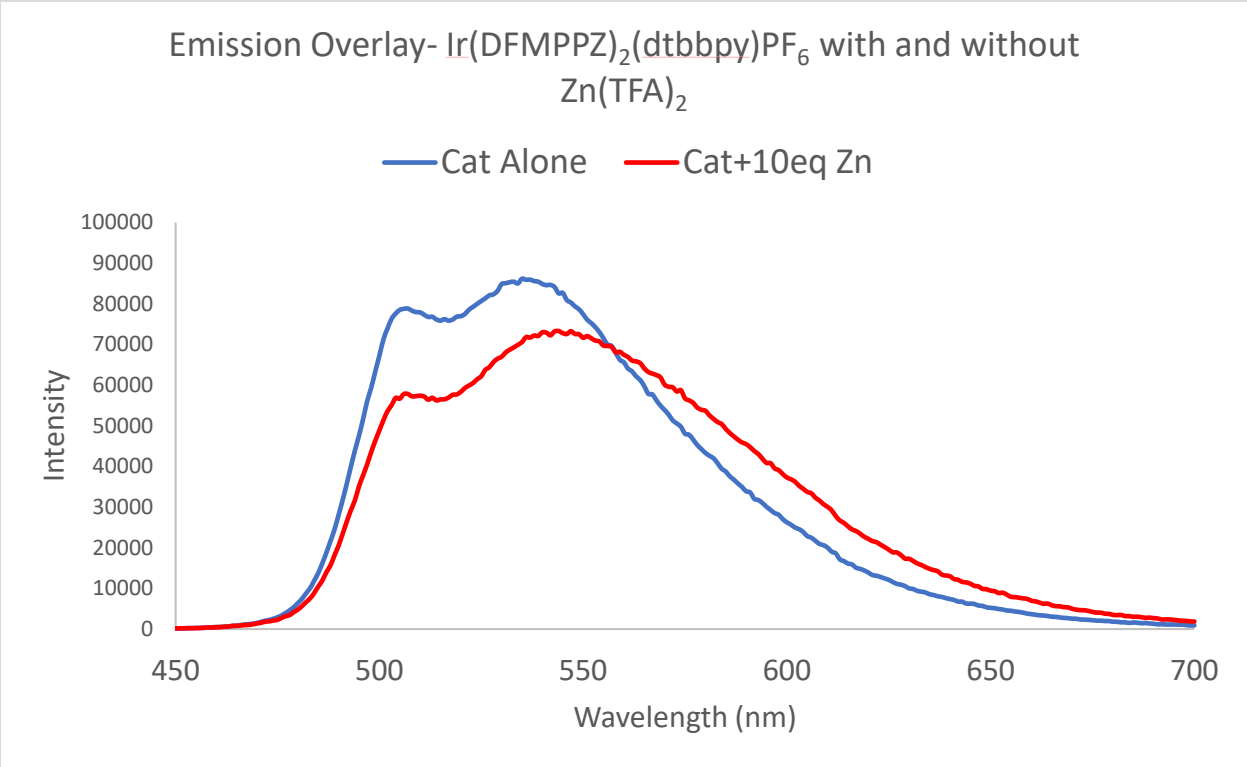
Emission Overlay- Ir(DFMPPZ)2(dtbbpy)PF6 with and without Zn(TFA)2
Cat Alone
Cat+10eq Zn
Intensity
100000
90000
80000
70000
60000
50000
40000
30000
20000
10000
0
450
500
550
600
650
700
Wavelength (nm)

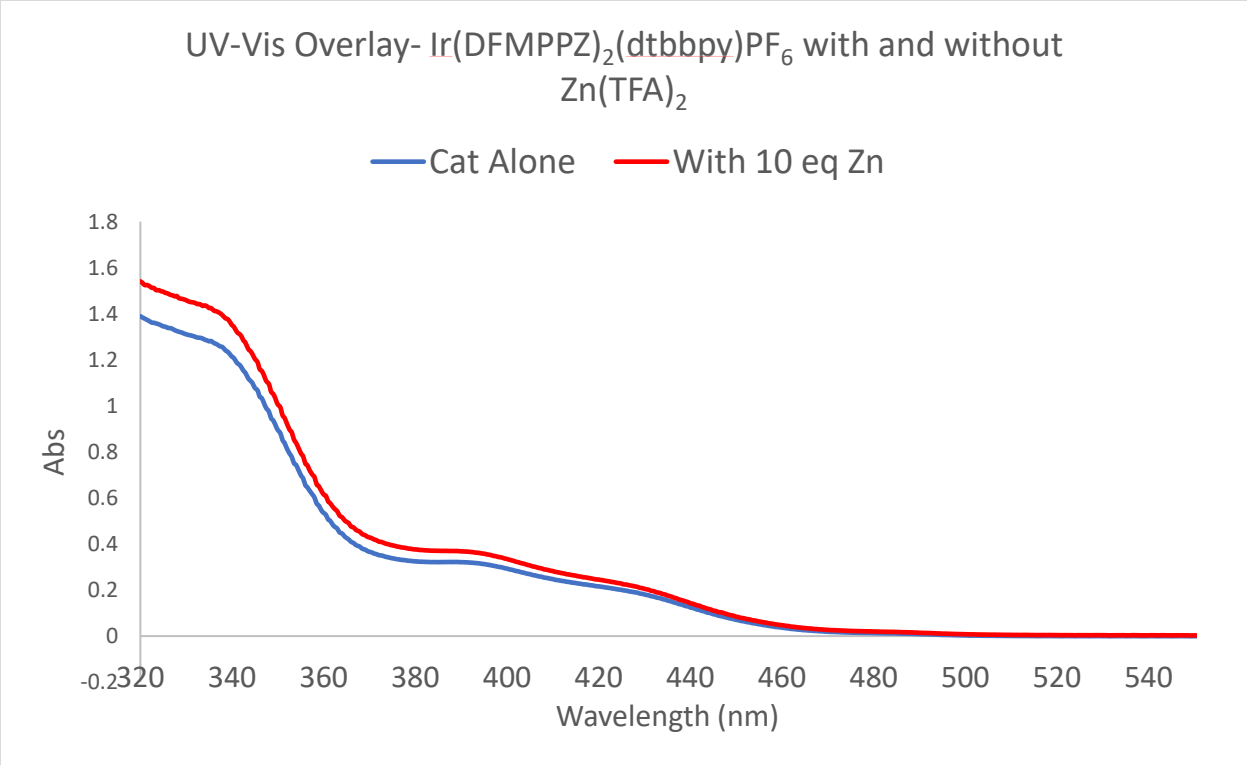
UV-Vis Overlay- Ir(DFMPPZ)2(dtbbpy)PF6 with and without Zn(TFA)2
Cat Alone
With 10 eq Zn
Abs
1.8
1.6
1.4
1.2
1
0.8
0.6
0.4
0.2
0
-0.2
320
340
360
380
400
420
440
460
480
500
520
540
Wavelength (nm)

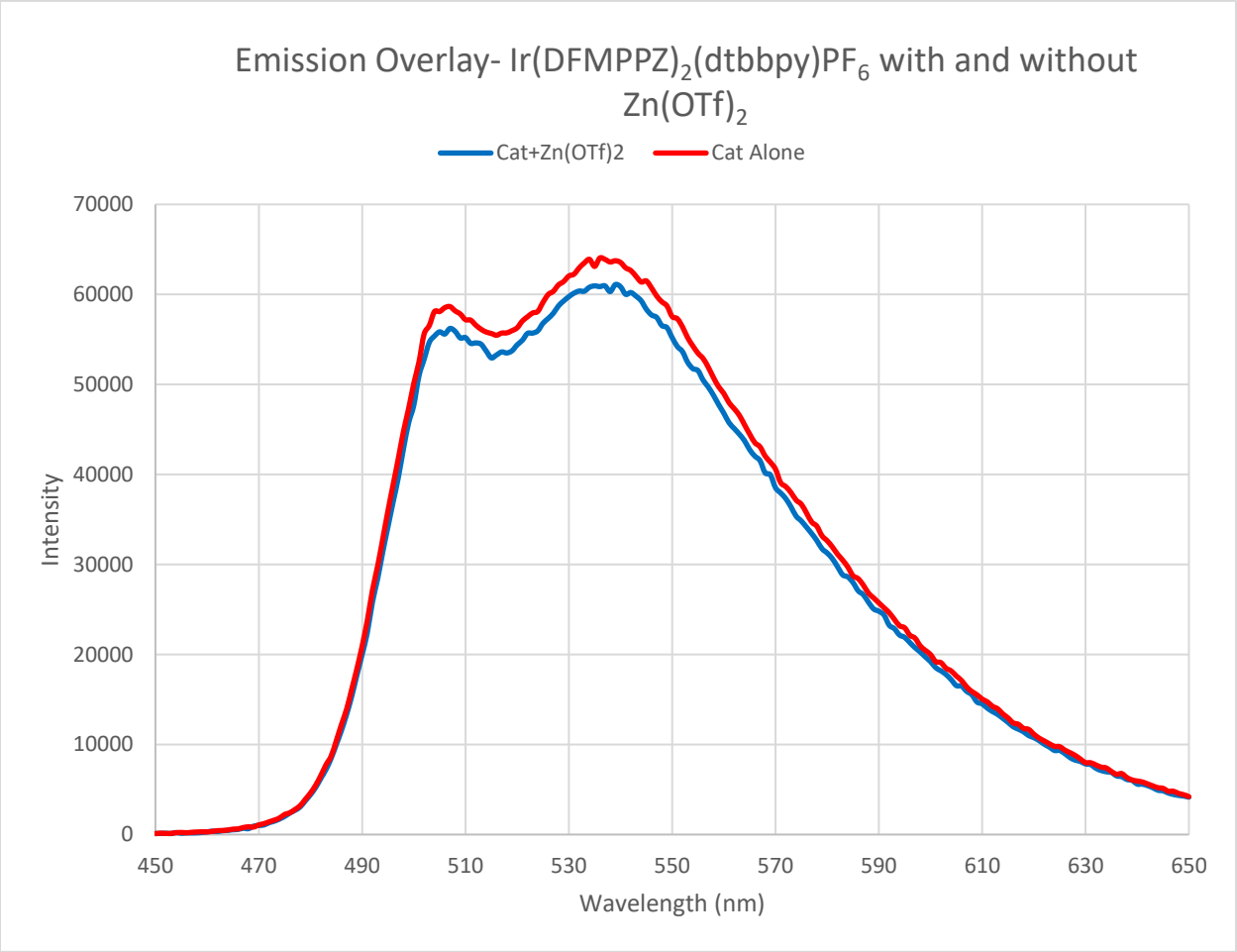
Emission Overlay- Ir(DFMPPZ)2(dtbbpy)PF6 with and without Zn(OTf)2
Cat+Zn(OTf)2
Cat Alone
Intensity
70000
60000
50000
40000
30000
20000
10000
0
450
470
490
510
530
550
570
590
610
630
650
Wavelength (nm)

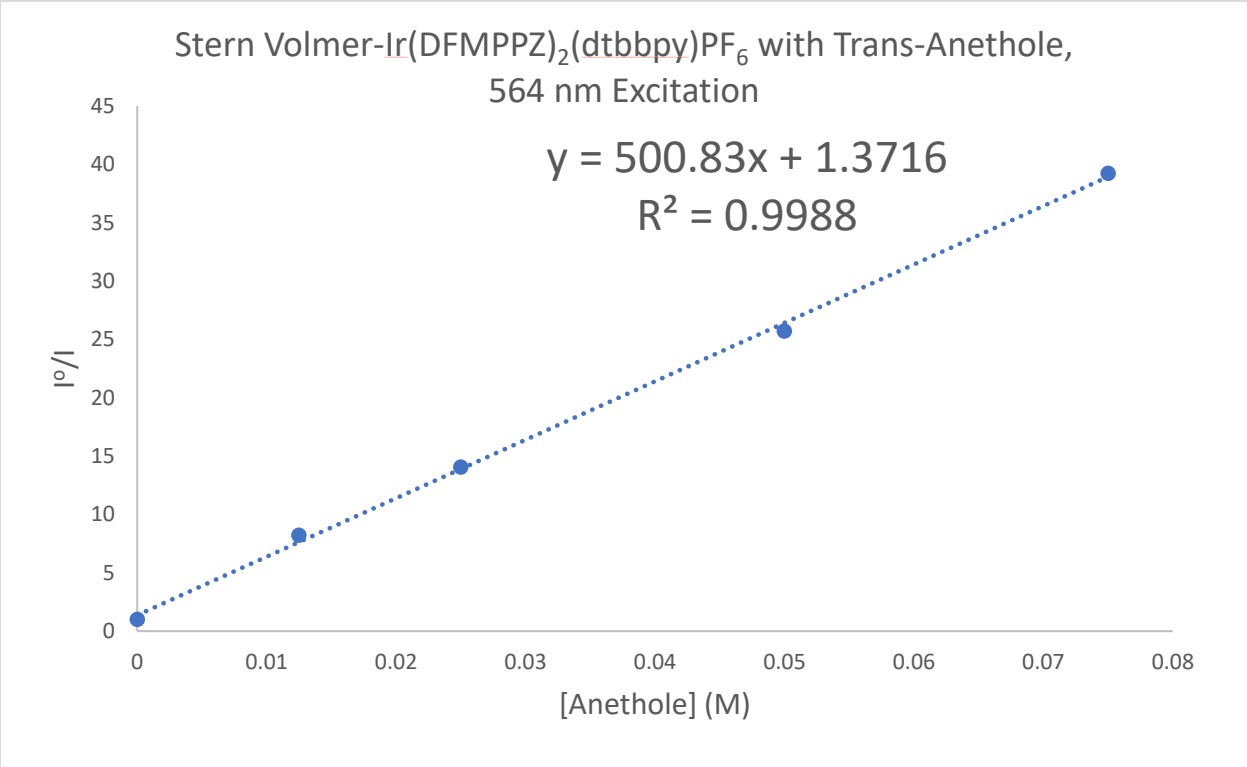
Stern Volmer-Ir(DFMPPZ)2(dtbbpy)PF6 with Trans-Anethole, 564 nm Excitation
y = 500.83x + 1.3716
R² = 0.9988
I°/I
[Anethole] (M)
0
5
10
15
20
25
30
35
40
45
0
0.01
0.02
0.03
0.04
0.05
0.06
0.07
0.08

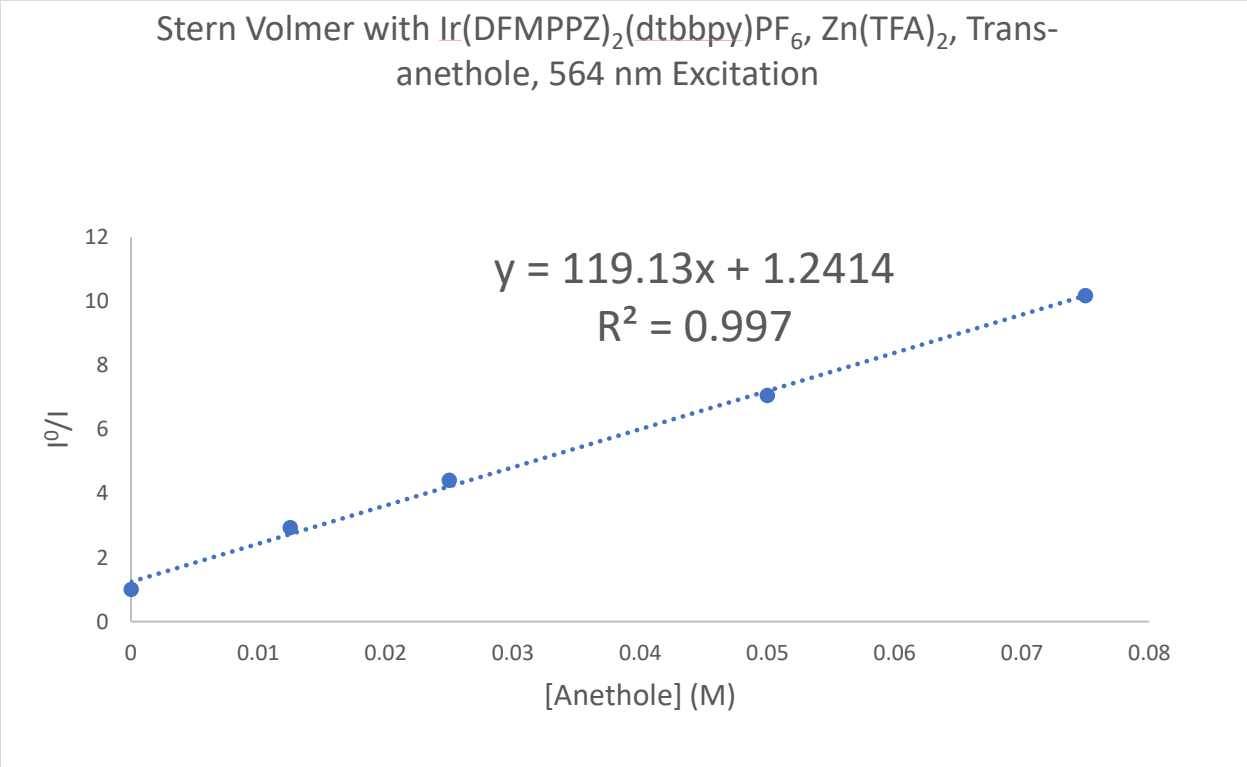
Stern Volmer with Ir(DFMPPZ)2(dtbbpy)PF6, Zn(TFA)2, Trans-anethole, 564 nm Excitation
y = 119.13x + 1.2414
R² = 0.997
I0/I
[Anethole] (M)
0
2
4
6
8
10
12
0
0.01
0.02
0.03
0.04
0.05
0.06
0.07
0.08

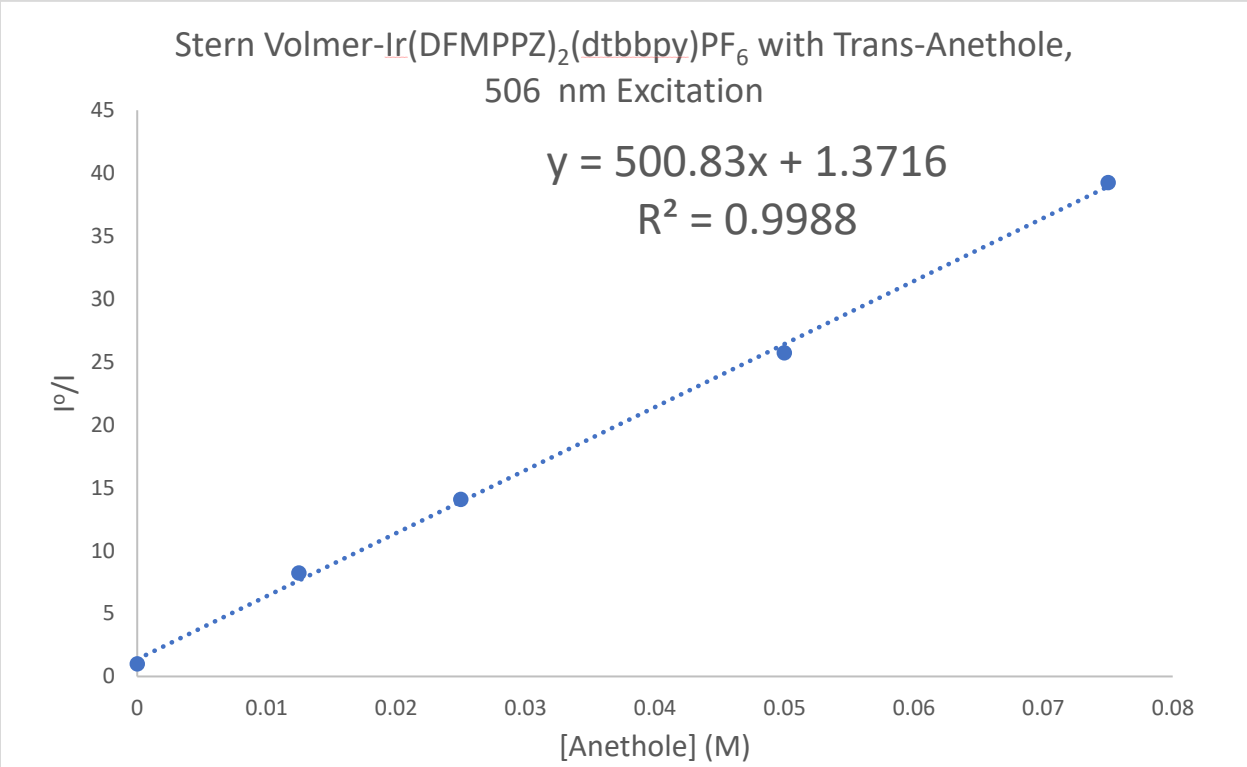
Stern Volmer-Ir(DFMPPZ)2(dtbbpy)PF6 with Trans-Anethole, 506 nm Excitation
y = 500.83x + 1.3716
R² = 0.9988
I°/I
[Anethole] (M)
0
5
10
15
20
25
30
35
40
45
0
0.01
0.02
0.03
0.04
0.05
0.06
0.07
0.08

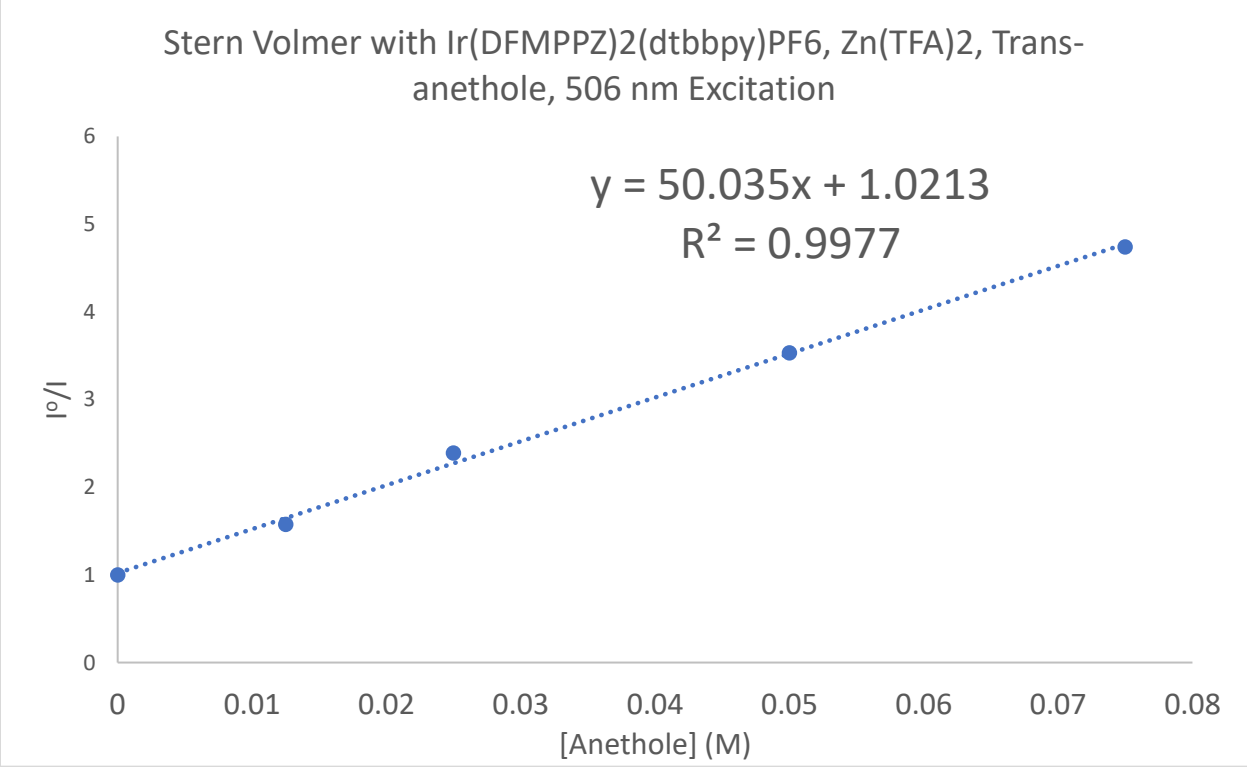
Stern Volmer with Ir(DFMPPZ)2(dtbbpy)PF6, Zn(TFA)2, Trans-anethole, 506 nm Excitation
y = 50.035x + 1.0213
R² = 0.9977
I°/I
[Anethole] (M)
0
1
2
3
4
5
6
0
0.01
0.02
0.03
0.04
0.05
0.06
0.07
0.08

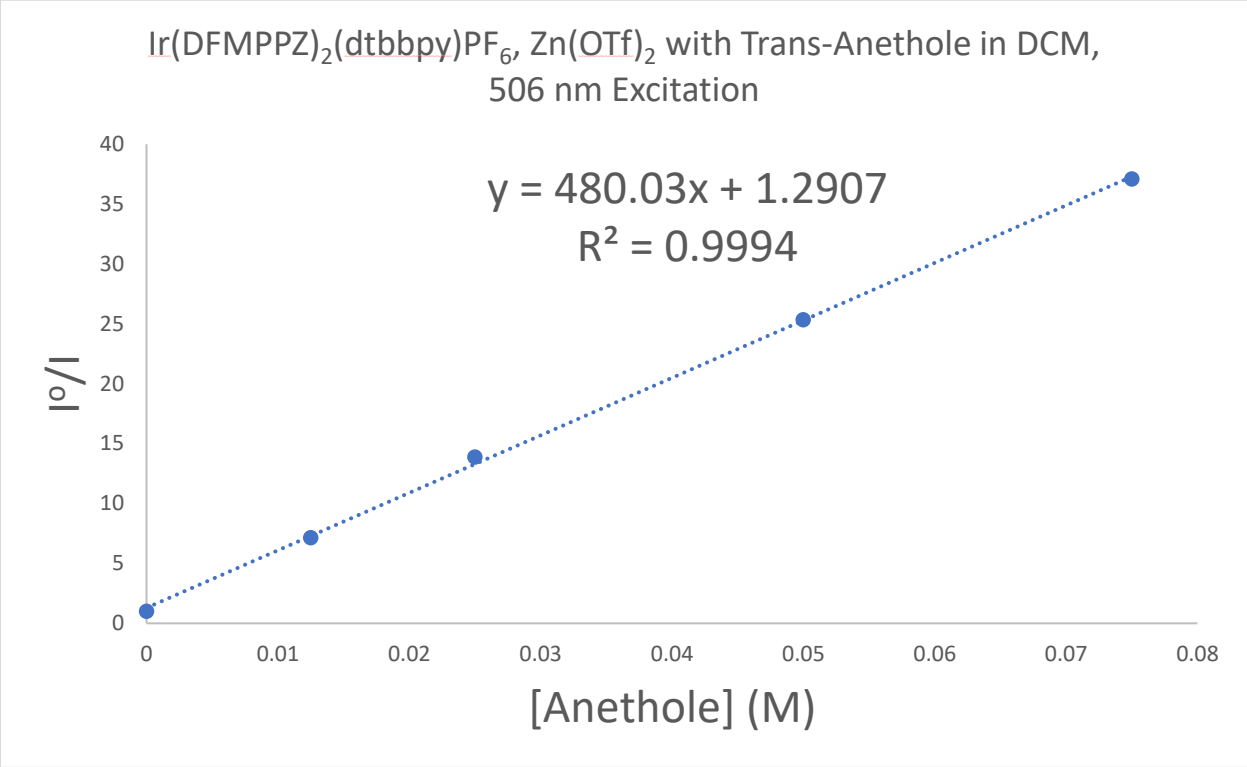
Ir(DFMPPZ)2(dtbbpy)PF6, Zn(OTf)2 with Trans-Anethole in DCM, 506 nm Excitation
y = 480.03x + 1.2907
R² = 0.9994
I°/I
[Anethole] (M)
0
5
10
15
20
25
30
35
40
0
0.01
0.02
0.03
0.04
0.05
0.06
0.07
0.08

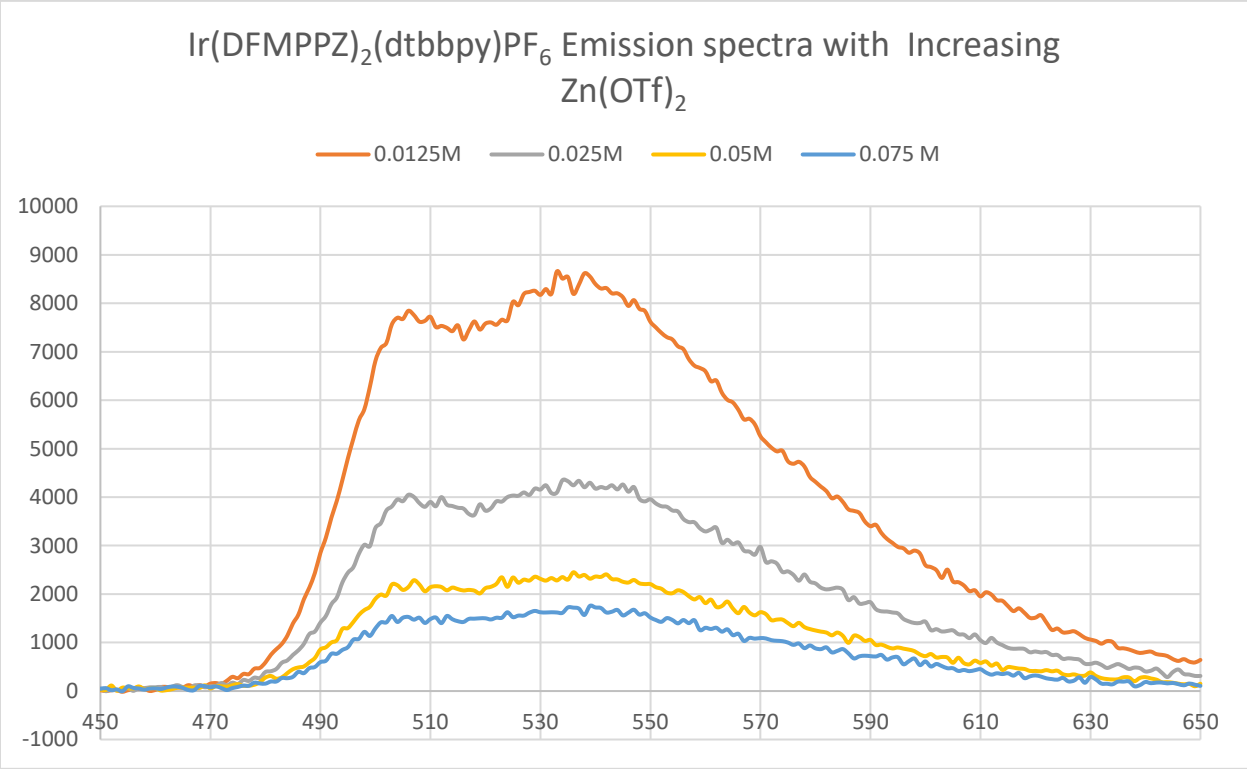
Ir(DFMPPZ)2(dtbbpy)PF6 Emission spectra with Increasing Zn(OTf)2
0.0125M
0.025M
0.05M
0.075 M
10000
9000
8000
7000
6000
5000
4000
3000
2000
1000
0
-1000
450
470
490
510
530
550
570
590
610
630
650

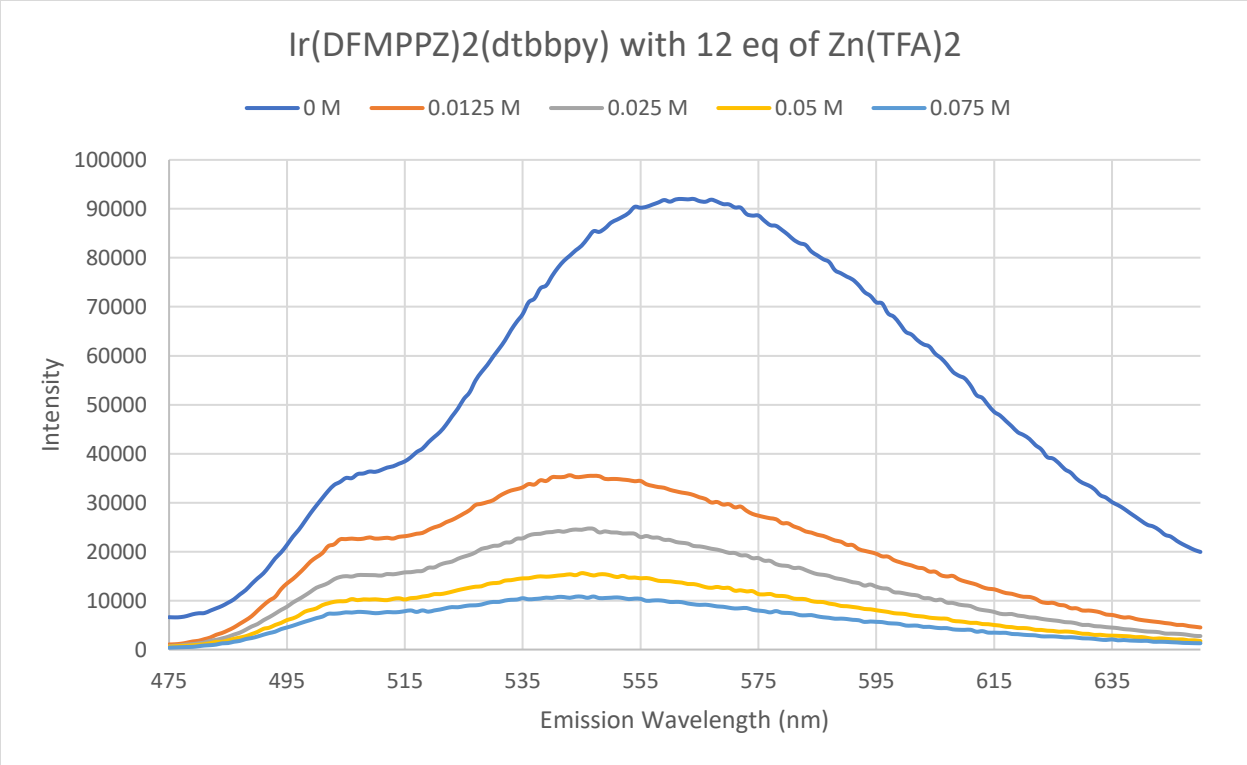
Ir(DFMPPZ)2(dtbbpy) with 12 eq of Zn(TFA)2
0 M
0.0125 M
0.025 M
0.05 M
0.075 M
Intensity
100000
90000
80000
70000
60000
50000
40000
30000
20000
10000
0
475
495
515
535
555
575
595
615
635
Emission Wavelength (nm)

3.6.7 Preliminary Scope studies for Lewis Acid Mediated Diels-Alder Reaction

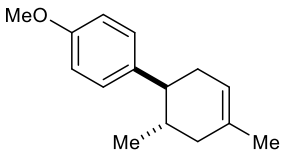

96%, 7:1 dr
15 min

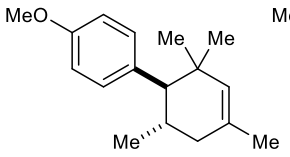

99%
1 hr

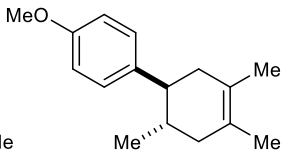

93%
15 min

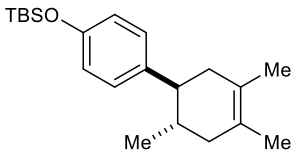

83%
4 hr

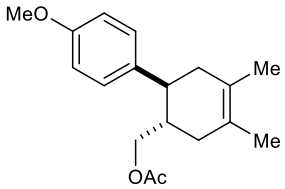

97%
4 hr

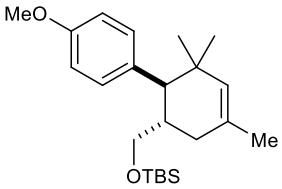

98%
2 hr

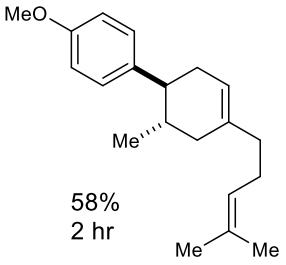

58%
2 hr

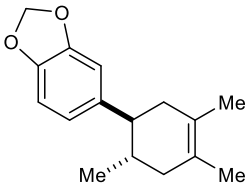

~13% conversion at 1 hr
~17% conversion at 20 hr

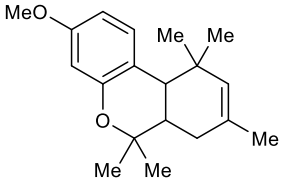

25% by IS, 48 hr
25% RSM (volatile)

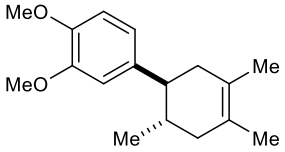

3% by IS, 5 hr
66% RSM

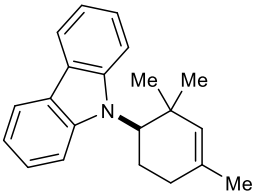

10% by IS, 24 hr
0% RSM

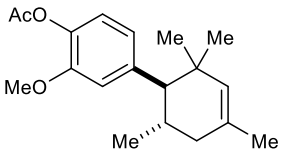

<10% conversion at 20 hr
(timecourse run)

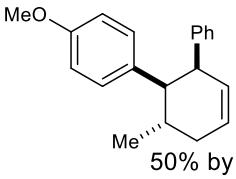

50% by IS
20 hr
trace RSM

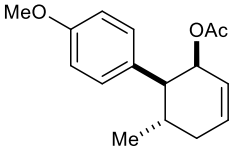

33% by IS
33% RSM
18 hr

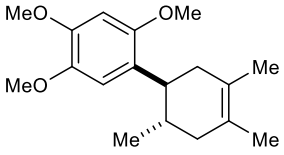

trace conversion at 20 hr
(timecourse run)

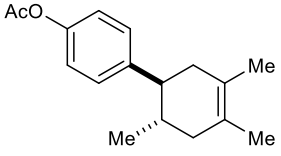

Trace at 4 hr with 0.5% Ir
<10% at 4 hr with 3% Ir

A preliminary scope for the Diels–Alder photocycloaddition catalyzed by zinc salts was explored using $Zn(TFA)_2$ and following the general procedure above using 100 mg of trans-anethole. Observed yields and deviations from standard conditions are listed.

3.7 References

(96) Skubi, K. L.; Kidd, J. B.; Jung, H.; Guzei, I. A.; Baik, M.-H.; Yoon, T. P. Enantioselective Excited-State Photoreactions Controlled by a Chiral Hydrogen-Bonding Iridium Sensitizer. *J Am Chem Soc* **2017**, *139* (47), 17186–17192. https://doi.org/10.1021/jacs.7b10586.

(97) Blum, T. R.; Miller, Z. D.; Bates, D. M.; Guzei, I. A.; Yoon, T. P. Enantioselective Photochemistry through Lewis Acid–Catalyzed Triplet Energy Transfer. *Science (1979)* **2016**, *354* (6318), 1391–1396.

(98) Miller, Z. D.; Lee, B. J.; Yoon, T. P. Enantioselective Crossed Photocycloadditions of Styrenic Olefins by Lewis Acid Catalyzed Triplet Sensitization. *Angewandte Chemie - International Edition* **2017**, *56* (39), 11891–11895. https://doi.org/10.1002/anie.201706975.

(99) Flamigni, L.; Barbieri, A.; Sabatini, C.; Ventura, B.; Barigelletti, F. Photochemistry and Photophysics of Coordination Compounds: Iridium BT - Photochemistry and Photophysics of Coordination Compounds II; Balzani, V., Campagna, S., Eds.; Springer Berlin Heidelberg: Berlin, Heidelberg, 2007; pp 143–203. https://doi.org/10.1007/128_2007_131.

(100) You, Y.; Nam, W. Photofunctional Triplet Excited States of Cyclometalated Ir(Iii) Complexes: Beyond Electroluminescence. *Chem Soc Rev* **2012**, *41* (21), 7061. https://doi.org/10.1039/c2cs35171d.

(101) Ashford, D. L.; Glasson, C. R. K.; Norris, M. R.; Concepcion, J. J.; Keinan, S.; Brennaman, M. K.; Templeton, J. L.; Meyer, T. J. Controlling Ground and Excited State Properties through Ligand Changes in Ruthenium Polypyridyl Complexes. *Inorg Chem* **2014**, *53* (11), 5637–5646. https://doi.org/10.1021/ic500408j.

(102) Henwood, A. F.; Zysman-Colman, E. Lessons Learned in Tuning the Optoelectronic Properties of Phosphorescent Iridium(Iii) Complexes. *Chemical Communications* **2017**, *53* (5), 807–826. https://doi.org/10.1039/C6CC06729H.

(103) Du, J.; Skubi, K. L.; Schultz, D. M.; Giles, A. C.; Rankin, C. H.; Kerr, R. A.; Robie, A. A.; Bender, J.; Perona, P.; Dickinson, M. H.; Robie, A. A.; Branson, S.; Branson, K.; Marchette, D. J.; Healy, D. M.; Chen, G.; Maggioni, M.; Edelsbrunner, H.; Harer, J.; Morozov, D.; Trosset, M. W.; Marchette, D. J.; Priebe, C. E.; Marchette, D. J.; Healy, D. M.; Khudanpur, S.; Eisner, J.; Priebe, C. E.; Groenen, P. J. F. A Dual-Catalysis Approach to Enantioselective [2 + 2] Photocycloadditions Using Visible Light. *Science (1979)* **2014**, *344*, 392–396.

(104) Wang, C.; Zheng, Y.; Huo, H.; Röse, P.; Zhang, L.; Harms, K.; Hilt, G.; Meggers, E. Merger of Visible Light Induced Oxidation and Enantioselective Alkylation with a Chiral Iridium Catalyst. *Chemistry – A European Journal* **2015**, *21* (20), 7355–7359. https://doi.org/10.1002/chem.201500998.

(105) Amador, A. G.; Yoon, T. P. A Chiral Metal Photocatalyst Architecture for Highly Enantioselective Photoreactions. *Angewandte Chemie - International Edition* **2016**, *55* (7), 2304–2306. https://doi.org/10.1002/anie.201511443.

(106) Prier, C. K.; Rankic, D. A.; MacMillan, D. W. C. Visible Light Photoredox Catalysis with Transition Metal Complexes: Applications in Organic Synthesis. *Chem Rev* **2013**, *113* (7), 5322–5363. https://doi.org/10.1021/cr300503r.

(107) Terrett, J. A.; Cuthbertson, J. D.; Shurtleff, V. W.; MacMillan, D. W. C. Switching on Elusive Organometallic Mechanisms with Photoredox Catalysis. *Nature* **2015**, *524* (7565), 330–334. https://doi.org/10.1038/nature14875.

(108) Shields, B. J.; Doyle, A. G. Direct C(Sp3)-H Cross Coupling Enabled by Catalytic Generation of Chlorine Radicals. *J Am Chem Soc* **2016**, *138* (39), 12719–12722. https://doi.org/10.1021/jacs.6b08397.

(109) Heitz, D. R.; Tellis, J. C.; Molander, G. A. Photochemical Nickel-Catalyzed C-H Arylation: Synthetic Scope and Mechanistic Investigations. *J Am Chem Soc* **2016**, *138* (39), 12715–12718. https://doi.org/10.1021/jacs.6b04789.

(110) Inagaki, A.; Edure, S.; Yatsuda, S.; Akita, M. Highly Selective Photo-Catalytic Dimerization of Alpha-Methylstyrene by a Novel Palladium Complex with Photosensitizing Ruthenium(II) Polypyridyl Moiety. *Chem Commun (Camb)* **2005**, No. 43, 5468–5470. https://doi.org/10.1039/b508013d.

(111) Shiba, Y.; Inagaki, A.; Akita, M. C-C Bond Forming Reductive Elimination from Diarylplatinum Complexes Driven by Visible-Light-Mediated Photoredox Reactions. *Organometallics* **2015**, *34* (20), 4844–4853. https://doi.org/10.1021/om501080v.

(112) Inagaki, A.; Yatsuda, S.; Edure, S.; Suzuki, A.; Takahashi, T.; Akita, M. Synthesis of Pd Complexes Combined with Photosensitizing of a Ruthenium(II) Polypyridyl Moiety through a Series of Substituted Bipyrimidine Bridges. Substituent Effect of the Bridging Ligand on the Photocatalytic Dimerization of α-Methylstyrene. *Inorg Chem* **2007**, *46* (7), 2432–2445. https://doi.org/10.1021/ic0612909.

(113) Murata, K.; Ito, M.; Inagaki, A.; Akita, M. Photocatalytic Styrene Polymerization by Novel Bichromophoric Pd Catalyst Having Long Excited-State Lifetime. *Chem Lett* **2010**, *39* (9), 915–917. https://doi.org/Doi 10.1246/Cl.2010.915.

(114) Murata, K.; Saito, K.; Kikuchi, S.; Akita, M.; Inagaki, A. Visible-Light-Controlled Homo- and Copolymerization of Styrenes by a Bichromophoric Ir–Pd Catalyst. *Chem. Commun.* **2015**, *51* (26), 5717–5720. https://doi.org/10.1039/C5CC00611B.

(115) Inagaki, A.; Nakagawa, H.; Akita, M.; Inoue, K.; Sakai, M.; Fujii, M. Synthesis of Pd Complexes Directly Linked to the Light-Absorbing [(Bpy)(3)Ru](2+) Unit and Their Photochemical Reactions toward Styrenes. *Dalton Trans* **2008**, No. 47, 6709–6723. https://doi.org/10.1039/b809020c.

(116) Murata, K.; Inagaki, A.; Akita, M.; Halet, J. F.; Costuas, K. Revelation of the Photoactive Species in the Photocatalytic Dimerization of α-Methylstyrene by a Dinuclear Ruthenium-Palladium Complex. *Inorg Chem* **2013**, *52* (14), 8030–8039. https://doi.org/10.1021/ic400666v.

(117) Son, C.; Inagaki, A. Synthesis and Photocatalytic Activity of a Naphthyl-Substituted Photosensitizing BINAP–Palladium Complex. *Dalton Transactions* **2016**, *45* (4), 1331–1334. https://doi.org/10.1039/C5DT04228C.

(118) Beauvilliers, E. E.; Meyer, G. J. Evidence for Cation-Controlled Excited-State Localization in a Ruthenium Polypyridyl Compound. *Inorg Chem* **2016**, *55* (15), 7517–7526. https://doi.org/10.1021/acs.inorgchem.6b00876.

(119) Lies, S.; Lin, S.; Yoon, T. P. Visible Light Photocatalysis of Radical Cation Diels–Alder Cycloadditions: Preparation of Tris(2,2'-Bipyrazyl) Ruthenium(II) Bis(Tetrakis(3,5-Bis(Trifluoromethyl)Phenyl)Borate). *Organic Syntheses* **2016**, *93* (Ii), 178–199. https://doi.org/10.15227/orgsyn.093.0178.

(120) Lin, S.; Ischay, M. A.; Fry, C. G.; Yoon, T. P. Radical Cation Diels–Alder Cycloadditions by Visible Light Photocatalysis. *J Am Chem Soc* **2011**, *133* (48), 19350–19353. https://doi.org/10.1021/ja2093579.

(121) Ischay, M. A.; Ament, M. S.; Yoon, T. P. Crossed Intermolecular [2 + 2] Cycloaddition of Styrenes by Visible Light Photocatalysis. *Chem Sci* **2012**, *3* (9), 2807–2811. https://doi.org/10.1039/C2SC20658G.

(122) Schultz, D. M.; Sawicki, J. W.; Yoon, T. P. An Improved Procedure for the Preparation of Ru(Bpz)3(PF6)2 via a High-Yielding Synthesis of 2,2'-Bipyrazine. *Beilstein J. Org. Chem.* **2015**, *11*, 61–65. https://doi.org/10.3762/bjoc.11.9.

(123) Ge, G.; He, J.; Guo, H.; Wang, F.; Zou, D. Highly Efficient Phosphorescent Iridium (III) Diazine Complexes for OLEDs: Different Photophysical Property between Iridium (III) Pyrazine Complex and Iridium (III) Pyrimidine Complex. *J Organomet Chem* **2009**, *694* (19), 3050–3057. https://doi.org/https://doi.org/10.1016/j.jorganchem.2009.05.037.

Chapter 4 Elucidating the Differences Between Electrochemical and Photochemical Systems

4.1 Abstract

Photoredox and electrochemical activation methods produce intermediates with common electronic structures. Despite this commonality, reaction outcomes for methods reported in the literature using these two approaches have comparatively little overlap. Our interest in photochemical reaction mechanisms, and indeed radical reaction mechanisms in general, led us to investigate the causes of this apparent disparity. Herein we report the development of an electrochemically initiated Giese addition and compare the mechanistic distinctions identified with an analogous photochemical system.

4.2 Background

Single electron oxidation and reduction of organic substrates has been used to enable a range of powerful synthetic transformations. Two methods for effecting these electron transfer events, photochemically initiated SET and electrochemistry, have received increased attention from the synthetic community over the past decade.[7,35,36,106,124–127] A cursory analysis of common reaction intermediates produced in both of these systems would suggest that both methods should be able to effect similar reaction outcomes. In practice, this does not seem to be the case, however. The bulk of electrochemical methods reported are net-reductive or, more commonly, net-oxidative in nature. On the other hand, reports of photochemical processes are dominated by net redox-neutral transformations. Development of net-

oxidative or reductive reactions in photochemical systems could, in fact, be argued to be a significant challenge that is still under active investigation.

While it is possible that the observed discrepancies between outcomes of these reactions is a coincidental consequence of problem selection in either field, there also exists the possibility that the differences are a direct manifestation of subtle mechanistic differences between the two modes of activation. We found this to be a compelling question and believed that the answer would be valuable to ongoing research in our lab and in the field in general. Coincidentally, several other reviews addressing similar subject matter have been published during the preparation of these results.[128,129]

4.3 Comparison of electrochemical and photochemical systems

We decided that a reasonable approach to address the question of mechanistic interchangeability between electrochemical and photochemical activation would be to develop a net redox-neutral reaction under electrochemical conditions. Our lab has developed several photochemical reactions of this type and we felt that we had a reasonable understanding of the mechanistic principles at work in those systems. If the development of an electrochemically activated analogue proved to be trivial, we would be able to offer comment on such an outcome and potentially inspire a new avenue of development for the synthetic electrochemical community. If, on the other hand, that proved to not be the case, the optimization

principles derived from the development process would surely inform mechanistic insights into the differences between the activation modes.

Based on first principles, there were a few reasons we imagined that there might be a tangible difference between photochemical and electrochemical activation. Many of these reasons relate to the nature and relative distributions of redox equivalents in each system. In photoredox reactions, oxidizing and reducing equivalents are generated from the same species, the photocatalyst, and are present in low concentrations. In electrochemical reactions, however, reduction at the cathode is spatially separated from corresponding oxidation at the anode, requiring mass transfer through solution to achieve a neutral redox cycle. Thus, it seems that photochemistry is poised to effect redox neutral transformations, while electrochemical systems might favor reactivity that requires sequential reduction or oxidation steps in a product-forming cascade.

Our approach to investigating this question began with efforts to develop electrochemical conditions for the reaction of α-silyl amines with Michael acceptors. The photochemical analogue of this reaction, first studied by Mariano and Pandey, is a well-studied, classic method in the literature and several labs, including our own, have reported asymmetric variants (Figure 4.1).[130–137] This reaction proceeds though one-electron oxidation and desilylation of an α-silyl amine (**4.1**) to yield an α-amino radical (**4.4**),

which then adds to a Michael acceptor (**4.2**). The radical product of the Michael addition is reduced by the photocatalyst, or by another equivalent of substrate, to yield the net redox-neutral transformation to product (**4.3**).

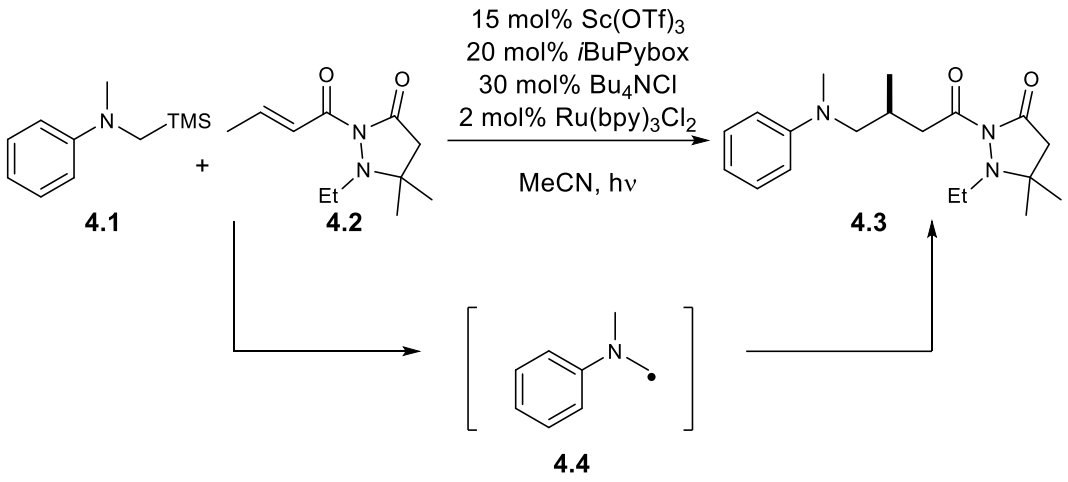

Figure 4.1

While the optimized conditions for our asymmetric variant of this transformation employ $Ru(bpy)_3Cl_2$ as a photoredox catalyst for the one-electron oxidation of **4.1** to yield α-amino radical **4.4**, we reasoned that replacement of the photocatalyst with an electrode should still allow us to access the same intermediate.[131] Analysis of the products of a reaction performed with this simple exchange did indicate the α-amino radical intermediate was formed; however, no Giese addition products were observed. Instead, while **4.1** was fully consumed, we identified N-methylaniline (**4.5**) and α-amino radical dimer (**4.6**) as the sole products of this reaction, Figure 4.2. Formation of dimer **4.6** can be easily rationalized by the relatively

high concentration of radical intermediates formed in close proximity at the electrode surface. N-methylaniline is proposed to be the product of hydrolysis of the corresponding iminium, which would be formed from a second oxidation of the α-amino radical (**4.4**). Exclusive formation of these products supported our hypotheses relating to the relative nature of redox events at an electrode surface versus with a photocatalyst.

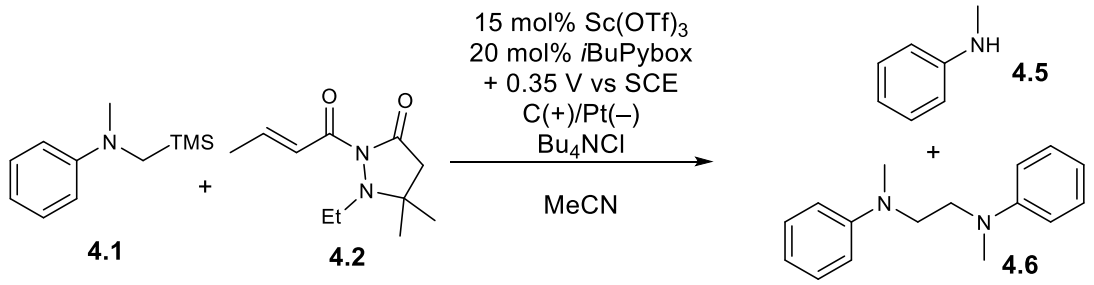

Figure 4.2

We imagined that two changes to the electrochemical system might rescue the desired reactivity, allowing us to further compare mechanistic differences between optimized conditions for these reactions. First, we proposed that use of a redox mediator could be used to reduce local concentration of α-amino radical intermediates near the anode surface, which would in turn reduce the likelihood of overoxidation and dimerization reactions. Second, we believed that using more electrophilic Michael acceptors would allow for faster capture of radical intermediates, further reducing the operation of unproductive side reactions. Application of these hypotheses and a short optimization led to the successful reaction conditions

in Figure 4.3. Use of ferrocene as a redox mediator for this reaction proved to be necessary to obtain good yields, entry 2. Additionally, while it was necessary to use relatively activated Michael acceptors, we also found that changing the electrolyte to a more Lewis acidic species, $LiClO_4$, facilitated formation of the desired product, entry 4. Finally, the electrochemical reaction performed much better in methanol as a solvent, as opposed to acetonitrile, the solvent found to be optimal for the photochemical reaction, entry 1 vs entry 5.

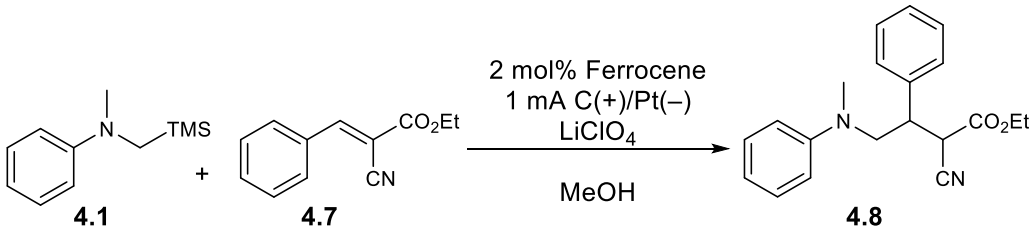

Entry	Deviation from Standard Conditions	Yield
1	None	91%
2	No Ferrocene	7%
3	–0.05 V vs Fc^+/Fc (costant potential)	90%
4	Bu_4NClO_4 instead of $LiClO_4$	65%
5	MeCN instead of MeOH	18%
6	$Ru(bpy)_3Cl_2$ instead of Ferrocene 509 nm light instead of Electrode	99%

Figure 4.3

With optimized conditions in hand, we were able to evaluate the qualitative distinctions between optimization factors in the electrochemical and photochemical reactions. First, the role of ferrocene as a

redox mediator was established. Direct electrolysis in the absence of ferrocene resulted in significant reduction in yield of the desired product, favoring overoxidation of the α-silyl amine. Furthermore, while we used constant current electrolysis for most of our experiments, the reaction also performed well when run at constant voltage set to oxidize ferrocene, Figure 4.3 entry 3. Finally, analytical CV experiments in the presence of α-silyl amine and ferrocene revealed a significant catalytic wave, consistent with the assertion that oxidized ferrocene is capable of mediating oxidation of the amine, see Supporting Information. Running the photochemical reaction under the optimized electrochemical conditions, replacing the electrode and ferrocene mediator with a ruthenium photocatalyst and irradiating with 509 nm light, yielded the product in quantitative yields, Figure 4.3 entry 6. The necessity of a mediator in our electrochemical reaction further affirms our assumptions about the difference in the nature of redox equivalents in the two systems.

Next, we examined more direct comparisons of the electrochemical and photochemical reactions. We imagined that a more quantitative metric for comparing the efficiency of these reactions could be informative, namely comparison of quantum and faradaic yields for the two systems. While reaction and conversion rates are common metrics for the efficiency of thermal reactions, the rates of photochemical and electrochemical processes are often dependent on not just the inherent reactivity of the substrates, but also

on external factors such as light intensity and applied current, respectively. Due to these external dependencies, comparing the two systems at hand based on their relative conversion rates would be meaningless. However, comparison of the faradaic yield for the electrochemical reaction and quantum yield for the photochemical reaction allows us to normalize the data for per-electron efficiency in each setup. As the intermediates being accessed by either mode of activation are the same in each process, it could be expected that the downstream chain propagation pathways would operate with similar efficiency. Indeed, extrapolation of the quantum and faradaic yields measured in methanol gave nearly identical chain lengths, Figure 4.4a.

Interestingly, performing the same analysis for the photochemical system in MeCN gave a much smaller chain length, Figure 4.4b, while the electrochemical system was relatively unaffected. These results can be rationalized, however, by considering the rate of competitive back-electron-transfer to the photocatalyst as an alternative chain termination event in the absence of a silophile, such as MeOH. Mariano and coworkers showed in their work that back-electron-transfer rates for an alpha-silyl amine were comparable to decay by desilylation. They reported that inclusion of MeOH in MeCN, or switching the solvent to MeOH, however, significantly enhanced desilylation rates such that the rates of other decay pathways, including back-electron-transfer to the photocatalyst, became less competitive.[138,139] Mariano

also showed in his work that $LiClO_4$, as well as several tert-butyl ammonium salts, promoted desilylation in a similar fashion. We presume that the combined use of $LiClO_4$ electrolyte and MeOH solvent, as in Figure 4.4a, is sufficient to outcompete back-electron-transfer as a possible chain-ending decay pathway. However, while back-electron-transfer to an electrode is not possible in the electrochemical system it could be surmised that such a pathway is responsible for the drastic drop in average chain length for the photochemical system in Figure 4.4b, where MeOH is absent. Based on these results we rationalized that comparison of quantum yield and faradaic efficiency do indeed provide a valid metric for evaluation of the efficiencies of the two systems, provided that the rates of other competing decay pathways are accounted for when drawing conclusions from the results obtained.

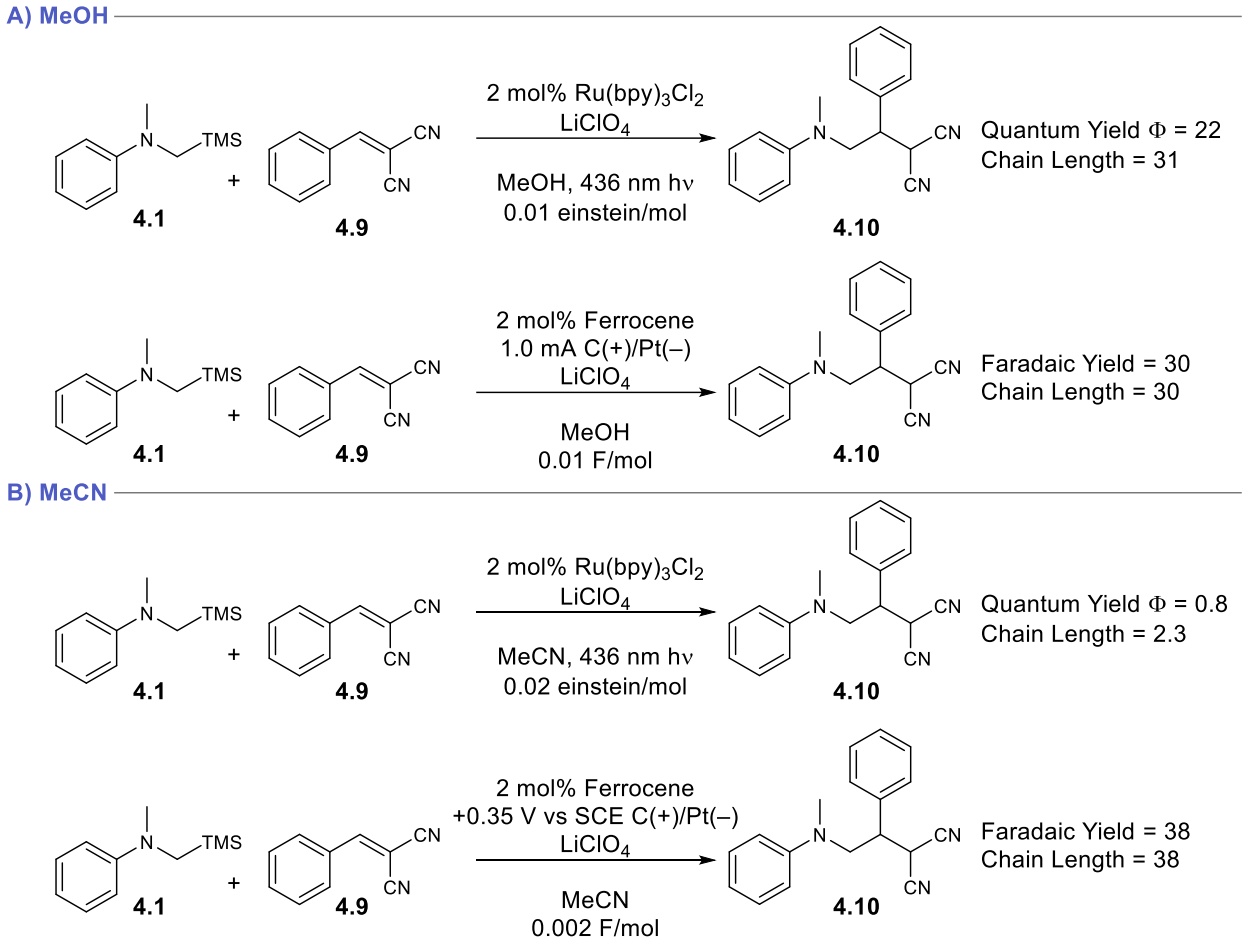

Figure 4.4

The last major difference between these two systems that we hoped to understand was the nature of the solvent dependance. While the propensity of MeOH to enhance the rate of desilylation can be used to rationalize the difference in photochemical and electrochemical chain lengths, the faradaic yields observed in the MeCN conditions were similar to those observed in MeOH and suggest that the reaction should perform similarly well in that solvent. However, when the reaction is run in MeCN, we observed relatively slow conversion and a stark decrease in yield of the desired product, Figure 4.3 entries 1 and 5,

with over-oxidation of the substrate observed as major byproducts. We hypothesized that the lack of an easily reduceable reaction partner in the electrochemical cell, especially at the beginning of the reaction, could also contribute to the sluggish reactivity observed in the MeCN conditions. Using MeOH as the solvent, however, might allow for relatively facile proton reduction at the cathode, which would help balance the electrochemical potential difference across the cell and avoid potential spikes leading to over-oxidation. In support of this hypothesis, analysis of the post-reaction headspace of the reaction performed in MeOH confirmed the presence of H_2, showing that our proposed reaction pathway is indeed operable under the optimized conditions, see Supporting Information. Based on these data we propose that use of MeOH as a reaction solvent facilitates the reaction via two pathways: 1) by promotion of desilylation to initiate and propagate product forming chain processes, and 2) by acting as a source of protons for H_2 reduction at the cathode to balance electrochemical potential across the cell.

4.4 Conclusions

In conclusion, we have been able to develop an electrochemically initiated Giese addition of α-silyl amines with activated Michael acceptors. This development has allowed us to compare optimization conditions for electrochemical and photochemical systems, highlighting differences in the largely physical constraints associated with the nature of reducing and oxidizing equivalents in each case. Our findings

support the assertion that electrochemical systems are inherently suited to net-reductive or -oxidative reaction development due to the chemical environment produced at the electrode surface. However, we were also able to show that use of a redox mediator and careful selection of electrolyte, solvent, and reaction partners could be used to overcome some of the inherent limitations in the development of redox neutral electrochemical methods. Additionally, our findings support the assertion that downstream chain propagation efficiencies are relatively unaffected by activation mode when appropriate conditions are met.

4.5 Contributions

Reaction optimization, controls, and quantum and faradaic yield determination were performed by Shane Lies. Intellectual contributions, reaction headspace analysis, and assistance in manuscript preparation were provided by the Sam Cahoon.

4.6 Supporting information

General Information

All reaction glassware was flame- or oven-dried prior to use. All commercially available chemicals were used as purchased from Sigma Aldrich or Oakwood Chemical. Acetonitrile (MeCN) was purified by elution through alumina and stored under Argon. MeOH was purchased as HPLC grade solvent from Fischer or Sigma Aldrich. Solvents for chromatography were used as received from Thermo Fischer or Sigma Aldrich. Flash column chromatography was performed with Purasil 60Å silica gel. Silyl amines were distilled prior to use. Ferrocene and electrolyte were also assessed for purity before use and recrystallized by reported procedures when necessary.

^{1}H,$^{13}C\{^{1}H\}$, and $^{19}F\{^{1}H\}$ data for all previously uncharacterized compounds were obtained using Bruker Avance-400 and Avance-500 spectrometers with BBFO+ and DCH probes. ^{1}H spectra were internally referenced to tetramethyl silane (TMS). Multiplicities are defined using the following abbreviations: s (singlet), d(doublet), t (triplet), q (quartet), p (pentet), sept (septet), m (multiplet), and combined variations. The NMR spectrometers used in this work are supported by the NSF CHE-1048642, a generous gift from Paul J. and Margaret M. Bender, and the University of Wisconsin.

High Resolution Mass spectrometry was performed using a Thermo Q Exactive™ Plus supported by the NIH 1S10 OD020022-1.

A simple undivided electrochemical cell was fabricated with the assistance of Dr. Mohammad Rafiee, Shannon Goes, and Tracy Drier. The cell consists of a single reaction chamber that seals via an O-ring connection to a head piece through which the electrodes are introduced to the reaction. The cell is sealed at the top by a rubber septum, through which the electrode wires are inserted.

Cyclic voltammetry and bulk electrolysis were performed using a Pine WaveNow potentiostat and Aftermath software version 1.3.6972.

Headspace analysis was performed using a Shimadzu GC-2010 Plus Gas Chromatograph.

4.6.1 Conjugate Addition of Electrochemically Generated α-Amino Radicals

General procedure: A solution of α-trimethylsilyl aniline (1.1–3 equiv), acceptor (1 equiv), ferrocene (0.02 equiv, 2 mol %), and $LiClO_4$ (1 equiv) in MeOH (0.05 M) was placed in the electrochemical cell and sparged with N_2 for at least 1 minute. The resulting solution was subjected to bulk electrolysis with stirring and a constant current of 1 mA. After electrolysis, the electrodes were rinsed with MeOH, and the solvent was removed under reduced pressure. The residue was purified by chromatography on SiO_2 to afford pure product.

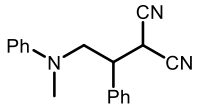

2-(2-(methyl(phenyl)amino)-1-phenylethyl)malononitrile (**S4.1**) Synthesized according to the general procedure. *N*-methyl-*N*-((trimethylsilyl)methyl)aniline (0.0432 g, 0.223 mmol), 2-benzylidenemalononitrile (0.0316 g, 0.205 mmol), ferrocene (0.0007 g, 0.004 mmol), $LiClO_4$ (0.0213g, 0.200 mmol), and MeOH (4 mL, 0.05 M) were added to the electrolysis cell and bulk electrolysis was performed for 30 minutes. After chromatography on SiO_2 (2:1 hexane:Et_2O), isolated the title compound (48.4 mg, 0.176 mmol, 86% yield) as a colorless oil.

^{1}H NMR (400 MHz, $CDCl_3$): δ 7.48 – 7.37 (m, 5H), 7.33 – 7.26 (m, 2H), 6.86 (t, *J* = 7.3 Hz, 1H), 6.81 (d, *J* = 7.8 Hz, 2H), 4.23 (d, *J* = 4.6 Hz, 1H), 3.90 (dd, *J* = 14.9, 10.2 Hz, 1H), 3.70 (dd, *J* = 14.9, 5.1 Hz, 1H), 3.66 – 3.58 (m, 1H), 2.97 (s, 3H);

^{13}C NMR (101 MHz, $CDCl_3$) δ 148.72, 135.06, 129.83, 129.61, 129.59, 128.33, 119.00, 114.03, 112.35, 111.95, 55.54, 45.01, 41.08, 27.19;

HRMS (ESI^+): $[M+H]^+$ calculated for $[C_{18}H_{18}N_3]^+$ required 276.1495 m/z, found 276.1493 m/z.

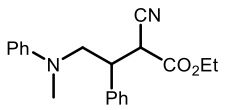

ethyl 2-cyano-4-(methyl(phenyl)amino)-3-phenylbutanoate (**S4.2**): Synthesized according to the general procedure. *N*-methyl-*N*-((trimethylsilyl)methyl)aniline (0.043 g, 0.222 mmol), ethyl (E)-2-cyano-3-phenylacrylate (0.041g, 0.201 mmol), ferrocene (0.0007 g, 0.004 mmol), $LiClO_4$ (0.0213g, 0.200 mmol), and MeOH (4 mL, 0.05 M) were added to the electrolysis cell and bulk electrolysis was performed for 30 min. After chromatography on SiO_2 (2:1 hexane:Et_2O), isolated the title compound (61.0 mg, 0.189 mmol, 94% yield, 1.3:1 *d.r.*) as a colorless oil.

^{1}H NMR (400 MHz, $CDCl_3$) (mixture of diastereomers): δ 7.41 – 7.22 (m, 7H), 6.84 – 6.72 (m, 3H), 4.10 – 3.75 (m, 5H), 3.67 – 3.57 (m, 1H), 2.95 & 2.83 (s, 3H), 1.07 & 1.00 (t, *J* = 7.2 Hz, 3H).

^{13}C NMR (101 MHz, $CDCl_3$) (mixture of diastereomers):δ 165.51, 164.91, 149.18, 148.95, 138.25, 136.86, 129.62, 129.43, 129.24, 129.10, 128.62, 128.46, 128.07, 118.02, 117.70, 116.20, 115.98, 113.37, 113.18, 63.04, 62.95, 56.76, 56.17, 44.38, 43.92, 42.86, 41.73, 40.66, 40.23, 13.99, 13.81.

HRMS (ESI$^+$): $[M+H]^+$ calculated for $[C_{20}H_{23}N_2O_2]^+$ required 323.1754 m/z, found 323.1751 m/z.

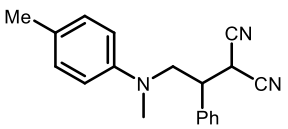

2-(2-(methyl(phenyl)amino)-1-phenylethyl)malononitrile (**S4.3**):

Synthesized according to the general procedure. *N*,4-dimethyl-*N*-((trimethylsilyl)methyl)aniline (0.0453 g, 0.218 mmol), 2-benzylidenemalononitrile (0.0310 g, 0.201 mmol), ferrocene (0.0007 g, 0.004 mmol), $LiClO_4$ (0.0213g, 0.200 mmol), and MeOH (4 mL, 0.05 M) were added to the electrolysis cell and bulk electrolysis was performed for 45 minutes. After chromatography on SiO_2 (5:1 hexane:Et_2O), isolated the title compound (50.4 mg, 0.175 mmol, 87% yield) as a colorless oil.

^{1}H NMR (400 MHz, $CDCl_3$): 7.48 – 7.37 (m, 5H), 7.11 (d, *J* = 8.3 Hz, 2H), 6.75 (d, *J* = 8.6 Hz, 2H), 4.28 (d, *J* = 4.3 Hz, 1H), 3.82 (dd, *J* = 14.4, 10.2 Hz, 1H), 3.67 – 3.54 (m, 2H), 2.94 (s, 3H), 2.29 (s, 3H).

^{13}C NMR (101 MHz, $CDCl_3$) δ 146.78, 135.09, 130.33, 129.55, 129.52, 128.82, 128.34, 114.87, 112.45, 111.96, 55.78, 45.01, 41.55, 27.14, 20.52.

HRMS (ESI$^+$): $[M+H]^+$ calculated for $[C_{19}H_{20}N_3]^+$ required 290.1652 m/z, found 290.1658 m/z.

4.6.2 Electrochemical Characterization of Mediated Electrolysis Conditions

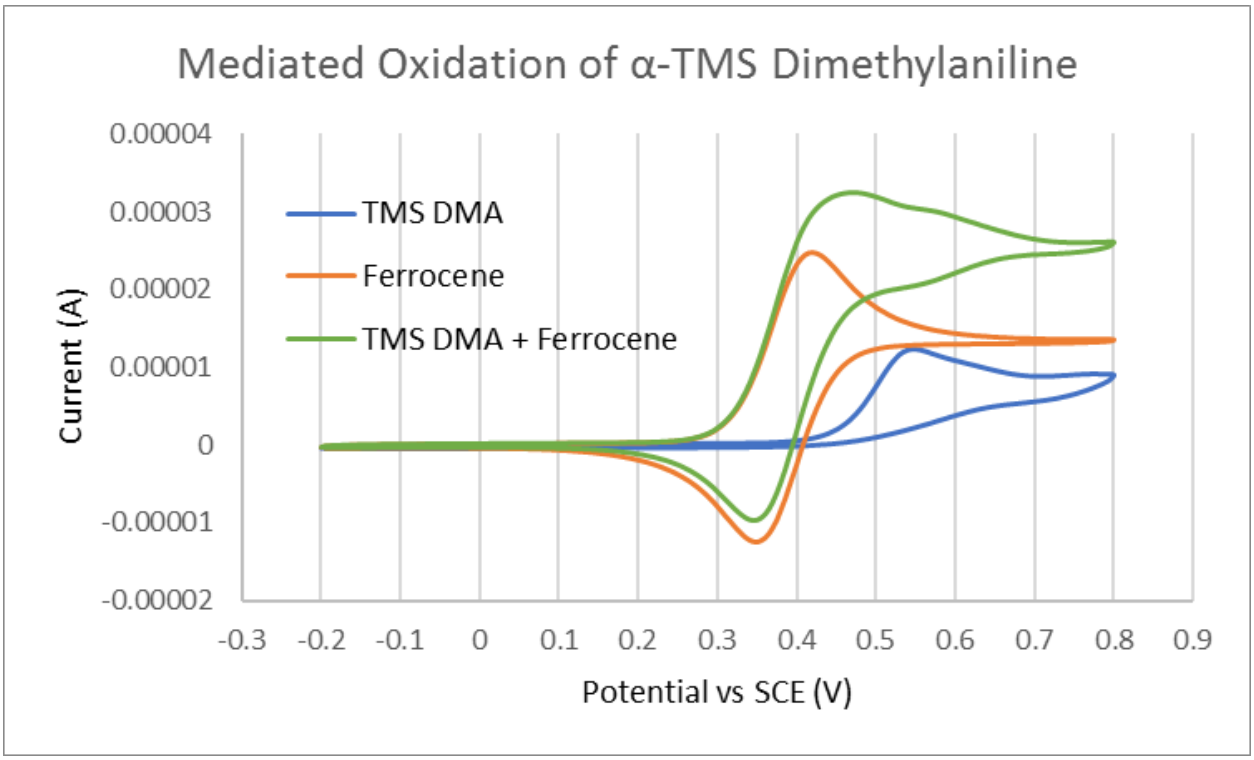

Observation of Catalytic Wave for Ferrocene Mediated Electrolysis. Working solutions for analysis by cyclic voltammetry were prepared to 1mM in substrate and 0.1 M $LiClO_4$ in MeOH. Solutions were prepared such that ferrocene was 1 mM when present. All solutions were sparged with N_2 for at least one minute prior to analysis and scans were performed under positive N_2 atmosphere provided by a Schlenk line. The working electrode was polished between each scan using alumina slurry and polishing pad, then rinsed with MeOH to ensure removal of any surface contaminants. A blank solution and each working solution were scanned from -500 mV to +900 mV vs Ag/0.01 M $AgNO_3$ in MeOH at a scan rate of 50 mV/s.

Electrodes:

Working Electrode - Glassy Carbon Plate

Counter Electrode - Pt wire

Reference Electrode - Ag wire in 0.01 M $AgNO_3$, 0.1 M $LiClO_4$ in MeOH.

4.6.3 Headspace Analysis of Reaction Mixture

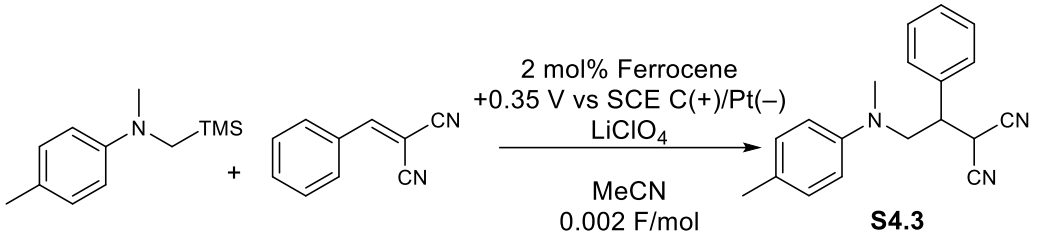

The reaction to form S4.3 was set up via the general procedure, sparging for 5 minutes. Before electrolysis was performed, the headspace of the reaction was analyzed by GC by taking an aliquot with a 100 μL syringe. Analysis confirmed the complete exclusion of O_2 and the lack of H_2 under the initial conditions. The cell was sealed with wax on top of the septum and electrolysis was performed according to the general procedure with omission of the normal connection to positive N_2 pressure provided by the Schlenk line. After the reaction period the headspace of the reaction was again sampled by syringe and GC analysis. Analysis of the post-reaction headspace confirmed the presence of H_2, as compared to an authentic sample. O_2 was also observed, presumably due to some amount of leakage through the septum. Analysis of ambient air, however, confirmed the lack of observable amounts of H_2 in the atmosphere, suggesting that H_2 was indeed being produced by the reaction process.

GC analyses were run on an RT Q-bond column, 30.0 m length, 20 μm film thickness, 0.53 mm inner diameter. Argon was used as a carrier gas. Measurements were provided by TCD analysis at 180 °C with a sampling rate of 40 msec, current of 45 mA at negative polarity. Instrumentation and GC method development were generously provided by the Hermans group at UW-Madison.

H2 (4.803 min)

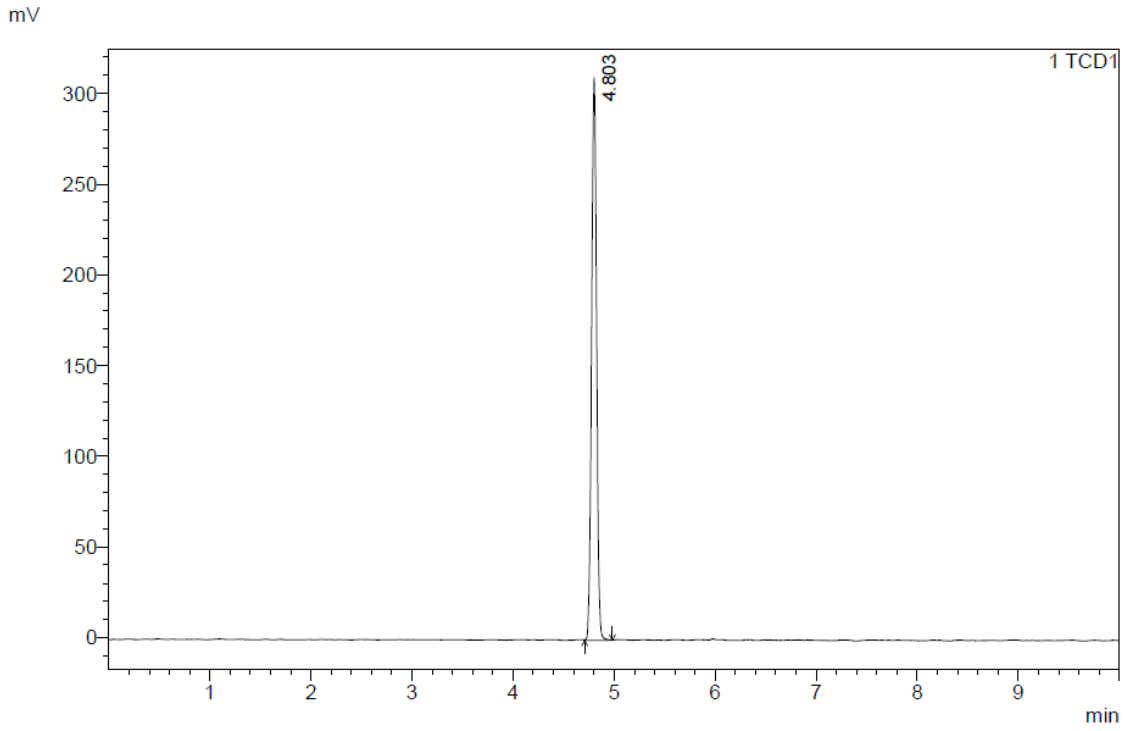

Air (5.277 min – O_2, 5.935 min – N_2)

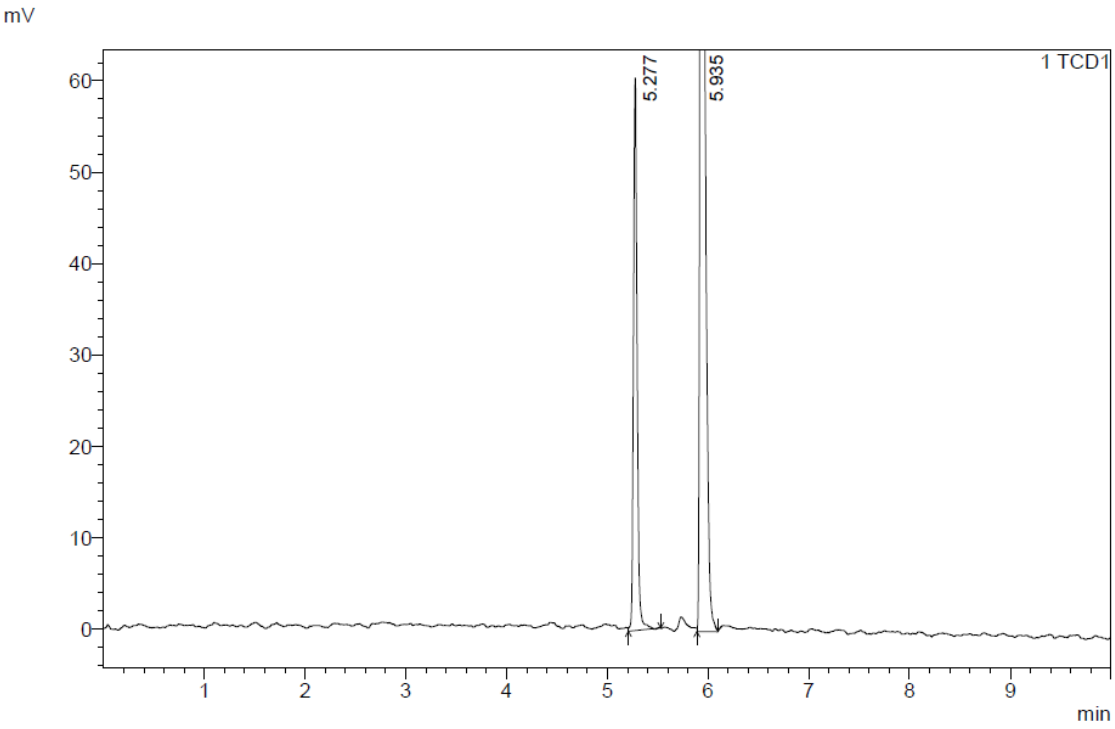

Pre-Reaction Headspace (5.943 min – N_2)

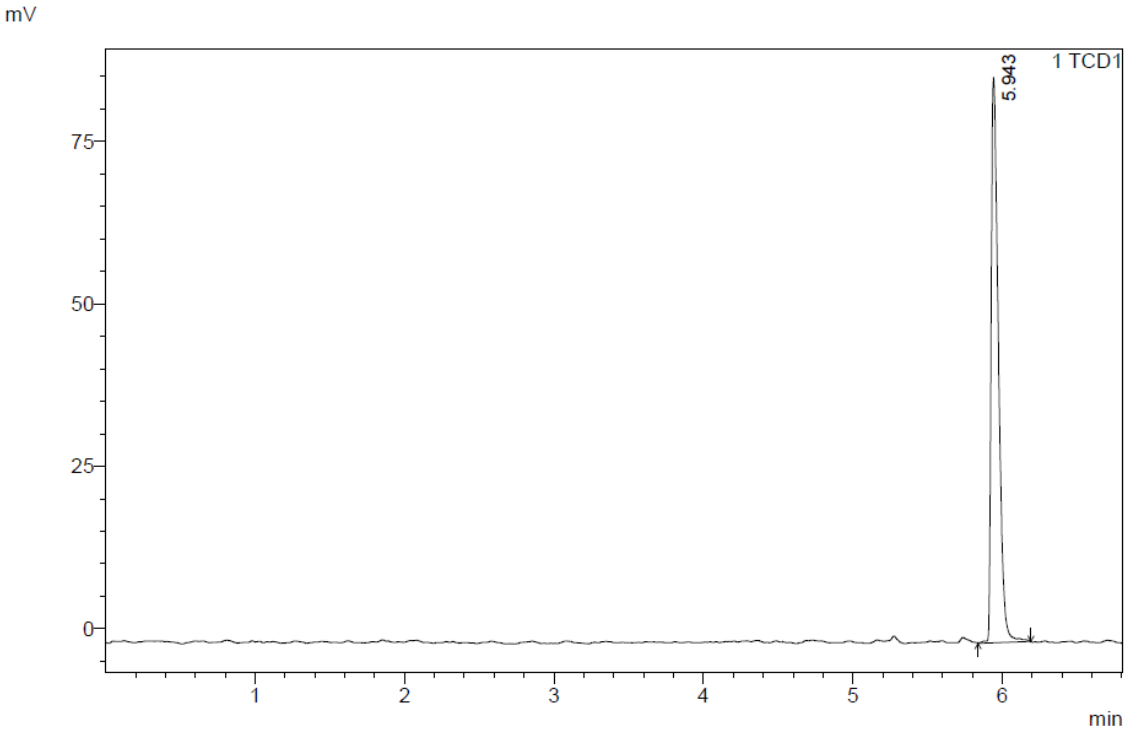

Post Reaction Headspace (4.792 min – H_2, 5.281 min – O_2, 5.936 min – N_2)

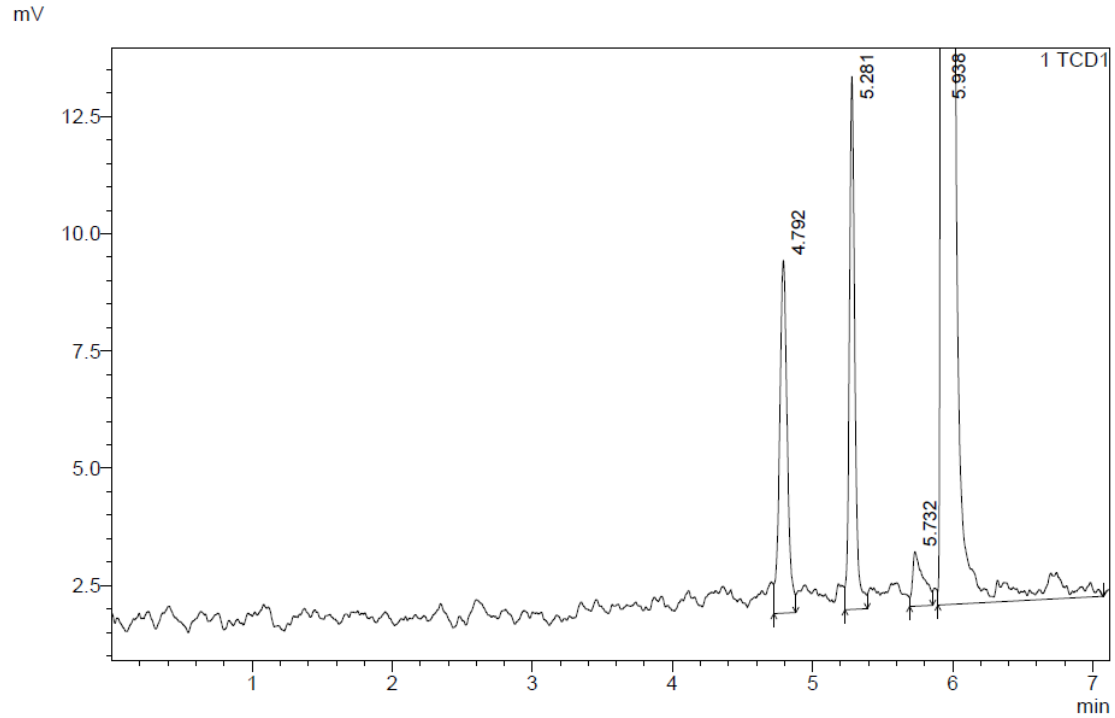

4.7 References

(124) Romero, N. A.; Nicewicz, D. A. Organic Photoredox Catalysis. *Chem Rev* **2016**, *116* (17), 10075–10166. https://doi.org/10.1021/acs.chemrev.6b00057.

(125) Narayanam, J. M. R.; Stephenson, C. R. J. Visible Light Photoredox Catalysis: Applications in Organic Synthesis. *Chem Soc Rev* **2011**, *40* (1), 102–113. https://doi.org/10.1039/b913880n.

(126) Sperr, J. B.; Wright, D. L. The Application of Cathodic Reductions and Anodic Oxidations in the Synthesis of Complex Molecules. *Chem Soc Rev* **2006**, *35* (7), 605–621. https://doi.org/10.1039/B512308A.

(127) Wiebe, A.; Gieshoff, T.; Möhle, S.; Rodrigo, E.; Zirbes, M.; Waldvogel, S. R. Electrifying Organic Synthesis. *Angewandte Chemie - International Edition* **2018**, *57* (20), 5594–5619. https://doi.org/10.1002/ANIE.201711060.

(128) Tay, N. E. S.; Lehnherr, D.; Rovis, T. Photons or Electrons? A Critical Comparison of Electrochemistry and Photoredox Catalysis for Organic Synthesis. *Chem Rev* **2022**, *122* (2), 2487–2649. https://doi.org/10.1021/ACS.CHEMREV.1C00384/ASSET/IMAGES/MEDIUM/CR1C00384_0144.GIF.

(129) Verschueren, R. H.; de Borggraeve, W. M. Electrochemistry and Photoredox Catalysis: A Comparative Evaluation in Organic Synthesis. *Molecules* **2019**, *24* (11), 2122. https://doi.org/10.3390/MOLECULES24112122.

(130) Ruiz Espelt, L.; Wiensch, E. M.; Yoon, T. P. Brønsted Acid Cocatalysts in Photocatalytic Radical Addition of α-Amino C-H Bonds across Michael Acceptors. *Journal of Organic Chemistry* **2013**, *78* (8), 4107–4114. https://doi.org/10.1021/JO400428M/SUPPL_FILE/JO400428M_SI_001.PDF.

(131) Ruiz Espelt, L.; McPherson, I. S.; Wiensch, E. M.; Yoon, T. P. Enantioselective Conjugate Additions of α-Amino Radicals via Cooperative Photoredox and Lewis Acid Catalysis. *J Am Chem Soc* **2015**, *137* (7), 2452–2455. https://doi.org/10.1021/ja512746q.

(132) Hasegawa, E.; Xu, W.; Mariano, P. S.; Yoon, U. C.; Kim, J. U. Electron-Transfer-Induced Photoadditions of the Silyl Amine Et2NCH2TMS to α,β-Unsaturated Cyclohexenones. Dual Reaction

Pathways Based on Ion-Pair-Selective Cation-Radical Chemistry. *J Am Chem Soc* **1988**, *110* (24), 8099–8111. https://doi.org/10.1021/JA00232A023/ASSET/JA00232A023.FP.PNG_V03.

(133) Brumfield, M. A.; Quillen, S. L.; Yoon, U. C.; Mariano, P. S. A Novel Method for Heteroatom-Substituted Free Radical Generation by Photochemical Electron-Transfer-Induced Desilylation of RXCH2Me3Si Systems. *J Am Chem Soc* **1984**, *106* (22), 6855–6856. https://doi.org/10.1021/JA00334A072/ASSET/JA00334A072.FP.PNG_V03.

(134) Pandey, G.; Devi Reddy, G.; Kumaraswamy, G. Photoinduced Electron Transfer (PET) Promoted Cyclisations of 1-[N-Alkyl-N-(Trimethylsilyl)Methyl]Amines Tethered to Proximate Olefin: Mechanistic and Synthetic Perspectives. *Tetrahedron* **1994**, *50* (27), 8185–8194. https://doi.org/10.1016/S0040-4020(01)85300-X.

(135) Pandey, G.; Kumaraswamy, G.; Bhalerao, U. T. Photoinduced Set Generation of α-Amineradicals : A Practical Method for the Synthesis of Pyrrolidines and Piperidines. *Tetrahedron Lett* **1989**, *30* (44), 6059–6062. https://doi.org/10.1016/S0040-4039(01)93854-7.

(136) Bauer, A.; Westkämper, F.; Grimme, S.; Bach, T. Catalytic Enantioselective Reactions Driven by Photoinduced Electron Transfer. *Nature* **2005**, *436* (7054), 1139–1140. https://doi.org/10.1038/nature03955.

(137) Xu, W.; Jeon, Y. T.; Hasegawa, E.; Yoon, U. C.; Mariano, P. S. Novel Electron-Transfer Photocyclization Reactions of α-Silyl Amine α,β-Unsaturated Ketone and Ester Systems. *J Am Chem Soc* **1989**, *111* (1), 406–408. https://doi.org/10.1021/JA00183A081/ASSET/JA00183A081.FP.PNG_V03.

(138) Zhang, X.; Yeh, S. R.; Hong, S.; Freccero, M.; Albini, A.; Falvey, D. E.; Mariano, P. S. Dynamics of α-CH Deprotonation and α-Desilylation Reactions of Tertiary Amine Cation Radicals. *J Am Chem Soc* **1994**, *116* (10), 4211–4220. https://doi.org/10.1021/JA00089A010/SUPPL_FILE/JA4211.PDF.

(139) Su, Z.; Mariano, P. S.; Falvey, D. E.; Yoon, U. C.; Oh, S. W. Dynamics of Anilinium Radical α-Heterolytic Fragmentation Processes. Electrofugal Group, Substituent, and Medium Effects on Desilylation, Decarboxylation, and Retro-Aldol Cleavage Pathways. *J Am Chem Soc* **1998**, *120* (41), 10676–10686. https://doi.org/10.1021/JA981541F/SUPPL_FILE/JA981541F_SA.PDF.